DOCTOR OF PHILOSOPHY

Understanding Vortex Reconnection in Complex Fluid Flows

McGavin, Philip

Award date:
2016

Understanding Vortex Reconnection in Complex Fluid Flows

By

Philip McGavin

A Thesis submitted for the degree of Doctor of Philosophy

Division of Mathematics

University of Dundee

Dundee

December 2016

Contents

List of figures

List of tables

Acknowledgements

I would like to thank my supervisor David for his immense help over the past 4 years. The rest of the MHD group; Gunnar, Alex, Simon, Peter, Gregor and Miriam and Nick who have also all been of great assistance with problems throughout.

Declaration

I declare that the following thesis is my own composition and that it has not been submitted before in application for a higher degree.

Philip McGavin

Certification

This is to certify that Philip McGavin has complied with all the requirements for the submission of this Doctor of Philosophy thesis to the University of Dundee.

Dr. David Pontin

Abstract

Reconnection of wingtip vortices behind aircrafts is thought to be a cause of wake turbulence, detrimental to air traffic control. We observe the reconnection process for three initial vortex tube set-ups; anti-parallel, orthogonal and anti-parallel with axial flow. From these we are able to identify each of the different reconnection processes observed and discussed for the magnetic reconnection case but not necessarily the vortex reconnection case; of both 2D and 3D reconnection. We use a finite different method to solve the Navier-Stokes equation for a large array of points.

We analyse the results of the first two scenarios for a range of Reynolds numbers ($Re = \Gamma/\nu$) to observe how the viscous term of Navier-Stokes affects the reconnection process. We were able to show that for an increase in Re we would see an increase in the reconnection rate due to the formation of thinner and stronger vortex sheets which are necessary for a faster reconnection. For higher values of Re we observed a Kelvin-Helmholtz instability within the vortex sheets and the formation of additional vortex rings during the reconnection process.

We simulate a range of axial flow values to observe how kinetic helicity and twist evolve with reconnection. We were able to identify the loss of twist in the vortex tubes due to 3D reconnection known as 'slipping'. In these and the orthogonal runs we observed the generation of null pairs and the formation of a separator

between them.

We utilised the plots of both vorticity isosurfaces and vorticity fieldlines to observe and analyse the reconnection process where isosurfaces have been the norm for vortex reconnection observations in previous work. The vorticity fieldlines allow us to observe the orientation of vorticity during reconnection and allow us to observe both the 'threads' and 'bridges' and their evolution together.

Chapter 1

Introduction

1.1 Motivation

Vortices are observed on a wide range of scales in fluids, and may be generated in various ways. Scales span from the meteorological; hurricanes, tidal currents and instabilities in clouds to the manmade; smoke rings, air cannons and from the wingtips of aircraft. Vorticity is even important in the natural world, with the v-like formation seen in migrating birds as they utilise the upward velocity of the vortices generated by the bird in front.

We will consider our results in the context of wingtip vortices as they are the primary cause of wake turbulence behind aircraft. Understanding of wingtip vortices is crucial for air traffic control where a delay, of the order of minutes depending on the size of aircraft, is imposed between the take-off or landing of aircraft. Wingtip vortices have been known to remain for up to 3 minutes after the aircraft has passed [32]. Measures have already been taken to mitigate their detrimental effect. The raised tips of aircraft wings are used to reduce the

strength of the wingtip vortices. Offsetting the location of the take-off or landing can also reduce this time however this is restricted by the length of the runway. Finding more ways of reducing the strength of these vortices or being able to fully understand their behaviour could save valuable time between flights and thus a great deal of money.

Under certain circumstances the topology of the vorticity fieldlines have been observed to change. The most commonly referred to instance of this is the Crow Instability [11] seen behind large aircraft such as a Boeing 747. Crow discussed the initial instability of the vortex tubes and how this leads to a sinusoidal perturbation of the tube with large amplitude that then reconnects. Motivated by this we shall begin with straight vortex tubes that have had a sinusoidal perturbation applied, and look into the process of reconnection in more detail. Vortex reconnection is also of importance for the discussion of singularities in fluids and could help towards solving one of the Millennium Prize problems.

1.2 Equations of Fluid Dynamics

The equations of fluid dynamics that will be used throughout are:

Navier-Stokes,

$$\frac{\partial \boldsymbol{v}}{\partial t} = -(\boldsymbol{v}\cdot\nabla)\boldsymbol{v} - \frac{1}{\rho}\nabla p + \nu\nabla^2\boldsymbol{v} + \frac{1}{3}\nu\nabla(\nabla\cdot\boldsymbol{v}) + \boldsymbol{g}, \tag{1.1}$$

vorticity,

$$\boldsymbol{\omega} = \nabla\times\boldsymbol{v}, \tag{1.2}$$

vorticity evolution,

$$\frac{D\boldsymbol{\omega}}{Dt} = (\boldsymbol{\omega}\cdot\nabla)\boldsymbol{v} - \boldsymbol{\omega}(\nabla\cdot\boldsymbol{v}) + \nu\nabla^2\boldsymbol{\omega}, \tag{1.3}$$

conservation of mass,

$$\frac{\partial \rho}{\partial t} = -\nabla\cdot(\rho\boldsymbol{v}), \tag{1.4}$$

conservation of energy,

$$\frac{\partial e}{\partial t} = -\nabla\cdot(e\boldsymbol{v}) - p\nabla\cdot\boldsymbol{v}, \tag{1.5}$$

and assuming an ideal gas,

$$p = (\gamma - 1)e. \tag{1.6}$$

It is common to assume that the velocity field is divergence free where it is known as incompressible flow. However work has been done on studying compressible vortex reconnection [57]. Incompressible flow is defined as

$$\nabla\cdot\boldsymbol{v} = 0. \tag{1.7}$$

This assumption allows us to simplify the equations (1.1), (1.3) and (1.4) for

incompressible flow:

Navier-Stokes,

$$\frac{\partial \boldsymbol{v}}{\partial t} = \nu \nabla^2 \boldsymbol{v} - \boldsymbol{v} \cdot \nabla \boldsymbol{v} - \frac{1}{\rho} \nabla p + \boldsymbol{g}, \tag{1.8}$$

vorticity evolution,

$$\frac{D\boldsymbol{\omega}}{Dt} = (\boldsymbol{\omega} \cdot \nabla)\boldsymbol{v} + \nu \nabla^2 \boldsymbol{\omega}, \tag{1.9}$$

and the conservation of mass,

$$\frac{\partial \rho}{\partial t} = -\boldsymbol{v} \cdot \nabla \rho, \tag{1.10}$$

where $\boldsymbol{v}$ is the velocity field, ν the kinematic viscosity, ρ the fluid density, p the pressure, $\boldsymbol{g}$ is the acceleration due to gravity, $\boldsymbol{\omega}$ the vorticity, γ the heat capacity ratio and e the internal energy.

Throughout the thesis we will refer to the Reynolds number (Re) [25] which is a dimensionless number giving the ratio of inertial and viscous forces within the fluid. The Reynolds number is defined as,

$$Re = \frac{vL}{\nu}, \tag{1.11}$$

where v, L and ν are a typical velocity, a typical length and the kinematic viscosity respectively. In line with previous studies of vortex tube dynamics we take

$$Re = \frac{\Gamma}{\nu}, \tag{1.12}$$

where Γ is the circulation of one of the vortex tubes, also equal to the vorticity flux through the tube. We use Γ as it is well defined and $\Gamma = \oint \boldsymbol{v} \cdot \mathrm{d}l$ around the cross-section of the vortex tube.

1.2.1 Volume Integrals

Throughout this thesis we will consider various volume-integrated quantities that give insight into the global evolution of the fluid. Their expected time evolution can be derived from the equations in Subsection 1.2, as described below. We will be interested principally in the enstrophy, kinetic energy and kinetic helicity [12]. Simplest to describe would be kinetic energy which measures the total velocity density of the box and we expect to be fairly conserved. Enstrophy measures the same but for the vorticity and shows us when high gradients of velocity form in the box, especially useful for reconnection. Kinetic helicity is very important for discussing topology as it will help show change of twist within the vortex tube or any linking involved between fieldlines [29]. The volume integrals we are interested in are;

enstrophy,

$$\frac{1}{2}\int_V \boldsymbol{\omega}^2 \,\mathrm{d}V, \tag{1.13}$$

kinetic energy,

$$\frac{1}{2}\int_V \rho\boldsymbol{v}^2 \,\mathrm{d}V \tag{1.14}$$

and kinetic helicity,

$$\int_{V_4} \boldsymbol{v}\cdot\boldsymbol{\omega} \,\mathrm{d}V. \tag{1.15}$$

Enstrophy and kinetic energy are integrated over the entire simulated box. However due to symmetries that will be shown in Chapter 2 the kinetic helicity will always be zero integrated over the entire box. To observe the change in helicity over time we integrate over a quarter of the box, referred to as V_4. Here we derive the evolution equations for kinetic energy, enstrophy and helicity so that we can understand which elements of the system are changing these variables. The assumptions made in the derivations are such that $\boldsymbol{v}\cdot\boldsymbol{n} = 0$ and $\boldsymbol{\omega}\times\boldsymbol{n} = 0$,

where $\boldsymbol{n}$ is the normal vector on the boundary. Through initial tests we found the system to be barotropic and can therefore assume that $\rho^{-1}\nabla p = \nabla\tilde{p}$.

Consider the time derivative of the volume integral for kinetic energy, we can expand this using the product and chain rule as such:

$$\frac{\partial}{\partial t}\int_V \rho\frac{\boldsymbol{v}^2}{2}\,\mathrm{d}V = \int_V \left[\frac{\boldsymbol{v}^2}{2}\frac{\partial\rho}{\partial t} + \rho\boldsymbol{v}\cdot\frac{\partial\boldsymbol{v}}{\partial t}\right]\mathrm{d}V. \tag{1.16}$$

Using the continuity equation

$$\frac{\partial\rho}{\partial t} = -\nabla\cdot(\rho\boldsymbol{v}), \tag{1.17}$$

and Navier-Stokes equation,

$$\frac{\partial\boldsymbol{v}}{\partial t} = -(\boldsymbol{v}\cdot\nabla)\boldsymbol{v} - \nabla\tilde{p} + \nu\nabla^2\boldsymbol{v} + \frac{1}{3}\nu\nabla(\nabla\cdot\boldsymbol{v}) \tag{1.18}$$

$$= -\frac{1}{2}\nabla(\boldsymbol{v}^2) - \boldsymbol{\omega}\times\boldsymbol{v} - \nabla\tilde{p} + \frac{4}{3}\nu\nabla(\nabla\cdot\boldsymbol{v}) - \nu(\nabla\times\boldsymbol{\omega}), \tag{1.19}$$

we can eliminate the time derivatives from the right hand side

$$\frac{\partial}{\partial t}\int_V \rho\frac{\boldsymbol{v}^2}{2}\,\mathrm{d}V = \int_V \Bigg[-\frac{\boldsymbol{v}^2}{2}\nabla\cdot(\rho\boldsymbol{v}) + \rho\nu\boldsymbol{v}\cdot\left(\frac{4}{3}\nabla(\nabla\cdot\boldsymbol{v}) - \nabla\times\boldsymbol{\omega}\right) - \rho\boldsymbol{v}\cdot\left(\frac{1}{2}\nabla(\boldsymbol{v}^2) + \boldsymbol{\omega}\times\boldsymbol{v} + \nabla\tilde{p}\right)\Bigg]\mathrm{d}V. \tag{1.20}$$

By substituting

$$\boldsymbol{v}\cdot(\boldsymbol{\omega}\times\boldsymbol{v}) = 0, \tag{1.21}$$

$$\boldsymbol{v}\cdot(\nabla\times\boldsymbol{\omega}) = \boldsymbol{\omega}\cdot(\nabla\times\boldsymbol{v}) - \nabla\cdot(\boldsymbol{v}\times\boldsymbol{\omega}) = \boldsymbol{\omega}^2 - \nabla\cdot(\boldsymbol{v}\times\boldsymbol{\omega}), \tag{1.22}$$

we can further expand to

$$\frac{\partial}{\partial t}\int_V \rho\frac{\boldsymbol{v}^2}{2}\,\mathrm{d}V = \int_V -\frac{\boldsymbol{v}^2}{2}\nabla\cdot(\rho\boldsymbol{v}) + \rho\nu\boldsymbol{v}\cdot\left(\frac{4}{3}\nabla(\nabla\cdot\boldsymbol{v})\right) - \rho\nu\boldsymbol{\omega}^2 + \rho\nu\nabla\cdot(\boldsymbol{v}\times\boldsymbol{\omega}) - \rho\boldsymbol{v}\cdot\left(\frac{1}{2}\nabla(\boldsymbol{v}^2)\right) - \rho\boldsymbol{v}\cdot\nabla\tilde{p}\,\mathrm{d}V. \quad (1.23)$$

Using Gauss' theorem [38] we can obtain

$$-\frac{1}{2}\int_V[\boldsymbol{v}^2\nabla\cdot(\rho\boldsymbol{v}) + \rho\boldsymbol{v}\cdot\nabla(\boldsymbol{v}^2)]\,\mathrm{d}V = -\frac{1}{2}\int_S \boldsymbol{v}^2\rho\boldsymbol{v}\cdot\boldsymbol{n}\,\mathrm{d}A. \quad (1.24)$$

As the box is periodic the surface integrals will cancel leading us to the compressible equation for the rate of change of kinetic energy

$$\frac{\partial}{\partial t}\int_V \rho\frac{\boldsymbol{v}^2}{2}\,\mathrm{d}V = \int_V\left[-\rho\nu\boldsymbol{\omega}^2 + \rho\nu\boldsymbol{v}\cdot\left(\frac{4}{3}\nabla(\nabla\cdot\boldsymbol{v})\right) - \rho\nu\nabla\tilde{p} + \rho\nu\nabla\cdot(\boldsymbol{v}\times\boldsymbol{\omega})\right]\mathrm{d}V, \quad (1.25)$$

and the incompressible version

$$\frac{\partial}{\partial t}\int_V \rho\frac{\boldsymbol{v}^2}{2}\,\mathrm{d}V = -\rho\nu\int_V \boldsymbol{\omega}^2\,\mathrm{d}V. \quad (1.26)$$

As a large peak in enstrophy has been shown in equations (1.25) and (1.26) to cause a large drop in kinetic energy it will be of interest to observe when this peak will occur. This has been studied in the past by Doering and Lu [15] and Ayala and Protas [4]. To obtain the rate of change of the enstrophy within the box we first use the chain rule on the enstrophy derivative:

$$\frac{\partial}{\partial t}\int_V \frac{\boldsymbol{\omega}^2}{2}\,\mathrm{d}V = \int_V\left[\boldsymbol{\omega}\cdot\frac{\partial\boldsymbol{\omega}}{\partial t}\right]\mathrm{d}V, \quad (1.27)$$

substituting in the vorticity evolution equation we eliminate the time derivative

$$\frac{\partial}{\partial t}\int_V \frac{\boldsymbol{\omega}^2}{2}\,\mathrm{d}V = \int_V \left[\boldsymbol{\omega}\cdot\left((\boldsymbol{\omega}\cdot\nabla)\boldsymbol{v} - (\boldsymbol{v}\cdot\nabla)\boldsymbol{\omega} - \boldsymbol{\omega}(\nabla\cdot\boldsymbol{v}) + \nu\nabla^2\boldsymbol{\omega}\right)\right]\mathrm{d}V, \quad (1.28)$$

re-arranging the terms

$$\frac{\partial}{\partial t}\int_V \frac{\boldsymbol{\omega}^2}{2}\,\mathrm{d}V = \int_V \left[\boldsymbol{\omega}\cdot(\nabla\times(\boldsymbol{v}\times\boldsymbol{\omega}) - \nu\nabla\times(\nabla\times\boldsymbol{\omega}))\right]\mathrm{d}V, \quad (1.29)$$

and expanding out we obtain

$$\frac{\partial}{\partial t}\int_V \frac{\boldsymbol{\omega}^2}{2}\,\mathrm{d}V = \int_V [(\boldsymbol{v}\times\boldsymbol{\omega})\cdot(\nabla\times\boldsymbol{\omega}) - \nabla\cdot(\boldsymbol{\omega}\times(\boldsymbol{v}\times\boldsymbol{\omega})) - \nu(\nabla\times\boldsymbol{\omega})^2 + \nu\nabla\cdot(\boldsymbol{\omega}\times(\nabla\times\boldsymbol{\omega}))]\,\mathrm{d}V. \quad (1.30)$$

Using Gauss' theorem we can change some terms to surface integrals

$$\frac{\partial}{\partial t}\int_V \frac{\boldsymbol{\omega}^2}{2}\,\mathrm{d}V = \int_V [(\boldsymbol{v}\times\boldsymbol{\omega})\cdot(\nabla\times\boldsymbol{\omega}) - \nu(\nabla\times\boldsymbol{\omega})^2]\,\mathrm{d}V + \int_S [\nu\boldsymbol{\omega}\times(\nabla\times\boldsymbol{\omega}) - \boldsymbol{\omega}\times(\boldsymbol{v}\times\boldsymbol{\omega})]\cdot\boldsymbol{n}\,\mathrm{d}a. \quad (1.31)$$

Due to the periodicity of the box these surface integrals equal zero. We can therefore determine the rate of change of the enstrophy in the system as:

$$\frac{\partial}{\partial t}\int_V \frac{\boldsymbol{\omega}^2}{2}\,\mathrm{d}V = \int_V [(\boldsymbol{v}\times\boldsymbol{\omega})\cdot(\nabla\times\boldsymbol{\omega}) - \nu(\nabla\times\boldsymbol{\omega})^2]\,\mathrm{d}V, \quad (1.32)$$

which is also true for incompressible flow.

For the rate of change of helicity we use the product rule on the helicity time derivative:

$$\frac{\partial}{\partial t}\int_{V_4} \boldsymbol{v}\cdot\boldsymbol{\omega}\,\mathrm{d}V = \int_{V_4}\left[\boldsymbol{\omega}\cdot\frac{\partial\boldsymbol{v}}{\partial t} + \boldsymbol{v}\cdot\frac{\partial\boldsymbol{\omega}}{\partial t}\right]\mathrm{d}V, \quad (1.33)$$

we then substitute the vorticity equation into the second term

$$\boldsymbol{v} \cdot \frac{\partial \boldsymbol{\omega}}{\partial t} = \boldsymbol{v} \cdot [(\boldsymbol{\omega} \cdot \nabla)\boldsymbol{v} - (\boldsymbol{v} \cdot \nabla)\boldsymbol{\omega} + \nu \nabla^2 \boldsymbol{\omega}], \tag{1.34}$$

and expand out to

$$\boldsymbol{v} \cdot \frac{\partial \boldsymbol{\omega}}{\partial t} = -\nu \boldsymbol{v} \cdot \nabla \times (\nabla \times \boldsymbol{\omega}), \tag{1.35}$$

$$\boldsymbol{v} \cdot \frac{\partial \boldsymbol{\omega}}{\partial t} = -\nu \boldsymbol{\omega} \cdot (\nabla \times \boldsymbol{\omega}) + \nu \nabla \cdot (\boldsymbol{v} \times (\nabla \times \boldsymbol{\omega})), \tag{1.36}$$

we then substitute the Navier-Stokes equation into the second term of (1.33)

$$\boldsymbol{\omega} \cdot \frac{\partial \boldsymbol{v}}{\partial t} = \boldsymbol{\omega} \cdot \left[-\frac{1}{2}\nabla(\boldsymbol{v}^2) - \boldsymbol{\omega} \times \boldsymbol{v} - \nabla \tilde{p} + \frac{4}{3}\nu \nabla(\nabla \cdot \boldsymbol{v}) - \nu(\nabla \times \boldsymbol{\omega}) \right]. \tag{1.37}$$

(1.36) and (1.37) are substituted into (1.33). This provides us with the rate of change of the helicity for a quarter of the box

$$\begin{aligned} \frac{\partial}{\partial t} \int_{V_4} \boldsymbol{v} \cdot \boldsymbol{\omega} = \int_{V_4} \Bigg[& -2\nu \boldsymbol{\omega} \cdot (\nabla \times \boldsymbol{\omega}) + \frac{4}{3}\nu \boldsymbol{\omega} \cdot (\nabla(\nabla \cdot \boldsymbol{v})) \\ & - \frac{1}{2}\boldsymbol{\omega} \cdot \nabla(\boldsymbol{v}^2) - \boldsymbol{\omega} \cdot \nabla \tilde{p} + \nu \nabla \cdot (\boldsymbol{v} \times (\nabla \times \boldsymbol{\omega})) \Bigg] \, \mathrm{d}V. \end{aligned} \tag{1.38}$$

We simplify some terms with Gauss' theorem

$$\int_{V_4} \nu \nabla \cdot (\boldsymbol{v} \times (\nabla \times \boldsymbol{\omega})) \, \mathrm{d}V = \int_S \nu \boldsymbol{v} \times (\nabla \times \boldsymbol{\omega}) \cdot \boldsymbol{n} \, \mathrm{d}a, \tag{1.39}$$

$$\int_{V_4} \boldsymbol{\omega} \cdot \nabla \tilde{p} \, \mathrm{d}V = \int_S \tilde{p} \boldsymbol{\omega} \cdot \boldsymbol{n} \, \mathrm{d}a - \int_{V_4} \tilde{p} \, \nabla \cdot \boldsymbol{\omega} \, \mathrm{d}V, \tag{1.40}$$

$$\int_{V_4} \frac{1}{2}\boldsymbol{\omega} \cdot \nabla(\boldsymbol{v}^2) \, \mathrm{d}V = \int_S \frac{1}{2}\boldsymbol{v}^2 \boldsymbol{\omega} \cdot \boldsymbol{n} \, \mathrm{d}a - \int_{V_4} \frac{1}{2}\boldsymbol{v}^2 (\nabla \cdot \boldsymbol{\omega}) \, \mathrm{d}V, \tag{1.41}$$

as $(\nabla \cdot \boldsymbol{\omega}) = 0$ this simplifies further and we can therefore show that

$$\frac{\partial}{\partial t}\int_{V_4} \boldsymbol{v}\cdot\boldsymbol{\omega}\,\mathrm{d}V = \int_{V_4}\left[-2\nu\boldsymbol{\omega}\cdot(\nabla\times\boldsymbol{\omega}) + \frac{4}{3}\nu\boldsymbol{\omega}\cdot\nabla(\nabla\cdot\boldsymbol{v})\right]\mathrm{d}V + \int_S\left[\nu\boldsymbol{v}\times(\nabla\times\boldsymbol{\omega}) - \tilde{p}\boldsymbol{\omega} - \frac{1}{2}\boldsymbol{v}^2\boldsymbol{\omega}\right]\cdot\boldsymbol{n}\,\mathrm{d}a, \quad (1.42)$$

and the subsequent incompressible version

$$\frac{\partial}{\partial t}\int_{V_4} \boldsymbol{v}\cdot\boldsymbol{\omega}\,\mathrm{d}V = \int_{V_4}\left[-2\nu\boldsymbol{\omega}\cdot(\nabla\times\boldsymbol{\omega})\right]\mathrm{d}V + \int_S\left[\nu\boldsymbol{v}\times(\nabla\times\boldsymbol{\omega}) - \frac{1}{2}\boldsymbol{v}^2\boldsymbol{\omega}\right]\cdot\boldsymbol{n}\,\mathrm{d}a. \quad (1.43)$$

1.3 Vortex Reconnection

In inviscid flow, vortex lines are material lines meaning that fluid elements that exist on the same vorticity fieldline will still exist on the same vorticity fieldline at a different point in time. Neglecting the viscous terms of equation (1.3) we can show

$$\frac{D\boldsymbol{\omega}}{Dt} + \boldsymbol{\omega}(\nabla \cdot \boldsymbol{v}) = (\boldsymbol{\omega} \cdot \nabla)\boldsymbol{v}. \tag{1.44}$$

Using equation (1.4) and dividing through by ρ we can therefore show

$$\frac{1}{\rho}\frac{D\boldsymbol{\omega}}{Dt} - \frac{1}{\rho^2}\frac{D\rho}{Dt}\boldsymbol{\omega} = \frac{1}{\rho}(\boldsymbol{\omega} \cdot \nabla)\boldsymbol{v}, \tag{1.45}$$

$$\frac{D}{Dt}\left(\frac{\boldsymbol{\omega}}{\rho}\right) = \left(\frac{\boldsymbol{\omega}}{\rho} \cdot \nabla\right)\boldsymbol{v}, \tag{1.46}$$

comparing to the requirement to be 'frozen' into the fluid flow, $\boldsymbol{v}$, [29, 44]:

$$\frac{D}{Dt}(\delta\boldsymbol{x}) = (\delta\boldsymbol{x} \cdot \nabla)\boldsymbol{v}, \tag{1.47}$$

where $\delta\boldsymbol{x}$ is a material line element in the flow. We can therefore say that the vorticity is frozen into the fluid flow $\boldsymbol{v}$. However as viscosity is introduced to the system this frozen in condition may break down. As these fieldlines pass through certain 'reconnection regions' fluid elements that were once connected by a vortex line will no longer share the same fieldline. This is know as 'cut and connect' , 'cross linking' or reconnection but we shall refer to it as the latter. When discussing reconnection we generally use vortex tubes which are bundles of vorticity fieldlines with a Gaussian strength distribution such that there is a region of (near) zero vorticity initially between the vortex tubes. With this we can discuss the interaction between the two initially separate tubes and easily measure the reconnection by measuring the vorticity flux [1] of each tube. We

discuss in Section 1.4 the history of the study of vortex reconnection.

1.3.1 Parallels with Magnetic Reconnection

Magnetic reconnection has been researched more vigorously than the vortex case. It is a key process in astrophysical and laboratory plasmas, and is thought to be responsible for facilitating solar flares and heating the Sun's outer atmosphere. The theory behind magnetic reconnection in three dimensions is discussed in Hesse and Schindler [22]. We hope to use the previous work in magnetic reconnection and apply it to the vorticity case to help explain some of the phenomena. To do this we find the parallels between the magnetic and vorticity equations involved [23].

We begin by comparing the Vorticity Evolution Equation (1.9) with the Magnetic Induction Equation assuming $\boldsymbol{v}$ is incompressible

$$\frac{D\boldsymbol{B}}{Dt} = (\boldsymbol{B} \cdot \nabla)\boldsymbol{v} + \frac{1}{\mu_0 \sigma}\nabla^2 \boldsymbol{B}. \tag{1.48}$$

We look to find the analogous variables such that we can obtain the vortex equivalent of the magnetic reconnection rate similar to the work by Kuznetsov and Ruban [35]. Hesse and Schindler [22] demonstrated that 3D magnetic reconnection requires a non-zero component of the electric field parallel to the magnetic field. Then they showed that the rate of change of connectivity between plasma elements can be measured by evaluating the integral of the electric field parallel to the magnetic field along a magnetic fieldline, and then taking the maximum of this quantity over all magnetic fieldlines passing through what is known as the 'reconnection region' where $\boldsymbol{E} \cdot \boldsymbol{B} \neq 0$. This is known as the 3D magnetic

reconnection rate

$$\left(\int \boldsymbol{E}_{\parallel} dl \right)_{max}. \tag{1.49}$$

To find the vortex analogue of this we begin by utilising Maxwell's equations

$$\nabla \times \boldsymbol{E} = -\frac{\partial \boldsymbol{B}}{\partial t}, \tag{1.50}$$

$$\nabla \times \boldsymbol{A} = \boldsymbol{B}, \tag{1.51}$$

$$\boldsymbol{E} = -\frac{\partial \boldsymbol{A}}{\partial t} - \nabla \phi, \tag{1.52}$$

and Ohm's Law

$$\boldsymbol{E} + \boldsymbol{v} \times \boldsymbol{B} = \boldsymbol{R}, \tag{1.53}$$

where $\boldsymbol{R}$ is the non-ideal component of Ohm's Law and equal to

$$\boldsymbol{R} = \frac{1}{\sigma}\boldsymbol{j} = \frac{1}{\mu\sigma}\nabla \times \boldsymbol{B} = \eta \nabla \times \boldsymbol{B}. \tag{1.54}$$

We can then re-arrange and compare Navier-Stokes (1.8) with Ohm's Law (1.53)

$$-\frac{\partial \boldsymbol{v}}{\partial t} - \nabla \left(\tilde{p} + \frac{\boldsymbol{v}^2}{2} - \frac{4}{3}\nu(\nabla \cdot \boldsymbol{v}) \right) + \boldsymbol{v} \times \boldsymbol{\omega} = \nu \nabla \times \boldsymbol{\omega}, \tag{1.55}$$

$$-\frac{\partial \boldsymbol{A}}{\partial t} - \nabla \phi + \boldsymbol{v} \times \boldsymbol{B} = \eta \nabla \times \boldsymbol{B}. \tag{1.56}$$

We find the following analogues between the magnetic and vorticity cases

$$\boldsymbol{A} \leftrightarrow \boldsymbol{v} \qquad \boldsymbol{B} \leftrightarrow \boldsymbol{\omega}, \tag{1.57}$$

$$\phi \leftrightarrow \tilde{p} + \frac{\boldsymbol{v}^2}{2} - \frac{4}{3}\nu(\nabla \cdot \boldsymbol{v}) \qquad \eta \nabla \times \boldsymbol{B} \leftrightarrow \nu \nabla \times \boldsymbol{\omega}, \tag{1.58}$$

giving us the 3D vortex reconnection rate

$$\left(\nu \int \nabla \times \boldsymbol{\omega}_{\parallel} dl\right)_{max}. \tag{1.59}$$

This is equivalent to the 2D reconnection case that will be discussed in Subsection 1.3.2 although describes a different surface that the vorticity flux is reconnecting through. We can therefore use the vortex-magnetic analogues and the 3D vortex reconnection rate to better understand the vortex reconnection. The fundamental difference between vortex and magnetic reconnection is due to the vorticity and magnetic field [20]. Vorticity is tied to the velocity field, see equation (1.2) whereas the magnetic field is not. This causes restrictions in ways we can set up our initial conditions in such a way that they reconnect.

1.3.2 2D and 3D Reconnection

Vortex lines can reconnect in different ways, generally described in the magnetic case as either 2D or 3D reconnection. 2D reconnection occurs in a plane, hence the name, and is dependent on the $(\nabla \times \boldsymbol{\omega})$ field being non-zero at a null point of the vorticity field which occurs when anti-parallel vorticity fieldlines approach each other. 3D reconnection on the other hand depends on $(\nabla \times \boldsymbol{\omega}) \cdot \boldsymbol{\omega}$ being locally non-zero. Here we shall discuss the different types of reconnection in more detail.

Often seen in low Reynolds number flow, vortex annihilation leads to a loss in vorticity flux for both tubes as shown in Figure 1.1(a). As the anti-parallel vortex lines meet at the null-line they cancel out. This type of annihilation depends upon a vorticity field independent of an x-component such that the fieldlines do not reconnect in a 2D X-null point manner to be discussed. We can find the rate of annihilation occurs by using Stokes' Theorem and the $(\nabla \times \boldsymbol{\omega})$ component

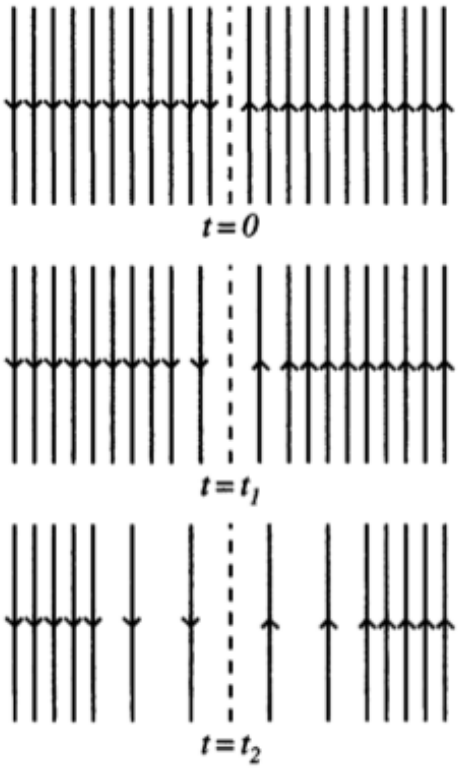

(a)

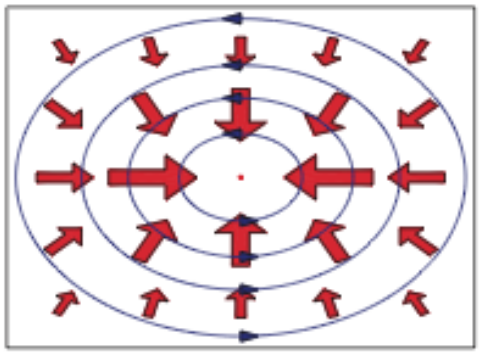

(b)

Figure 1.1: Examples of 2D annihilation (a) anti-parallel from Priest and Forbes [49] and (b) O-null vortex ring from Hornig [23].

perpendicular to the plane in Figure 1.1(a) and will be discussed later in this section. This is discussed in more detail in Buntine and Pullin [7] and in Priest and Forbes [49]. The annihilation of a vortex ring is illustrated in Figure 1.1(b) with the vortex ring pressed in on itself either due to viscous dissipation or an outside force. This occurs with an O-null in the centre which will have a non-zero perpendicular ($\nabla \times \boldsymbol{\omega}$) which can be used to measure annihilation in a similar manner to the 2D anti-parallel case in (a). This is discussed in more detail in Hornig [23].

The type of reconnection most common in discussions on vortex reconnection would be the 2D example occurring at an X-type null illustrated in Figure 1.2. We can see as the anti-parallel vortex tubes approach each other from the top

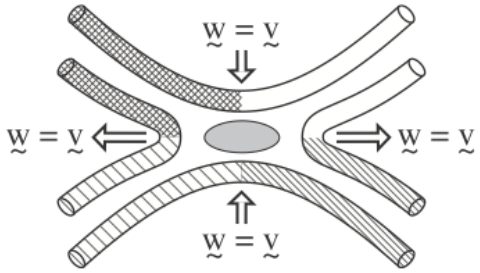

Figure 1.2: "Breaking and rejoining of two flux tubes in 2D to form two new flux tubes." Priest et al. [50].

and bottom of the image and pass through the null point (strictly speaking a null line) in the centre. The fieldlines break and connect with partners in the opposite tube leading to the vortex tubes moving away from the null point on either side. This type of reconnection is the one we will be discussing most throughout. It is observed in Melander and Hussain [41], Hussain and Duraisamy [24] and Van Rees et al. [56] which we will be comparing to. For the magnetic case it is discussed in detail in Priest and Forbes [49].

For measuring 2D annihilation or reconnection we first consider the rate of change of vorticity flux on a surface, S. S describes a surface in which one of the two vortex tube passes through and the null line between the two tubes forms part of the boundary of S,

$$\frac{\partial}{\partial t}\int_S \boldsymbol{\omega}\cdot\boldsymbol{n}\,\mathrm{d}S = \int_S \frac{\partial \boldsymbol{\omega}}{\partial t}\cdot\boldsymbol{n}\,\mathrm{d}S, \tag{1.60}$$

expanding the vorticity equation to eliminate the time derivative we obtain

$$\frac{\partial}{\partial t}\int_S \boldsymbol{\omega}\cdot\boldsymbol{n}\,\mathrm{d}S = \int_S [(\boldsymbol{\omega}\cdot\nabla)\boldsymbol{v} - (\boldsymbol{v}\cdot\nabla)\boldsymbol{\omega} + \nu\nabla^2\boldsymbol{\omega}]\cdot\boldsymbol{n}\,\mathrm{d}S \tag{1.61}$$

$$= \int_S [\nabla\times(\boldsymbol{v}\times\boldsymbol{\omega}) - \nu\nabla\times(\nabla\times\boldsymbol{\omega})]\cdot\mathrm{d}S, \tag{1.62}$$

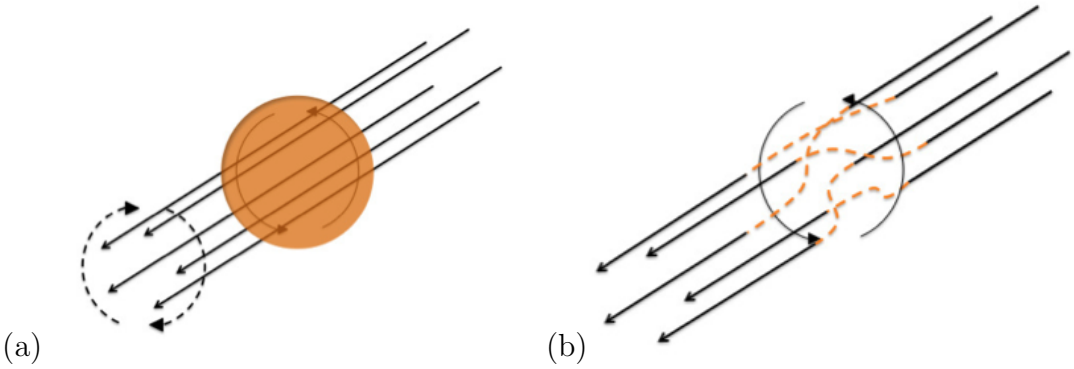

Figure 1.3: Vorticity fieldlines (a) before and (b) after 3D reconnection from Wyper and Hesse [59].

using Stokes' Theorem [40] this becomes

$$\frac{\partial}{\partial t}\int_S \boldsymbol{\omega}\cdot\boldsymbol{n}\,\mathrm{d}S = \oint_{\partial S} \boldsymbol{v}\times\boldsymbol{\omega}\cdot\mathrm{d}l - \nu\oint_{\partial S}(\nabla\times\boldsymbol{\omega})\cdot\mathrm{d}l. \tag{1.63}$$

As this is 2D the reconnection occurs where the vorticity is zero so this becomes

$$\frac{\partial}{\partial t}\int_S \boldsymbol{\omega}\cdot\boldsymbol{n}\,\mathrm{d}S = -\nu\oint_{\partial S}(\nabla\times\boldsymbol{\omega})\cdot\mathrm{d}l. \tag{1.64}$$

We can therefore calculate the reconnection rate for the 2D case by integrating along the null-line then around the vortex tube.

We now move on to 3D reconnection, also known as 'slipping reconnection', illustrated in Figure 1.3. We can visualise the simplest form of this reconnection within a single vortex tube. As a reconnection region, shown in orange where $(\nabla\times\boldsymbol{\omega})\cdot\boldsymbol{\omega}$ is non-zero, forms within the tube the fieldlines begin 'slipping' and reconnecting with neighbouring fieldlines. This reconnection leads to a change in helicity and twist within the vortex tube measured by $(\nu\int\nabla\times\boldsymbol{\omega}_{\parallel}dl)_{max}$. This type of reconnection has been discussed in depth for the magnetic case [21] and we hope to find the vorticity counterpart and its effect on the wingtip vortices'

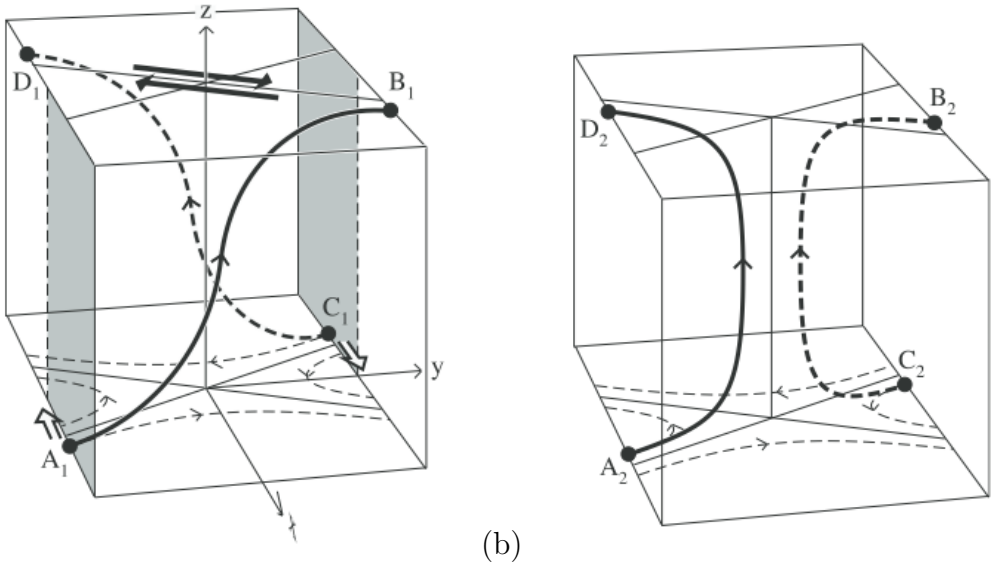

(a) (b)

Figure 1.4: Fieldlines (a) before and (b) after 3D Reconnection from Priest et al. [50].

evolution.

Non-zero $(\nabla \times \boldsymbol{\omega}) \cdot \boldsymbol{\omega}$ can also be found between two vortex tubes illustrated in Figure 1.4. In the xy-plane we see a similar scenario to Figure 1.2 but the X-null point instead has a vorticity component perpendicular to the plane in z. In (a) we can see the fieldlines as they approach the centre of the box are at an angle to each other leading to this non-zero $(\nabla \times \boldsymbol{\omega}) \cdot \boldsymbol{\omega}$ component in the z-axis. The reconnection region of non-zero $(\nabla \times \boldsymbol{\omega}) \cdot \boldsymbol{\omega}$ is not restricted to the central axis and fills a volume around it and there will be 'slipping' of fieldlines as they approach the central axis before they reconnect with the other vortex tube. This has been shown in the magnetic case previously [50]. In (b) we can see the reconnected fieldlines as they leave the reconnection region. We hope to find a vorticity set-up that will lead to a reconnection like this so that we can compare its behaviour to the 2D case.

As we shall see below, in some of our simulations a pair of 3D null points can

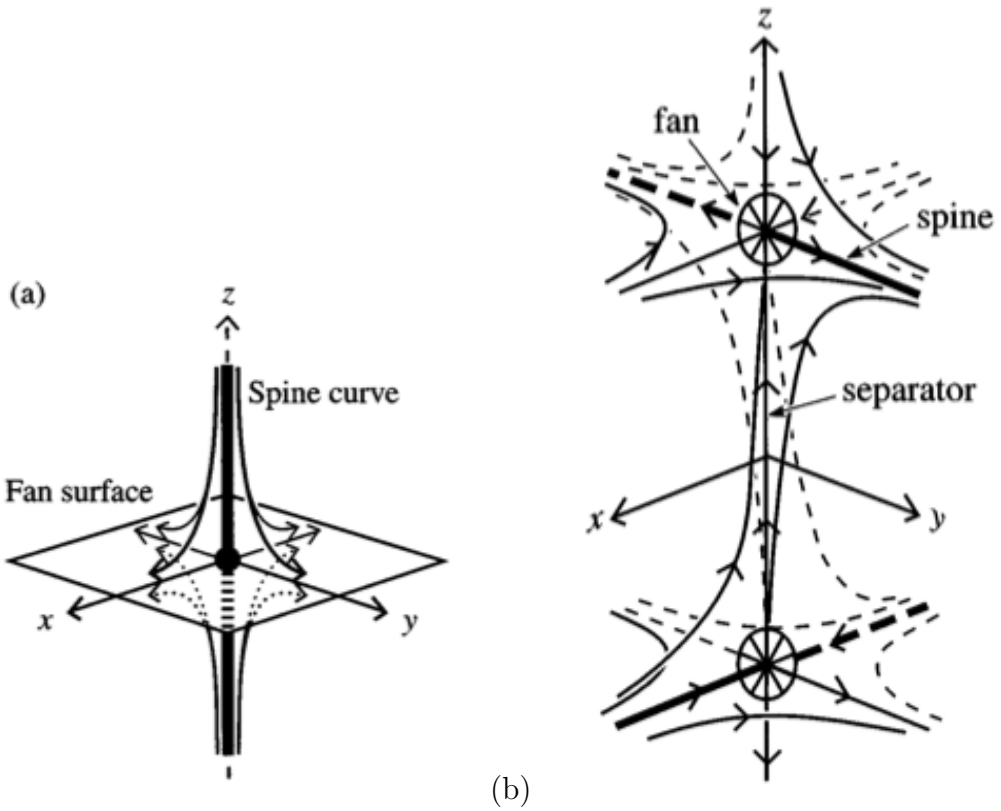

(a) (b)

Figure 1.5: Example of (a) 3D null point and (b) separator from Priest and Forbes [49].

be created in the z-axis shown in Figure 1.4 leading to a special case of this reconnection. 3D null points, shown in Figure 1.5(a) are always created in pairs. Each one has a 'spine' curve and a 'fan' surface leading to and from it or vice versa. The spine and fan can be found using the eigenvectors of the vorticity field around the null point. The fieldline between these nulls is known as a 'separator' and is part of a fan of both null points. The formation of this structure alters the approach and reconnection of the fieldlines observed in Figure 1.5. The separator and null points are discussed for the magnetic case in Priest and Forbes [49] and we hope to find some vorticity examples in the results chapters.

1.4 History

Vortex reconnection took off from Crow's work in 1970 [11]. Crow discussed the behaviour of wingtip vortices and their tendency to undergo a sinusoidal instability which then cause the vortices to reconnect with each other and form vortex rings. This had been observed to occur behind aircraft due to moisture forming along the centres of the wingtip vortices. Vortex Reconnection has been discussed in more detail in Greene [20] and Kida and Takoaka [29]. From Crow's work many people have used a model of two anti-parallel vortex tubes with a sinusoidal perturbation angled towards each other such that they will reconnect. Pumir and Kerr [51] discussed the formation of vortex sheets with this set up with a Reynolds number up to 5000 in 1987 and this was continued in more detail for a Reynolds number of 3200 in Kerr and Hussain [28]. Melander and Hussain [41, 42] discussed the topological aspects of reconnection in 1989 with a Reynolds number of 1000. Reconnection with a Reynolds number of 3500 was observed by Weiguo et al. [58] in 1995 with a range of different initial conditions observing the subsequent effects. Hussain and Duraisamy [24] observed the topological aspects with a Reynolds number of 9000 demonstrating instabilities due to the high Reynolds number in 2011. Most recently in 2012 van Rees et al. [56] simulated anti-parallel vortex reconnection with a Reynolds number of 10^4 and discussed the topology and the changes in helicity density during reconnection. More work has been done utilising this anti-parallel set-up discussing different aspects of its evolution [8, 18, 19, 26, 34, 39, 48, 54, 57]. Other set-ups have been investigated such as the collision of two vortex rings in Ashurst and Meiron [3] and Kida et al. [30] and more recently the reconnection of a trefoil knot in Kerr [27].

Spalart [55] discussed the wingtip vortices and their effects on air traffic control

and the issues that arise from this with an ongoing battle of safety, waiting long enough for the vortices to decay or move out the way, and efficiency, with airlines wanting the delay between aircraft take-off and landing minimal. So it is clear to see why a thorough understanding of the vortices' behaviour is important. Kleckner and Irvine [33] showed a method of 3D printing hydrofoils to generate vortices including knotted vortices to view their evolution with micro-bubbles.

From these papers we will draw most detailed comparisons with Melander and Hussain [41], Hussain and Duraisamy [24] and Van Rees et al. [56]. The first two provide great insight on the evolution of the vortex tubes and vorticity isosurfaces we will be able to compare to. The latter provides an in-depth discussion on changes of local helicity throughout the evolution.

1.5 Computational Code

We use a fully 3D computational code to study the fluid evolution, originally written with the option of studying magnetohydrodynamic evolution of a plasma [46]. By turning off the magnetic field the code simply becomes a hydrodynamic code. It solves Navier-Stokes equation with a finite difference method and is ideally suited for large arrays which will be needed for the Reynolds numbers we hope to simulate. This code utilises High Performance Fortran and conserves mass, momentum and energy. A Fortran file is used to create an array of the initial momentum of the system. The code solves equations (1.4), (1.1), (1.5) and (1.6). This code uses a sixth-order accurate method for finding partial derivatives and subsequently a fifth-order accurate method for interpolating the results to the staggered grid. The high-order differencing reduces numerical dissipation. For the time-stepping a third-order predictor-corrector method is used with a fourth-order error in Δt. Multiple conditions are in place to restrict the size of the time step, Δt, depending on the sound speed of the system and the viscous diffusion respectively,

$$(U + c_s)\Delta t/\Delta x \leq C < 1, \tag{1.65}$$

$$\nu f \Delta t/\Delta x^2 \leq C, \tag{1.66}$$

where U is the speed of the fluid, c_s is the sound speed, Δt is the time step, Δx is the grid spacing, C is the Courant number and f is a factor dependent on the diffusion quenching which is equal to 20 in this case [46]. These conditions are evaluated on all grid points to find the largest possible value of Δt that satisfies all of them. For the simulations we observed Δt remains roughly constant throughout at $\sim 3 \times 10^{-4}$ with $C = 0.1$ to avoid numerical errors we experienced

at higher values. The St Andrews MHD cluster was utilised to run the simulations each time with 32 nodes. Each node contains 12 cores (two 2/8/2.93 GHz 6-core Intel Xeon X5660/X5670 processors), 24GB of memory and 60GB of local scratch.

1.6 Goals

We aim to find a set-up similar to previous papers with two separate vortex tubes that will rotate towards each other and ultimately reconnect. Using knowledge from the magnetic case we hope to better understand the reconnection process. Due to the finite difference method utilised on the rectangular grid we can easily view the velocity and vorticity fieldlines at chosen points in time and can observe the behaviour of the fieldlines which has not been used as much as the vorticity isosurfaces in previous analyses of vortex reconnection. These previous studies implicitly assumed that the vorticity isosurfaces can be considered as flux surfaces describing the vortex lines, although it has been pointed out that this is not in fact the case [29]. Once a satisfactory initial condition is found we shall run the simulation for a range of Reynolds numbers to see how the viscous and convective terms affect the reconnection. With the velocity output at chosen times we can easily track the volume integrals throughout the simulation and will see how the Reynolds numbers affect this also.

We expect that the anti-parallel vortex tubes used in previous papers that we will be simulating will undergo a 2D reconnection with one another. In later chapters we study different configurations of vortex tubes, and observe different types of reconnection to occur. In particular, we shall find an initial condition with axial flow within the vortex tubes similar to Van Rees et al. [56]. We use two set-ups with axial flow, one with the axial flow in the same direction which will better simulate the wingtip vortices of aircraft and another with opposite axial flow such that we have non-zero helicity initially and we can observe the helicity of the system in more depth.

Chapter 2

Anti-Parallel Vortex Tubes

2.1 Set-Up

2.1.1 Velocity and Vorticity

We use a similar set-up used in previous papers [24] in which two vortex tubes are positioned so that they are anti-parallel. A sinusoidal perturbation is applied to both vortex tubes in the same direction such that they rotate towards each other and undergo 2D reconnection. This set-up can be thought of as modelling the wingtip vortices behind an aircraft, which are anti-parallel, that have undergone either the Crow Instability [11] or the plane has experienced some turbulence leading to the perturbation. The anti-parallel tubes have a Gaussian-like distribution such that there is a region of zero vorticity between the vortex tubes initially. This is similar to wingtip vortices observed behind aircraft [55]. The region of zero vorticity also prevents reconnection occurring immediately and we are able to observe the reconnection of two vortex tubes that were once entirely separate.

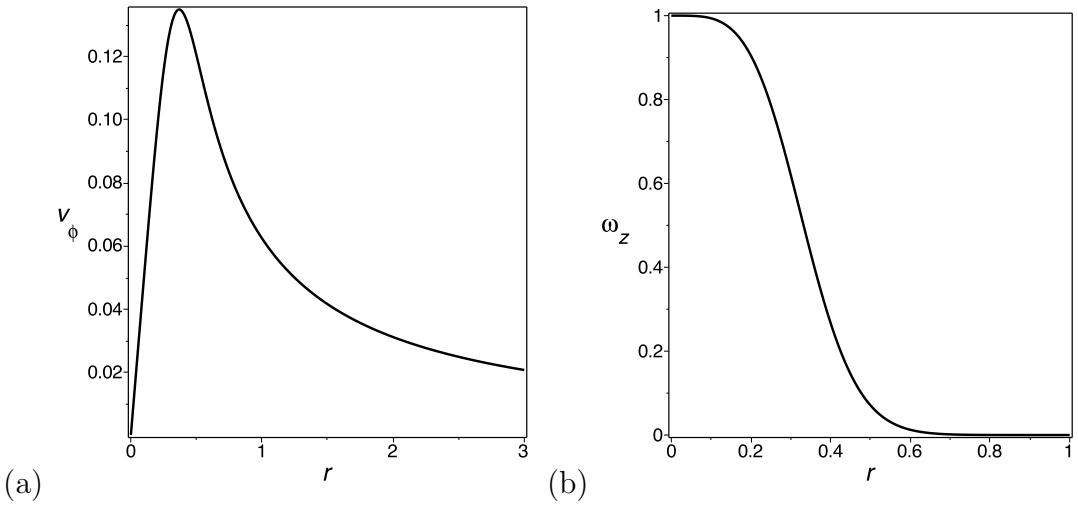

Figure 2.1: (a) Velocity and (b) vorticity distribution of a single vortex tube.

We begin the process of creating this initial condition by first considering a single unperturbed vortex tube. In cylindrical coordinates (r,ϕ,z'), where r is the distance to the axis, ϕ is the angle in the plane perpendicular to the axis and z' is the distance along the axis, we use a velocity distribution of

$$v_\phi = \frac{\tanh(8r^2)}{16r}, \tag{2.1}$$

which gives us a vorticity distribution

$$\omega_{z'} = -\frac{1}{\cosh^2(8r^2)}. \tag{2.2}$$

v_ϕ and $\omega_{z'}$ are plotted in Figure 2.1. This vorticity distribution means the vorticity is smaller at larger radii than a Gaussian distribution to ensure the region between the vortex tubes has zero vorticity. This vortex tube has a vorticity flux of $\pi/8$ or ≈ 0.39.

We choose to orient the axis of our vortex tube parallel to the x-axis, offset to $y = 1$, with the perturbation being in the z-direction. The additional tube is added anti-parallel to the first but centred at $y = -1$. The separation between

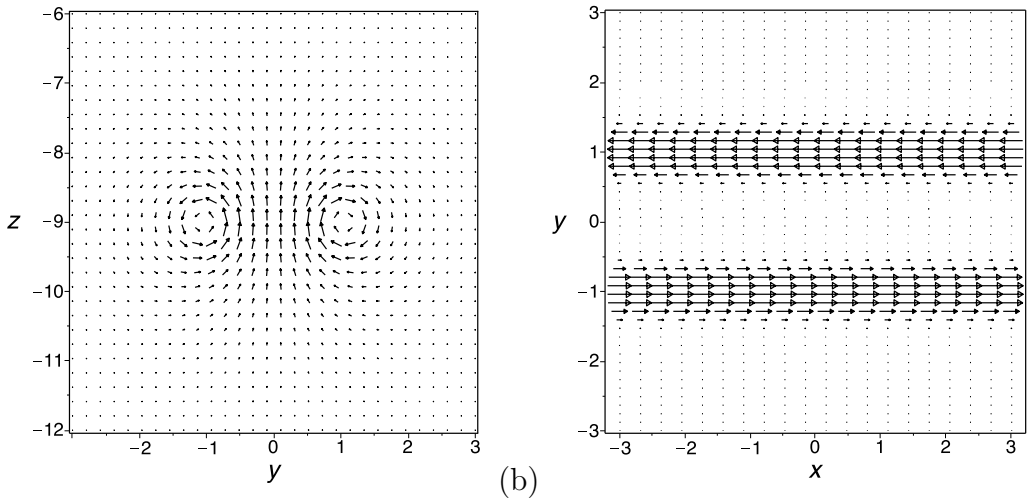

Figure 2.2: (a) Velocity field arrows and (b) vorticity field arrows of pair of unperturbed vortex tubes.

them is chosen such that there is the region of extremely small vorticity between them but will still allow for reconnection once the perturbation is introduced. The new velocity flow is shown in Figure 2.2(a). This velocity flow resembles a velocity field behind an aircraft, perpendicular to the aircraft's velocity. However this velocity field is upside down as we can see from the v_y component at $y = 0$. This is chosen to be consistent with previous papers for aiding comparisons. The vorticity field arrows are shown in Figure 2.2(b) demonstrating the anti-parallel nature of the fieldlines and the region of zero vorticity. When discussing the reconnection process in the next section we will refer to certain planes to aid discussion. The $x = 0$ plane will be referred to as the 'symmetry plane' due to the symmetry of the velocity field with this plane. With this set-up the reconnection is expected to occur along the z-axis so the movement of the vortex tubes in the symmetry plane toward this axis will be of importance particularly before reconnection. The $y = 0$ plane will be referred to as the 'dividing plane' due to it initially dividing both vortex tubes. This will be of importance post reconnection to discuss the vorticity that now exists in that plane. The transfer of vorticity fieldlines from the symmetry plane through the central axis to the dividing plane

will be what we are looking to describe in this chapter. We define the central axis as the z-axis ($x = 0$, $y = 0$).

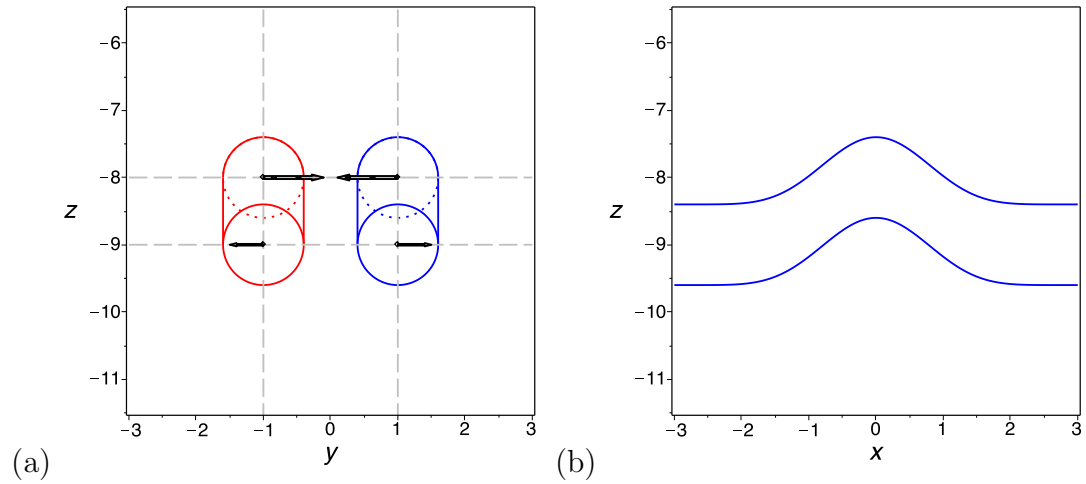

Figure 2.3: (a) Vortex pair and their initial movements, (b) perturbation of the vortex tube.

2.1.2 Generation of the Perturbation

To induce reconnection the vortex tubes are perturbed in such a way that they will rotate and press against each other forming a vortex sheet shown in Figure 2.3(a). As a curvature is introduced to a vortex tube, the sections of curved tube behave as if they were part of a vortex ring and propel themselves perpendicular to the curvature and vorticity field line. In previous papers a sinusoidal perturbation is chosen such that the peaks in the centre will move towards each other. In this case we use a perturbation of $\cos^6(\pi X/6)$ shown in Figure 2.3(b), this is used in an attempt to keep the reconnection event in the centre of the box and have room to evolve in z after the reconnection before being influenced by neighbouring reconnections due to the periodicity of the simulation. A pull-back of a 1-form [17] is used on the velocity field by mapping the perturbation. This will allow us to transform the vorticity field in the same way to give the desired perturbation in the vortex tubes although the velocity field will no longer be divergence free.

Consider the velocity field of an unperturbed vortex tube in cartesian co-ordinates:

$$\boldsymbol{v}(x,y,z) = \left[0, \frac{z\tanh(8(y^2+z^2))}{16(y^2+z^2)}, -\frac{y\tanh(8(y^2+z^2))}{16(y^2+z^2)}\right], \tag{2.3}$$

and the mapping, f, that we wish to apply to introduce the perturbation

$$f(x,y,z) = (X,Y,Z) = (x,y,z+p(x)), \tag{2.4}$$

where $p(x)$ describes the perturbation that we wish to add to the tube. We can therefore describe an inverse mapping, g:

$$g(X,Y,Z) = f^{-1}(X,Y,Z) = (x,y,z) = (X,Y,Z-p(X)). \tag{2.5}$$

With our desired perturbation $p(X)$:

$$p(X) = \cos^6\left(\frac{\pi X}{6}\right), \tag{2.6}$$

this inverse mapping (2.5) becomes

$$g = \left[X, Y, Z - \cos^6\left(\frac{\pi X}{6}\right)\right]. \tag{2.7}$$

We use this inverse mapping to perform a pull-back on the 1-form, $\boldsymbol{v}$, to find the perturbed velocity field $\boldsymbol{V}$:

$$\boldsymbol{V}(X,Y,Z) = \boldsymbol{v}_i(g(X,Y,Z))\frac{\partial g^i}{\partial X^j}\,\mathrm{d}X^j, \tag{2.8}$$

where $(X^1,X^2,X^3) = (X,Y,Z)$ and we sum over the repeated indices, i and j.

For our perturbation $p(X)$ we have

$$\boldsymbol{v}(g(X,Y,Z)) = \Bigg[0, \frac{(Z-\cos^6\!\left(\frac{\pi X}{6}\right))\tanh(8(Y^2+(Z-\cos^6\!\left(\frac{\pi X}{6}\right))^2))}{16(Y^2+(Z-\cos^6\!\left(\frac{\pi X}{6}\right))^2)}, - \frac{Y\tanh(8(Y^2+(Z-\cos^6\!\left(\frac{\pi X}{6}\right))^2))}{16(Y^2+(Z-\cos^6\!\left(\frac{\pi X}{6}\right))^2)}\Bigg], \quad (2.9)$$

$$\partial g = \begin{pmatrix} 1 & 0 & 0 \\ 0 & 1 & 0 \\ \frac{\partial g^z}{\partial X} & 0 & 1 \end{pmatrix}, \quad (2.10)$$

$$\frac{\partial g^z}{\partial X} = \pi \sin\!\left(\frac{\pi X}{6}\right)\cos^5\!\left(\frac{\pi X}{6}\right). \quad (2.11)$$

Substituting (2.9) and (2.10) into (2.8) we get:

$$\boldsymbol{V}(X,Y,Z) = (v_x\frac{\partial g^x}{\partial X} + v_y\frac{\partial g^y}{\partial X} + v_z\frac{\partial g^x}{\partial Z}, v_x\frac{\partial g^x}{\partial Y} + v_y\frac{\partial g^y}{\partial Y} + v_z\frac{\partial g^z}{\partial Y}, v_x\frac{\partial g^x}{\partial Z} + v_y\frac{\partial g^y}{\partial Z} + v_z\frac{\partial g^z}{\partial Z}) = (v_x + v_z\frac{\partial g^z}{\partial X}, v_y, v_z), \quad (2.12)$$

which corresponds to a vorticity field, $\boldsymbol{\Omega}$, of

$$\boldsymbol{\Omega}(X,Y,Z) = \Bigg[1-\tanh\left(8\left(Y^2\right)+\left(Z-\cos^6\!\left(\frac{\pi X}{6}\right)\right)^2\right), 0, \pi\sin\!\left(\frac{\pi X}{6}\right)\cos^5\!\left(\frac{\pi X}{6}\right)\left(\tanh\left(8\left(Y^2\right)+\left(Z-\cos^6\!\left(\frac{\pi X}{6}\right)\right)^2\right)-1\right)\Bigg]. \quad (2.13)$$

With this we now have a vortex tube with a perturbation in z of $p(x)$. With this we are able to assemble an initial condition to induce reconnection. From now on we shall return to using x, y, z, $\boldsymbol{v}$ and $\boldsymbol{\omega}$ for the coordinates and velocity and vorticity fields. Generating the perturbation in this way allows us to preserve the divergence-free nature of the vorticity field unlike in Melander and Hussain [41] who had to adjust their vorticity field to satisfy this.

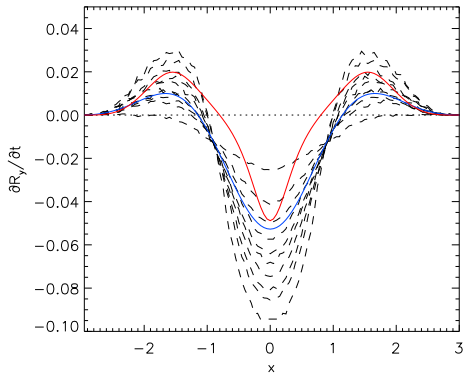

Figure 2.4: Initial velocity along the vortex tube. Velocity predicted by (2.14) (red), velocity of centroid (blue) and velocity of each 10% contour (dashed) with the core moving faster than the whole tube for $Re = 800$.

2.1.3 Initial Movement

Using the Localised Induction Approximation (LIA) for a Vortex Filament [2] we can estimate the initial movement and behaviour of the vortex tubes and position them such that this movement will press the tubes together for reconnection. This is defined for thin vortex filaments as [53]:

$$\frac{\partial \boldsymbol{R}}{\partial t} = -\frac{\Gamma \log a}{4\pi} \frac{\partial \boldsymbol{R}}{\partial s} \times \frac{\partial^2 \boldsymbol{R}}{\partial s^2}, \tag{2.14}$$

where R, Γ, a and s are the curve, circulation, radius and arc length of the vortex filament. As (2.14) is for thin vortex filaments of constant vorticity over the cross-section this will provide only a rough estimate to the initial velocity of the tube. As we have a vorticity distribution that changes in magnitude with radius we replace $\Gamma \log a$ with $\int_0^a (1 + 2\log(r))\pi r \omega_z(r)\,\mathrm{d}r$.

This estimate describes well in magnitude the initial movement of the centroid of the vortex tube as can be seen in Figure 2.4. The approximation however does not account for the separation of the vortex tubes at the boundaries. This estimate only applies for the initial set-up of the vortex tubes as the perturbation alters

its shape and the vorticity distribution of the tubes deforms quickly. However, the estimate is good at early times, and allows for a suitable placement of the tubes that ensures that they press against one another.

2.1.4 Set-up of Array

Another tube of opposite vorticity is positioned next to the initial tube. The centre axes of the tubes are positioned at $y = \pm 1$ leaving a gap of extremely small vorticity of size ≈ 0.6, see Figure 2.6. As the tubes begin to rotate and the perturbations approach each other they should form a vortex sheet and reconnect. For no flow to leave the box we want to get $\boldsymbol{v} \cdot \boldsymbol{n} = 0$ on the boundaries. We do this as we wish to measure volume integrals of the system and this allows these to be easily measured without taking into consideration any flux entering the system through the boundaries. The computational code uses periodic boundary conditions but we must create an initial condition with zero flow through the boundary. To achieve this another pair of tubes are positioned symmetrically in the xy-plane with opposite vorticity. The two pairs of tubes are positioned at $z = \pm 9$. The vortex tubes at $z = -9$ are shown in Figure 2.6. The pairs of tubes will approach $z = 0$ and will eventually be affected by the opposite pair so this positioning in z is chosen to give sufficient time for the reconnection process to complete before this interaction occurs. The periodic perturbation satisfies the boundary condition in x so for y and z a 9×9 array of boxes containing two pairs each is created to satisfy this.

A box of sides [6,12,24] was chosen for the two pairs of vortex tubes. The pair of tubes whose interaction we will analyse is contained within the sub-domain $-3 \leq x \leq, -6 \leq y \leq 6, -12 \leq z \leq 12$. This allows the vortex tubes to evolve without being affected by other pairs of vortex tubes until the pair approaches $z = 0$. A resolution of [120,240,480] is chosen for the above sub-domain with points closer together at $y = 0$ in y to resolve the vortex sheet that will form there that will become very thin for high Reynolds numbers, see Figure.

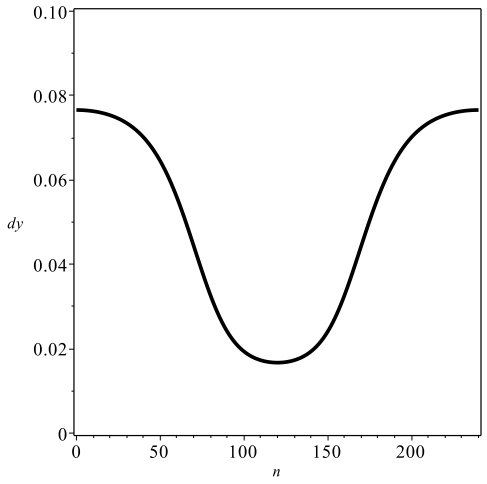

Figure 2.5: Stretched grid spacing, dy, in y to resolve vortex sheets.

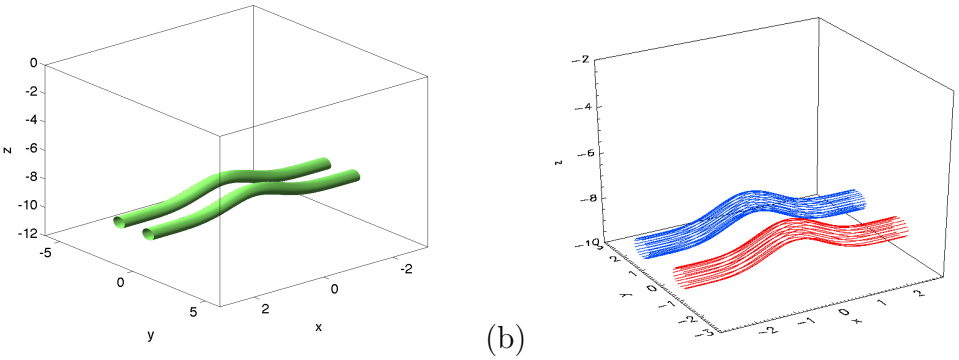

(a) (b)

Figure 2.6: (a) $|\boldsymbol{\omega}|$ isosurface of 30% maximum $\boldsymbol{\omega}$ at $x = -3$ boundary and (b) vorticity fieldlines plotted from 30% contours at $x = -3$ and 3 boundaries.

2.1.5 Parameters

We choose the following values for our parameters; $\rho = 0.1$, $e = 0.09$, $g = 0$ and $\gamma = 5/3$ which corresponds to the density, the internal energy, gravity and the heat capacity ratio [31]. The value of g was chosen for simplicity, γ such that the system is monatomic and ρ and e are chosen to given a sound speed, c_s [36], of ≈ 0.8. The ρ and e values were tested to observe the evolution of density at the cores of the vortex tubes with the values chosen here preserving it best. This allows us to treat the system as near incompressible which is useful for comparing to previous runs that guaranteed this.

The maximum velocity is chosen to ensure the system does not become supersonic. With this chosen we are then given the velocity of the perturbation of the tube towards the other and the mutual velocity upwards. v_{tube} is the maximum velocity found from section 2.1.3, v_{mutual} was found from (2.1) using the distance between tube centres $r = 2$ adjusting for the new v_{0max}.

$$c_s \approx 0.8 \qquad v_{0max} = 0.2 \qquad v_{tube} \approx 0.07 \qquad v_{mutual} \approx 0.03$$

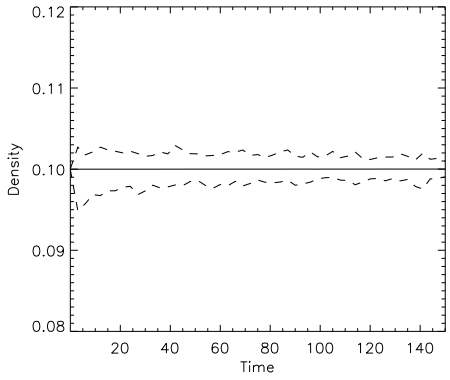

Figure 2.7: Maximum, mean and minimum density, $Re = 800$.

2.1.6 Density

With the introduction of a divergence in the velocity field due to the pull-back the maximum, minimum and average densities are plotted to ensure they stay roughly constant throughout in Figure 2.7. With the chosen density there is only an initial change in density and it converges back to the background value. The constant density throughout the domain is of importance when comparing different reconnections of different Reynolds numbers. With a constant density we will get a constant kinematic viscosity.

2.2 Results

We first look at the results of the simulation with a Reynolds number of 800. This value of Re is chosen to be discussed first as it demonstrates the reconnection process in a typical fashion to previous papers unlike some of the other differing Re simulations. The differences that the changes in Reynolds number introduce will be discussed in the following chapter.

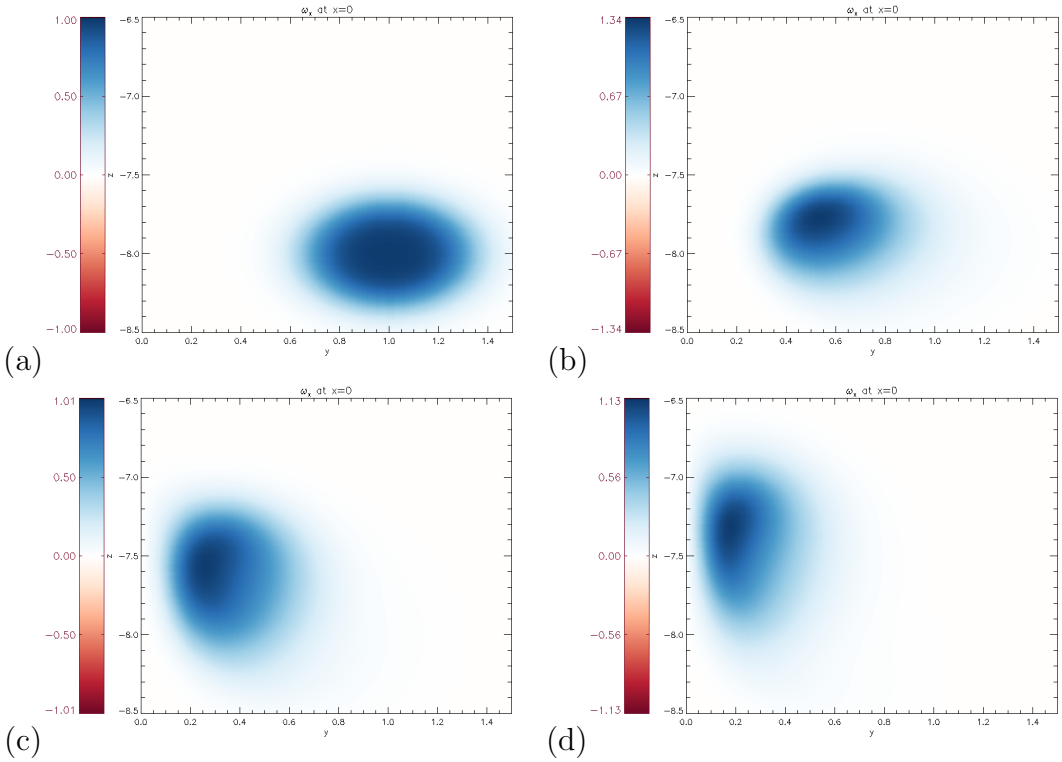

Figure 2.8: ω_x at $x = 0$ for one tube at (a) $t = 0$, (b) $t = 9$, (c) $t = 21$ and (d) $t = 30$.

2.2.1 Approach and Core Deformation

Considering Equation (1.3) to observe the initial movement of vortex tubes. At $t = 0$ the $(\boldsymbol{\omega} \cdot \nabla)\boldsymbol{v}$ and $\boldsymbol{\omega}(\nabla \cdot \boldsymbol{v})$ terms are equal due to the divergence introduced by the method to generate the perturbation of the tube. Because of this at $t = 0$ the vortex tubes only move upward (in z). By $t = 0.2$ the divergence has diminished due to the back-reaction of the fluid due to the compression of the flow and the $(\boldsymbol{\omega} \cdot \nabla)\boldsymbol{v}$ term has remained the same. Then as predicted in Subsection 2.1.3 the perturbations introduced to each of the tubes move towards each other at $x = 0$ in the symmetry plane, see Figure 2.8. Initially the tubes at the $x = \pm 3$ boundaries separate slightly unlike in the LIA due to the proximity to the lower z boundary and the image pair of vortex tubes. This does not affect the reconnection process and as the tubes begin their movement and the

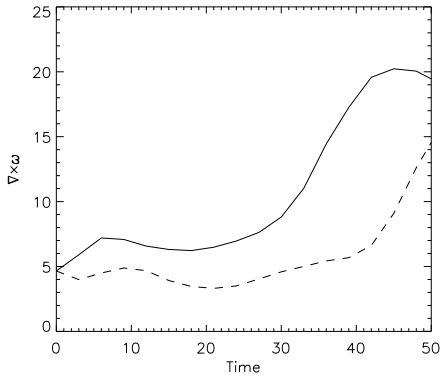

Figure 2.9: Maximum $(\nabla \times \boldsymbol{\omega})$ on side of vortex tube facing towards dividing plane (solid) and away (dashed).

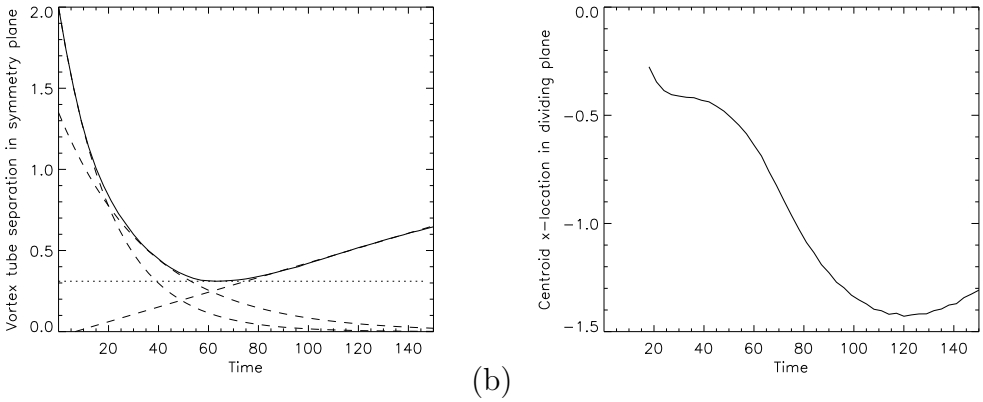

(a) (b)

Figure 2.10: (a) Vortex tubes centroid separation in symmetry plane ($x = 0$) (solid) with fitted curves (dashed) and minimum separation (dotted) and (b) vortex tube centroid position in dividing plane ($y = 0$).

tube shape changes the tubes at the boundaries begin separating at a rate more similar to the velocity predicted further along the tube. This downside to using this particular perturbation has negligible effects on the process apart from in the lowest Reynolds number case which will be discussed later. Observing the cross-section of the tubes within the symmetry plane we see that the Gaussian distribution of the vorticity is lost quite quickly due to the $(\boldsymbol{\omega} \cdot \nabla)\boldsymbol{v}$ term in the vorticity evolution equation. This term causes the entire rotation of the vortex tubes. The other consequence is an increased maximum vorticity and a change in the $\partial\omega_x/\partial y$ across the tube increasing in strength in the direction of travel

and weakening on the other side as seen in Figure 2.9. This is due to the core of the vortex tube rotating faster than the outer shell. This process causes the breakdown of the Gaussian distribution very early in the evolution of the tube. This process of stronger vorticity fieldlines pressing against weaker ones creates a vortex sheet on each tube facing towards one another with an increasingly large $\partial\omega_x/\partial y$. This vortex sheet formation and high $\partial\omega_x/\partial y$ will be the catalyst for reconnection and affect the speed of the reconnection process.

We can find the position of the centroid in the symmetry plane with the following equation,

$$C_y = \frac{\int y\omega_x \, \mathrm{d}A}{\int \omega_x \, \mathrm{d}A} \qquad C_z = \frac{\int z\omega_x \, \mathrm{d}A}{\int \omega_x \, \mathrm{d}A}, \tag{2.15}$$

where C_y and C_z are the y and z-position of the centroid in the symmetry plane. The movement of the centroid of the vortex tube in Figure 2.10(a) can be described in different steps. In each of these steps we empirically fit a curve (plotted as dashed lines) to describe the approach of the vortex tube centroids. From $t \approx 0 \rightarrow 20$ the tubes rotate towards each other without resistance from the other following a path described roughly by $y = 2\exp(-t/21)$. From $t \approx 20 \rightarrow 60$ the tubes begin pressing into each other with motion described by $y = 1.35\exp(-t/36)$. A minimum distance to the dividing plane of ~ 0.311 is reached at $t \approx 63$. The centroid then moves at a linear rate of $y = -0.03 + t/220$. In Figure 2.10(b) we plot the vortex tube centroid position after it appears in the dividing plane. This movement will be discussed in detail later.

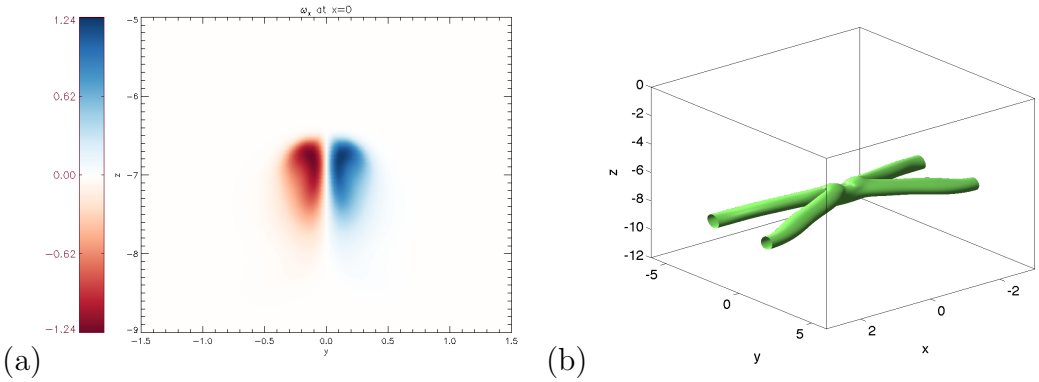

Figure 2.11: (a) ω_x contour plot at $x = 0$ and (b) vorticity isosurface exhibiting the double vortex sheet at $t = 45$.

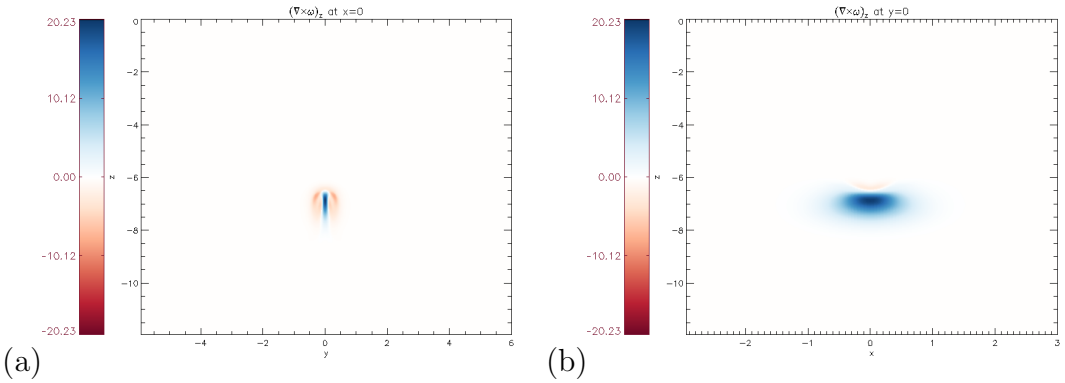

Figure 2.12: $(\nabla \times \boldsymbol{\omega})_z$ contour plot at (a) $x = 0$ and (b) $y = 0$ at $t = 45$.

2.2.2 Double Vortex Sheet

As the vortex sheets formed in each vortex tube move towards each other they form a double vortex sheet seen in Figure 2.11 and between these sheets a sheet of $(\nabla \times \boldsymbol{\omega})_z$ is formed as the positive and negative ω_x concentrations get closer to each other. Within this reconnection sheet lies the central axis of the box (the z-axis) where the vorticity is zero by symmetry. This line of zero vorticity and non-zero $(\nabla \times \boldsymbol{\omega})_z$ is the location at which the reconnection occurs and is measured as discussed in Subsection 1.3.2.

We can see from the reconnection sheet in the dividing plane in Figure 2.12(b) that it stretches quite far along the tube leading to the z-location of the reconnected

flux that was seen in Figure 2.10(b). Also here we can see negative $(\nabla \times \boldsymbol{\omega})_z$ from the recently reconnected vorticity slowing the process until they separate and this effect diminishes [42]. This will discussed further in Subsection 3.1.2.

2.2.3 Visualising the Reconnection Process - Vorticity Isosurfaces

We observe the isosurface of $|\boldsymbol{\omega}|$ in Figure 2.13. We take the value of isosurface to be 30% of the maximum ω_x at the $x = \pm 3$ boundaries of the box. We chose this method to help compare the vorticity isosurfaces of different Reynolds numbers in the next chapter. This is due to the maximum vorticity of the system being highly dependant on Reynolds number so basing the isosurface on a percentage of the maximum $|\boldsymbol{\omega}|$ will give vastly different images for different Re. Using a static value throughout time caused issues for the lower Reynolds number runs as the isosurfaces appeared to disappear as the vorticity dissipated. This method of defining the isosurfaces using a fraction of the maximum vorticity at the boundary means that the isosurfaces will appear consistent throughout the run but still leaving the detail of reconnection that we are hoping to observe.

Through the evolution of the system the isosurfaces demonstrate the approach of the vortex tubes and formation of vortex sheets. The initial reconnection at the top of the vortex tubes forms the "bridges" with threads still with their original topology. Any reconnected fieldlines will be referred to as 'bridges' from now, with still connected fieldlines referred to as 'threads'. The final stage involves the bridges and the wrapping of the threads around them [41]. This is consistent with the isosurfaces seen in previous papers [24]. An issue of using isosurfaces to view this process arises at the final figure where the threads appear to have disconnected from the bridges which is not the case here but will be discussed in Subsection 2.2.4.

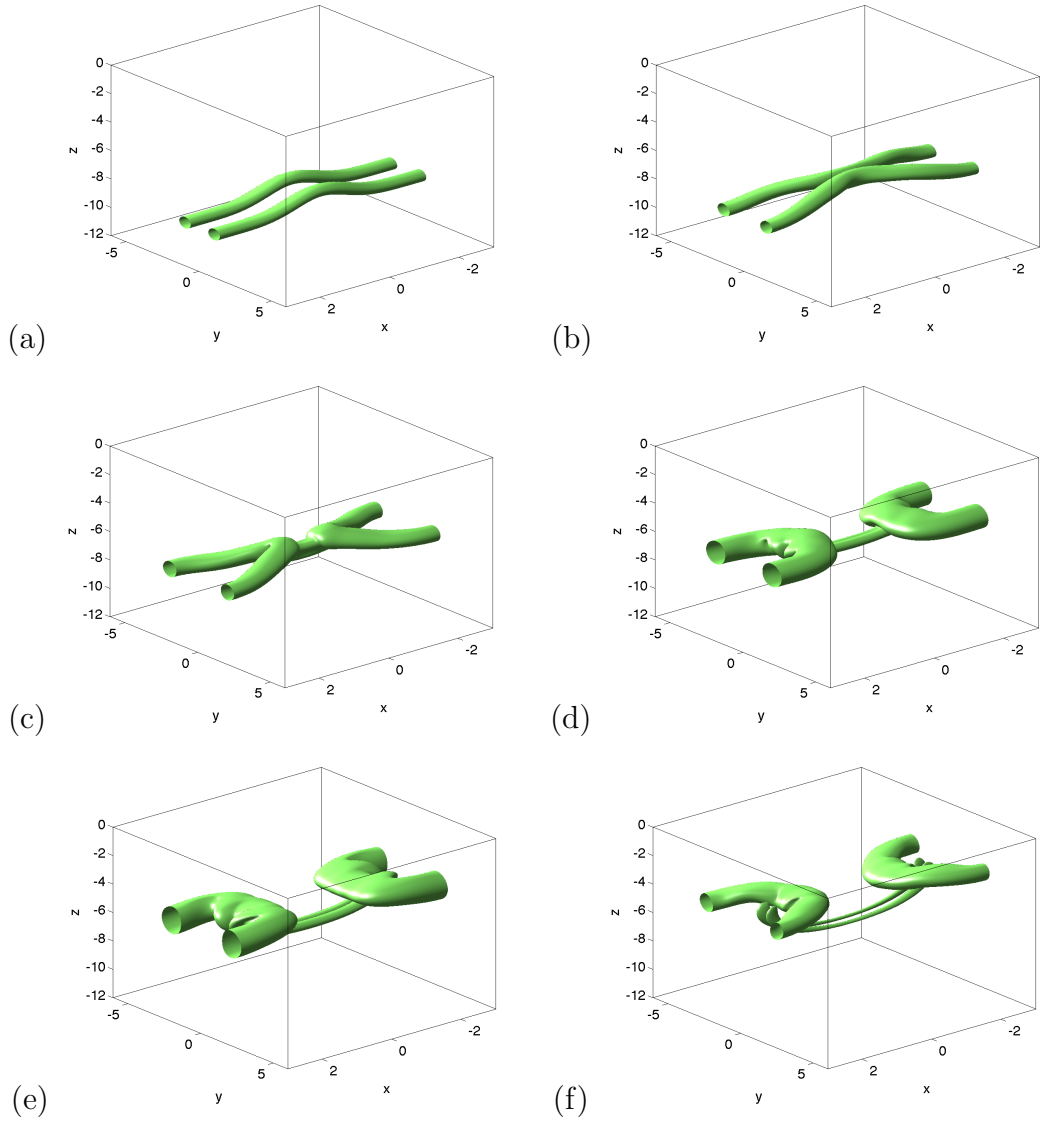

Figure 2.13: $|\boldsymbol{\omega}|$ isosurface of 30% maximum $\boldsymbol{\omega}$ at $x = -3$ boundary at (a) $t = 0$, (b) $t = 30$, (c) $t = 60$, (d) $t = 90$, (e) $t = 120$ and (f) $t = 150$.

2.2.4 Visualising the Reconnection Process - Vorticity Fieldlines

To achieve a better understanding of the reconnection process vorticity fieldlines are plotted from the boundaries at $x = \pm 3$ in Figure 2.14. We us a 5th order accurate Adams-Bashforth method for fieldlines tracing. Visualising the vorticity fieldlines allows a proper analysis of the topological changes in the vorticity field during the reconnection process. We choose to follow 50 fieldlines from either boundary, 25 for each vortex tube. The start points of these fieldlines are chosen from contours equal to 30% of the maximum vorticity in the plane. This allows us to visualise the shape of the vortex tube using a small number of fieldlines. The advantages of observing fieldlines compared to the isosurfaces seen previously are the ability to see direction, better evidence of reconnection as we can see the fieldlines changing topology and a better visualisation of a change in radius of the vortex tubes. From Figure 2.14 we observe the rotation of the vortex tubes and evidence of reconnection. The reconnection process begins at the top of the vortex tubes in z explaining the bridges seen in Figure 2.13(c). This is due to the shape of the double vortex sheet seen earlier with the stronger vorticity moving faster along z with weaker vorticity trailing behind known as the 'head-tail' [42]. The higher vorticity leads to a higher $(\nabla \times \boldsymbol{\omega})_z$ which induces reconnection. Lower in z the threads remain 'un-reconnected'. As the bridges evolve the threads begin wrapping around the bridges and the curvature of the thread fieldlines change. This new curvature means the thread fieldlines begin separating, slowing the reconnection process, and is the reason why this reconnection process can not be complete [41]. This separation will be discussed later.

To observe the interaction between the threads and bridges we choose to plot in Figure 2.15 fieldlines from $x = 0$ and $y = 0$. It is important to note that

the threads and bridges are not of equal vorticity magnitude at the planes they are being plotted from. However each is showing the typical behaviour of the fieldlines through that plane. From this we can see the earlier reconnection of the weak vorticity fieldlines pressed together in the double vortex sheet first. In Figure 2.15(c) we can see the bridges begin moving away from the central axis and rotating on top of the threads. At later times we see the new curvature of the threads and their separation essentially all but stopping the reconnection process [41].

Following the fieldlines from the boundary we can observe the order in which they reconnect. Plotted in Figure 2.16 is the vorticity for a single tube at $x = -3$, if the fieldlines plotted from that grid point end at $x = +3$ after travelling through the symmetry plane it will be red and considered a 'thread'. If the fieldline ends back at $x = -3$ passing through the dividing plane this means that this fieldline has reconnected and is plotted as blue so we can observe the behaviour of the boundaries between these neighbouring fieldlines with differing topologies. Starting predictably from one side of the tube the fieldlines at the boundary continue to circulate around the centre as the fieldlines reconnect such that the reconnection process seems to be avoiding the central axis of the vortex tube. At $t = 75$ a spiral effect appears where a thread begins from the centre of the vortex tube which then separates from the majority of the fieldlines surrounding it to eventually pass through the symmetry plane whilst its neighbours pass through the dividing plane. These central threads are then lost as more of the cross section is swept out and reconnects leaving a more simple plot of threads and bridges.

To further understand the bridge we plot a selection of the fieldlines in the xy-plane in Figure 2.17. In Figure 2.17(a) we can see the hairpin structure of the newly reconnected bridges and their evolution, smoothing themselves out into a lower curvature line in Figure 2.17(b). When we discuss hairpin structures we

describe fieldlines that change direction in such a way that they are near anti-parallel to themselves such that they continue to propel themselves even after reconnection.

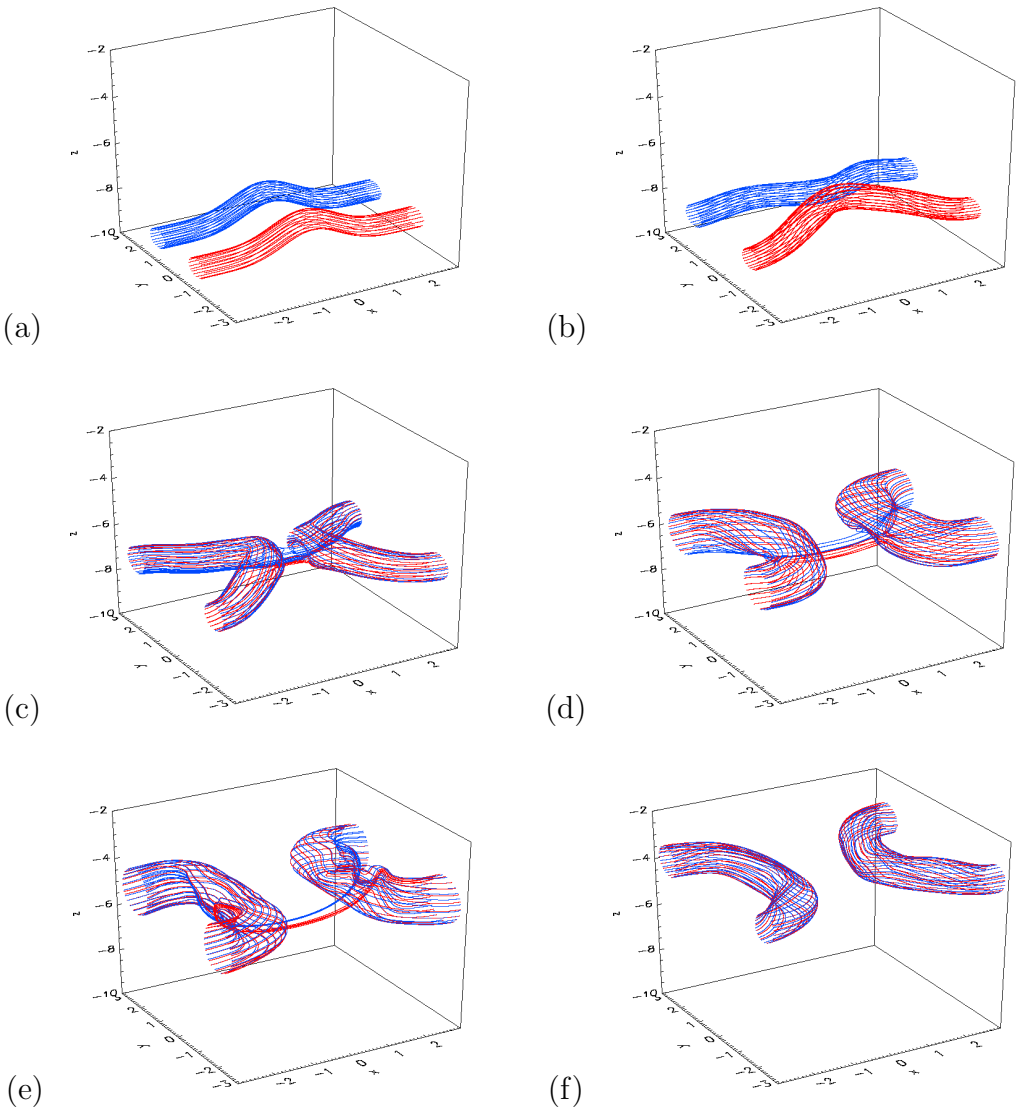

Figure 2.14: Vorticity fieldlines plotted from 30% contours at $x = -3$ and 3 boundaries at (a) $t = 0$, (b) $t = 30$, (c) $t = 60$, (d) $t = 90$, (e) $t = 120$ and (f) $t = 150$.

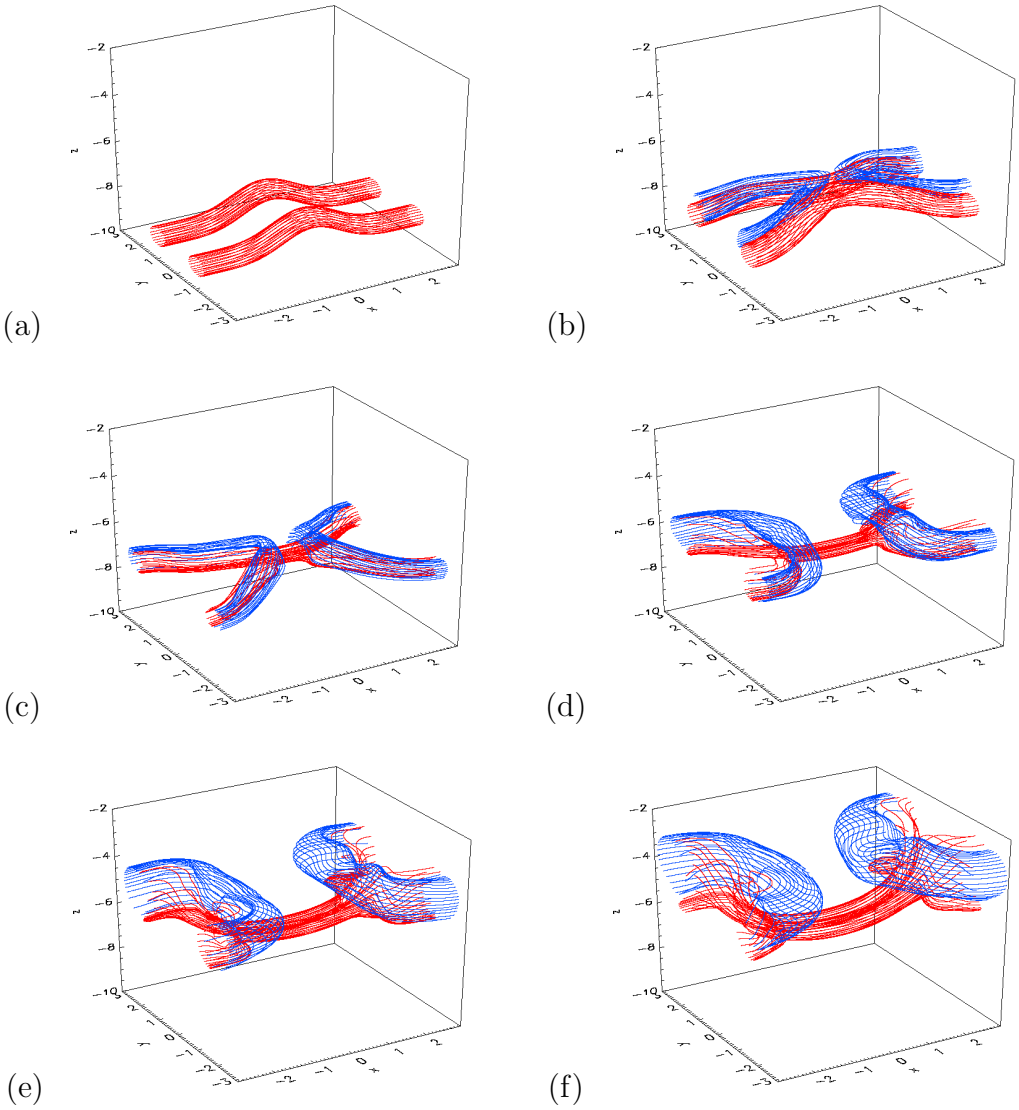

Figure 2.15: Vorticity fieldlines plotted from 30% contours at $x = 0$ (red) and $y = 0$ (blue) at (a) $t = 0$, (b) $t = 30$, (c) $t = 60$, (d) $t = 90$, (e) $t = 120$ and (f) $t = 150$.

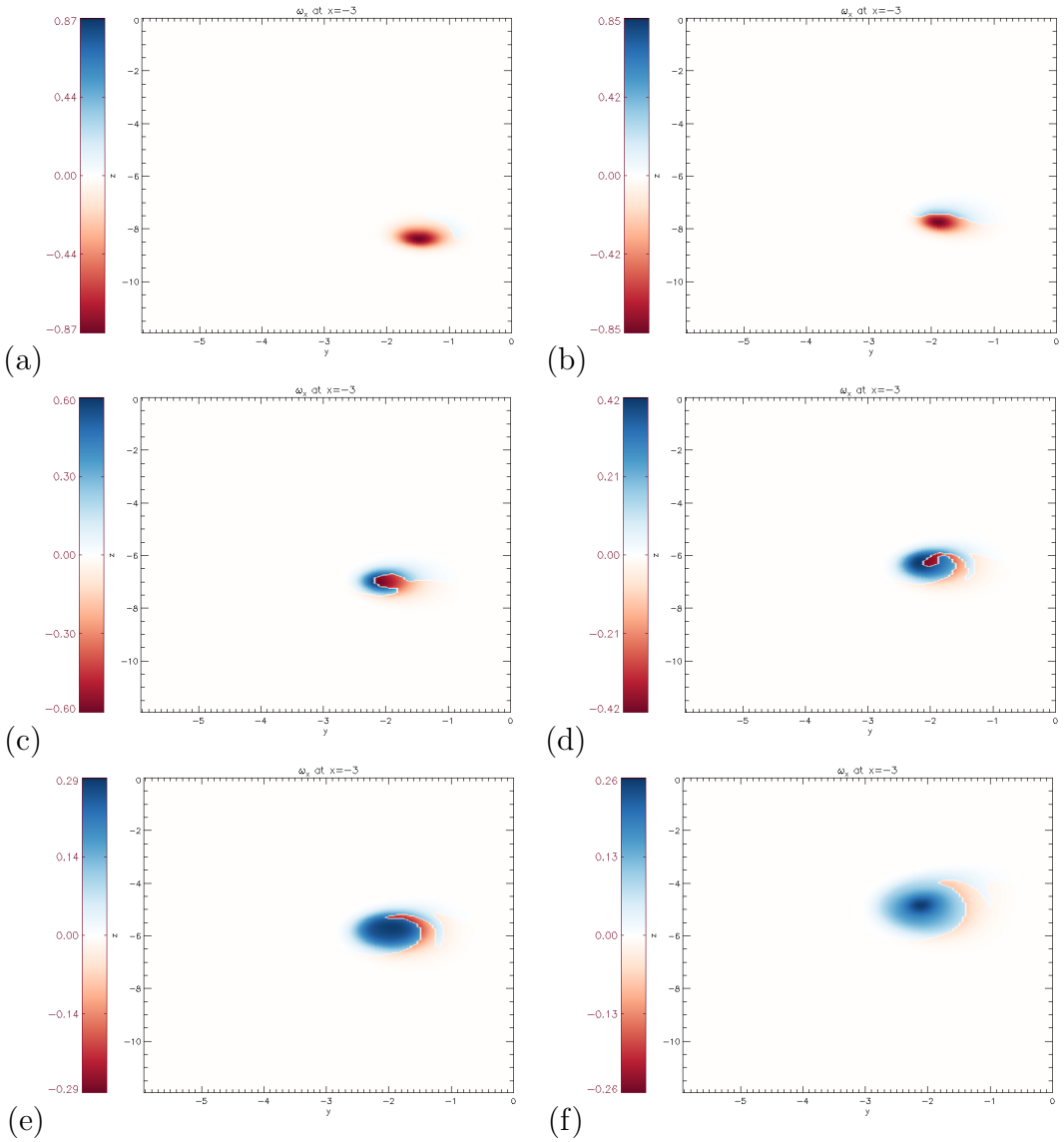

Figure 2.16: ω_x contour plots at $x = -3$ boundary, with the colour depicting whether the field line is a bridge or a thread. Threads (unreconnected fieldlines) are in red, and bridges (reconnected fieldlines) are in blue at (a) $t = 30$, (b) $t = 45$, (c) $t = 60$, (d) $t = 75$, (e) $t = 90$ and (f) $t = 120$.

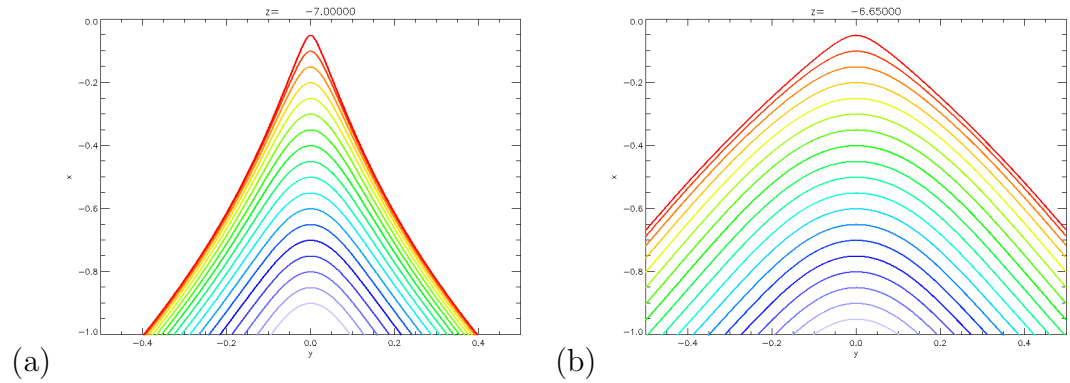

(a) (b)

Figure 2.17: Vorticity fieldlines plotted from dividing plane at (a) $t = 24$ and $z = -7$ and (b) $t = 48$ and $z = -6.65$.

2.2.5 Symmetry and Dividing Plane Contour Plots

As the reconnection process describes the change from the symmetry plane to the dividing plane we observe vorticity contour plots in both planes to see the behaviour in each. In the symmetry plane seen on the left side of Figures 2.18 and 2.19 there is little change in the plots of ω_x aside from the magnitude of vorticity once reconnection has begun. The 'head-tail' structure is observed from $t \sim 60$ onwards and the separation of threads mentioned earlier is apparent in Figure 2.19(e).

The vorticity however in the dividing plane changes dramatically. In Figures 2.18(b) and (d) we see the vorticity building up as the fieldlines reconnect. Once the bridges become strong enough they begin to separate due to their curvature and continue moving upwards (in the positive z-direction) now as a vortex ring. The vorticity contour plots show a strong core with spirals coming off the core as seen in Figures 2.18(f) and 2.19(b) and (d). These spirals are the slowly reconnecting threads forming long hairpin structures winding around the core of the bridges. These hairpins evolve towards the rest of the tube and in Figure 2.18(f) we see a contour similar to that of the initial condition in the symmetry plane however with a local minima of vorticity in the centre. This lower vorticity in the centre is possibly due to the later reconnection of the centre of the vortex tube illustrated in Figure 2.16(d).

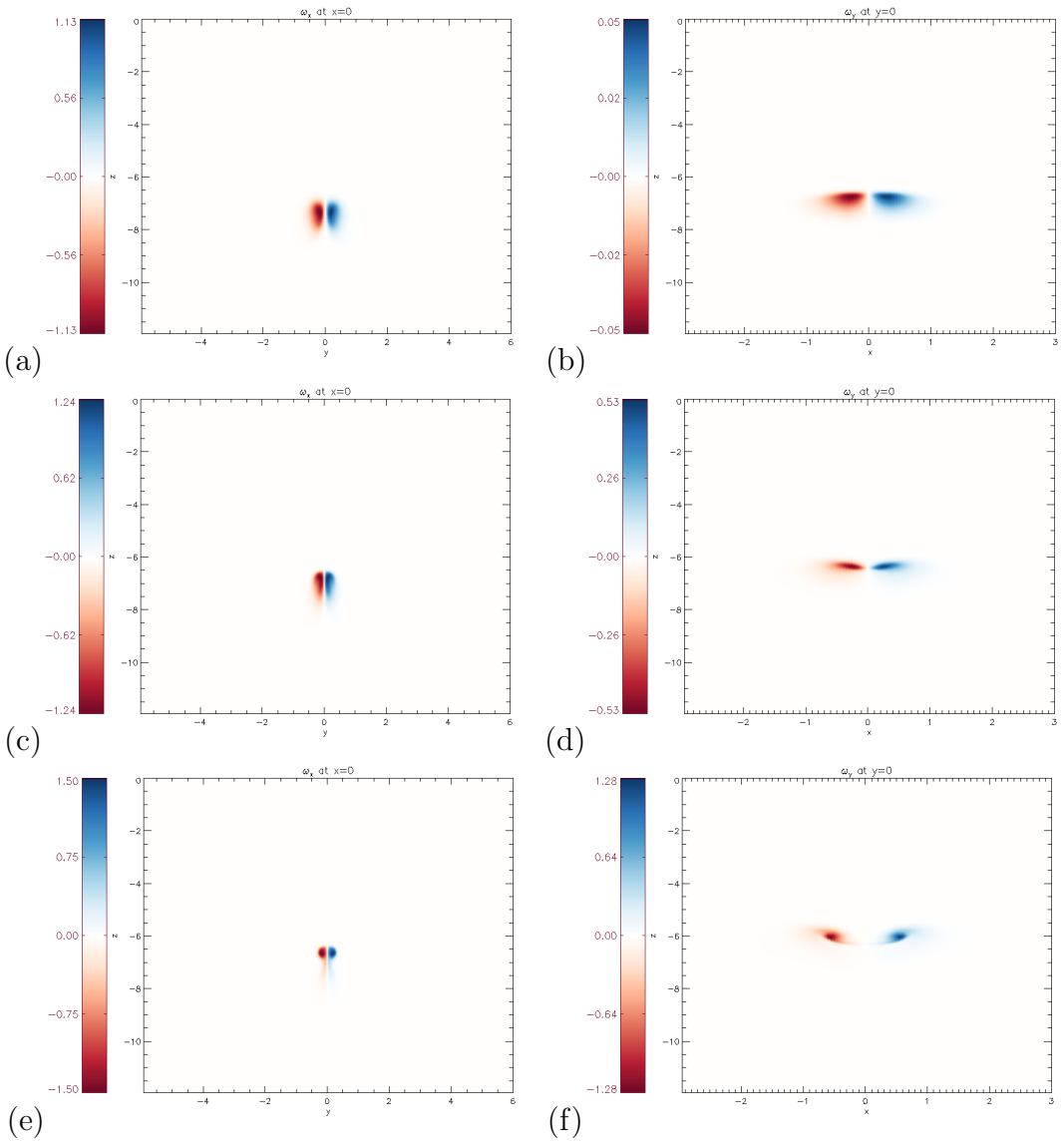

Figure 2.18: ω_x contour plots at $x = 0$ (symmetry plane) (left) and ω_y contour plots at $y = 0$ (dividing plane) (right), at $t = 30$ (top), $t = 45$ (middle), and $t = 60$ (bottom).

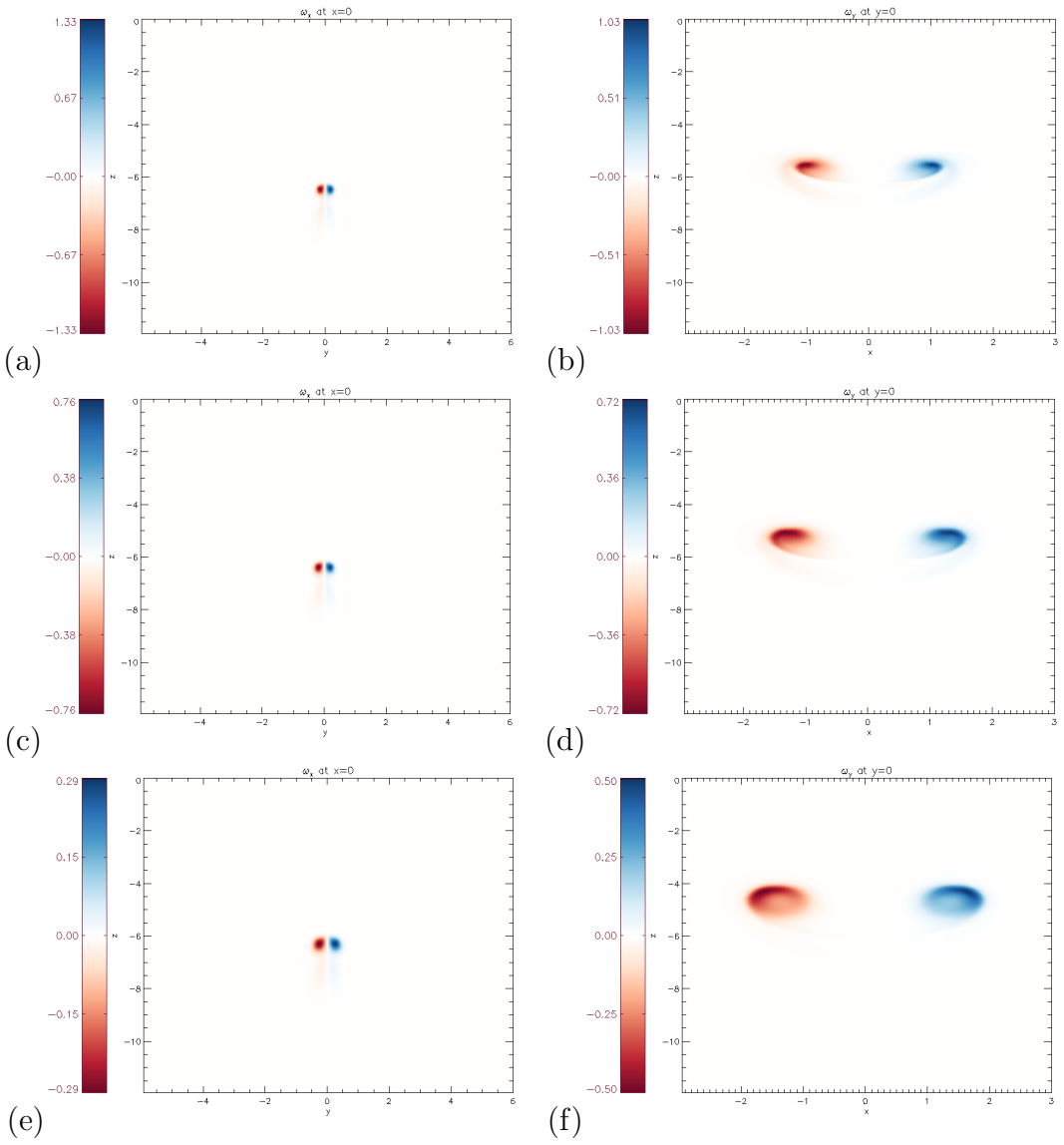

Figure 2.19: ω_x contour plots at $x = 0$ (symmetry plane) (left) and ω_y contour plots at $y = 0$ (dividing plane) (right), at $t = 75$ (top), $t = 90$ (middle), and $t = 120$ (bottom).

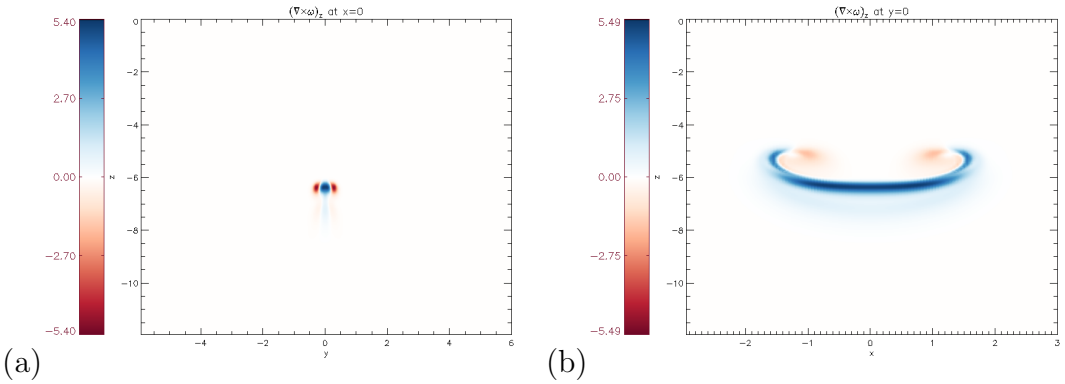

(a) (b)

Figure 2.20: $(\nabla \times \boldsymbol{\omega})_z$ contour plots at $t = 90$ at (a) $x = 0$ and (b) $y = 0$.

2.2.6 Post-Reconnection Behaviour

After the majority of reconnection has occurred the threads continue a slow process of reconnection. This is demonstrated by the weaker reconnection sheet. The reconnection sheet now stretches far along the threads, as can be seen in Figure 2.20, leading to newly reconnected bridges having a long hairpin structure. We can also see in Figure 2.20(b) the new shape of the threads and how, due to the LIA, they are no longer moving towards each other. As the threads weaken the mutual induction between them shrinks and they slow down. Because they slow down in the symmetry plane but continue their movement at the boundaries the curvature of the thread fieldlines change such that they induce themselves to now separate and move away from the dividing plane observed in Figure 2.10. The bridges form a vortex ring. The shape of this ring is elliptical and the shape of this oscillates as it travels upward [14, 56].

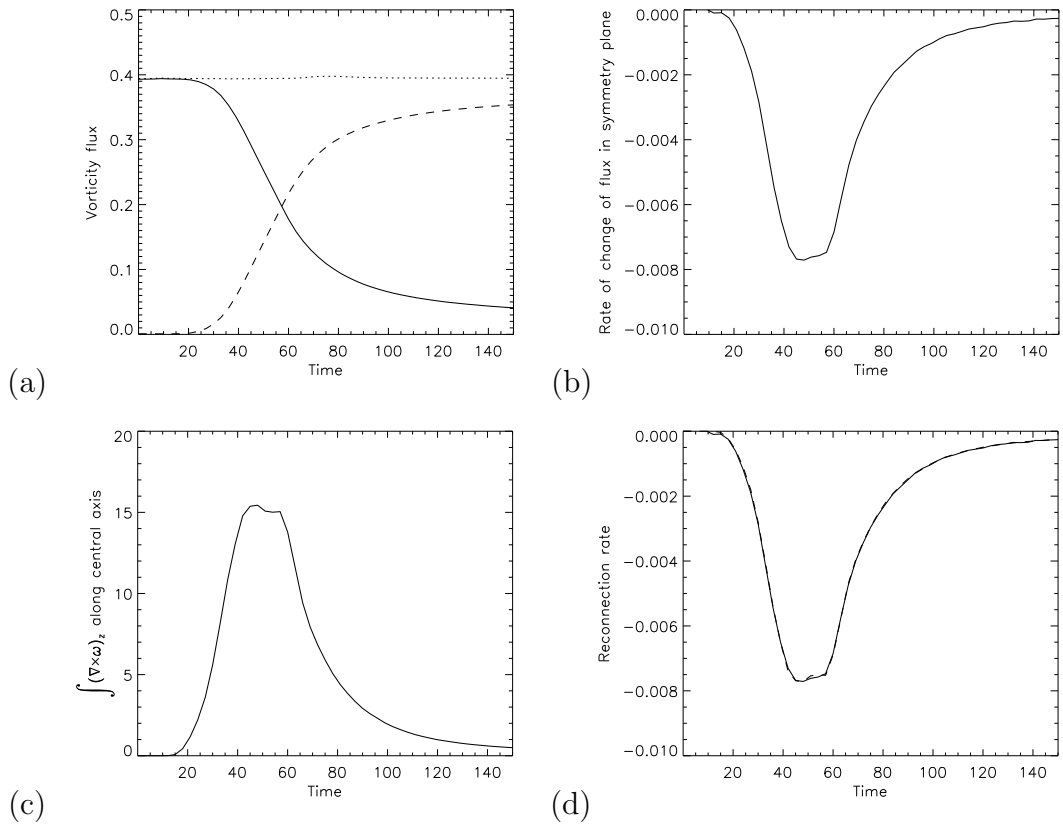

Figure 2.21: (a) Vorticity flux measured at $x = 0$ (solid), $y = 0$ (dashed) and total of both (dotted) as a function of time, (b) rate of change of vorticity flux at $x = 0$, (c) integral of $(\nabla \times \boldsymbol{\omega})_z$ along central axis as a function of time and (d) reconnection rate measured from rate of change of vorticity flux (solid) and from Stokes' Theorem (dashed).

2.2.7 Flux Evolution

To measure the reconnection process we simply measure the vorticity flux in both the symmetry plane and the dividing plane as in Figure 2.21(a) as solid and dashed respectively. The sum of these is plotted with the dotted line, the reason for this not being constant will be discussed later in Subsection 3.1.7. From the reconnection rate in Figure 2.21(b) we can see that the reconnection ramps up quickly to the maximum where it plateaus as the newly reconnected bridges slow down subsequent fieldlines from reconnecting. The reconnection rate then slowly goes down to zero as the elongated threads reconnect after the main

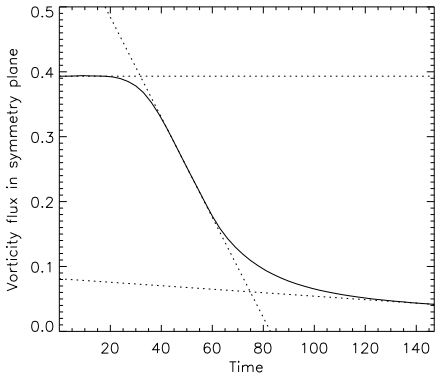

Figure 2.22: Vorticity flux in symmetry plane (solid) with straight lines (dashed) describing the three different stages of the reconnection process.

event. Integrating $\nu(\nabla \times \boldsymbol{\omega})_z$ along the central axis, utilising Stokes' Theorem from Subsection 1.3.2, gives an accurate measure for the reconnection rate as seen in Figure 2.21(d).

From Figure 2.21(a) we can describe the solid line measuring flux in the symmetry plane in three stages [41] which we will refer to as pre, main and post reconnection. The pre reconnection phase is when the vortex tubes begin to move and press into one another, this is observed by the constant flux until around $t \approx 25$. The main reconnection then begins as we see the vorticity flux drop and then smooth out. Afterwards however the reconnection does not stop as discussed in Subsection 2.2.6 but continues slowly. We look to define these stages separately so that we can compare reconnection times in the next chapter when discussing the dependance on Reynolds number. We do this by plotting 3 straight lines to best define the vorticity flux, see Figure 2.22. The pre, main and post reconnection phases are described by a line of constant initial flux, a straight line drawn from the point of highest reconnection rate with the reconnection rate as its gradient and a line drawn from the end of the simulation with the lowest reconnection rate post reconnection respectively. The points where these lines meet we shall define as the start and end of the main reconnection.

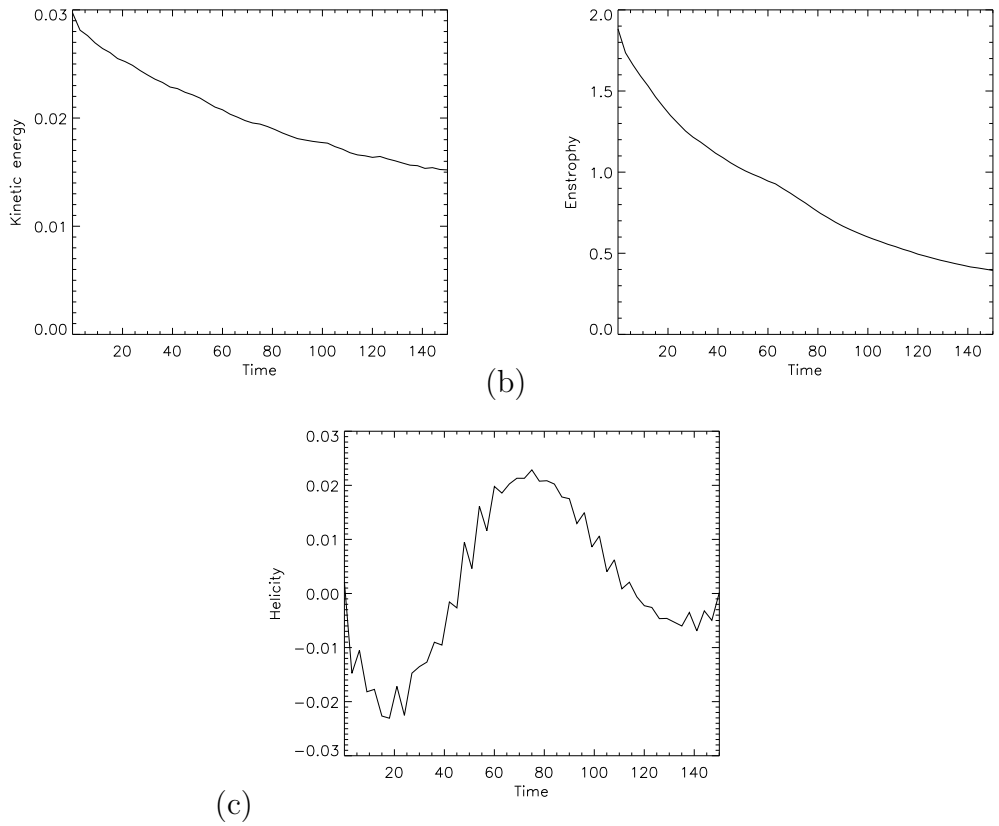

Figure 2.23: (a) Kinetic energy, (b) enstrophy and (c) kinetic helicity of a quarter of the box.

2.2.8 Volume Integrals

We look now into the volume integrals discussed in Subsection 1.2.1; kinetic energy, enstrophy and kinetic helicity. All integrals throughout were found using a 2nd order accurate trapezoidal method. Plotting these quantities will allow us to understand how the entire fluid is evolving with time. The kinetic energy, see Figure 2.23(a), dissipates throughout the entire run. We can see from incompressible evolution of kinetic energy (1.26) that this is because it is linked to the enstrophy. We expect to see from the enstrophy, see Figure 2.23(b), a peak where the double vortex sheet forms. At $t \approx 65$ there is a slight 'bump' due to this but the double vortex sheet is not thin enough to make it more pronounced. We expect from a large spike in enstrophy to correspond to a large drop in kinetic energy but this

is not seen at this Reynolds number. We see from the enstrophy evolution (1.32) that it dissipates in a similar way to kinetic energy but with $\nu \int_V (\nabla \times \boldsymbol{\omega})^2 \, \mathrm{d}V$ instead. Any increase in enstrophy must be from the $\int_V (\boldsymbol{v} \times \boldsymbol{\omega}) \cdot (\nabla \times \boldsymbol{\omega}) \, \mathrm{d}V$ term so in future work investigating enstrophy this will prove useful.

Due to the symmetries discussed previously we only find the helicity over a quarter of the box, see Figure 2.23(c). The helicity oscillates over time [56], although the oscillations appear to drop in amplitude. From the helicity evolution (1.43) the term $\int_S \frac{1}{2} \boldsymbol{v}^2 \boldsymbol{\omega} \cdot \boldsymbol{n} \, \mathrm{d}a$ causes this oscillation. This can be thought of as the vorticity fieldlines on different surfaces rotating around the core at different angular velocities, introducing twist into the tube. For future studies we would look at how these fieldlines rotate on each surface and compare this for bridges and threads to see if that explains the exact reason for oscillations. The $\int_{V_4} -2\nu \boldsymbol{\omega} \cdot (\nabla \times \boldsymbol{\omega}) \, \mathrm{d}V$ term is due to the fieldline 'slipping' but its contribution to the evolution of kinetic helicity is an order of magnitude less than the $\int_S \frac{1}{2} \boldsymbol{v}^2 \boldsymbol{\omega} \cdot \boldsymbol{n} \, \mathrm{d}a$ term.

2.2.9 Spectra

We look to observe the directional spectra of the enstrophy and kinetic energy of the system to see how these quantities behave at different wavelengths. Using the numpy package from Python we took the fast Fourier transform (FFT) of a line of grid points of each velocity component in a particular direction. Finding the dot product of these with their respective complex conjugate we obtained the FFT of the kinetic energy for that line of grid points. The kinetic energy spectra of that line of grid points was found then by integrating over k-shells, where k is the wavenumber. This was performed on each line of grid points in that particular direction and averaged to give the plots in Figure 2.24. The same method was also used for the vorticity for the enstrophy spectra in Figure 2.25. The higher values of k plotted for the y-direction spectra is due to the lower grid spacing in y.

We plot the kinetic energy spectra in Figure 2.24. As can be observed in (b) and (c) the kinetic energy is lost at all wavenumbers apart from at $t = 45$ around $k = 10$ possibly due to high kinetic energy surrounding the vortex sheets. We see the most notable change in Figure 2.24(a) as the kinetic energy shifts to higher wavenumbers most likely due to the initially anti-parallel vortex tubes reconnecting into vortex rings in the x-direction.

We do the same for the enstrophy spectra in Figure 2.25. In Figure 2.25(a) we see the shift towards higher wavenumbers as the anti-parallel vortex tubes become vortex rings. We can also observe in (b) the formation of the vortex sheets as we see the shift to higher wavenumbers at $t = 45$ and 90.

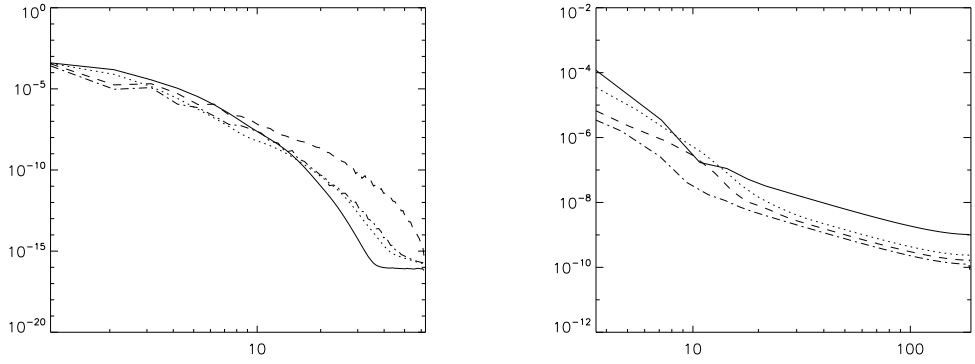

Figure 2.24: Directional spectra of the kinetic energy in (a) the x-direction, (b) the y-direction and (c) the z-direction with $t = 0, 45, 90, 135$ (solid, dotted, dashed and dash-dotted respectively).

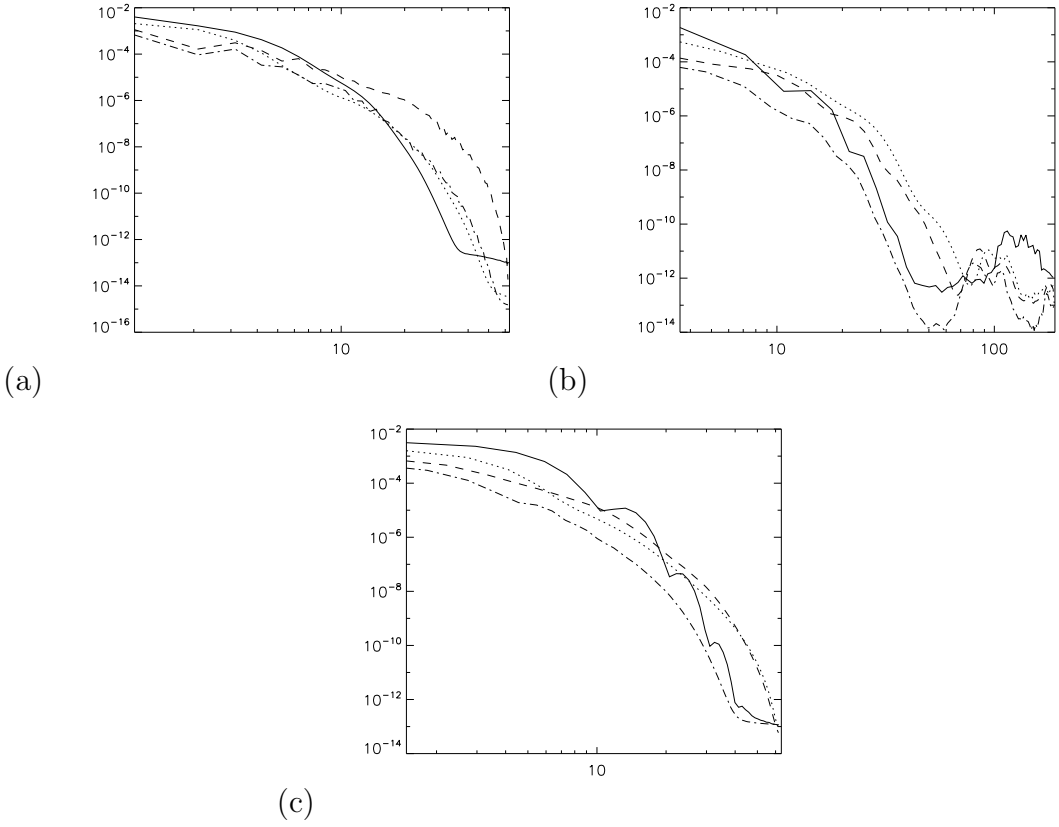

Figure 2.25: Directional spectra of the enstrophy in (a) the x-direction, (b) the y-direction and (c) the z-direction with $t = 0, 45, 90, 135$ (solid, dotted, dashed and dash-dotted respectively).

2.2.10 Helicity

For the initial condition, a single perturbed tube has zero helicity. As the perturbation and thus vortex filament exists in a single plane each vorticity fieldline has no self twist [5]. Finding the dot product of the initial velocity and vorticity of a single perturbed tube we find zero helicity as well when each of these vortex filaments are placed together to form the vortex tube. Once the opposite tube of the pair is introduced a small helicity of $\sim 3.4 \times 10^{-4}$ appears in each half of the tube with the curvature of the each tube leading to a mutual helicity between the pair.

To understand where this helicity was being created we visualised the absolute helicity density isosurfaces in Figure 2.26. The helicity density is a local value equal to $\boldsymbol{\omega} \cdot \boldsymbol{v}$ with absolute helicity density being $|\boldsymbol{\omega} \cdot \boldsymbol{v}|$ allowing us to see how these values change within different parts of the vortex tubes in the isosurfaces. In Figure 2.26(a) we see at the centre of the box the helicity generated between the two tubes. As these regions are generated, reconnection regions of non-zero $(\nabla \times \boldsymbol{\omega})_{\parallel}$ are also generated. This is displayed on the right hand side of Equations (1.42) and (1.43). As twist is introduced within the vortex tubes, these regions cause the fieldlines to slip and the twist is lost. We hypothesise that the absolute helicity is generated from the fluid elements at the symmetry plane rotating faster than those at the $x = \pm 3$ boundaries creating the twist and subsequent reconnection regions. Later in the simulation the helicity regions appear most prominently within the threads as shown in Figure 2.26(e). This helicity is due to the threads wrapping around the reconnected bridges and the flow from the bridges being near parallel to the wrapped thread.

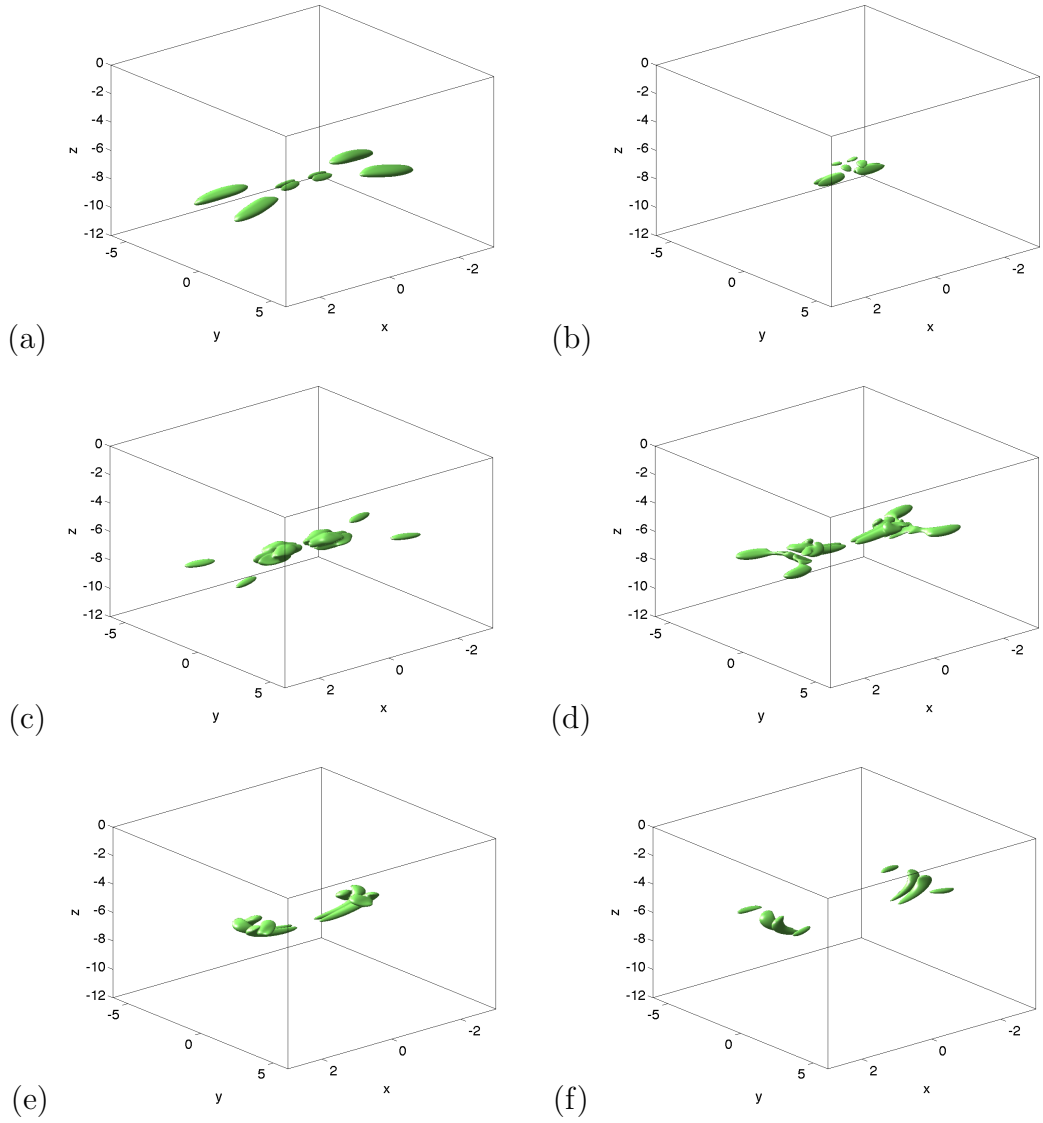

Figure 2.26: Absolute helicity density = 0.01 isosurfaces at (a) $t = 30$, (b) $t = 45$, (c) $t = 60$, (d) $t = 75$, (e) $t = 90$ and (f) $t = 120$.

2.2.11 Fieldline Measurements

To get a better understanding of the behaviours of the helicity within the threads and bridges we look at the helicity measurements along the length of each fieldline from the boundary until it reaches either the symmetry or dividing plane. Due to the symmetries of the velocity and vorticity any fieldline measurement from one boundary to another will have zero net helicity. We also measure the $(\nabla \times \boldsymbol{\omega})_{\parallel}$ term along the vorticity fieldlines to see how these terms are correlated with the helicity. By doing so we hope to demonstrate the vortex analogue of 3D reconnection or 'slipping' as discussed in Subsection 1.3.2. We shall refer to the $\int \boldsymbol{v} \cdot \boldsymbol{\omega} \, \mathrm{d}l$ and $\int (\nabla \times \boldsymbol{\omega})_{\parallel} \, \mathrm{d}l$ terms as fieldline helicity and fieldline 'slipping' rate respectively.

In Figures 2.27(a) and (b) we see the negative fieldline helicity of the threads apparent at the beginning of the simulation and the positive fieldline helicity appearing from the sides. As some of the fieldlines begin reconnecting we can see a difference between those and the threads comparing Figure 2.27(d) and Figure 2.16(d). This shows us the much more concentrated fieldline helicity in the threads compared to the bridges due to the threads wrapping around the bridge. As the simulation evolves the helicity in the bridges becomes apparent in Figure 2.27(f). We can observe these distinct events more clearly plotting the maximum and minimum values of fieldline helicity in Figure 2.28. From Figure 2.28(b) we see the initial jump in negative helicity for the threads, of course at the beginning there are no bridges, however as reconnection begins we see a small jump in negative helicity within these fieldlines but this disappears around $t \approx 50$. In Figure 2.28(a) the helicity in both the threads and bridges build up as reconnection occurs with the threads reaching a maximum of almost 3 times that of the bridges. This diminishes after the majority of reconnection

occurs as the tubes smooth out and dissipate.

To try and visualise the 3D reconnection that each fieldline is undergoing we measure the slipping rate of the fieldlines following them from the boundary in Figure 2.29 to the symmetry or dividing plane as with the helicity (using the integral measure above). The positive and negative contours of these plots give an idea of the different positive and negative reconnection regions the fieldlines passed through before meeting the symmetry or dividing planes. The positive and negative regions lead to a change in twist in either direction. There are many similarities between the contours plotted in Figure 2.27 and 2.29 demonstrating how these two phenomena are related. From these plots we are able to give an estimate of the amount of vorticity flux that has changed topology in Figure 2.30. The minimum estimate for the fieldline slipping rate is [59]

$$\left(\frac{\mathrm{d}\phi}{\mathrm{d}t}\right)_{min} = |\Xi_{max}| + |\Xi_{min}|, \tag{2.16}$$

and the maximum estimate

$$\left(\frac{\mathrm{d}\phi}{\mathrm{d}t}\right)_{max} = |\Xi_{max}| + |\Xi_{min}| + \sum_i |\Xi_{local\ extrema,i} - \Xi_{associated\ s.p.,i}|, \tag{2.17}$$

where ϕ is the flux and Ξ are values found in Figure 2.29 at local extrema and their associated saddle points (s.p.). We use both these estimates as finding the corresponding saddle point for each local extrema proved difficult. The minimum possible flux reconnected, see Figure 2.30,is roughly that of the total flux of the vortex tube. This estimate totals twists in either direction so is misleading to say the vortex tube now twists once around its centre before reaching the same plane. However it would be accurate to say that at least on average it seems that each field line is reconnected once 'internally' within the tube during the whole evolution. We can see from Figure 2.30(a) that the maximum and minimum

fieldline 'slipping' rate occur after reconnection due to the helicity oscillations observed in each quarter of the box.

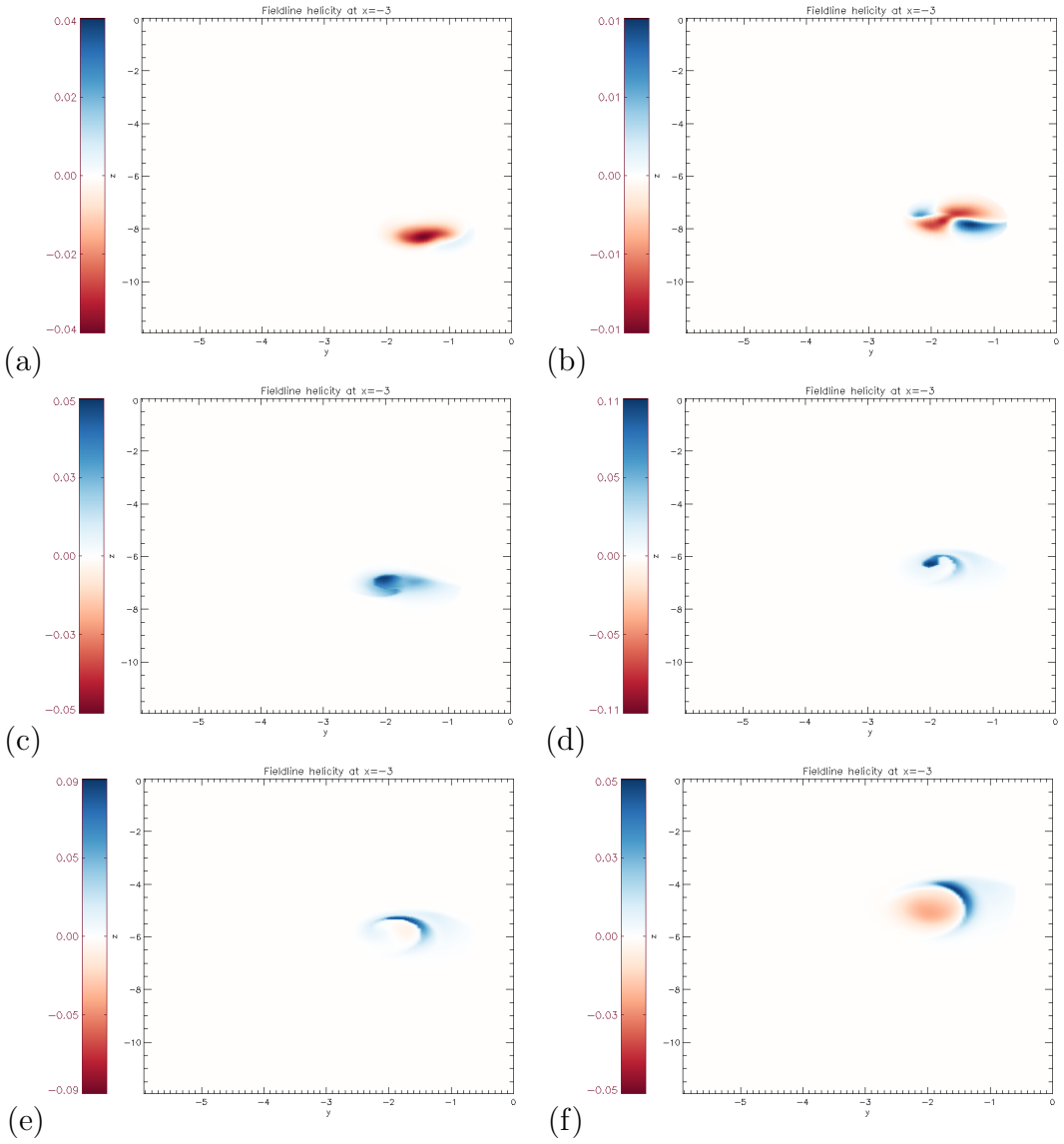

Figure 2.27: Fieldline helicity plots in the plane $x = -3$ at (a) $t = 30$, (b) $t = 45$, (c) $t = 60$, (d) $t = 75$, (e) $t = 90$ and (f) $t = 120$.

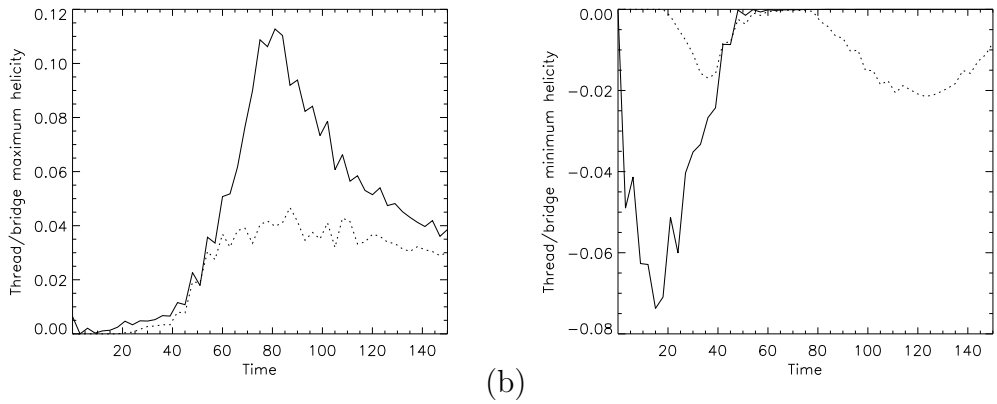

(a) (b)

Figure 2.28: (a) Maximum and (b) minimum of the total helicity measure along each vorticity fieldline, threads (solid) and bridges (dashed).

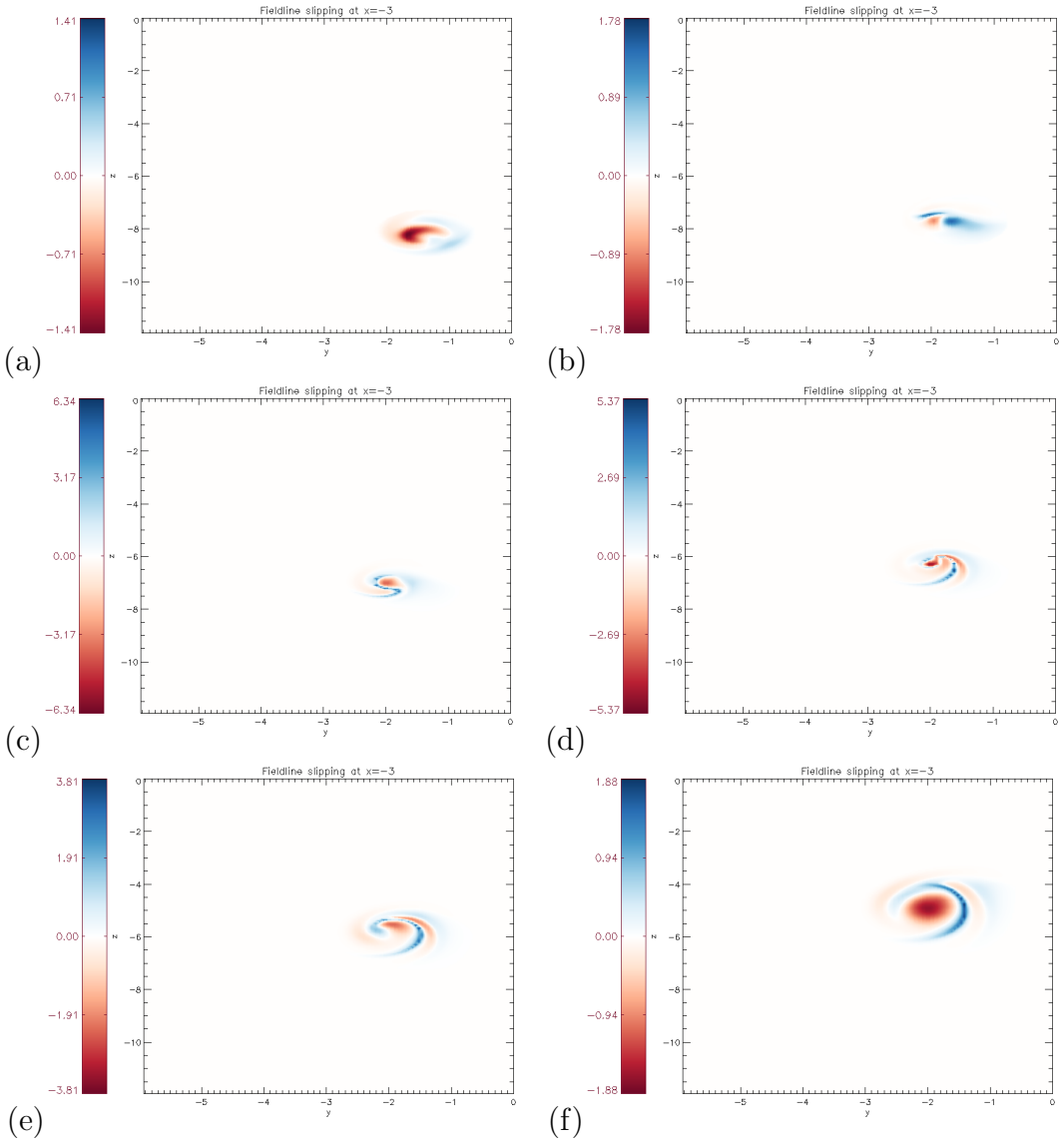

Figure 2.29: Fieldline 'slipping' rate plots in the plane $x = -3$ at (a) $t = 30$, (b) $t = 45$, (c) $t = 60$, (d) $t = 75$, (e) $t = 90$ and (f) $t = 120$.

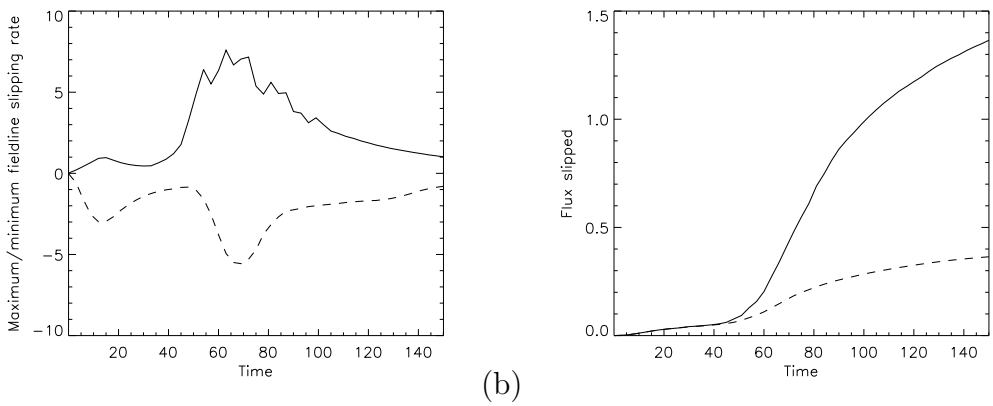

(a) (b)

Figure 2.30: (a) Maximum (solid) and minimum (dashed) fieldline 'slipping' rate and (b) maximum (solid) and minimum (dashed) possible change in flux due to 3D reconnection as discussed in Wyper and Hesse [59].

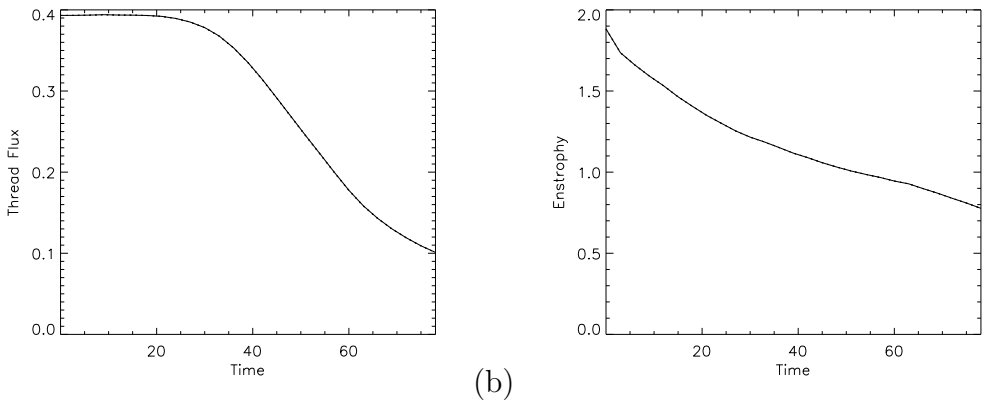

(a) (b)

Figure 2.31: Comparison of three simulations at different resolutions; [120,240,480] (solid), [120,160,480] (dotted) and [120,360,480] (dashed) showing (a) thread flux, and (b) enstrophy.

2.2.12 Convergence Study

Due to the formation of the vortex sheets becoming thin in y during the reconnection process we look to make sure the y-resolution near the dividing plane is sufficient to model this. We ran three simulations with 160, 240 and 360 grid points in the y-direction. To compare these simulations we plot the enstrophy and the vorticity flux to observe how this change in resolution affected these quantities. As shown in Figure 2.31 the plots for both these quantities are near identical, from this we can assume that the y-resolution of 240 used in this chapter was sufficient to resolve the vortex sheets.

2.3 Conclusions

We have demonstrated here a method that allows us to perturb two anti-parallel vortex tubes in such a way that they will undergo reconnection. Although this introduces a small divergence to the velocity field the density of the system remains near constant. With this in mind we are able to compare it to previous work done which has generally been incompressible.

The reconnection process, visualised by contours in the symmetry and dividing plane and as isosurfaces, was very similar to previous work [24, 41, 56]. The bridges forming at the top of the anti-parallel vortex tubes and the threads separating post reconnection were observed as expected. Observing the vorticity fieldlines which is not utilised in other work as much as the isosurfaces we were able to observe further details of the reconnection process. Here we were able to observe the threads wrapping around the bridges and the oscillations in axial flow also seen in Van Rees et al. [56]. Observing the spectra of the volume integrals enstrophy, kinetic energy and absolute helicity allowed to see how the system was behaving at different wavelengths and to observe if any numerical noise had occurred which it had not. Kolmogorov's 5/3 Law was observed during the reconnection process, consistent with previous work. We were able to observe 3D reconnection known as 'slipping' within the vortex tubes. Due to the symmetry of the box however it was difficult to see if this was a product or cause of the axial flow oscillations.

In the next chapter we will see how the Reynolds number of the system affects the reconnection process. It would be of interest to study this scenario in more detail. The generation of local helicity would be of particular interest. The different terms in (1.38) could be helpful but it will be of more interest to see how it fully ties in with the slipping of the vortex tubes. Following the hairpin

structures of the bridges is also important. How these fieldlines move when still in a highly anti-parallel state as additional fieldlines are reconnecting and pushing against them were not seen from these plots.

Chapter 3

Reynolds Number Dependence of Anti-Parallel Vortex Reconnection

3.1 Results

We repeat the simulation from Chapter 2 for a range of Reynolds numbers, Re. Where the Reynolds number is defined as:

$$Re = \frac{\Gamma}{\nu}, \tag{3.1}$$

where Γ and ν are the circulation of the vortex tube and the kinematic viscosity. Simulating this range of Reynolds numbers will allow us to observe how the viscous term of the vorticity evolution equation (1.9) will affect the reconnection process. The same initial condition and parameters are used apart from a change in the viscosity term to alter Re. We will run simulations with Re values of 40,

Re	Resolution
40	$120 \times 240 \times 360$
80	$120 \times 240 \times 360$
200	$120 \times 240 \times 360$
400	$120 \times 240 \times 480$
800	$120 \times 240 \times 480$
2000	$240 \times 240 \times 960$
4000	$240 \times 600 \times 960$

Table 3.1: Resolutions used for runs of different Re.

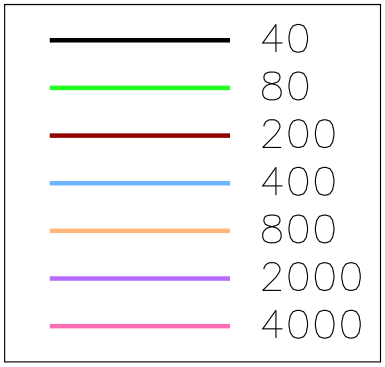

Figure 3.1: Plot colours corresponding to Re values.

80, 200, 400, 800, 2000 and 4000. For $Re < 40$ the tubes dissipate too quickly. Higher Re runs cannot be resolved with the computational power available due to the formation of thinner vortex sheets than we have the resolution for. Higher values of Re are desirable as the highest value here is still $\sim 2-3$ orders of magnitude lower than that in the wake behind an aircraft. Table 3.1 shows the different resolutions needed to resolve the thinner vortex sheets. Figure 3.1 refers to the different line colours for each value of Re for plots in this chapter.

3.1.1 Approach and Core Deformation

To observe the effects of the change of Re we first observe the vortex tubes as they behave before reconnection. We monitor the values of a single vortex tube, particularly the amplitude, the angle, the volume and the average height in z as can be seen plotted in Figure 3.2 respectively. This initial vortex tube behaviour has been discussed in more detail in Crow [11] and Garten et al. [18]. For the amplitude of the vortex tube, initially the value of the size of the perturbation, seen in Figure 3.2(a) we see the expected increase for $Re \geq 200$ described in previous work. For the lower Re runs however the amplitude diminishes. The dissipation of vorticity and thus expansion of the vortex tubes leads to this loss in amplitude which will affect the rotation of the vortex tube and subsequent formation of the vortex sheet. This can be seen in Figure 3.2(b) as the higher Re vortex tubes appear to rotate at roughly the same angular velocity up until the tubes begin to meet and this is slowed. By contrast, the lower Re cases see a much slower rotation due to this loss in amplitude and vortex tube expansion. The quick expansion is observed in (c) whilst the higher Re runs maintain their volume. Plotting the centre of mass for $|\boldsymbol{\omega}|$ during the entire run we see a clear loss in z-velocity as Re is lowered. From these plots it appears that even before reconnection the change in Reynolds number has affected the individual vortex tubes in a considerable manner.

Plotting the separation of the vortex tube centroids in the symmetry plane in Figures 3.3(a) and (b) we can see that the minimum distance between the tubes gets smaller at higher values of Re which is to be expected. The lower Re (≤ 200) reach this minimum quickly due to the large and weak cores that they evolve into. After the closest approach they evolve away from each other since the vortex tubes press against one another only weakly in the dividing plane. The tubes

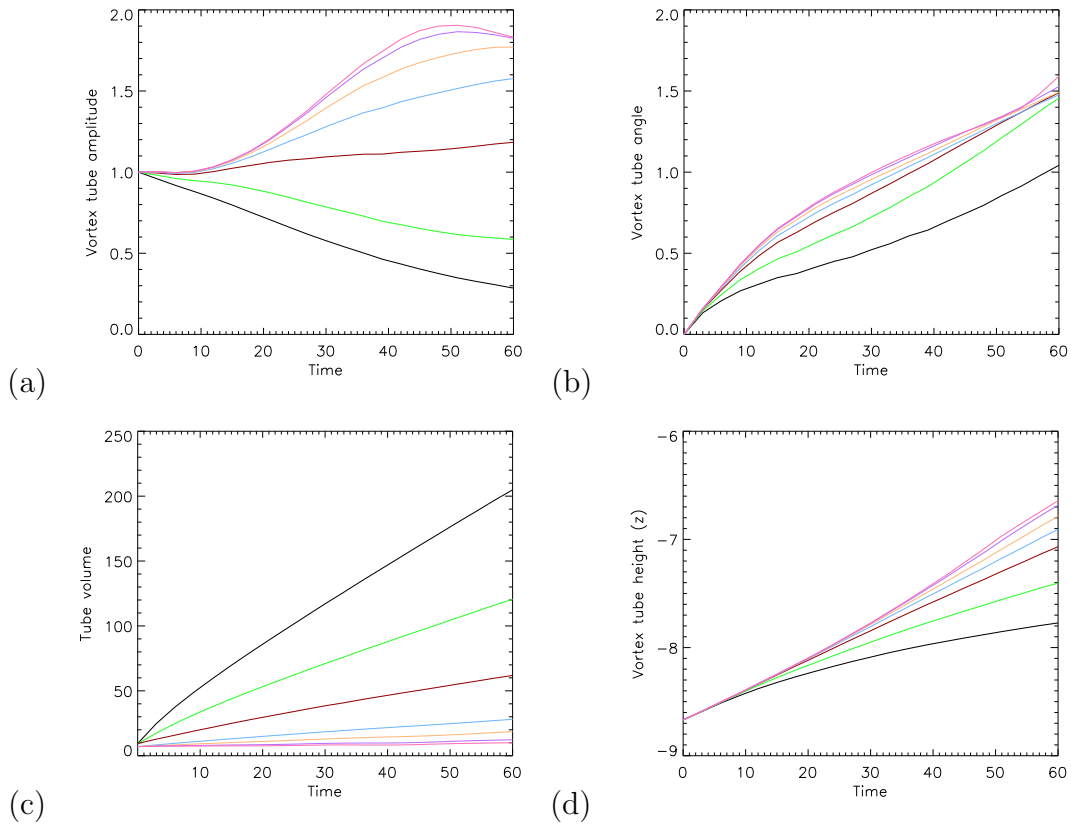

Figure 3.2: (a) Amplitude of the perturbation of the vortex tubes, (b) angle of the perturbation of vortex tube in yz-plane (measured from z-axis), (c) volume of vortex tube with $|\boldsymbol{\omega}| > 0.1\%$ of the maximum $|\boldsymbol{\omega}|$ and (d) z-position of centre of mass of vorticity over whole box.

also quickly expand outwards since there is little resistance to this dissipation. For the high Re simulations (≥ 2000) the closest approach occurs roughly at the time predicted by the LIA, demonstrating the vortex tubes have maintained their size and strength through this initial process. However as will be discussed the circular cross-section is not preserved, but instead a long elliptical shape in the dividing plane or vortex sheet. The closest approach of the tubes for high Re is dictated by how thin the vortex sheet becomes. After this the tube separation is seen to follow a similar profile to the low Re cases. However as we will observe later the vortex tubes still existing at $x = 0$, referred to as threads, are very weak in comparison to the tubes at the beginning unlike the low Re case where

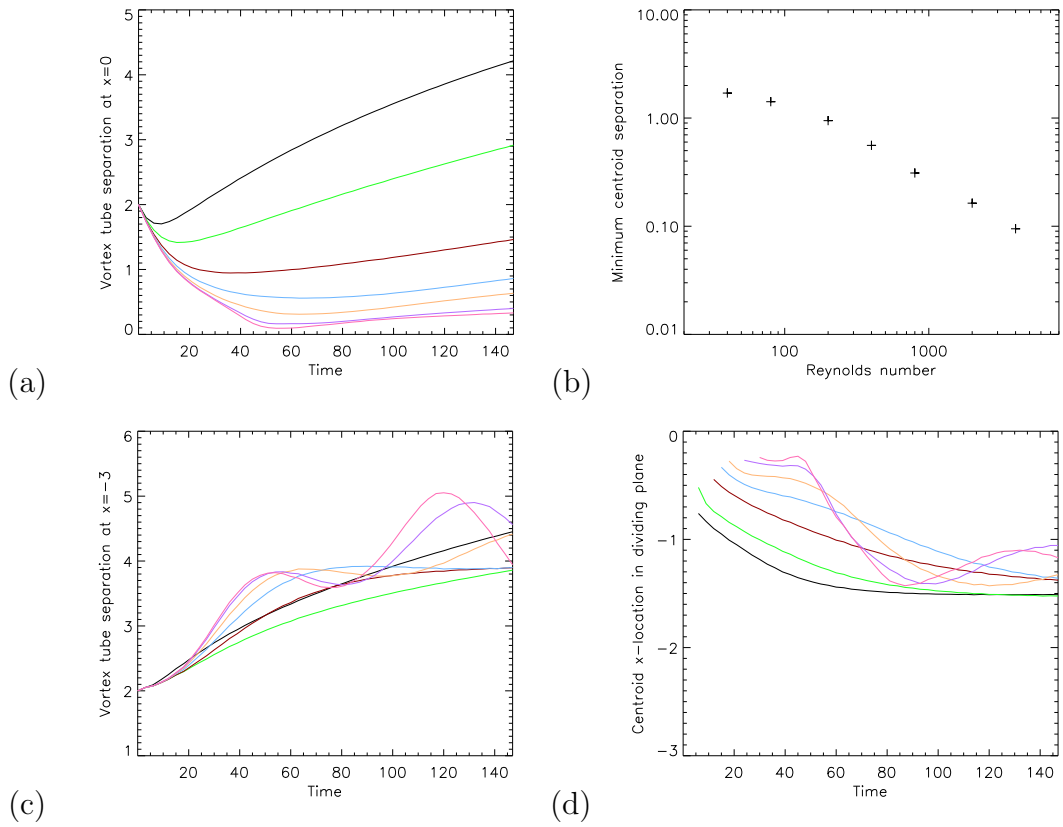

Figure 3.3: (a) Centre of mass of vortex tube y-location in symmetry plane, (b) minimum y-location as a function of Re, (c) centre of mass of vortex tube y-location at $x = -3$ boundary and (d) centre of mass of vortex tube x-location in dividing plane after reconnection.

the majority of fieldlines still pass through this plane. As the bridges continue moving in z, the threads slow down their z movement as they have become weaker. This leads to the curvature of the threads changing sign and when this occurs they begin moving apart from one another. For the medium Re cases between these extremes we see a late approach as the tubes press against each other in a similar way to the high Re case but due to the expansion of the tubes they slowly squeeze together to form the double vortex sheet at this later time. The values and times of these closest approaches, or minimum centroid separation, are shown in Table 3.2. The separation after the closest approach is then due to a combination of both the thread dissipation and new curvature of the threads.

Re	S	t_S	X	t_X
40	1.70	9	-0.760	6
80	1.42	15	-0.519	6
200	0.946	36	-0.446	12
400	0.558	63	-0.333	15
800	0.311	63	-0.276	18
2000	0.163	54	-0.269	24
4000	0.0947	54	-0.242	30

Table 3.2: Minimum separation between centroids in symmetry plane, S, the time of minimum separation, t_S, x-location of centroid in dividing plane, X and time centroid appears in dividing plane, t_X.

As vorticity begins to appear in the dividing plane (see Figure 3.3(c)) indicating that reconnection has begun we follow the z-location of the centroid of this new flux. As expected from the tube separation the lower Re simulations begin reconnection at an earlier time and vorticity passes between the tubes through the dividing plane. This begins before the minimum separation in the symmetry plane as the fieldlines with lower vorticity on the outer shell between the tubes get reconnected as the tubes are still pressing against each other forming the double vortex sheet. As the flux in the dividing plane appears it does not do so at the centre of the box as might be expected, but further along the tubes, more-so for the lower Re cases. This will be discussed in Subsection 3.1.2. These values and the time they are observed are shown in Table 3.2.

3.1.2 Double Vortex Sheet

From the previous chapter it was shown that the formation of the double vortex sheet leads to 2D reconnection with a non-zero $(\nabla \times \boldsymbol{\omega})$ term existing along a line of zero vorticity. We look to plot $\nu(\nabla \times \boldsymbol{\omega})_z$ in Figure 3.4 along the central axis as this is a product of the double vortex sheet and gives us the reconnection rate of the anti-parallel tubes. By doing so we can observe the dependence on Re of the double vortex sheet that forms as the tubes press together. To achieve a better understanding of the $\nu(\nabla \times \boldsymbol{\omega})_z$ term in the central axis we plot the two components $\nu\partial\omega_x/\partial y$ and $-\nu\partial\omega_y/\partial x$ (in Figures 3.5 and 3.6 respectively) in an attempt to see the behaviour and shape of the fieldlines lying close to the central axis. The $\nu\partial\omega_x/\partial y$ term will correspond to the threads and the $-\nu\partial\omega_y/\partial x$ term corresponds to the reconnected bridges.

We observe the behaviour of $\nu(\nabla \times \boldsymbol{\omega})_z$ in Figure 3.4 first observing the integral along the central axis, which provides the reconnection rate in Figure 3.4(a) and (b). We observe a large increase in $\int \nu(\nabla \times \boldsymbol{\omega})_z \, \mathrm{d}z$ as Re is increased due to the thinner vortex sheets forming on either side of the central axis. This corresponds to a larger reconnection rate for higher Re. This will be discussed further in Subsection 3.1.6. We look at the local values of $\nu(\nabla \times \boldsymbol{\omega})_z$ in the central axis in Figure 3.4(c)-(f). These increase in magnitude with Re as expected apart from at the lowest values of Re, the reasons for this will also be discussed in Subsection 3.1.6. The negative values of $\nu(\nabla \times \boldsymbol{\omega})_z$ appear due to the formation of the bridges, indicating they slow down the reconnection process. The double peak profile of the $Re = 4000$ plots will be explained in Subsection 3.1.3 due to an instability.

To aid in comparison between the different Re simulations we plot these values and the time they occur in Table 3.3. These show that the times of the higher

reconnection rates, and local maximum and minimum $\int \nu(\nabla \times \boldsymbol{\omega})_z \, \mathrm{d}z$ occur later for higher Re. This is consistent with the tube separation discussed earlier as the lower Re tubes dissipate. We are also able to get an idea of the length (in z) of the double vortex sheet along the central axis by comparing the integral to the maximum local value. I_{max} and L_{max} are roughly the same for $Re \leq 800$ but L_{max} becomes much greater at higher Re. This is due to the vortex tubes maintaining their volume at high Re and therefore having a smaller double vortex sheet length.

To observe the effects of the threads and bridges we plot their contribution to the reconnection rate $\int \nu(\nabla \times \boldsymbol{\omega})_z \, \mathrm{d}z$ separately. In Figure 3.5 we plot the contribution of the threads. For more detail we also show these values and the time they occur in Table 3.4. These values are very similar to the $\nu(\nabla \times \boldsymbol{\omega})_z$ values indicating that the $\nu \partial \omega_x / \partial y$ component from the bridges has not affected the process at the time of maximum reconnection rate.

In Figure 3.6 we can observe the vortex bridge's effect on the reconnection due to the $-\nu \partial \omega_y / \partial x$ component of the reconnection rate. We can see for the majority of the runs, this is less than zero throughout the whole simulation slowing down the reconnection somehow. We can observe from Figure 3.6(b) that this slowing down of the reconnection process from the bridges gets smaller with an increase in Re. Although the local value continues to increase, see Figure 3.6(d). The positive results from $Re = 2000$ and 4000, see Figure 3.6(a), are due to additional vortex rings forming around the central axis which will be discussed later in Subsection 3.1.7. Comparing Table 3.5 to Table 3.4 we see a much smaller contribution to the reconnection rate from the bridges.

We can see from the Figure 3.7(a) the reconnection occurring on top of the reconnection sheet due to the head-tail structure of the vortex sheets leading to a

Re	$I_z(\times 10^{-3})$	t_I	$L_{max}(\times 10^{-3})$	t_{max}	$L_{min}(\times 10^{-5})$	t_{min}
40	6.30	12	5.23	9	-2.29	3
80	5.01	18	4.49	15	-15.2	69
200	4.75	30	4.84	24	-48.2	57
400	5.41	42	6.09	42	-89.3	51
800	7.72	48	10.5	57	-143	48
2000	16.7	51	31.5	51	-252	45
4000	22.8	54	83.0	54	-317	69

Table 3.3: Comparison of the maximum value of $\int \nu(\nabla \times \boldsymbol{\omega})_z \, \mathrm{d}z$ along the central axis, I_z, the time it occurs, t_I, the maximum local value of $\nu(\nabla \times \boldsymbol{\omega})_z$ in the central axis, L_{max}, the time it occurs, t_{max}, the minimum local value of $\nu(\nabla \times \boldsymbol{\omega})_z$ in the central axis , L_{min} and the time it occurs, t_{min} for different values of Re.

Re	$I_z(\times 10^{-3})$	t_I	$L_{max}(\times 10^{-3})$	t_{max}
40	6.75	12	5.49	9
80	5.39	18	4.70	15
200	5.11	30	4.96	27
400	5.84	42	6.20	42
800	8.08	45	10.5	57
2000	16.8	51	31.7	51
4000	22.8	54	83.0	54

Table 3.4: Comparison of the maximum value of $\int \nu \partial \omega_x / \partial y \, \mathrm{d}z$ along the central axis, I_z, the time it occurs, t_I, the maximum local value of $\nu \partial \omega_x / \partial y$ in the central axis, L_{max} and the time it occurs, t_{max} for different values of Re.

Re	$I_z(\times 10^{-4})$	t_I	$L_{min}(\times 10^{-4})$	t_{min}
40	-6.29	24	-3.73	18
80	-5.68	36	-4.10	30
200	-4.76	45	-6.64	48
400	-4.46	48	-10.5	48
800	-3.88	45	-15.9	48
2000	-2.34	45	-26.9	45
4000	-1.66	45	-33.9	45

Table 3.5: Comparison of the minimum value of $\int -\nu \partial \omega_y / \partial x \, \mathrm{d}z$ along the central axis, I_z, the time it occurs, t_I, the minimum local value of $-\nu \partial \omega_y / \partial x$ in the central axis, L_{min} and the time it occurs, t_{min} for different values of Re.

higher $(\nabla \times \boldsymbol{\omega})_z$ nearer the top of the reconnection sheet. As the vorticity travels through the dividing plane within the dashed area there is a section of fieldlines where $(\nabla \times \boldsymbol{\omega})_z$ and more importantly $\partial\omega_z/\partial y$ is zero where the fieldlines form a smooth curve of low curvature through the dividing plane as we would expect after reconnection. However there exists a large section of fieldlines that continue to have a non-zero $\partial\omega_z/\partial y$ indicating a hairpin structure of the newly reconnected bridge fieldlines. We plot in Figure 3.7(b) $\int(\nabla \times \boldsymbol{\omega})_z \, \mathrm{d}z$ in the dividing plane for different values of x. We expect the highest value to be at the centre, where the vortex tubes meet, and the value at the boundaries to be zero as the vortex tubes should be separate here. We so not see this for the low, $Re \leq 80$, runs indicating that annihilation is occurring between the vortex tubes as they have expanded into each other all along the tube which will be discussed in more detail later. The additional peaks observed in the $Re \geq 2000$ runs are due to the formation of additional vortex rings around the central axis and shall be discussed later.

In this subsection we have demonstrated the dependence of the double vortex sheet on Re. Higher Re led to smaller vortex sheets with higher $\nu(\nabla \times \boldsymbol{\omega})_z$ components indicating a higher reconnection rate which we shall show later. Lower Re led to larger but very weak vortex sheets, even stretching across the entirety of the tube which leads to annihilation of vorticity. We were also able to show that the vortex bridges will slow down the rest of the reconnection as they form seen from the negative $\nu(\nabla \times \boldsymbol{\omega})_z$ regions in the central axis after reconnection.

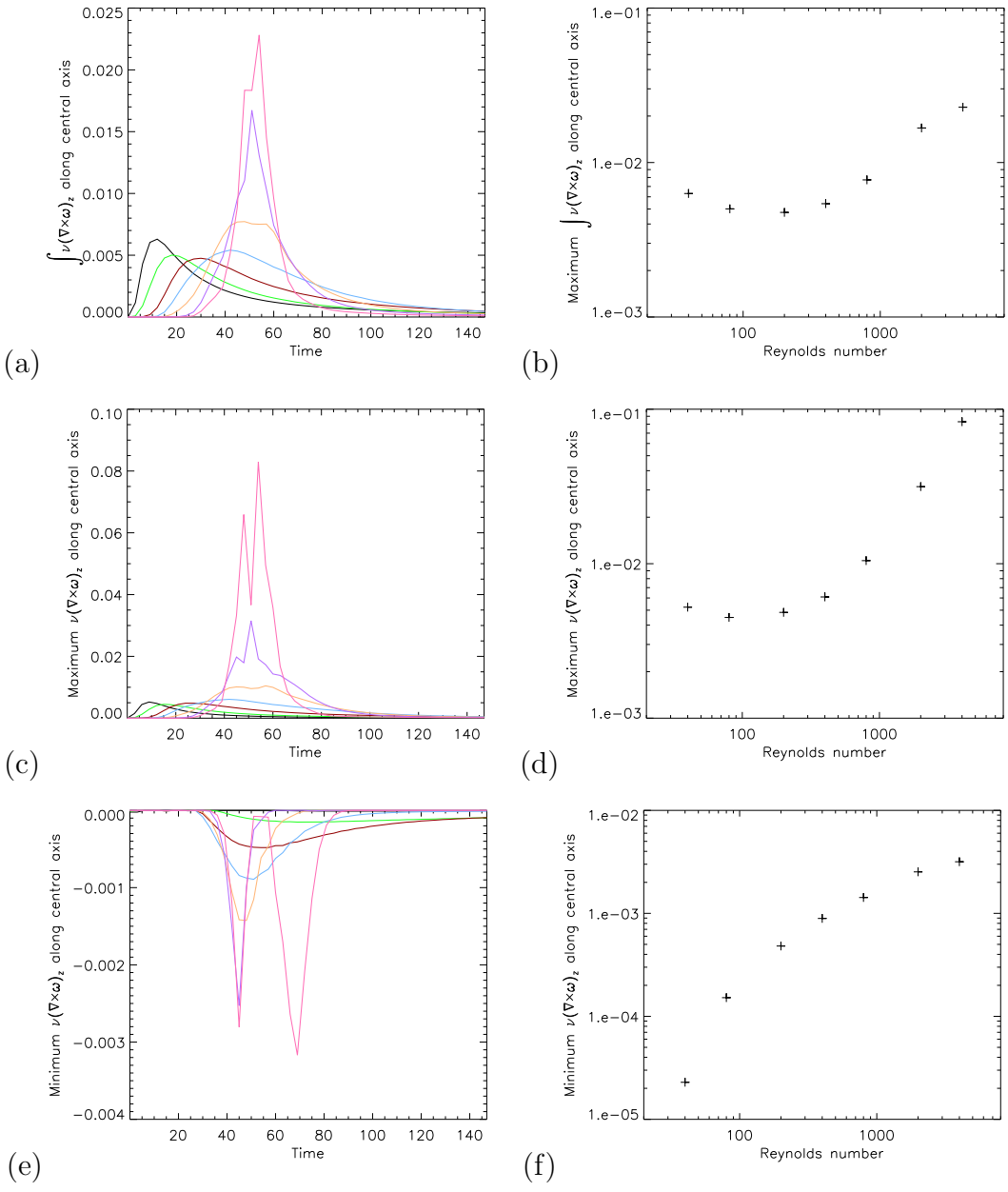

Figure 3.4: (a) $\int \nu(\nabla \times \boldsymbol{\omega})_z \, \mathrm{d}z$ along central axis, (b) maximum $\int \nu(\nabla \times \boldsymbol{\omega})_z \, \mathrm{d}z$ as a function of Re, (c) maximum value of $\nu(\nabla \times \boldsymbol{\omega})_z$ along central axis, (d) maximum $\nu(\nabla \times \boldsymbol{\omega})_z$ as a function of Re, (e) minimum value of $\nu(\nabla \times \boldsymbol{\omega})_z$ along central axis, (f) maximum $-\nu(\nabla \times \boldsymbol{\omega})_z$ as a function of Re.

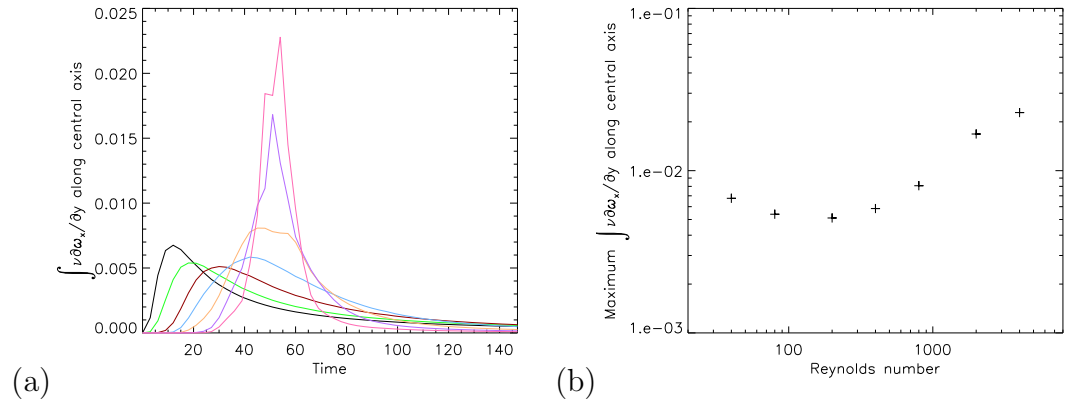

Figure 3.5: (a) $\int \nu\partial\omega_x/\partial y$ along central axis, (b) maximum $\int \nu\partial\omega_x/\partial y$ as a function of Re, (c) maximum value of $\nu\partial\omega_x/\partial y$ along central axis, (d) maximum $\nu\partial\omega_x/\partial y$ as a function of Re.

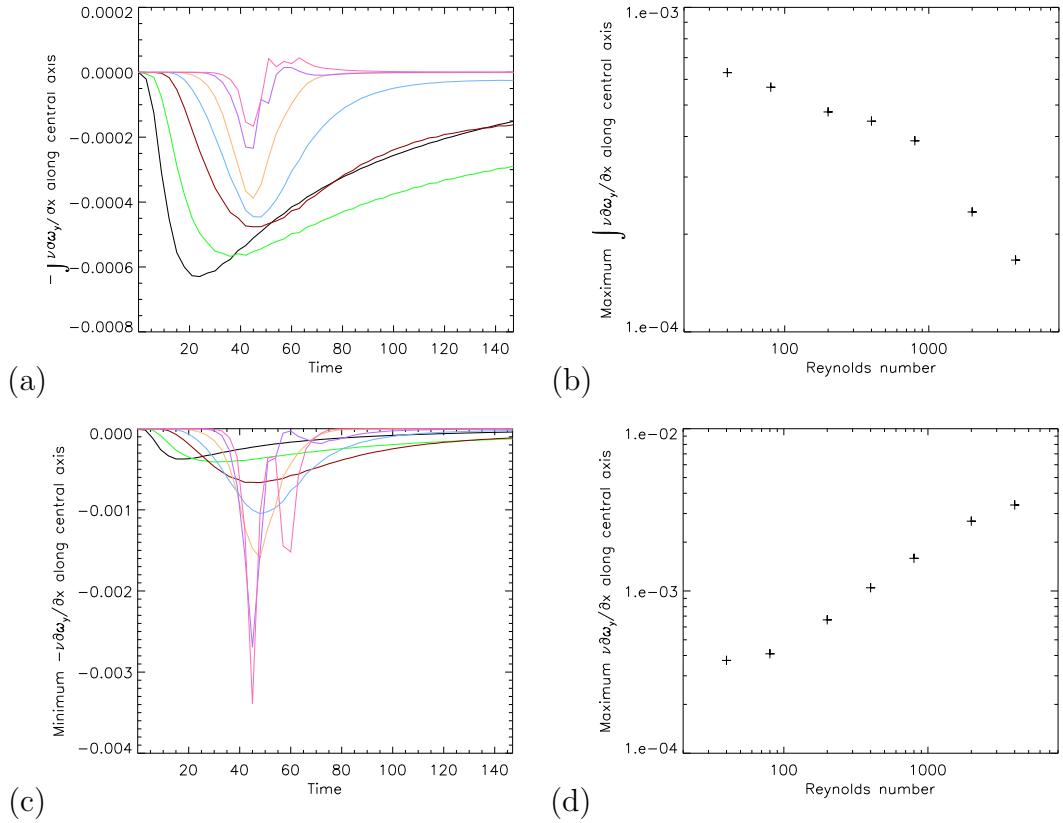

Figure 3.6: (a) $\int -\nu\partial\omega_y/\partial x$ along central axis, (b) maximum $\int \nu\partial\omega_y/\partial x$ as a function of Re, (c) minimum value of $-\nu\partial\omega_y/\partial x$ along central axis, (d) maximum $\nu\partial\omega_y/\partial x$ as a function of Re.

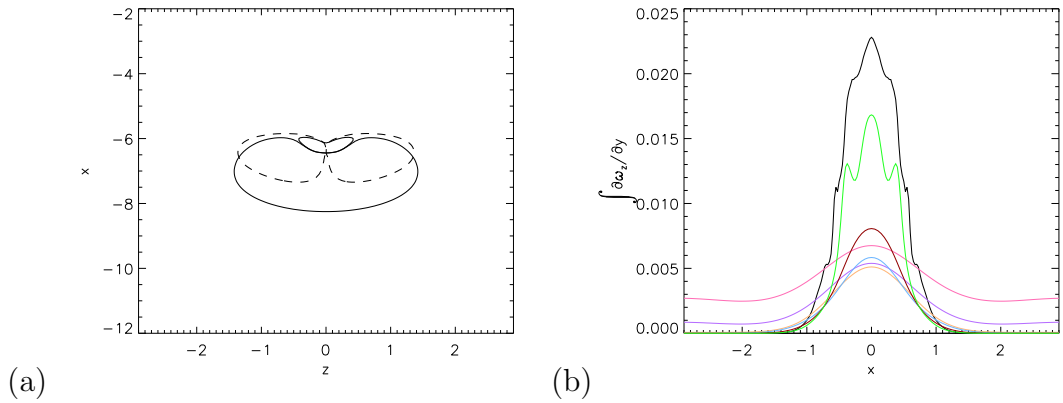

Figure 3.7: (a) Contours of non-zero $(\nabla \times \boldsymbol{\omega})_z$ (solid line) and ω_y (dashed line) in dividing plane at $t = 48$ and (b) $\int (\partial\omega_z/\partial y)\,\mathrm{d}z$ along the length of the tube as a function of x at time of maximum reconnection rate.

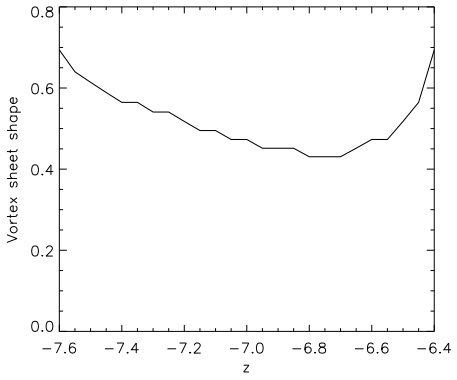

Figure 3.8: y-location of minimum value of v_z in dividing plane for $Re = 800$ at $t = 42$ demonstrating shape of vortex sheet.

3.1.3 Kelvin-Helmholtz Instability

As Re is increased, the vortex sheets become increasingly thin as seen in the previous subsection. As the vortex sheets get thinner they could become susceptible to instability. This is of particular relevance here because such an instability would likely break the symmetries that allow us to quantify the reconnection process by making measurements in the symmetry and dividing planes and along the central axis. We look to find the criteria for a Kelvin-Helmholtz instability to occur and observe whether the vortex sheets become unstable for all values of Re. For the Kelvin-Helmholtz instability to occur in a single shear flow layer the following conditions must be met [10]:

$$\frac{\kappa}{1+e^{-\kappa}} < J + 1 < \frac{\kappa}{1-e^{-\kappa}}, \tag{3.2}$$

where J and κ are defined as

$$J = \frac{-g}{\rho_0}\frac{\Delta\rho/2d}{(\mathrm{d}U/\,\mathrm{d}z)^2}, \tag{3.3}$$

$$\kappa = 2kd, \tag{3.4}$$

where g is gravity, ρ_0 is the mean density, $\Delta\rho$ is the difference in density between layers, d is half of the thickness of the layer, $\mathrm{d}U/\,\mathrm{d}z$ is the velocity derivative, and k is the wavenumber, $k = 2\pi/\lambda$. As $g = 0$, $J = 0$ and assuming $k = 1$ we can therefore show from (3.2) that

$$0 < \kappa < 1.28. \tag{3.5}$$

κ must be greater than zero so we only need to work with the right hand side of this equation. Re-arranging this in terms of the wavelength and the thickness of the layer, $2d$, we get

$$\lambda > \frac{2\pi}{1.28} 2d \approx 4.9(2d), \tag{3.6}$$

from this we expect to observe an instability when the following criterion is met

$$R = \frac{T}{H} \approx 0.2, \tag{3.7}$$

where T and H are the thickness in y and height in z of the vortex sheet respectively. We can use this ratio to observe how the vortex sheets of differing Re approach this value and become unstable.

The distance between the position of maximum v_z, along the central axis, and the position of minimum v_z is found along the vortex sheet shown in Figure 3.8. Across the length of the vortex sheet we find the region in z with the smallest value of R using the length in z as the height, H, and the maximum thickness of the sheet in that region as the thickness, T. This is a conservative measure as it does not take into account the overall thickness but instead the maximum thickness at any point along the length of the vortex sheet. We plot v_z in the dividing plane at the time of lowest thickness/length at the z value of maximum v_z in Figure 3.9(d). We can see here the dependence of the vortex sheet with Re.

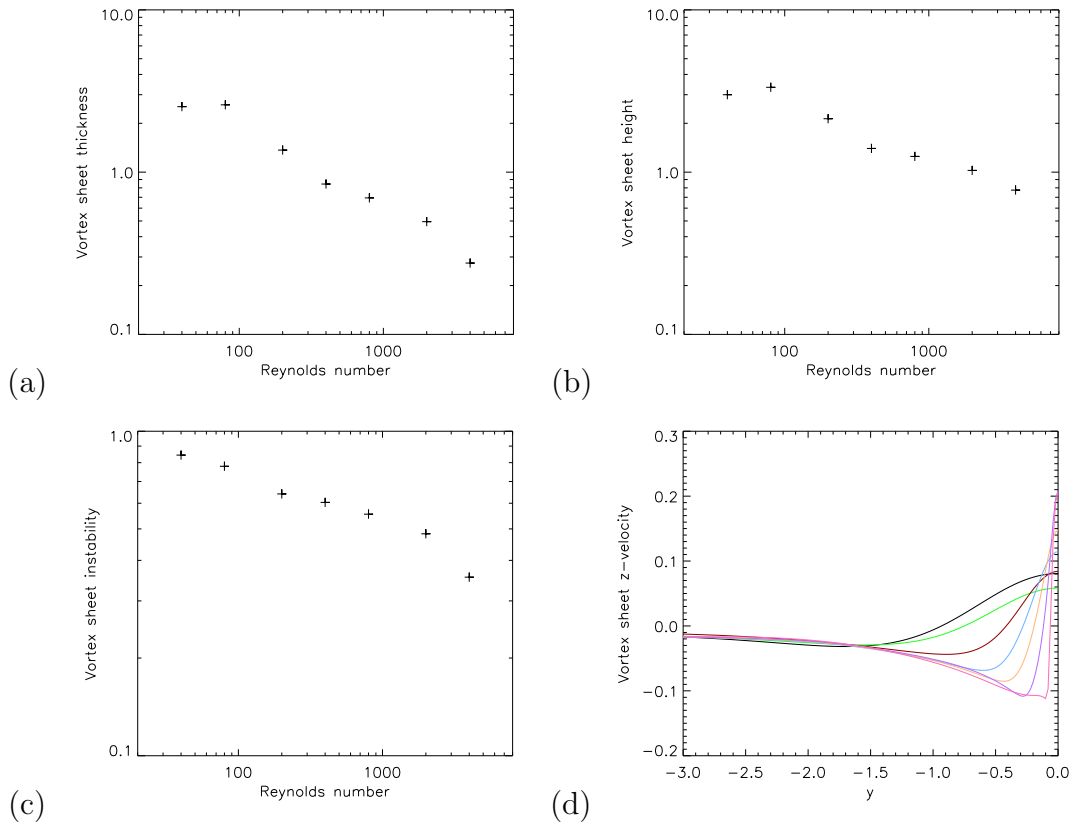

Figure 3.9: (a) Vortex sheet thickness as a function of Re, (b) vortex sheet height as a function of Re, (c) R of vortex sheet as a function of Re and (d) v_z as a function of y at time of minimum R value in dividing plane.

We plot T, H and R for the vortex sheet at the time of minimum R as a function of Re in Figure 3.9(a)-(c). It is clear from (c) how the instability is approached with increased Re.

As we can see from Table 3.6 as Re decreases the instability occurs at a later time, for a thicker and longer vortex sheet, in each case roughly achieving the theoretical prediction given by Equation (3.7). We can see the general shape of the vortex sheet in Figure 3.8 for $Re \approx 800$. We see a notable sharp decrease in R for our highest Re run in Figure 3.9. Observing the contour plots of the vortex tubes in the symmetry plane we can clearly see this instability. Vorticity was measured within the central axis for the $Re = 4000$ run but this was zero for

Re	T	H	R	t
40	2.53	3.00	0.844	15
80	2.60	3.33	0.780	39
200	1.37	2.13	0.641	36
400	0.845	1.40	0.603	42
800	0.694	1.25	0.555	42
2000	0.495	1.03	0.483	42
4000	0.275	0.775	0.355	48

Table 3.6: Vortex sheet thickness, T, and height, H, at time, t, of lowest value of R (T/H).

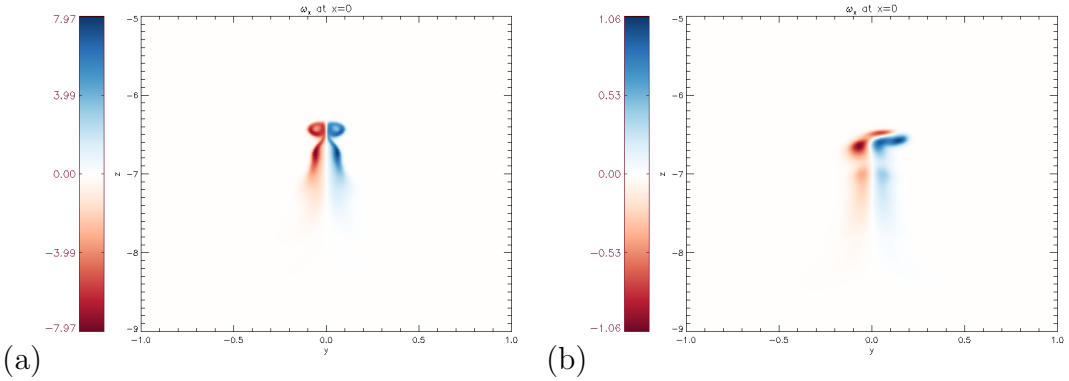

(a) (b)

Figure 3.10: ω_z contour demonstrating K-H instability in dividing plane, $Re = 4000$, at (a) $t = 48$ and (b)$t = 75$.

all other values of Re.

Considering now the highest Reynolds number simulation, we note that the lowest measure for the instability is met at $t = 48$. However it is not until $t = 75$ that the instability is visible in the contour plots seen in Figure 3.10(b). This is similar to the instability in Hussain and Duraisamy [24]. Measures of vorticity in the central axis show that vorticity is non-zero there from as early as $t = 54$. This instability evolved from this non-zero vorticity in the x-axis explaining the later time observing the instability visually. This time discrepancy due to the linear phase of the instability occurring at $t = 54$ yet we are observing the non-linear evolution of this at $t = 75$. It is worth noting that this instability can cause significant complications in analysing the reconnection of flux during the

simulation. In particular for the highest Re case in that flux measured through the dividing plane may not be reconnected flux but in fact these unstable threads. For this reason care must be taken when making flux measurements for high Re. It is also unclear whether this affects the symmetry of the fieldline measurements discussed in Subsection 2.2.11 and will be of interest in future work.

3.1.4 Visualising the Reconnection Process - Isosurfaces

To address first the case of low Re we plot the $|\boldsymbol{\omega}|$ isosurfaces for the $Re = 200$ simulations in Figure 3.11 and compare to the $Re = 800$ case seen in Subsection 2.2.3. From Figure 3.11(b) onwards we observe the most notable change being the greater thickness of the vortex tubes than in the higher Re simulation. This is due to the increased dissipation with the higher value of ν. We see no clear formation of vortex sheets near the centre of the box and therefore no double vortex sheet that would indicate reconnection has occurred. However in (c) bridges have formed on top of the vortex tubes between them demonstrating that some vorticity flux has changed to now pass through the dividing plane. The area in the dividing plane that these bridges are passing through is much thicker than $Re = 800$. As the vortex tubes continue to interact it appears to be a much simpler evolution than before, the threads do not wrap around the bridges but maintain their original orientation. The curvature of the threads does not change direction but instead straightens out in the z-direction suggesting that the separation of the centre of the tubes after reconnection is purely by dissipation. This leads us to believe that the reconnection is continuing at a higher rate than the higher Re case after the majority of reconnection has occurred as the threads will keep pressing together due to dissipation. The entire reconnection process here appears to be driven far more by the dissipative term than relying on the formation of vortex sheets to achieve a higher $(\nabla \times \boldsymbol{\omega})_z$ term.

We now perform the same visualisation for the highest Reynolds number ($Re = 4000$) run, shown in Figure 3.12. Figures 3.12(a)-(c) look fairly similar to the $Re = 800$ figures, with the main difference in (c) we can see the Kelvin-Helmholtz instability appearing as ripples in the vortex sheets in the centre of the box. In (d) the differences are more apparent with the thickness of the tubes remaining

more consistent through the simulation as we would expect due to the smaller dissipative term and we see the increased wrapping of the threads around the vortex tube, also occurring earlier than in the $Re = 800$ run. As the bridge vortex ring moves upwards the shape changes whereas it was more static in the lower Re run. We observe the same disconnect of the threads from the rest of the isosurfaces as we did in the medium Re run. However instead of being at the region close to the vortex tube wrapping it is now happening at the centre of the box. This suggests that some of the fieldlines that have wrapped around the vortex tubes have reconnected in long hairpin structures alongside the threads leading to this weaker region of vorticity in the centre of the box. Having described the isosurface evolution we now go on in the next section to analyse the structure of the vortex tubes in more detail by plotting the vortex lines themselves.

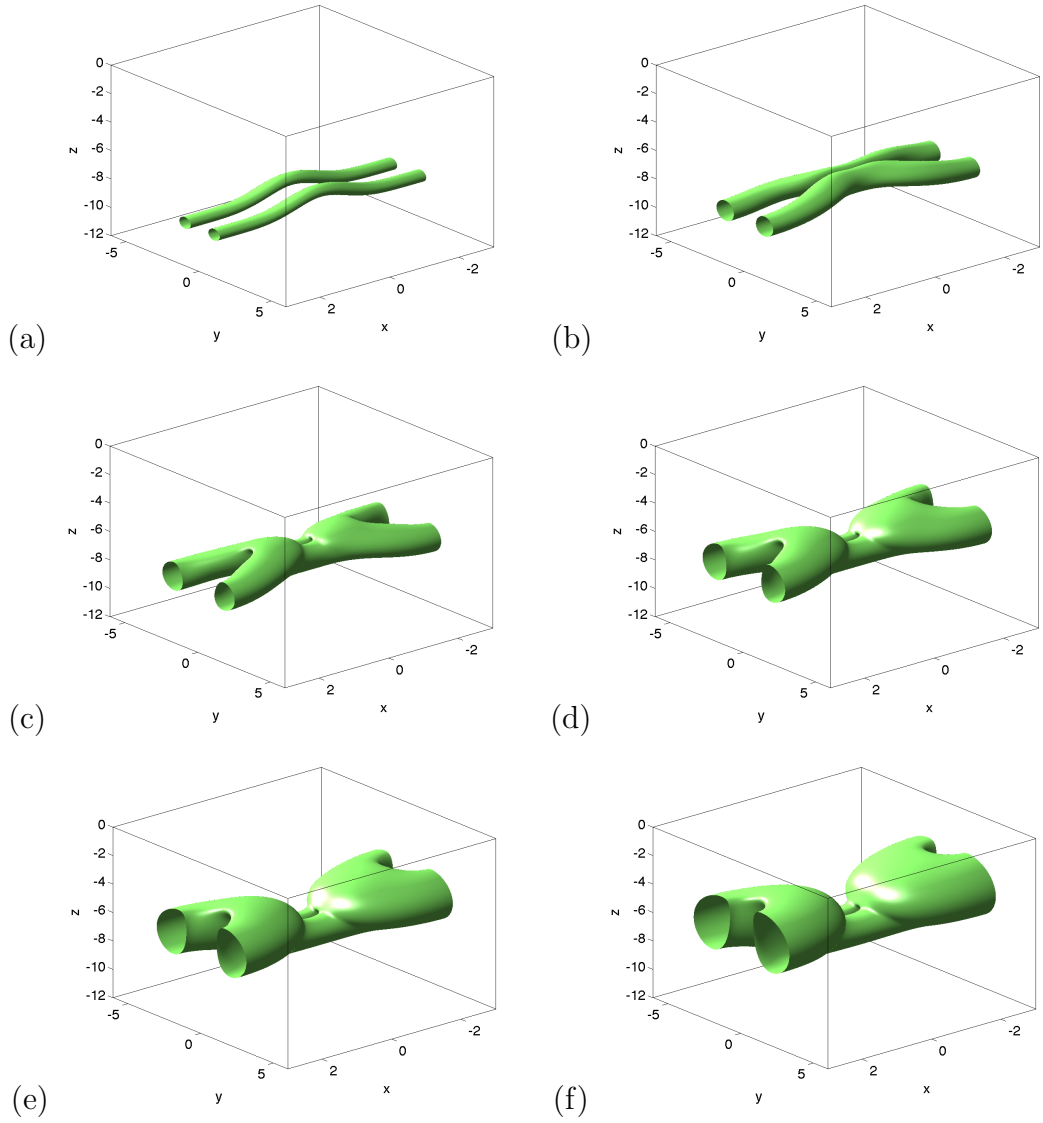

Figure 3.11: $|\boldsymbol{\omega}|$ isosurface of 30% maximum $|\boldsymbol{\omega}|$ at $x = -3$ boundary, $Re = 200$, at (a) $t = 0$, (b) $t = 30$, (c) $t = 60$, (d) $t = 90$, (e)$t = 120$ and (f) $t = 150$.

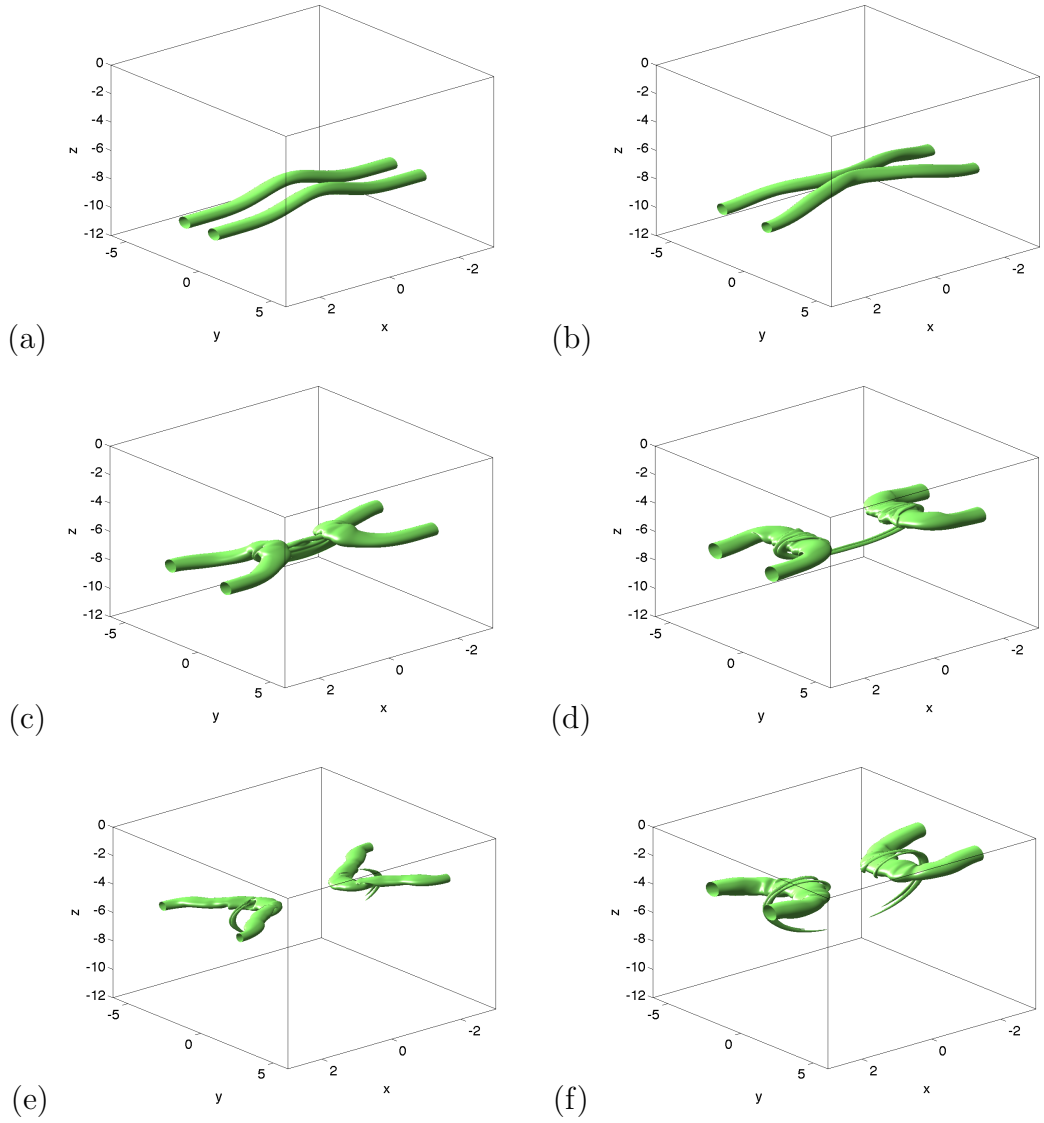

Figure 3.12: $|\boldsymbol{\omega}|$ isosurface of 30% maximum $|\boldsymbol{\omega}|$ at $x = -3$ boundary, $Re = 4000$, at (a) $t = 0$, (b) $t = 30$, (c) $t = 60$, (d) $t = 90$, (e)$t = 120$ and (f) $t = 147$.

3.1.5 Visualising the Reconnection Process - Vorticity Fieldlines

For a better understanding of the behaviour of the vorticity fieldlines during reconnection we plot the $Re = 200$ simulation in Figure 3.13 to see how they evolve compared to the $Re = 800$. From Figure 3.13(b) we already see some important events missed by the isosurface plots as reconnection has already begun, at an earlier time than the $Re = 800$ case. From observing the fieldlines near the central axis we can see the X-null point of the reconnection event. The vorticity fieldlines meet at a greater angle than the higher Re case indicating a slower separation of the bridges due to no hairpin structure forming in the bridge fieldlines. As in the isosurface plots the tubes are thicker and the area mapped out by the reconnected bridge fieldlines in the dividing plane is also bigger than that of the higher Re cases. The evolution again is much simpler and we can see clearly the threads do not wrap around the bridges, but instead just straighten out and continue propagating towards positive z.

We do the same for the highest Re case, $Re = 4000$, in Figure 3.14. The most obvious thing here is the reconnection process seems to be complete much earlier, with no threads visible by $t = 90$, see Figure 3.14(d). This demonstrates that the entirety of the fieldlines with a vorticity greater than 30% of the maximum value have reconnected with only the field lines from the weaker vorticity regions on the outside of the vortex tubes remaining as relatively weak threads. In (c) we can see two distinct bundles of threads going through the symmetry plane due to the formation of the 'head-tail' structure and the subsequent Kelvin-Helmholtz instability. We also see the oscillating shape of the bridge vortex ring that was apparent in the isosurface plots. However with the added information that the fieldlines bring we see there is a noticeable amount of twisting of the vortex tubes

seen in (d)-(f), completely non-existent in the low Re fieldline plots. From the boundaries of (f) we also see that the vortex rings are further upward than in the $Re = 800$ case meaning the vortex rings are stronger for higher Re cases which is most likely due to more flux being reconnected and less being dissipated which is consistent with lack of threads observed.

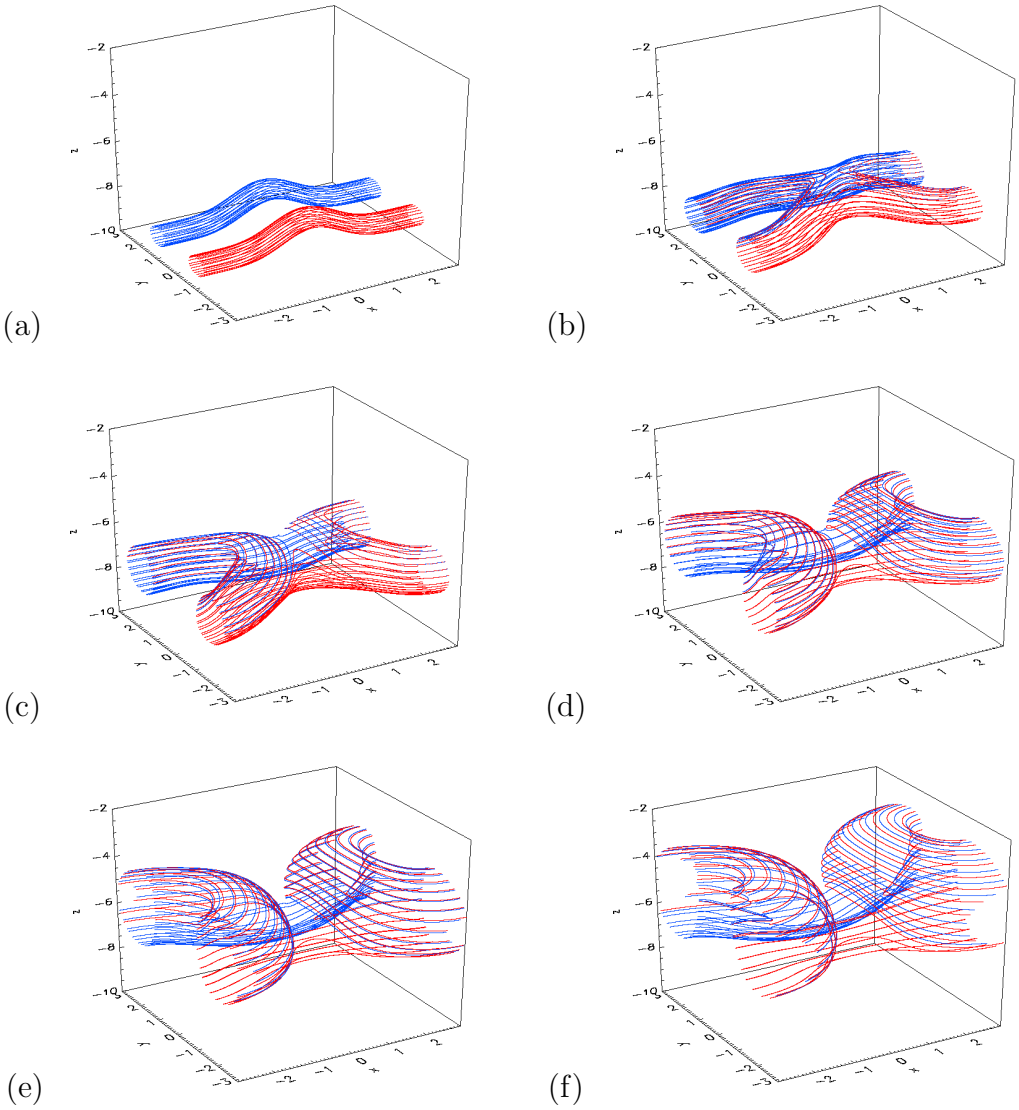

Figure 3.13: Vorticity fieldlines plotted from 30% contours at $x = \pm 3$ boundaries, $Re = 200$, at (a) $t = 0$, (b) $t = 30$, (c) $t = 60$, (d) $t = 90$, (e)$t = 120$ and (f) $t = 150$.

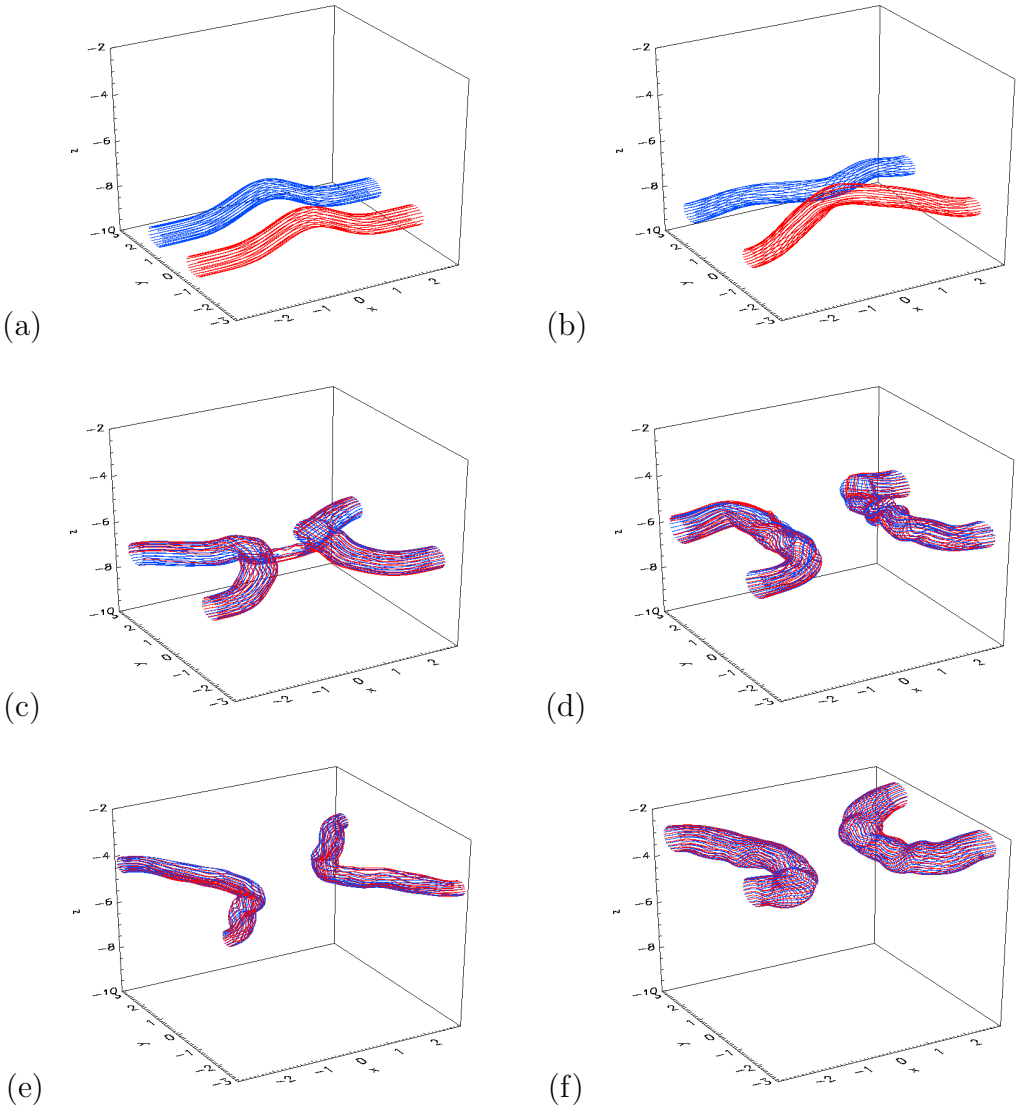

Figure 3.14: Vorticity fieldlines plotted from 30% contours at $x = \pm 3$ boundaries, $Re = 4000$, at (a) $t = 0$, (b) $t = 30$, (c) $t = 60$, (d) $t = 90$, (e)$t = 120$ and (f) $t = 147$.

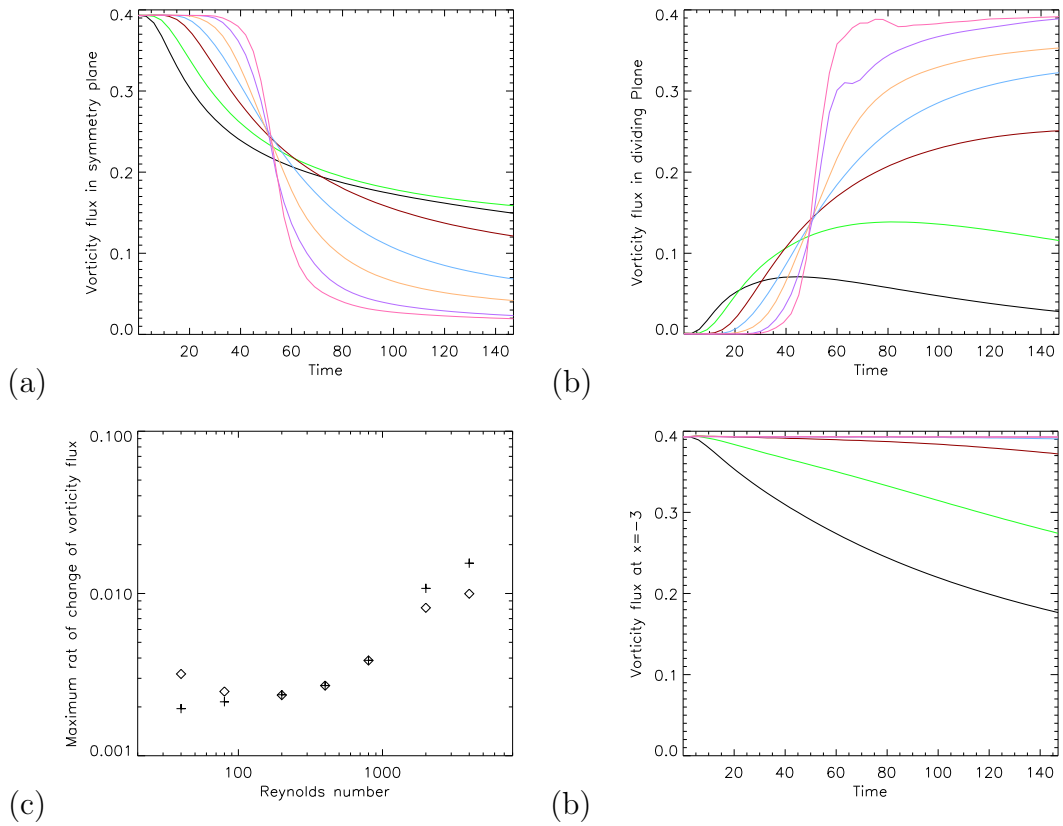

Figure 3.15: (a) ω_x flux in symmetry plane, (b) ω_y flux in dividing plane, (c) maximum rate of change of flux in symmetry plane (crosses) and dividing plane (diamonds) and (d) ω_x flux at boundary $x = -3$.

3.1.6 Flux Evolution

As an initial attempt at comparing the reconnection rate between the different simulations we plot the vorticity flux measured in both the symmetry and dividing plane in Figures 3.15(a) and (b) respectively. From the later times of (a) right at the cut-off of the simulation we observe the strength of the leftover threads showing a clear dependence on *Re* excluding the lowest case although comparing these is tricky due to the reconnection process never quite finishing. Longer runs would be required to observe any limits approached by the thread flux and this would require a larger simulation box and more computational time. The most important thing seen with these two plots is that the fluxes in (a) and (b) do

Re	R_M	t_M	R_N	t_N	R_E
40	6.25	12	1.79	12	42.5
80	4.96	18	1.46	21	28.8
200	4.72	30	1.48	36	45.1
400	5.36	42	1.98	54	44.8
800	7.71	48	3.86	60	26.8
2000	15.1	51	7.07	54	15.7
4000	19.4	54	10.7	57	5.6

Table 3.7: Comparison of reconnection rates for different values of Re. Maximum rate of change of vorticity flux in symmetry plane ($\times 10^{-3}$), R_M, and the time it occurs, t_M, maximum percentage change of flux in symmetry plane as a function of leftover thread flux, R_N, and the time it occurs, t_N, and the rate of change of flux in symmetry plane at the end of the simulation $t = 147$ ($\times 10^{-5}$), R_E.

Re	t_s	t_e	Δt
40	4.8	36.4	31.6
80	9.0	50.7	41.7
200	16.4	66.4	50.0
400	23.9	78.8	54.9
800	31.8	74.9	43.1
2000	41.3	65.0	23.7
4000	44.2	63.2	19.0

Table 3.8: Comparison of reconnection rates for different values of Re. Time reconnection begins, t_s, time reconnection ends, t_e, and the total time of reconnection, Δt.

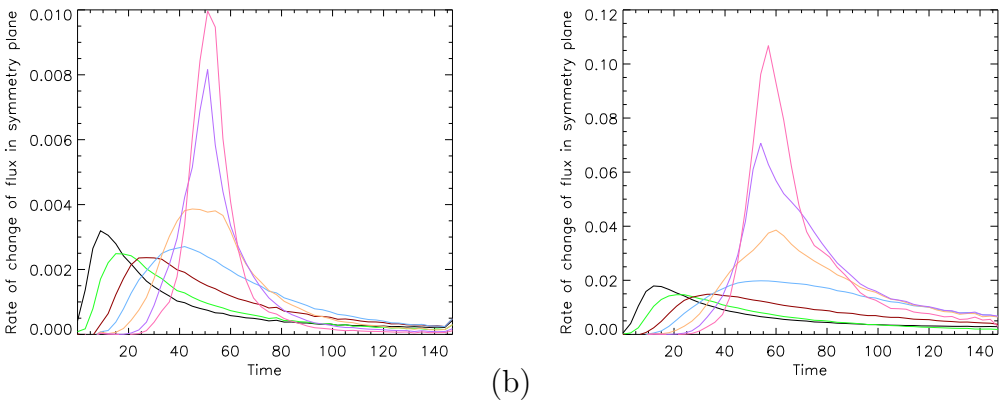

(a) (b)

Figure 3.16: (a) Rate of change of ω_x flux in symmetry plane and (b) rate of change of ω_x flux in symmetry plane divided by ω_x flux in symmetry plane.

not sum to a constant, the original flux. We would expect that a loss in the flux in the symmetry plane would directly correspond to a gain in flux in the dividing plane. This is true for Re of 200, 400 and 800 but lower and higher Re have different explanations why these flux measurements do not match up. To understand this more clearly we measure the maximum rate of change of flux in both the symmetry and dividing plane and compare them in Figure 3.15(c). Here we can see that the dividing plane flux rate is greater than the symmetry plane flux rate for low Re and vice versa for the high Re. We can see the reason for the difference in the low Re cases in Figure 3.15(d) from the vorticity flux measured at the $x = -3$ boundary. The vortex tubes are not simply reconnecting at the central axis like in the medium Re simulations but instead the vortex tubes are pressing against each other all along the length of the tube. The vorticity fieldlines are annihilating, as discussed in Subsection 1.3.2, explaining the loss of flux at the boundaries for the lower values of Re. This high dissipation rate causes the early reconnection and the bridge vortex rings are pressed together at the boundary at $x = -3$. This gives the impression that there is a particular value of Re for which we could find for the lowest total reconnected flux possible for the system of ≈ 200, where Re lower than this loses flux primarily to annihilation

caused by dissipation and higher Re undergoes the reconnection process we have discussed previously. The reasons for the additional flux found in high Re cases will be discussed in Subsection 3.1.7. A small amount of the additional flux in the $Re = 4000$ plot is due to the Kelvin -Helmholtz instability but this is negligible compared to the fluxes found due to the other reasons described later.

For simplicity we only compare the change in flux in the symmetry plane, due to the nature of the reconnection we also plotted the rate of change of flux as a fraction of the current thread flux to see the maximum amount of flux that was at any point reconnecting of the leftover threads seen in Figure 3.16(a) and (b) respectively. From Figure 3.16(a) we can see the differences that the change in Re introduces to the system. For the lower Re we see earlier reconnection and this both begins later and peaks later as Re is increased and appears to approach a limiting time by which the tubes must have reconnected. From $Re = 200$ upwards we see an increase in maximum rate of change of flux, the different values of which and time of occurrence are available in Table 3.7. t_M as seen in Table 3.7 increases with Re due to the additional time taken to form the thinner vortex sheets. As the threads become weaker so does the reconnection rate. However as seen in (b) the fraction at which they are reconnecting continues to increase after the peak seen in (a) due to the double vortex sheet continuing to form and stretch as vorticity fieldlines change plane. This is also seen in t_N as it is later than t_M for all Re. We also look to see the reconnection rate at the end of the simulation. The vortex reconnection process is never complete, but it is also not clear whether it will ever end. We can see from Table 3.7 that for the lower Re runs there is still a notable reconnection rate well after the 'main' bout of reconnection has ended. For future studies it would be of interest to increase the height of the box simulated to see how the threads continue, whether they ever split apart and cease reconnecting completely or if they continue to expand into each other and

continue reconnection.

We now look to quantify the time it takes for the vortex tubes to reconnect. This is difficult as the reconnection process is never complete. We use the same process discussed in Chapter 2 to separate the simulation into 3 parts. These are pre reconnection (where the tubes rotate and begin forming the double vortex sheet), main reconnection (where the majority of the flux changes plane) and post reconnection (where the threads continue to reconnect but at a slower rate). We define t_s and t_e as the start and end times of the main reconnection process shown in Table 3.8. We also show the length of the process, Δt. We can see from this clearly the later start to reconnection as Re is increased due to the higher Re runs forming thinner vortex sheets before reconnecting. With this definition we find that $Re = 400$ has the longest reconnection process. This is possibly due to the difficulty of defining the separate processes for lower Re. These reconnection times are consistent with the higher reconnection rates shown earlier. Now that we have discussed the simple reconnection of vorticity from threads to bridges we now look to discuss the additional vorticity observed within the dividing plane due to the formation of additional vortex rings around the central axis.

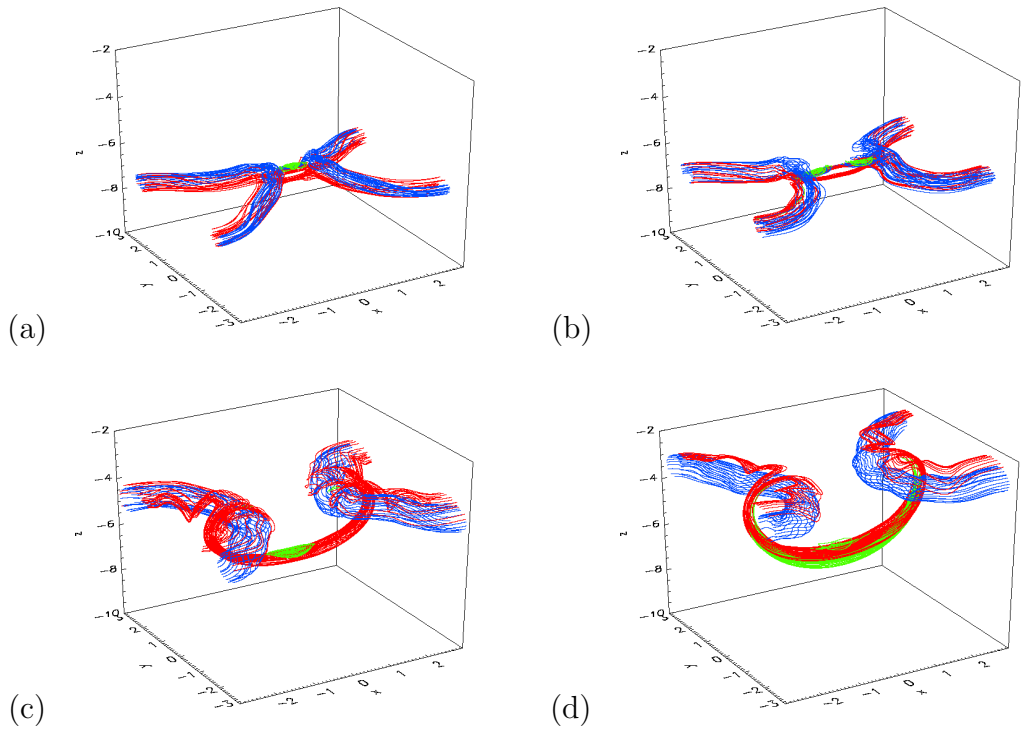

Figure 3.17: Threads (red) plotted from 30% maximum ω_x contours at $x = 0$, bridges (blue) plotted from 30% maximum ω_y contours at $y = 0$, additional vortex ring fieldlines (green) plotted from 30% maximum ω_y (of opposite sign to bridges) contours at $y = 0$, $Re = 4000$ at (a) $t = 54$, (b) $t = 63$, (c) $t = 111$ and (d) $t = 138$.

3.1.7 Additional Vortex Rings

From a value of Re of ~ 800 we begin to observe reconnection events further along the threads instead of within the symmetry plane where the main reconnection occurs. This additional reconnection creates new vortex rings, shown by green field lines in Figure 3.17. These additional vortex rings form along the fieldlines and create additional flux in the dividing plane. The introduction of these vortex rings add more null points in the system along the dividing plane, both X and O nulls. As can be seen from Figure 3.18 there is a sharp peak beginning after reconnection for the flux in these additional rings and then it quickly dissipates. Due to the threads being very close together when they reconnected the rings

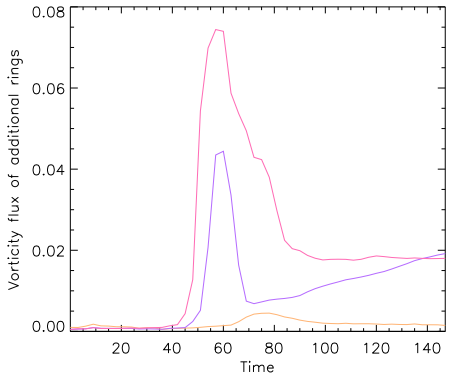

Figure 3.18: Vorticity flux in dividing plane due to additional vortex rings as a function of time.

are very thin and quickly annihilate afterwards. Small remnants of the rings are left over after this annihilation and further into the reconnection process the elongated threads wrapping around the vortex tubes reconnect creating very long vortex rings seen in Figure 3.17(d). It is expected that even more of these rings would appear and annihilate at higher values of Re but this was not possible to check with available processor power. These additional vortex rings appear to be very similar to the 'curved vortex belts' of Weiguo et al. [58].

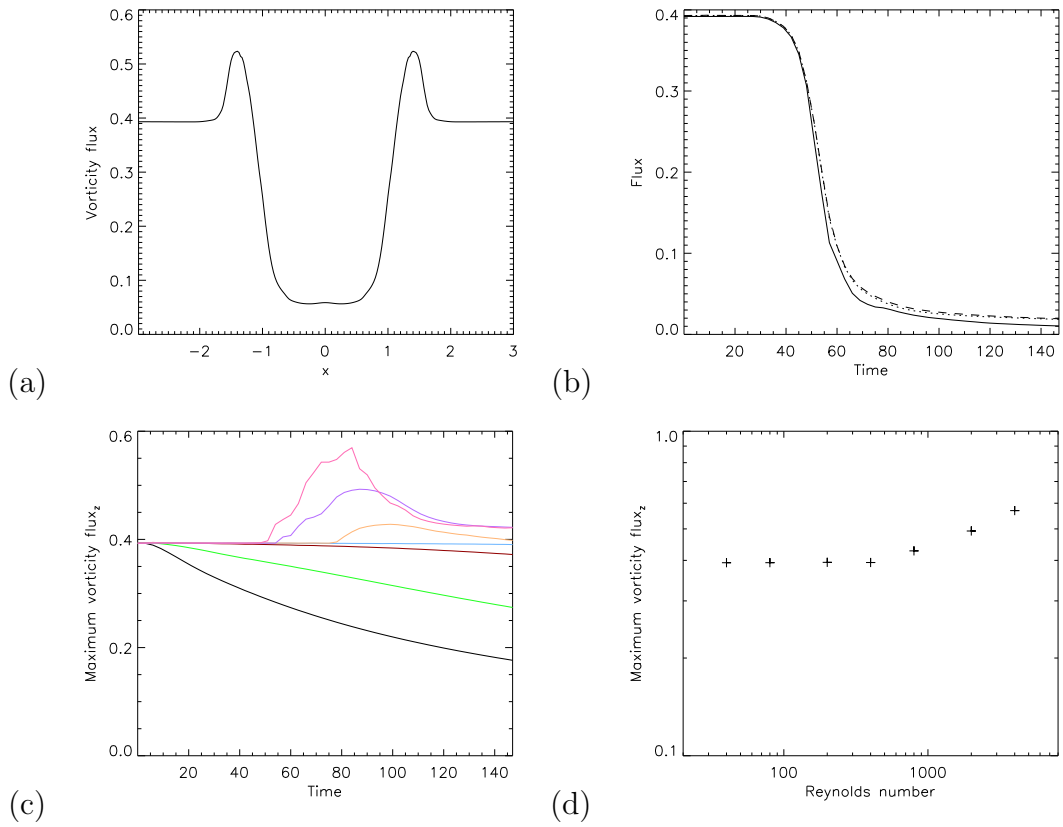

Figure 3.19: (a) Surface integral of $|\omega_x|$ in yz-plane as a function of x at $t = 69$, $Re = 4000$, (b) ω_x flux at $x = 0$ (dashed), minimum $|\omega_x|$ flux anywhere along the tube (dotted) and thread flux (solid), $Re = 4000$, (c) maximum $|\omega_x|$ flux anywhere along the tube as a function of time and (d) maximum $|\omega_x|$ flux as a function of Re.

3.1.8 Different Measures of Flux

Initially we may expect that for vorticity flux measurements in any yz-plane the minimum will occur at $x = 0$ (where the reconnection occurs) and the maximum at the $x = -3$ boundary (where no reconnection occurs). This is true for low Re but not the case as Re is increased. We can demonstrate this by measuring the vorticity flux in the yz-plane as a function of x, see Figure 3.19(a). The slight increase of flux at $x = 0$ is due to the additional vortex rings around the central axis so therefore the minimum flux measurement is no longer at the centre of the box. The minimum value of vorticity flux seen in (a) is also not necessarily the

vorticity flux of the threads as there may be no yz-plane where only threads pass through. The different measures due to this are plotted in (b). In Figures 3.19(c) and (d) we can see the maximum ω_x flux measured throughout the box, for low Re we see the annihilation of vorticity explained before. For medium Re we observe a near constant maximum ω_x flux indicating no wrapping of threads or annihilation. The highest Re cases where we observe maximum ω_x flux greater than our initial flux is due to the wrapping of threads around the bridges.

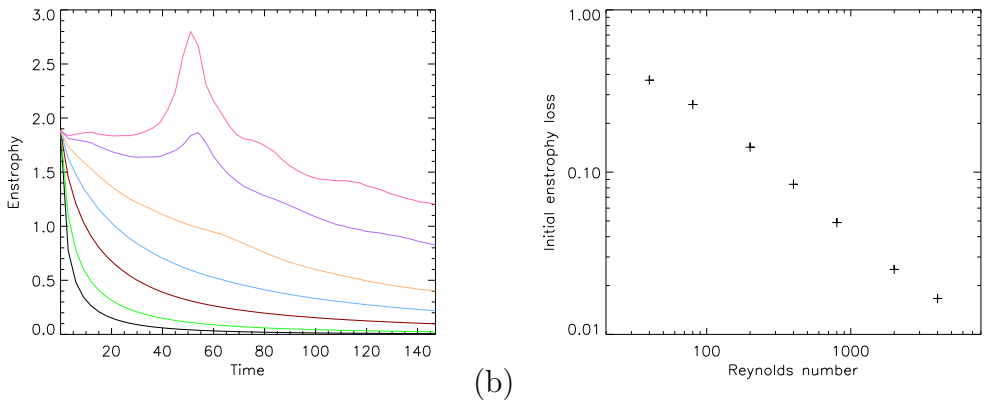

(a) (b)

Figure 3.20: (a) Enstrophy and (b) initial loss of enstrophy (between $t = 0$ and 3) as a function of Re.

3.1.9 Volume Integrals

In this section we investigate the global properties of the reconnection process as a function of Re by examining the following integral quantities; enstrophy, kinetic energy and helicity. We also use this subsection to discuss the maximum vorticity in the box over time.

There is a clear increase in enstrophy with Re seen in Figure 3.20(a) which is to be expected due to the decreased dissipation. Most notable is that for the higher Re simulations a peak enstrophy is observed at the time of the double vortex sheet being its strongest. This is only visible in the two highest Re cases with a small bump in the third as the lower Re do not form a strong enough double vortex sheet to show a large enough increase in enstrophy. Comparing to the enstrophy plots of Kerr and Hussain [28] we do not see the initial loss that we have for the range of our Re runs. This is likely due to initial angle of their vortex tubes so that the vortex tubes reconnect sooner. They still see the same peak for their simulations of $Re = 2300$ and 3200 however their simulations end just after peak enstrophy so we cannot compare for the rest of the run.

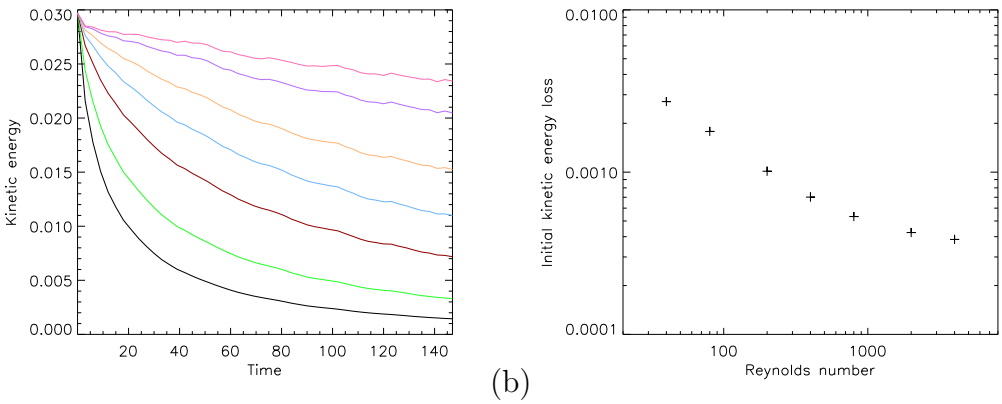

(a) (b)

Figure 3.21: (a) Kinetic energy and (b) initial loss of kinetic energy (between $t = 0$ and 3) as a function of Re.

No notable events occur for the kinetic energy plotted in Figure 3.21 as it dissipates through time. As expected the higher Re simulations conserve the kinetic energy better demonstrated in Figure 3.21(b).

Due to the symmetry of the tubes in the symmetry and dividing plane the total helicity of the box is zero throughout the entire simulation. Taking the helicity of a quarter of the box however is non zero seen plotted in Figure 3.22(a). Instead it demonstrates a quick jump in helicity followed by dissipation for lower Re. For higher Re we see the same oscillations as discussed in Subsection 2.2.8. As Re is increased the period of the oscillation becomes smaller and the amplitude becomes greater. We hypothesise this is due to the tube rotating quicker at the symmetry and dividing plane for high Re possibly expelling the oscillations. We hypothesise the increase in amplitude is due to the increased twisting of the tubes as they maintain their size and strength. We observe the absolute net helicity for the whole box in Figure 3.22(b). We can see clearly the increase with Re with the oscillations seen in (a) also apparent. It is clear from these points that the axial flow of one quarter of the box is not simply oscillating, but axial flow of different signs dominating the other. In Figure 3.22(c) and (d) we show the local maximum and minimum helicity density in a quarter of the box and the

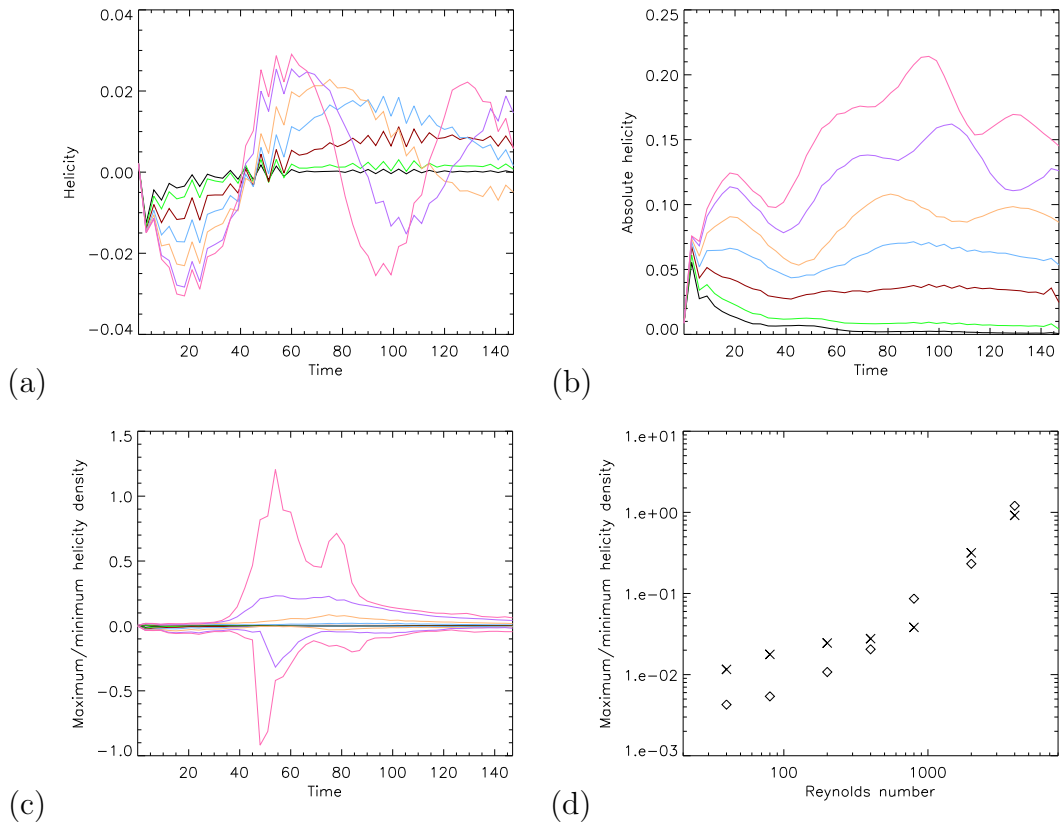

Figure 3.22: (a) Net helicity in quarter of the box, (b) absolute net helicity over the whole box, (c) maximum and minimum helicity density in quarter of the box and (d) maximum positive (diamonds) and negative (crosses) helicity density in quarter of the box as a function of Re.

dependence on Re is clear.

Unlike in enstrophy where no peak value could be found for lower Re, with the maximum vorticity being a local variable it is much easier to identify. As Re is increased the maximum vorticity throughout the box, through the symmetry plane and through the dividing plane increase, as seen in Figure 3.23(a)-(c) respectively. Low Re simulations experience their maximum vorticity at the initial condition as the dissipation is too strong, or slightly after when a small vortex sheet is formed before the dissipation becomes too great. For higher Re the maximum vorticity occurs at the time of the formation of the double vortex sheet

Re	M	t_M	M_x	t_x	M_y	t_y
40	1.29	0	0.998	0	0.0236	24
80	1.29	0	0.998	0	0.0512	45
200	1.29	0	1.05	3	0.164	69
400	1.29	0	1.22	6	0.469	75
800	1.57	66	1.57	66	1.31	63
2000	4.77	51	3.81	48	4.63	51
4000	11.9	51	10.3	51	9.23	48

Table 3.9: Comparison of maximum $|\boldsymbol{\omega}|$ anywhere in the box, M, the time it occurs, t_M, the maximum $|\omega_x|$ in the symmetry plane, M_x, the time it occurs, t_x, the maximum $|\omega_y|$ in the dividing plane, M_y, and the time it occurs, t_y, for different values of Re.

observed in Table 3.9. We plot the maxima found in both the symmetry and dividing plane in Figure 3.23(d), due to the initial condition the maximum vorticity through the symmetry plane can not be below 1. However we see a very strong correlation of the maximum vorticity in the dividing plane of the reconnected bridge fieldlines due to the thickness of the tube and the amount of flux once reconnected. Assuming this correlation is of the form $c \cdot Re^m$ we find $c \approx 2 \times 10^{-4}$ and $m \approx 1.3$. These values are compared with the time they occur in Table 3.9. For $Re \geq 2000$ this maximum vorticity is no longer simply a measure of ω_x and the time it occurs at roughly the same time of peak reconnection. This could prove useful for those looking into vorticity singularities [8].

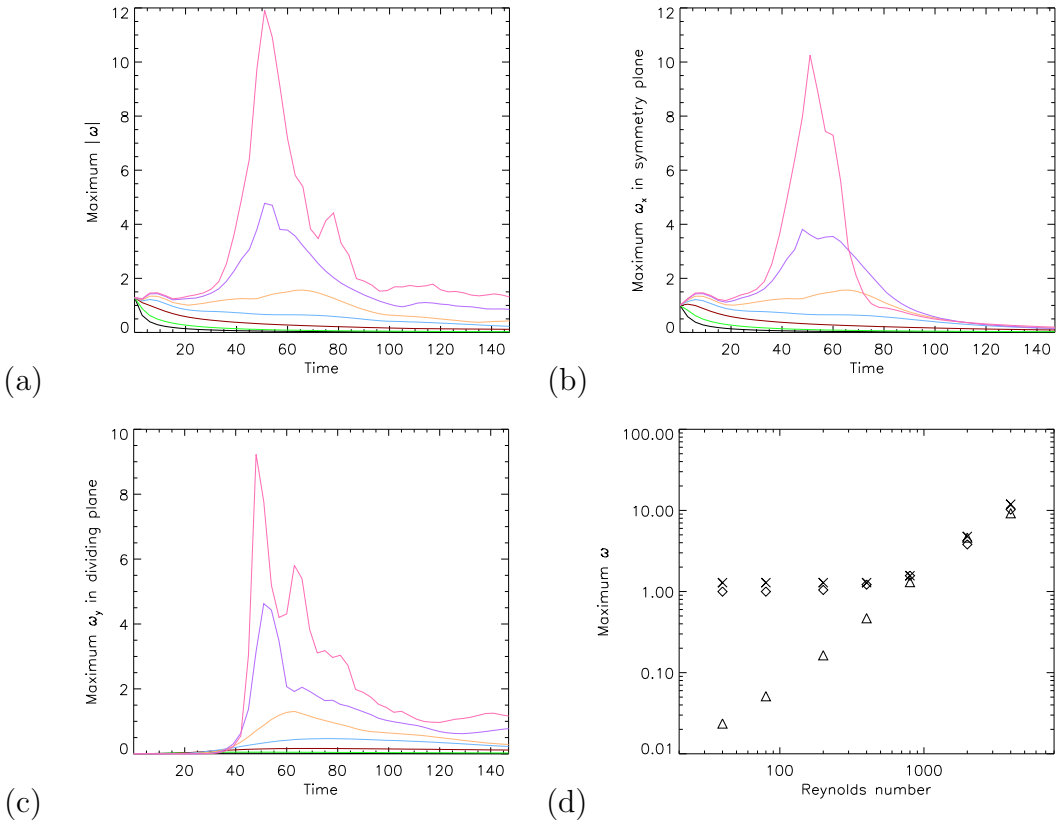

Figure 3.23: (a) Maximum $|\boldsymbol{\omega}|$, (b) maximum ω_x in the symmetry plane, (c) maximum ω_y in the dividing plane and (d) maximum $|\boldsymbol{\omega}|$ (crosses), maximum ω_x (diamonds) and maximum ω_y (triangles) as a function of Re.

3.1.10 Spectra

We plot the spectra of both the kinetic energy and enstrophy of the $Re = 80$ and $Re = 4000$ run to see how they compare at different wavelengths. The integral of kinetic energy and enstrophy over the box was maintained better at the higher Re but that does not give a clear idea to the local behaviour of $\boldsymbol{v}^2$ or $\boldsymbol{\omega}^2$. We expect to see the high Re run have higher values at higher wavenumbers, k, as the thin vortex sheets form whereas the vortex tubes of the low Re run expand considerably.

Using the same method discussed in Subsection 2.2.9 we plot the kinetic energy spectra of the high and low Re simulations in Figure 3.24. As expected for the $Re = 80$ run we see a loss of kinetic energy at all wavenumbers. For the $Re = 4000$ run in (b) and (d) we observe similar features to the $Re = 800$ run discussed in Subsection 2.2.9. The increase in kinetic energy spectra in (d) due to the formation of the vortex sheet is larger than in the previous chapter and also at a higher wavenumber due to the thinner and stronger vortex sheet forming.

We do the same for enstrophy spectra in Figure 3.25. We again see a loss at all wavenumbers for the low Re run as expected. For the high Re run however we see a shift to high waveumbers at $t = 45$ but this then diminishes at all wavenumbers after the majority of reconnection has occurred seen at $t = 90$ and 135.

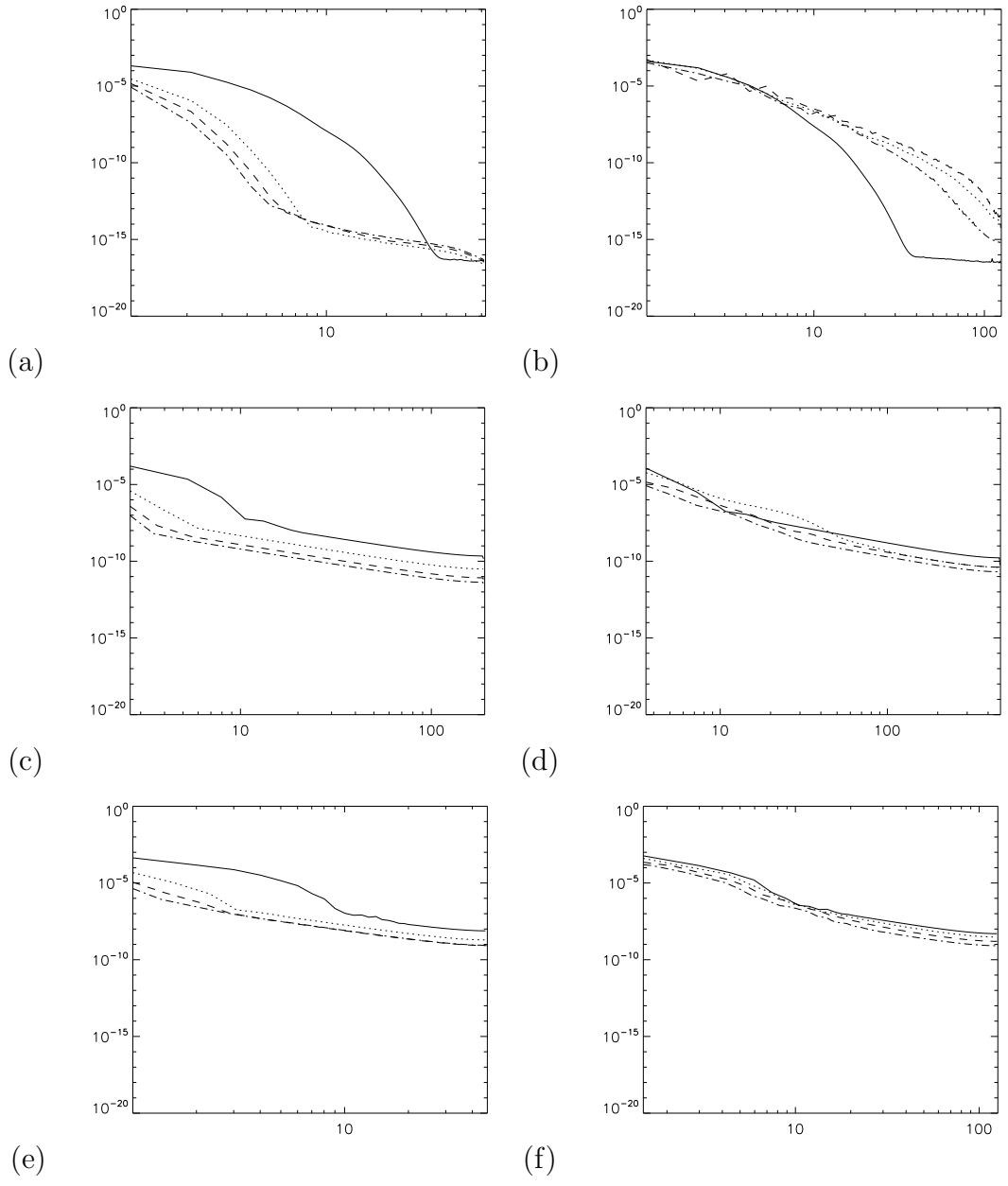

Figure 3.24: Directional spectra of the kinetic energy for $Re = 80$ (left) and $Re = 4000$ (right) in the x-direction (top), the y-direction (middle) and the z-direction (bottom) with $t = 0, 45, 90, 135$ (solid, dotted, dashed and dash-dotted respectively).

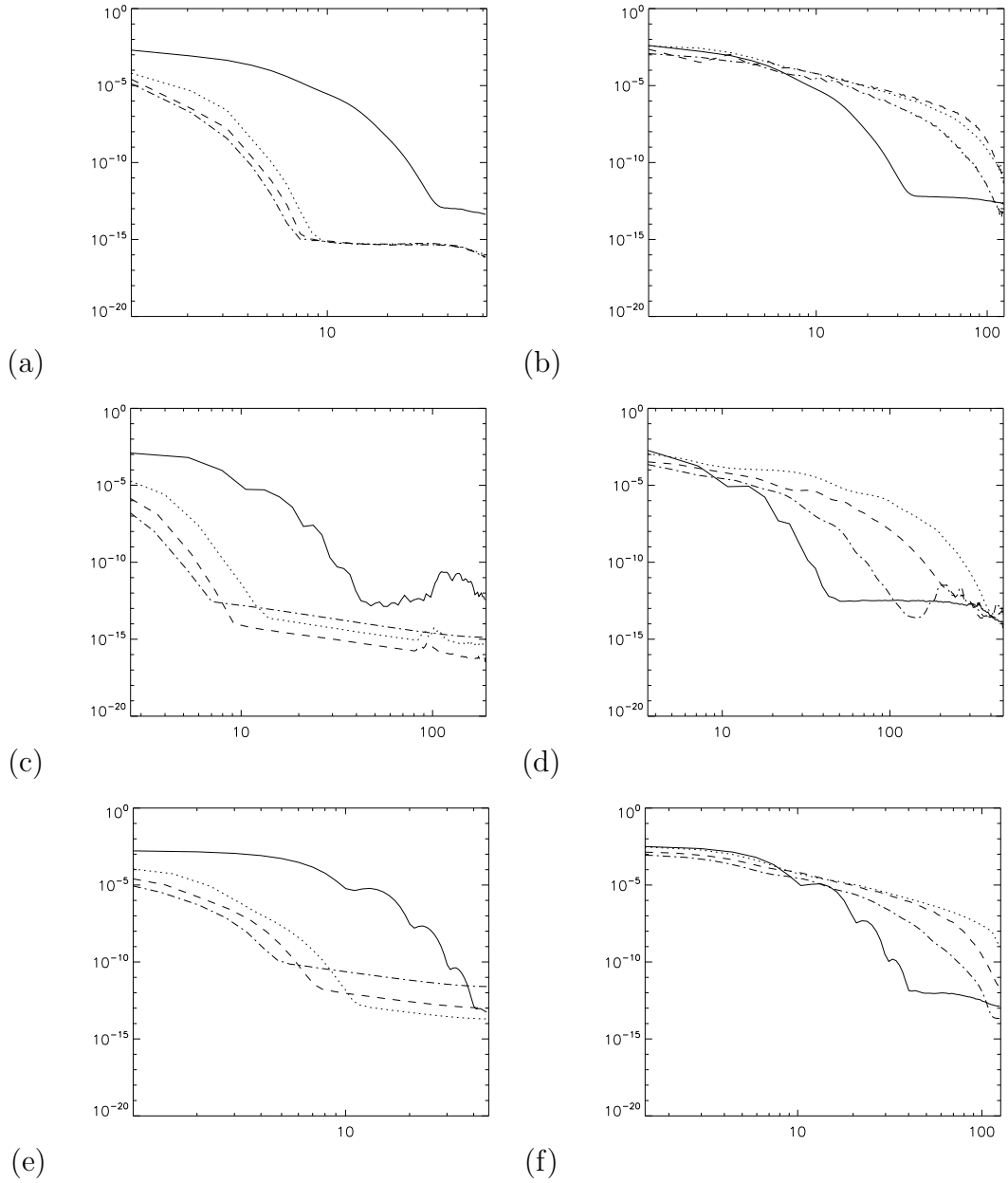

Figure 3.25: Directional spectra of the enstrophy for $Re = 80$ (left) and $Re = 4000$ (right) in the x-direction (top), the y-direction (middle) and the z-direction (bottom) with $t = 0, 45, 90, 135$ (solid, dotted, dashed and dash-dotted respectively).

3.1.11 Fieldline Measurements

We now look to observe the fieldline slipping, also known as 3D reconnection, and its dependence on Re. We know from previous sections that we have higher helicity with the increase of Re but it is not immediately clear how this affects the total slipping of the vorticity fieldlines in the simulations.

We follow the vorticity fieldlines of a single tube from the $x = -3$ boundary until they meet the symmetry or dividing plane. We do not consider the full length of the field line between x=-3 and 3 because the net slippage of the field line, measured by $\int(\nabla \times \boldsymbol{\omega})_{\parallel} \, \mathrm{d}l$, will always be zero due to symmetry. We plot the maximum and minimum $\int(\nabla \times \boldsymbol{\omega})_{\parallel} \, \mathrm{d}l$ values in Figure 3.26. There is a strong dependence of both on Re visible in (b) and (d). This corresponds to an increase in fieldline slipping in either direction with an increase in Re. We plot the estimated total rate of fieldline slipping, see Wyper and Hesse [59], in (e) and (f). We observe a strong correlation with Re in (f).

From the fieldline slipping rates in Figure 3.26 we are able to find the total vorticity flux that has reconnected in this 3D manner throughout the simulations for a quarter of the box. For further studies we would hope to refine the procedure imitated from Wyper and Hesse [59] as it gives a range of a full magnitude for the higher Re runs. As this was not possible we present both the minimum and maximum possible estimates in Figure 3.27. In (b) there is a clear dependence on Re for the total flux slipped. This dependence does not appear to be consistent. For low Re runs the increase in Re leads to a much greater change in flux slipped than the higher Re simulations. This would be something we would like to investigate in the future.

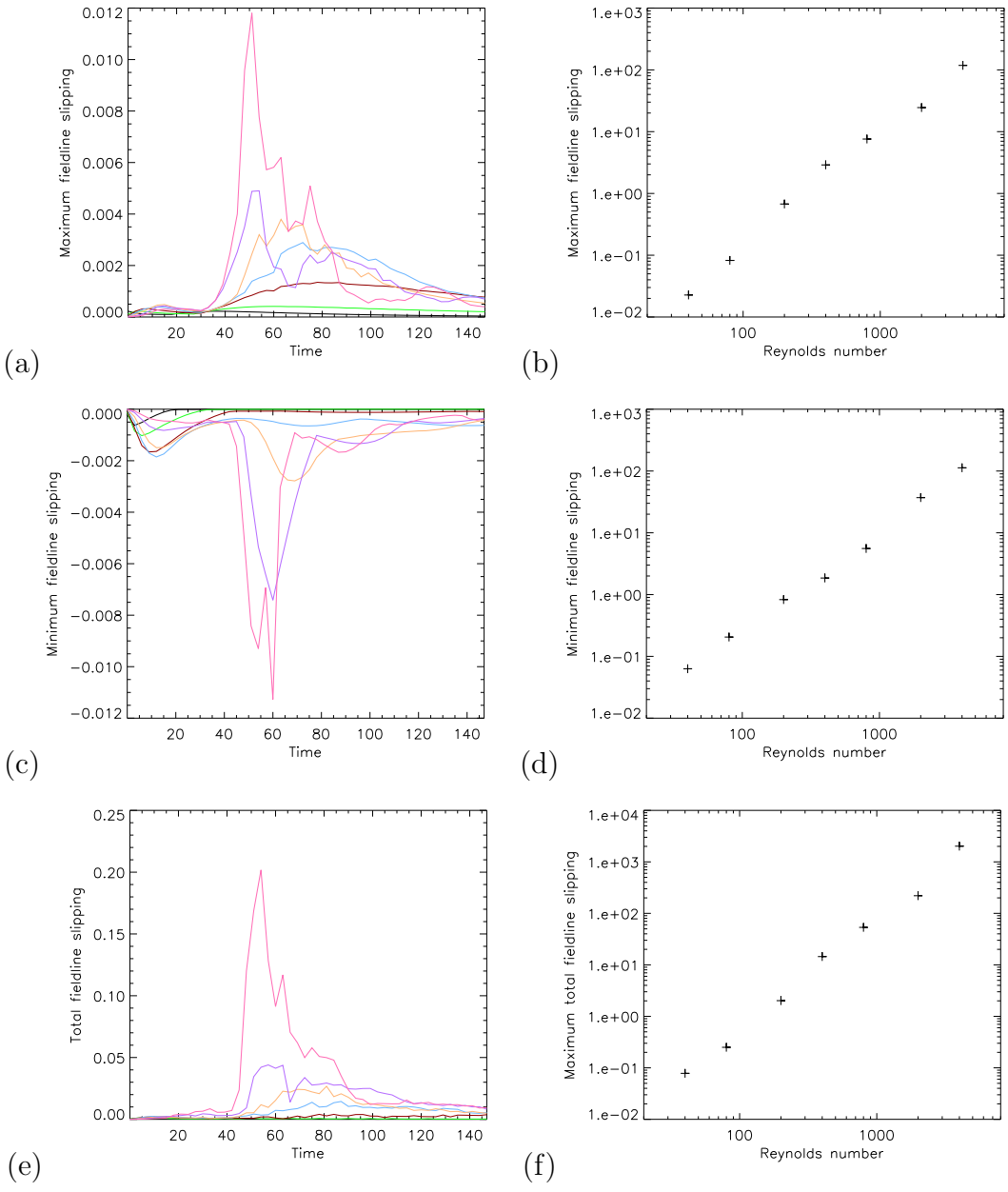

Figure 3.26: Slipping measurements for a quarter of the box. (a) Maximum fieldline slipping, (b) maximum fieldline slipping as a function of Re, (c) minimum fieldline slipping, (d) maximum negative fieldline slipping as a function of Re, (e) net fieldline slipping and (f) net fieldline slipping as a function of Re.

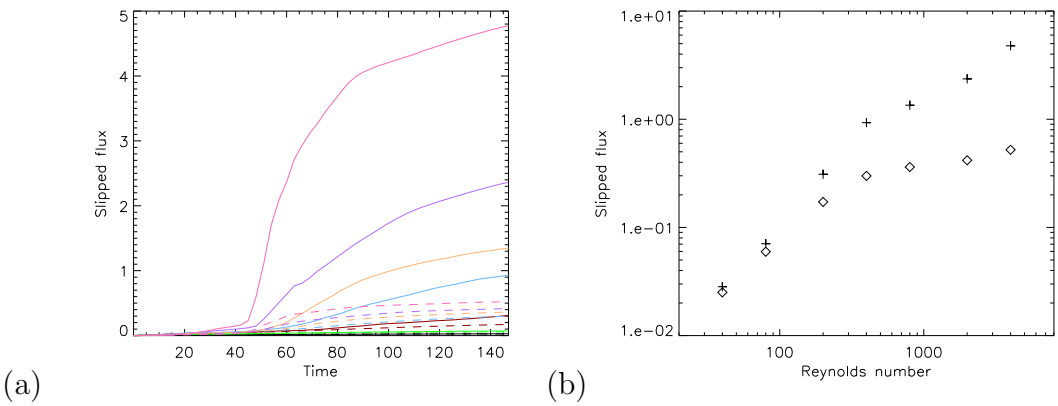

(a) (b)

Figure 3.27: (a) Maximum (solid) and minimum (dashed) possible amount of flux 'slipped' in a quarter of the box and (b) total maximum (crosses) and minimum (diamonds) possible flux 'slipped' as a function of Re for a quarter of the box.

3.2 Conclusions

We have shown here how the reconnection process of two anti-parallel vortex tubes is affected by the Reynolds number, Re, from a range of values from 40 to 4000. We have shown how the process changes from the formation of thin vortex sheets that lead to a fast reconnection at high Re. Whereas for low Re the reconnection is due to the dissipation and expansion of vortex tubes leading to a weak but large vortex sheet forming all along the vortex tube. This reconnection begins quickly and even has a higher reconnection rate than some runs with higher Re. This reconnection leads to 2D annihilation at the boundaries and vorticity flux is lost.

For the high Re runs we have shown that care must be taken when analysing the data due to the possibility that instabilities may arise. We also discovered the appearance of additional vortex rings that formed during the reconnection process. These additional vortex rings led to additional flux in the dividing plane and could be a cause of the turbulence behind aircraft. We were also able to measure the 3D reconnection, or 'slipping' of the vortex tubes within a quarter of the box and how this changes with Re.

For future work we would hope to work with even higher Reynolds numbers. Re of 10^4 [56] has already been accomplished but this is still 2 orders of magnitude lower than what is experienced behind aircraft. As Re is increased to these levels we should expect to see more instabilities and additional vortex rings appearing during the reconnection process.

Chapter 4

Perpendicular Vortex Tubes

4.1 Set-Up

In the anti-parallel set-up in the previous chapter we were able to observe and measure a relatively simple 2D reconnection along the central axis of the box between the two vortex tubes. We so far have observed and discussed three types of reconnection introduced in Subsection 1.3.2, annihilation, 2D X-point reconnection and 3D 'slipping'. We now look to find a vortex tube set-up to obtain the 3D reconnection and observe how this differs from the case discussed in Chapter 2.

To obtain this different type of reconnection between vortex tubes we look to find a scenario such that there is a strong $\nabla \times \boldsymbol{\omega}$ between the vortex tubes in the central axis, like the anti-parallel set-up, but in which we also have a non-zero $\boldsymbol{\omega}$ term within the central axis such that $(\nabla \times \boldsymbol{\omega}) \cdot \boldsymbol{\omega}$ is non-zero at the location in which the reconnection is occurring. We keep the same initial velocity field as the anti-parallel case and introduce an additional vortex tube perpendicular

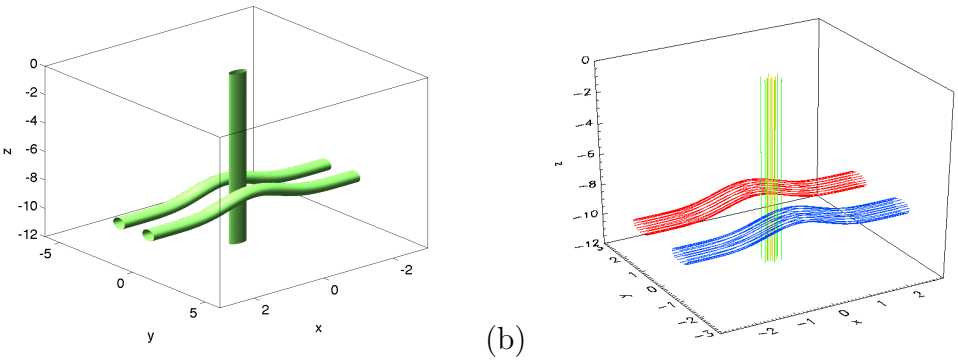

Figure 4.1: (a) Vorticity isosurfaces equal to 30% of the maximum vorticity at the $x = -3$ boundary and (b) 30% of maximum vorticity fieldlines at $x = -3, 3$ boundaries (red and blue) and $z = -12, 0$ boundaries (green ($\mathcal{C}_O$) and yellow ($\mathcal{C}_I$)) of initial condition.

to both anti-parallel tubes along the central axis seen in Figure 4.1. This set-up should lead to a similar reconnection as before and we will be able to see the effect of the perpendicular vortex tube and the non-zero $(\nabla \times \boldsymbol{\omega}) \cdot \boldsymbol{\omega}$ region on the reconnection process. With this set-up for the perpendicular vortex tube the 3D reconnection rate measurement will likely be the same as the Stokes' Theorem 2D reconnection measurement from the anti-parallel case assuming the vorticity fieldline with the maximum integrated $(\nabla \times \boldsymbol{\omega}) \cdot \boldsymbol{\omega}$ is coincident with the central axis.

Reconnection of initially orthogonal vortex tubes has been studied previously by Zabusky and Melander [60] and Boratov et al. [6] with only two tubes. In these scenarios the vortex tubes reposition themselves before reconnecting such that they appear to be anti-parallel. With the three vortex tube set-up we will be able to guarantee 3D reconnection along the central axis due to the symmetry of the box.

As before we do want the vortex tubes to be separate initially so we can observe the entire reconnection process. This means the perpendicular vortex tube will

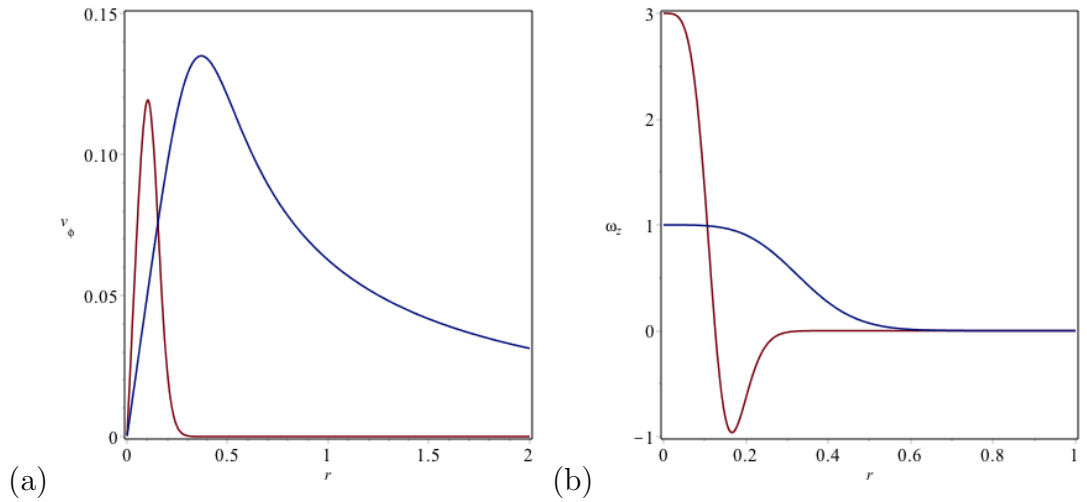

(a) (b)

Figure 4.2: (a) Velocity distribution of central tube (red) and anti-parallel tubes (blue) and (b) vorticity distribution of central tube (red) and anti-parallel tubes (blue). In each case r is the perpendicular distance from the tube axis.

be thinner than the anti-parallel tubes with a radius of ~ 0.3 compared to ~ 0.6. To create an array of these perpendicular tubes in a similar fashion to the anti-parallel tubes to maintain $\boldsymbol{v}\cdot\boldsymbol{n} = 0$ we would need to simulate a 2×2 array of these in the x and y direction. We do not have the computational power to do this at a sufficient resolution. To keep our boundary conditions and simulation resolution we find an initial velocity for our vortex tube that approaches zero quickly and will have zero effect on the boundary conditions. This introduces a vorticity 'shell' of opposite sign around the perpendicular vortex tube. Our perpendicular vortex tube now has zero net vorticity flux and from small runs simulating this vortex tube on its own the absolute vorticity flux quickly dissipates so we need to ensure the vorticity is strong enough such that it has not cancelled out before reconnection has occurred. For the first run discussed we will be modelling a perpendicular vortex tube with a maximum vorticity three times that of the anti-parallel tubes. The velocity and vorticity distributions of this perpendicular tube are compared to the anti-parallel tubes in Figure 4.2. The velocity from the

perpendicular tube will likely rotate the anti-parallel tubes slightly in an anti-clockwise direction viewed from above and introduce an axial flow in each but this shall be discussed in the results. To aid discussion the anti-parallel vortex tubes will be referred to as $\mathcal{A}_1$ and $\mathcal{A}_2$. The 'central' perpendicular vortex tube referred to as $\mathcal{C}$. The inner and outer 'shell' of $\mathcal{C}$ shall be referred to as $\mathcal{C}_I$ and $\mathcal{C}_O$.

In cylindrical co-ordinates (r, ϕ, z') we use a velocity distribution:

$$v_\phi = \frac{\omega_0}{4r}\left(\tanh(50r^2) - \tanh(48r^2)\right), \tag{4.1}$$

which leads to a vorticity distribution of:

$$\omega_{z'} = -\omega_0 \frac{(24\cosh(50r^2) - 25\cosh(48r^2))}{\cosh(50r^2)^2\cosh(48r^2)^2}, \tag{4.2}$$

which can be compared to the anti-parallel distributions in Figure 4.2 with $\omega_0 = 3$. The ω_0 term is used to control the vorticity strength of $\mathcal{C}$. $\omega_0 = 1$ gives a value of the maximum vorticity in $\mathcal{C}$ equal to the maximum vorticity of $\mathcal{A}_1$ and $\mathcal{A}_2$. In cartesian co-ordinates and positioned on the z-axis this gives us a velocity field of:

$$\begin{aligned}\boldsymbol{v} = \Bigg[&\frac{\omega_0 y}{4(x^2+y^2)}\tanh(8(x^2+y^2)) - \tanh(6(x^2+y^2)),\\ &-\frac{\omega_0 x}{4(x^2+y^2)}\left(\tanh(8(x^2+y^2)) - \tanh(6(x^2+y^2))\right), 0\Bigg],\end{aligned} \tag{4.3}$$

and the vorticity field for the central tube:

$$\boldsymbol{\omega} = \left[0, 0, -\omega_0 \frac{(24\cosh(50(x^2+y^2)) - 25\cosh(48(x^2+y^2)))}{\cosh(50(x^2+y^2))^2\cosh(48(x^2+y^2))^2}\right]. \tag{4.4}$$

The tube is positioned in such a way that the fieldlines of $\mathcal{C}_O$ are oriented in the

positive z-direction. This velocity field is added to the velocity field discussed in Section 2.1 to become the initial condition used in this chapter.

For the simulations we use the same parameters as in the anti-parallel runs in Chapter 2 and the same dimensions for the box. The resolutions for the majority of the simulations were chosen to be $240 \times 480 \times 120$ increasing to $360 \times 480 \times 120$ and $960 \times 480 \times 120$ for the highest Reynolds number runs in order to fully resolve the double-vortex sheet that forms in the vicinity of the $y = 0$ plane. Due to limitations of the simulation code and the boundary conditions desired there are no longer stretched grid points between $\mathcal{A}_1$ and $\mathcal{A}_2$ to resolve the formation of the vortex sheet but the resolutions picked here were sufficient to model this new reconnection process. We do not expect the reconnection event to be notably quicker than the anti-parallel set-up so the time dumps for the simulations are kept the same however they are no longer run until $t \approx 150$ rather $t \approx 100$ as we are not interested in the post reconnection evolution of this system as that has been covered already. We will compare the results for Reynolds numbers between ~ 80 and ~ 2000 and for the $Re = 800$ case a range of $\mathcal{C}$ strengths from $\omega_0 = 1$ to $\omega_0 = 5$.

From these simulations we will look to see if there a difference in the reconnection process due to the presence of $\mathcal{C}$ and compare a 2D reconnection and 3D reconnection event. We will also look to see if the 3D magnetic reconnection rate analog will be an accurate measure. We will also want to observe the evolution of $\mathcal{C}$ in terms of maximum/minimum vorticity and absolute flux over time and its topology post reconnection. And finally how the system will evolve depending on the Reynolds number and the value of ω_0.

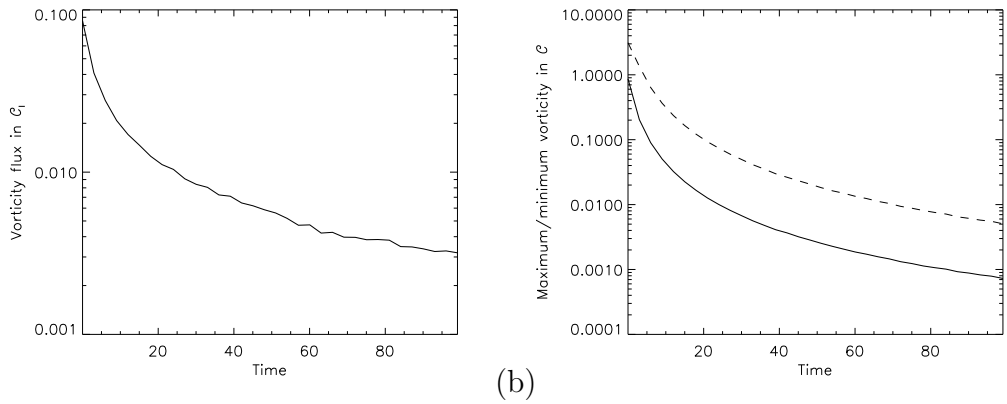

(a) (b)

Figure 4.3: (a) Net positive vorticity flux through $z = 0$ boundary and (b) maximum positive (solid) and negative (dashed) ω_z at $z = 0$ boundary with $Re = 800$ and $\omega_0 = 3$.

4.2 Results for $\omega_0 = 3$

4.2.1 Initial Movement

Due to the set-up of $\mathcal{C}$ the system begins with null regions of vorticity containing non-zero $\nabla \times \boldsymbol{\omega}$. This occurs within the surface between $\mathcal{C}_I$ and $\mathcal{C}_O$ and causes $\mathcal{C}$ to annihilate itself. This can be measured analytically by integrating along a closed curve between the shells:

$$(\nabla \times \boldsymbol{\omega})_\phi = 8\omega_0 r \frac{(625 \sinh(50r^2)\cosh(48r^2)^3 - 576\cosh(50r^2)^3 \sinh(48r^2))}{(\cosh(50r^2)^3 \cosh(48r^2)^3)}. \quad (4.5)$$

At the radius at $t = 0$ between $\mathcal{C}_I$ and $\mathcal{C}_O$ $r \approx 0.125$ we have for $\omega_0 = 3$

$$(\nabla \times \boldsymbol{\omega})_\phi|_{r=0.125} \approx 46.9. \quad (4.6)$$

And therefore our annihilation rate is given by

$$\nu \oint_{r=0.125} (\nabla \times \boldsymbol{\omega})_\phi \, \mathrm{d}l \approx 0.037. \quad (4.7)$$

At our first snapshot $t \approx 3$ we see the vorticity flux of both $\mathcal{C}_I$ and $\mathcal{C}_O$ has dropped by ≈ 0.045. Our estimate for the annihilation rate is greater due to the drastic rate of flux loss from $\mathcal{C}$. As $\mathcal{C}$ loses flux, the annihilation rate also drops demonstrated in Figure 4.3(a). From this plot we can see that although the absolute net flux of $\mathcal{C}$ drops a great deal it is still enough to affect the anti-parallel reconnection in some way. In Figure 4.3(b) we plot the maximum and minimum ω_z, within $\mathcal{C}_O$ and $\mathcal{C}_I$ respectively, at the $z = 0$ boundary. This plot demonstrates the sharp loss of each of these values as $\mathcal{C}$ annihilates itself.

As $\mathcal{A}_1$ and $\mathcal{A}_2$ rotate towards each other $\mathcal{C}$ is squeezed. This will change the value of the integral along z within $\mathcal{C}$ to no longer be constant. This will change the 2D annihilation occurring initially to a 2D reconnection. The reconnected vorticity fieldlines between $\mathcal{C}_I$ and $\mathcal{C}_O$ will form a vortex torus. The vorticity fieldlines of this vortex torus will be in a poloidal direction as opposed to the toroidal direction seen in the bridges after anti-parallel reconnection. The null surface between $\mathcal{C}_I$ and $\mathcal{C}_O$ will be reduced to a ring of nulls where $\mathcal{C}$ was squeezed, see Figure 4.4(a), and a ring of nulls at the boundary, see Figure 4.4(b).

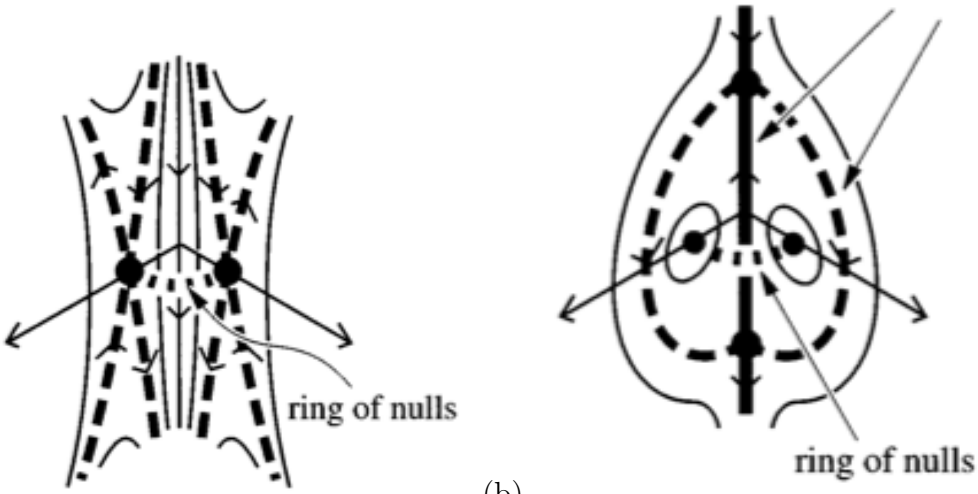

(a) (b)

Figure 4.4: Illustration of reconnection forming a spheromak from Priest and Forbes [49]. (a) Illustrating ring of nulls formed along the line of reconnection and (b) illustrating ring of nulls formed along line of zero reconnection.

4.2.2 Visualising the Reconnection Process - Vorticity Isosurfaces

As a first step to understanding the reconnection process of the vortex tubes we plot the absolute vorticity surfaces seen in Figure 4.5. The fast weakening of $\mathcal{C}$ is apparent already by Figure 4.5(b) where the tube has disappeared from the isosurface plot. $\mathcal{A}_1$ and $\mathcal{A}_2$ appear to be approaching each other in a similar fashion as when there was no perpendicular tube between them implying that it is offering little resistance to their movement. Due to the velocity associated with this new tube an asymmetry is now present in $\mathcal{A}_1$ and $\mathcal{A}_2$ meaning the vortex sheet will not form nicely along the dividing plane ($y = 0$) but now at a slight angle which will cause issue with the flux measurement. Through (c) and (f) the evolution looks very similar to the anti-parallel case without $\mathcal{C}$ and it looks like $\mathcal{A}_1$ and $\mathcal{A}_2$ have reconnected and left behind threads as before. The evolution of $\mathcal{C}$ is completely unknown with this visualisation though. It is difficult to tell from these plots whether a vortex sheet forms between $\mathcal{A}_1$ and $\mathcal{A}_2$ like before or if $\mathcal{C}$ inhibits that in some fashion.

As the evolution of $\mathcal{C}$ was not visible in Figure 4.5 we created some isosurface plots of a lower value related to the strength of $\mathcal{C}$ in Figure 4.6. From these plots we can see what appears to be bridges forming on the outer sides of $\mathcal{A}_1$ and $\mathcal{A}_2$ towards the upper region of $\mathcal{C}$ and other bridges between $\mathcal{A}_1$ and $\mathcal{A}_2$ forming towards the lower region of $\mathcal{C}$. In (a) there is a clear rotation in the bridges forming upwards leading us to believe there is a change in helicity of the tubes. Due to the close proximity of these tubes it is difficult to tell where the vorticity in these bridge regions originated and will end up. Later in this chapter we will attempt to find this and accurately measure the reconnection between all three tubes by examining the connectivity of the vortex lines themselves.

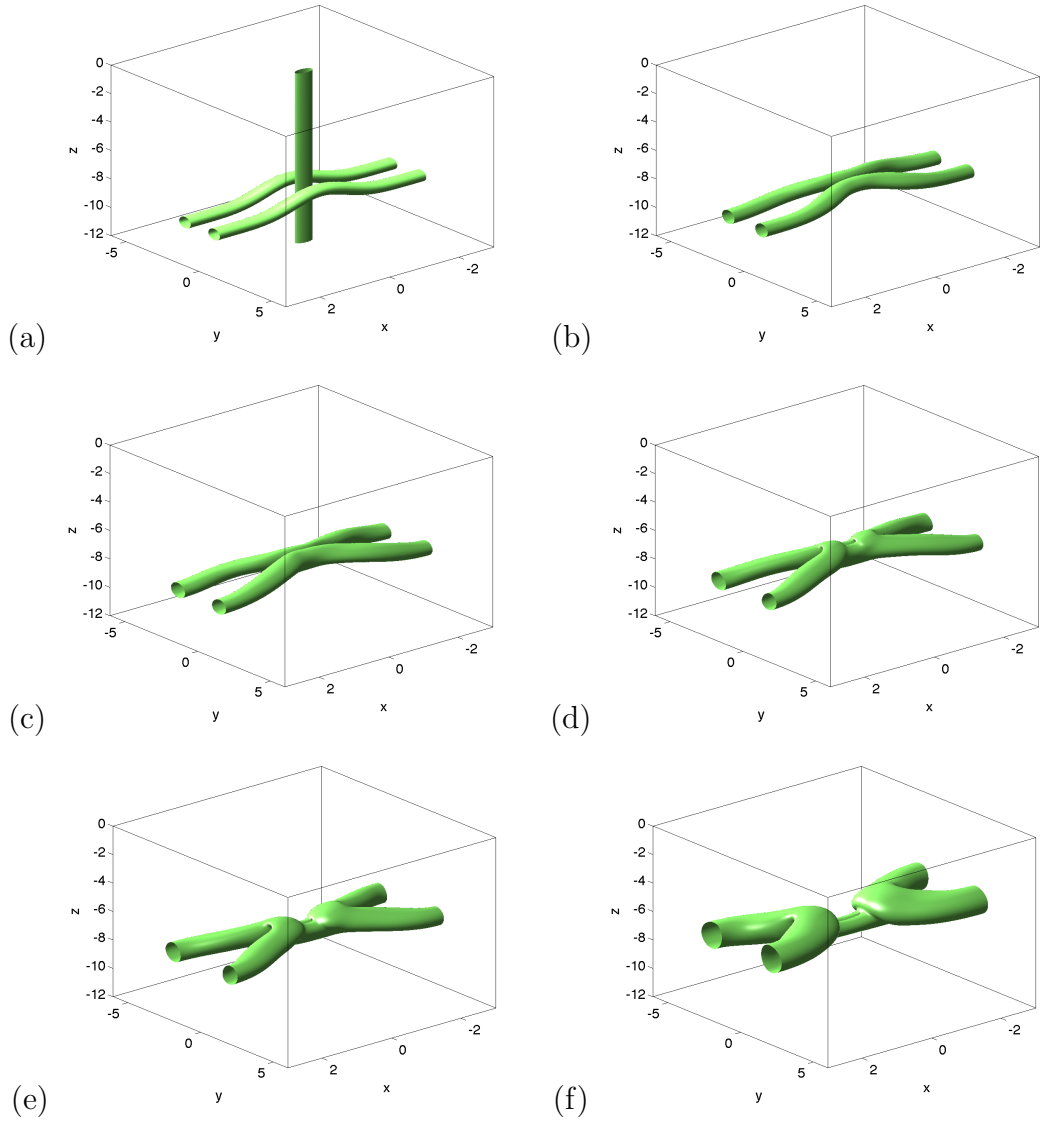

Figure 4.5: Vorticity isosurfaces equal to 30% of the maximum vorticity at the $x = -3$ boundary at (a) $t = 0$, (b) $t = 15$, (c) $t = 30$, (d) $t = 45$, (e) $t = 60$ and (f) $t = 90$.

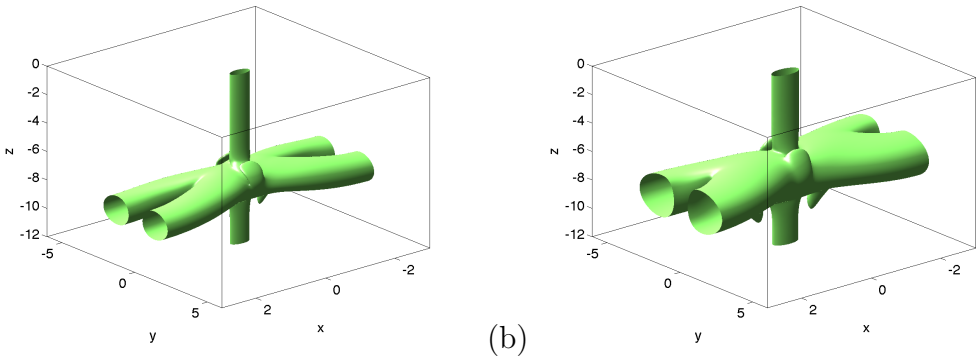

(a) (b)

Figure 4.6: Vorticity isosurfaces equal to 30% of the maximum vorticity at the $z = 0$ boundary at (a) $t = 30$ and (b) $t = 60$.

4.2.3 Visualising the Reconnection Process - Vorticity Fieldlines

In an attempt to better visualise the reconnection process we plot fieldlines from the $x = \pm 3$ and the $z = -12$ and 0 boundaries for $\mathcal{A}$ and $\mathcal{C}$ respectively. In the same fashion as in Subsection 2.2.4 we plot 50 fieldlines, 25 for both $\mathcal{A}_1$ and $\mathcal{A}_2$, from each x boundary to illustrate the anti-parallel vortex tubes. We do the same at the z boundaries for $\mathcal{C}_I$ and $\mathcal{C}_O$ but only 20 fieldlines as $\mathcal{C}$ is weaker than $\mathcal{A}$ for the majority of the simulation. The fieldlines for all vortex tubes are chosen from contours of 30% maximum absolute vorticity of each respective tube or shell. We hope to give a better idea of the evolution of $\mathcal{C}$ and where the reconnections occur between which tubes. Already from Figure 4.7(b) we can see both green and yellow fieldlines, of $\mathcal{C}_O$ and $\mathcal{C}_I$ respectively, now connected to $\mathcal{A}_1$ and $\mathcal{A}_2$. We suspect that the reconnection between $\mathcal{C}$ and $\mathcal{A}$ to be similar to previous orthogonal vortex reconnection scenarios where the reconnecting fieldlines move into an anti-parallel fashion before reconnecting [6]. By this point there has already been significant cancellation of the oppositely signed vorticity between $\mathcal{C}_I$ and $\mathcal{C}_O$, meaning that the vorticity magnitude associated with $\mathcal{C}_I$ and $\mathcal{C}_O$ has decreased by a factor of 20 and 40 respectively. This means that $\mathcal{C}$ has already weakened enough by this point that the fieldlines plotted for $\mathcal{A}_1$ and $\mathcal{A}_2$ appear unaffected by this so the flux reconnected at this point will still be relatively low. Twisting of the vortex lines of $\mathcal{C}$ is already visible but again due to the relative magnitudes of the vorticity will have little effect on $\mathcal{A}_1$ and $\mathcal{A}_2$. This continues in (c). In (d) we see the reconnection between $\mathcal{A}_1$ and $\mathcal{A}_2$ very similar to the case with no $\mathcal{C}$. From the fieldlines plotted it appears that $\mathcal{C}$ has almost entirely reconnected with $\mathcal{A}_1$ and $\mathcal{A}_2$ in some fashion, however possibly the most important fieldline is the fieldline in the centre of the box not plotted here but

will be studied later in the chapter as the reconnected anti-parallel fieldlines had to pass through the central fieldline to reconnect but it is unclear what happens to this central fieldline during this process. From (e) and (f) onwards the system evolves as expected from the anti-parallel case without $\mathcal{C}$.

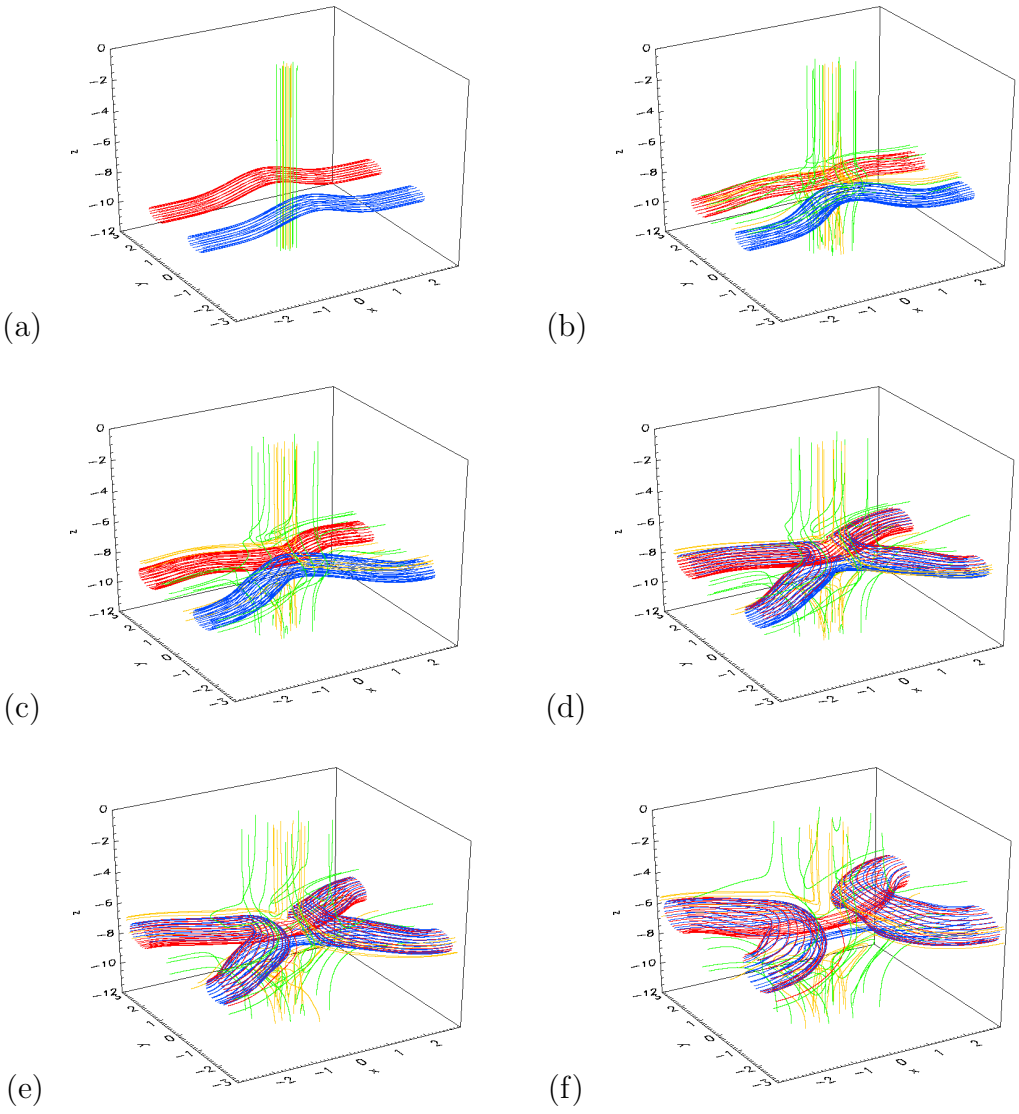

Figure 4.7: 30% of maximum vorticity fieldlines at $x = -3, 3$ boundaries (red and blue) and $z = -12, 0$ boundaries (green ($\mathcal{C}_O$) and yellow ($\mathcal{C}_I$)) at (a) $t = 0$, (b) $t = 15$, (c) $t = 30$, (d) $t = 45$, (e) $t = 60$ and (f) $t = 90$.

4.2.4 Vorticity Contour Plots

Due to the strong ω_z component around the central axis, contour plots of ω_x and ω_y in the symmetry and dividing planes respectively were misleading. These contours were being affected by $\mathcal{C}$ which was very weak in these contours to being near parallel to each plane. To observe the interaction of all three tubes we plot the absolute vorticity in both planes although this means we will not be able to tell which tube is which in certain regions. However, combining with the fieldline plots in Figure 4.7 we can get a better picture.

In Figure 4.8(a) we see the initial set-up with $\mathcal{A}_1$ and $\mathcal{A}_2$ either side of the, initially, stronger $\mathcal{C}$. By $t = 15$ in (b) $\mathcal{A}_1$ and $\mathcal{A}_2$ have already begun reconnecting with $\mathcal{C}_O$, the fieldlines of which are heading upwards, green fieldlines in Figure 4.7, positively in z and have pressed far enough together that they are also reconnecting with $\mathcal{C}_I$. We hope to see in the flux measurements a notable difference in time between the reconnection of $\mathcal{C}_O$ and then $\mathcal{C}_I$ as $\mathcal{A}_1$ and $\mathcal{A}_2$ make their way through both. The top part of $\mathcal{C}$ now has a noticeable separation between $\mathcal{C}_O$ and $\mathcal{C}_I$. The curve in $\mathcal{C}_O$ around $z = -7$ explain the bridges seen in Figure 4.6(b) later in time. This same separation can be seen at the bottom part of $\mathcal{C}$ but will be studied closer in the dividing plane contours. From (c) onwards the stronger regions of absolute vorticity, $\mathcal{A}_1$ and $\mathcal{A}_2$, evolve in a very similar manner to the case without $\mathcal{C}$, consistent with the isosurface and fieldline plots. The most important part of these plots is what appears to be a null point above $\mathcal{A}_1$ and $\mathcal{A}_2$, this will need to be investigated to see its effect on the central axis fieldline as this will alter the reconnection rate measurement taken along this axis. This will be discussed further in Subsection 4.3.2.

In Figure 4.9 the same absolute vorticity plots are shown in the dividing plane. In (b) we are seeing a similarity to Figure 4.6(b) in terms of the separation of $\mathcal{C}_O$ and

$\mathcal{C}_I$. The two regions forming on either side of the tube are similar to the ones in Figure 4.6(b) however only appear in this plane due to the rotation caused by $\mathcal{C}$. Here we also get a better image of the evolution of $\mathcal{C}$ and how it is being affected by $\mathcal{A}_1$ and $\mathcal{A}_2$. We see it being squeezed in around $z = -7$ where the perturbations of $\mathcal{A}_1$ and $\mathcal{A}_2$ are pressing. This change in $\mathcal{C}$ has caused the annihilation between $\mathcal{C}_O$ and $\mathcal{C}_I$ to become anti-parallel reconnection with a closed curve on the upper and lower z boundaries forming tori after reconnection demonstrated in Figure 4.4. This squeezing and reconnection explains the maximum absolute vorticity region observed in the lower part of the tube. From (c) onwards we observe the appearance of strong vorticity regions either side of the z-axis that are the signature of the reconnection between $\mathcal{A}_1$ and $\mathcal{A}_2$. The main difference between this run and the simulations without $\mathcal{C}$ are the additional contours of vorticity appearing due to the rotation of $\mathcal{C}$. Due to this loss of symmetry flux can not reliably be measured in the dividing plane for determining the reconnection rate.

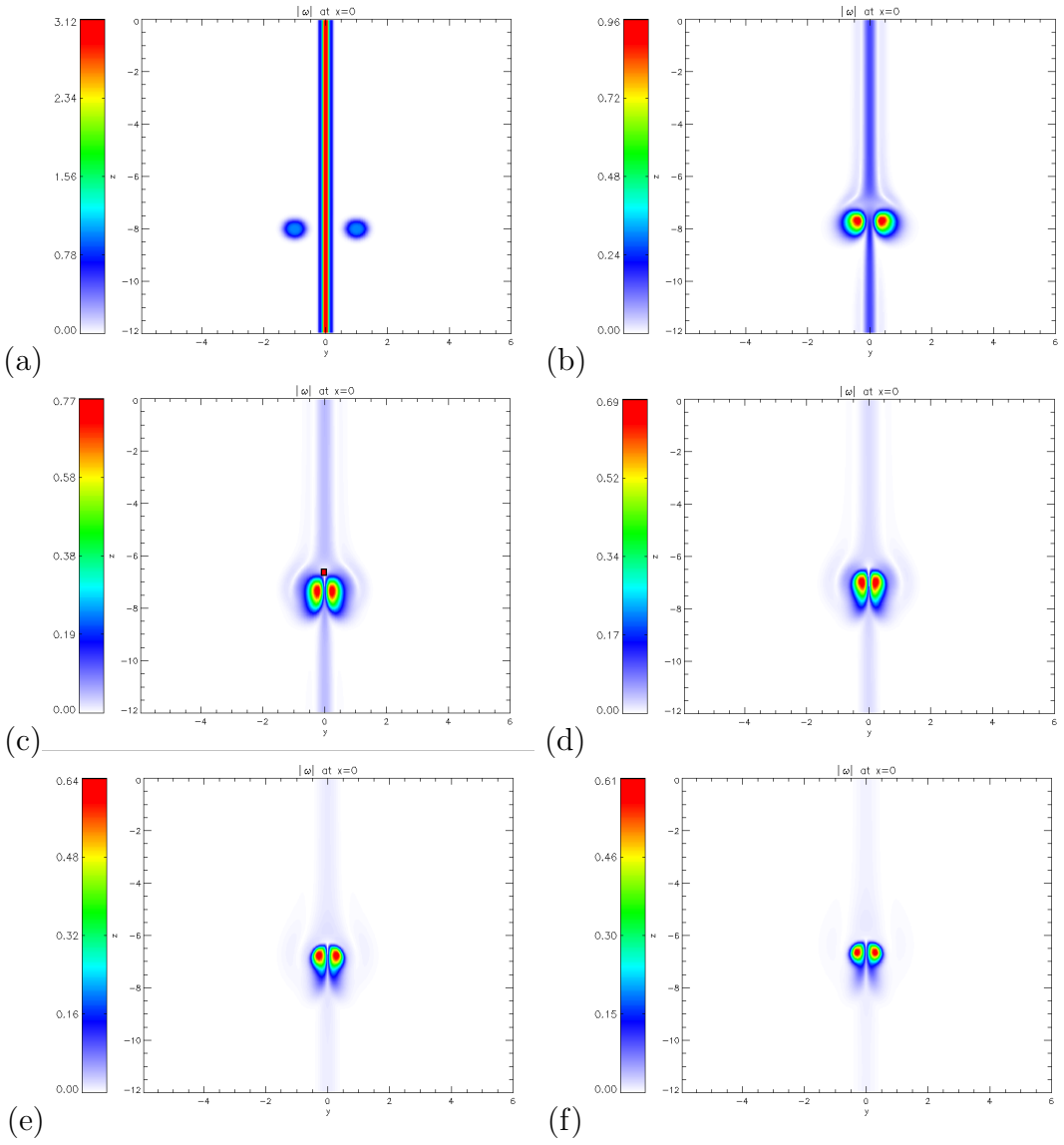

Figure 4.8: Contours of absolute vorticity in symmetry plane $x = 0$ at (a) $t = 0$, (b) $t = 15$, (c) $t = 30$, (d) $t = 45$, (e) $t = 60$ and (f) $t = 75$.

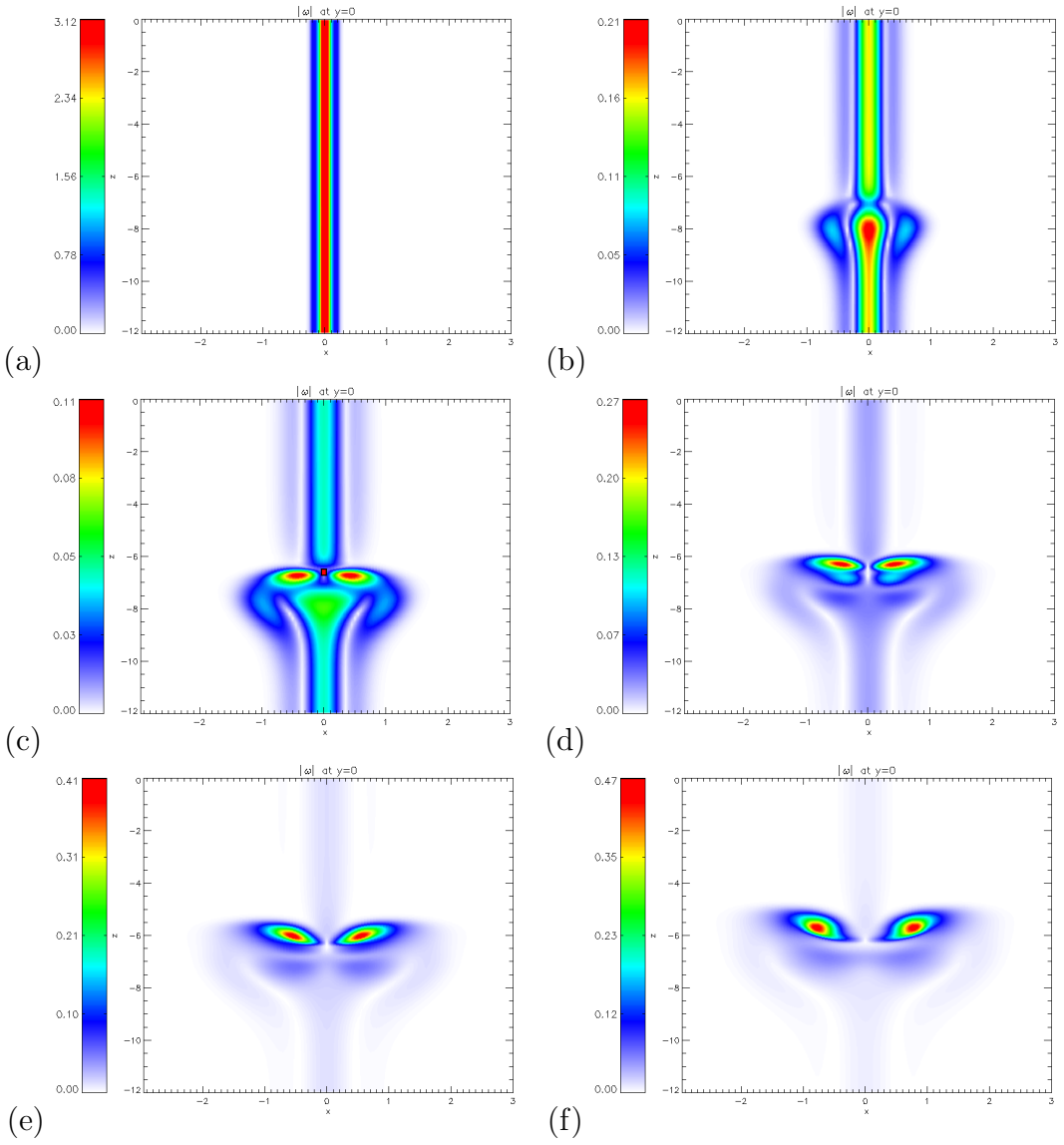

Figure 4.9: Contours of absolute vorticity in dividing plane $y = 0$ at (a) $t = 0$, (b) $t = 15$, (c) $t = 30$, (d) $t = 45$, (e) $t = 60$ and (f) $t = 75$.

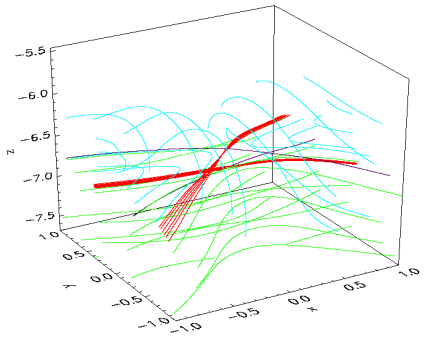

Figure 4.10: 30% of maximum vorticity fieldlines at $x = 0$ (green) and $y = 0$ (blue) with fans (red) and spines (black) plotted from null points at $t = 48$

4.2.5 Null points

As $\mathcal{A}_1$ and $\mathcal{A}_2$ reconnect with $\mathcal{C}$ the thread fieldlines of each meet at the central axis. $\mathcal{A}_1$ and $\mathcal{A}_2$ begin reconnecting through this central axis, which before had a vorticity component in negative z, and reverse the vorticity component along the central axis generating a pair of vorticity null points forming a separator in the central axis as discussed in Subsection 1.3.2. To understand the nature of the vorticity field around the null point pairs we plot the fans and spines of them, discussed in Subsection 1.3.2, with the vortex tubes in Figure 4.10. The null points are found with linear interpolation within the central axis. The fans and spines are then found from the eigenvector of $\nabla\boldsymbol{\omega}$ at the position of the null point. The fans and spines are seen to follow the vortex tubes and they fit between the threads and the reconnected vortex rings as expected from the separator discussion in Subsection 1.3.2. One value of the fan eigenvalue is much larger than the other for the null points which leads to the fan fieldlines tending to go in either direction. The overall size of the separator is also illustrated here in comparison to the vortex tubes.

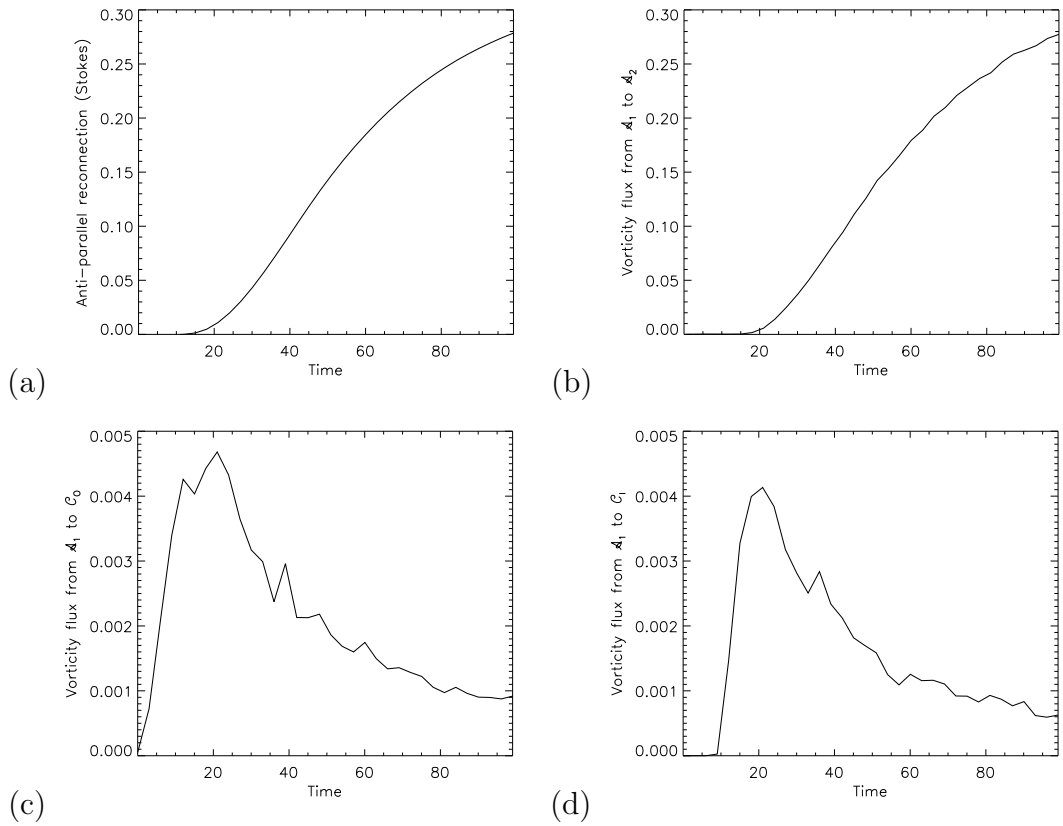

Figure 4.11: (a) Estimated change in flux between $\mathcal{A}_1$ and $\mathcal{A}_2$ by integrating $\nu(\nabla \times \boldsymbol{\omega})_z$ along the central axis, (b) change in flux between $\mathcal{A}_1$ and $\mathcal{A}_2$, (c) change in flux between $\mathcal{A}_1$ and $\mathcal{C}_O$ and (d) change in flux between $\mathcal{A}_1$ and the $\mathcal{C}_I$

4.2.6 Flux Evolution

Due to the breaking of symmetry in the $x = 0$ and $y = 0$ plane, the vorticity flux measurements from there can not be used to measure the flux reconnected between two particular tubes. To measure the flux reconnected between each tube we use a brute force method, we trace the vorticity fieldlines from $\mathcal{A}_1$ and track their end point in the system. If it has reconnected with $\mathcal{A}_2$, $\mathcal{C}_O$, $\mathcal{C}_I$ or not at all it will end at $x = -3$, $z = 0$, $z = -12$ or $x = 3$ respectively. This is done for a grid of fieldlines within $\mathcal{A}_I$, and fluxes are estimated by weighting the area corresponding to each grid point by the local modulus of the vorticity. These

reconnection measurements are shown in Figure 4.11(b), (c) and (d) respectively. In (a) we plot the estimated flux reconnected between $\mathcal{A}_1$ and $\mathcal{A}_2$ using Stokes' Theorem. Comparing (a) and (b) we see the brute force method has a small error compared to the smoother estimate. We see for (c) and (d) they follow a similar shape after their peak due to $\mathcal{C}$ annihilating. The delay in reconnection with $\mathcal{C}_I$ can be seen clearly in (d) as no flux appears until around $t \approx 10$.

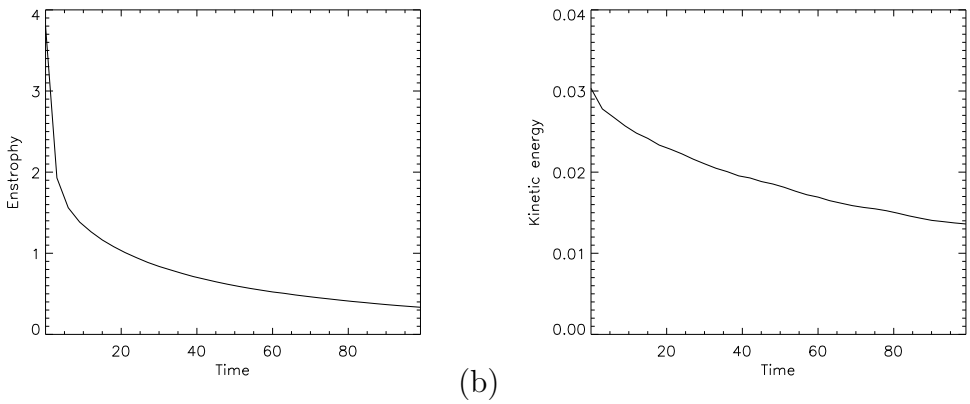

(a) (b)

Figure 4.12: (a) Enstrophy and (b) kinetic energy.

4.2.7 Volume Integrals

Checking the volume integrals in Figure 4.12 we see for the enstrophy in (a) a very sharp drop initially not seen in the anti-parallel case due to the quickly dissipating perpendicular tube. This however is not seen in (b) for the kinetic energy. No 'bump' is apparent in the enstrophy plot indicating that a strong vortex sheet was not formed as in the anti-parallel case without $\mathcal{C}$.

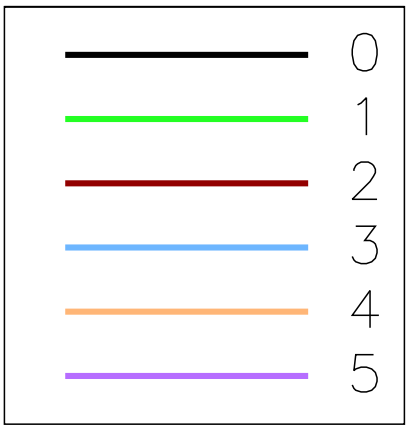

Figure 4.13: Plot colours corresponding to ω_0 values.

4.3 Differences with Perpendicular Tube Strength, ω_0

In hopes of achieving a better understanding of the role $\mathcal{C}$ plays on the reconnection we run the same set-up as before but with $\omega_0 = 1$, 2, 4 and 5, with the case in the previous section corresponding to $\omega_0 = 3$. For reference the corresponding colours for plots is shown in Figure 4.13. One key aspect of the simulations that we shall investigate is the reconnection rate dependence between the different cases. Since the reconnection is measured in terms of $\nabla \times \boldsymbol{\omega}$ we could expect that $\mathcal{C}$ might resist the squeezing of $\mathcal{A}_1$ and $\mathcal{A}_2$ enough to slow down the reconnection process. Whether this occurs or not will be investigated below. The range of ω_0 was chosen such that $\mathcal{C}$ would not be mostly annihilated by the time of reconnection, lower limit, and not make the system supersonic, upper limit. We will also compare the range of ω_0 to the case without $\mathcal{C}$ which will be denoted here as $\omega_0 = 0$.

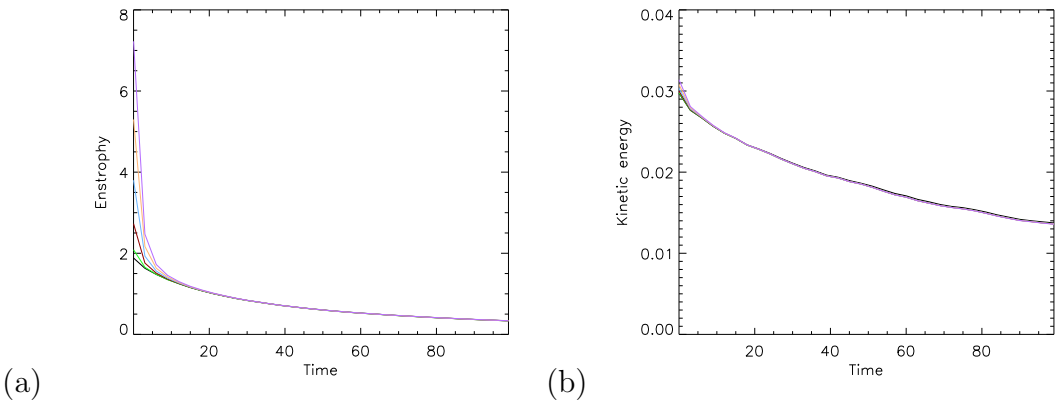

(a) (b)

Figure 4.14: (a) Enstrophy and (b) kinetic Energy.

4.3.1 Volume Integrals

From the enstrophy and kinetic energy plots seen in Figure 4.14 it appears that the strength of $\mathcal{C}$ and even its existence are negligible after $t \approx 10$ as we see all the curves in Figure 4.14 diverge to the $\omega_0 = 0$ value. In (b) for the kinetic energy there is a very small difference that quickly diminishes. For (a) we see a large difference initially but the rapid initial decay and close proximity of all curves at later time suggest that $\mathcal{C}$ annihilates very quickly. Below we investigate further the simulations to see if there is any difference in the reconnection of the tubes with $\mathcal{C}$.

4.3.2 Flux Evolution

We plot the vorticity flux between $\mathcal{A}_1$ and $\mathcal{A}_2$ in Figure 4.15(a) for each of the five runs of ω_0 and also the anti-parallel run with $\omega_0 = 0$. This is defined as any fieldline that starts and ends at $x = -3$ meaning it has passed through the dividing plane due to reconnection. To achieve a better idea of how the value of ω_0 is affecting the reconnection we plot the difference in reconnected flux compared to the anti-parallel case in (b). We can see the error caused by the flux calculation method compared to being able to measure from either the symmetry or dividing plane directly. From these plots it appears that the larger the value of ω_0 the less $\mathcal{A}_1$ and $\mathcal{A}_2$ reconnect. The maximum difference observed is around 5% of the total flux, for the range of ω_0 simulated. A possible reason for the decrease in reconnected flux between $\mathcal{A}_1$ and $\mathcal{A}_2$ is that when $\mathcal{C}$ has a larger amount of flux, more of the flux from $\mathcal{A}_1$ will be reconnected to $\mathcal{C}$, rather than to $\mathcal{A}_2$. We check the flux reconnected between the $\mathcal{A}_1$ and $\mathcal{A}_2$ and both $\mathcal{C}_O$ and $\mathcal{C}_I$ in (c) and (d) respectively. As predicted we see more flux reconnected with increased ω_0 scaling that appears to be linear for both $\mathcal{C}_O$ and $\mathcal{C}_I$. We see for all runs the delayed reconnection to $\mathcal{C}_I$ as $\mathcal{A}_1$ and $\mathcal{A}_2$ has to make its way through $\mathcal{C}_O$. This time difference between shell reconnections looks to be around the same for all runs. To see if this explains the decreased reconnection of flux between $\mathcal{A}_1$ and $\mathcal{A}_2$ for increased ω_0 we plot Figure 4.15(f) the total of (a), (c) and (d) to compare to the anti-parallel case in (e). This being equivalent to comparing the thread flux we can observe the amount of reconnection that has occurred from $\mathcal{A}_1$ to any other tube. Again, like for (a) and (b) we plot the difference to better observe the changes. In (f) we see two different stages for which runs are reconnecting at higher rates. From $t = 0$ to ~ 50 the higher value of ω_0 causes $\mathcal{A}_1$ to reconnect faster with the $\mathcal{C}$, the higher vorticity of one tube leading to higher $\nabla \times \boldsymbol{\omega}$ between both tubes and this higher reconnection rate. However for $t \sim 50$

onwards we see a reversal of the behaviour to an increase in reconnected flux compared to the anti-parallel case. The existence of $\mathcal{C}$ slows down the formation of the vortex sheet and leads to a different kind of reconnection seen between the nulls discussed previously Subsection 1.3.2. It would be interesting to see how $\mathcal{C}$ would affect reconnection if the set-up allowed for the tube to be of a single sign of vorticity rather than having zero net flux, though this is beyond the scope of what we have done here.

As a comparison with the brute-force flux calculations discussed above, we have also estimated the reconnection rate using the integral methods employed in previous sections. We chose again to integrate $\nabla \times \boldsymbol{\omega}$ along the central axis using Stokes' Theorem in an attempt to get the reconnection rate for each of our simulations, the results being plotted in Figure 4.16. This provides us with the expected amount of reconnected flux for each run and gives us a much smoother result than the brute force method of flux measurement used previously. In (b) we can see that even though the vorticity is stronger in the central axis the $\nabla \times \boldsymbol{\omega}$ term is in fact weaker possibly indicating that the stronger $\mathcal{C}$ is acting to inhibit the reconnection between $\mathcal{A}_1$ and $\mathcal{A}_2$.

The interpretation of the reconnection rate as an integral along the central axis is complicated significantly for certain portions of the simulations due to the creation of the nulls. These nulls mean the central axis is no longer a continuous vorticity fieldline for us to integrate $(\nabla \times \boldsymbol{\omega})_{\|}$ along. We can see the locations and separations of these null points that exist in the central axis of the box in Figure 4.17. Examining first Figure 4.17(c) we see that the maximum separation of the null points decreases as ω_0 is increased. This can be understood by considering the fact that the nulls are created when a strong reversal of the vorticity on the axis is generated by the impinging $\mathcal{A}_1$ and $\mathcal{A}_2$. This reversal has to first cancel the pre-existing vorticity component along the axis, and so the stronger

this existing vorticity component on the axis, the smaller is the region in which the sign reversal takes place (and so the smaller the null separation). With (a) and (b) it is clear that the lower values of ω_0 lead to a larger separation of nulls and also over a longer time. In future it would be interesting to see how these nulls behave for even smaller values of ω_0 possibly with nulls forming in the central axis to completely make way for $\mathcal{A}_1$ and $\mathcal{A}_2$. For the smallest value of ω_0 simulated here the null separation is still around half the radius of $\mathcal{A}_1$ and $\mathcal{A}_2$.

We integrate $\nabla \times \boldsymbol{\omega}$ along the separator between the nulls and plotted the flux in Figure 4.18. The total flux reconnected through the separator roughly matches up with the reduced reconnection rate for the higher values of ω_0. However, it is so far unclear how this different type of reconnection interacts with the other types of reconnection.

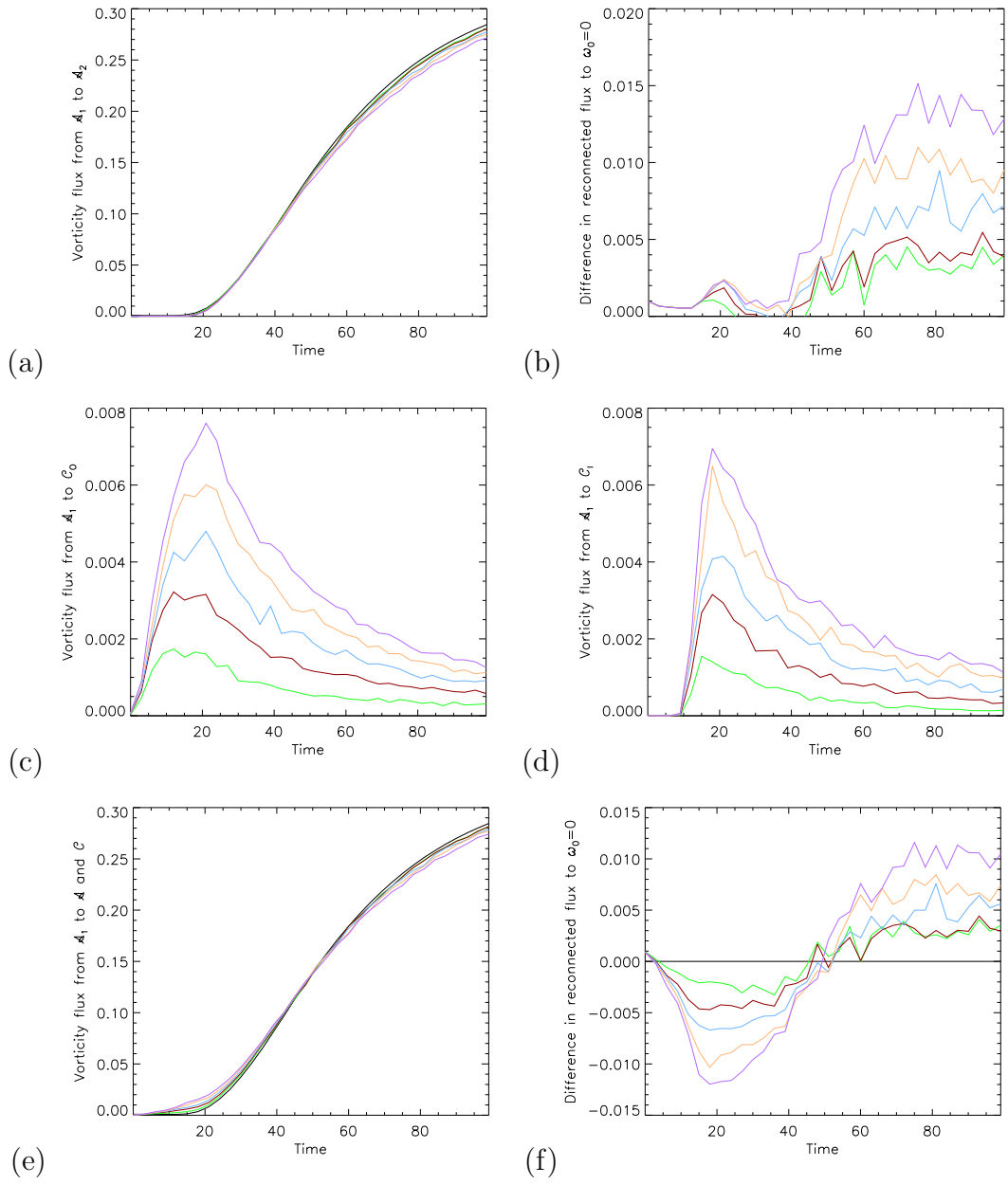

Figure 4.15: (a) Change in flux between $\mathcal{A}_1$ and $\mathcal{A}_2$, (b) negative difference in reconnected flux compared to $\omega_0 = 0$, (c) change in flux between $\mathcal{A}_1$ and $\mathcal{C}_O$, (d) change in flux between $\mathcal{A}_1$ and the $\mathcal{C}_I$, (e) sum of flux reconnected from $\mathcal{A}_1$ to $\mathcal{A}_2$, $\mathcal{C}_O$ and $\mathcal{C}_I$ and (f) difference in total flux reconnected to $\omega_0 = 0$.

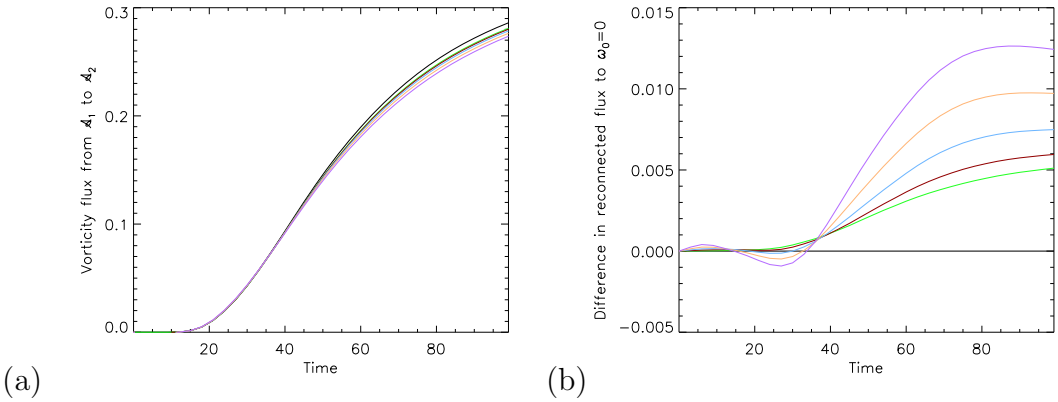

(a) (b)

Figure 4.16: (a) Flux measured with Stokes' Theorem and (b) difference in reconnected flux compared to $\omega_0 = 0$.

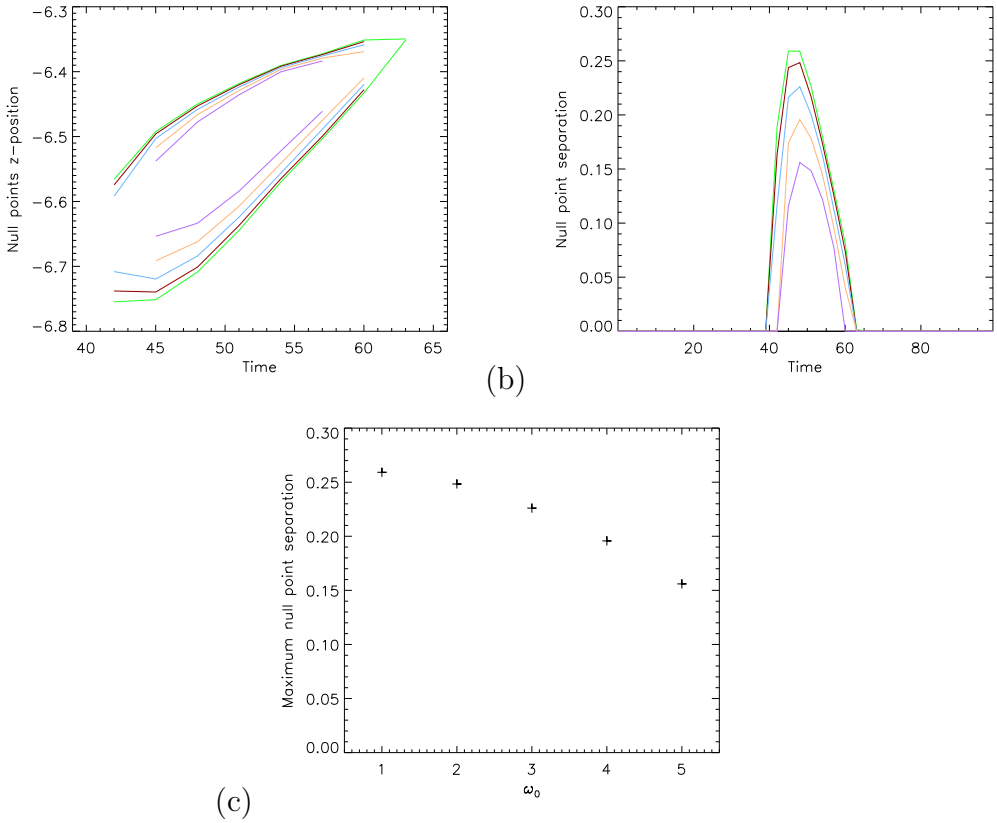

(a) (b) (c)

Figure 4.17: (a) Positions of null points as a function of time, (b) distance between null points and (c) maximum distance between null points as a function of ω_0.

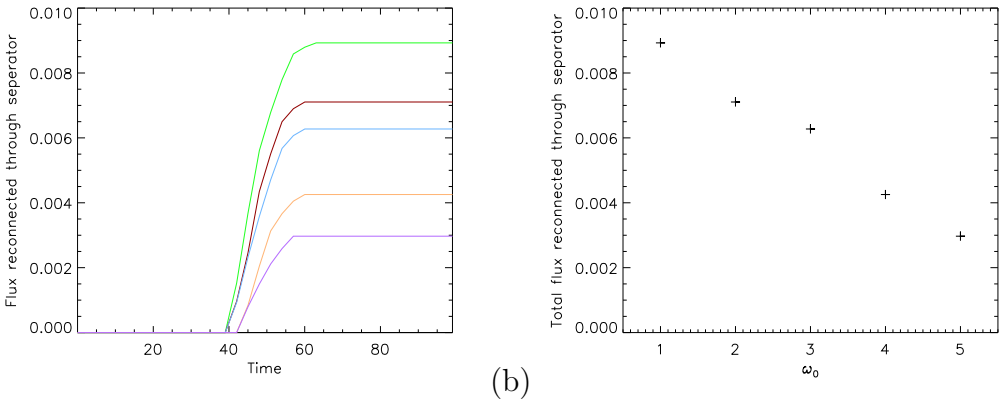

(a) (b)

Figure 4.18: (a) Flux reconnected through separator as a function of time and (b) total flux reconnected through separator as a function of ω_0.

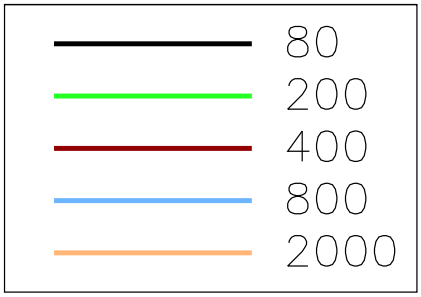

Figure 4.19: Plot colours corresponding to Re values.

4.4 Differences with Reynolds number

As in the anti-parallel case without $\mathcal{C}$ we simulated the same initial conditions but for a range of Reynolds numbers from $Re = 80$ to 2000. For reference the corresponding colours for plots is shown in Figure 4.19. For lower Reynolds numbers $\mathcal{C}$ would be too weak to affect the slow dissipative reconnection we have seen previously. We were also limited by computer power for higher Reynolds numbers but this range of five different viscosities should give a good idea of its role in the process. For all of these simulations we set $\omega_0 = 3$.

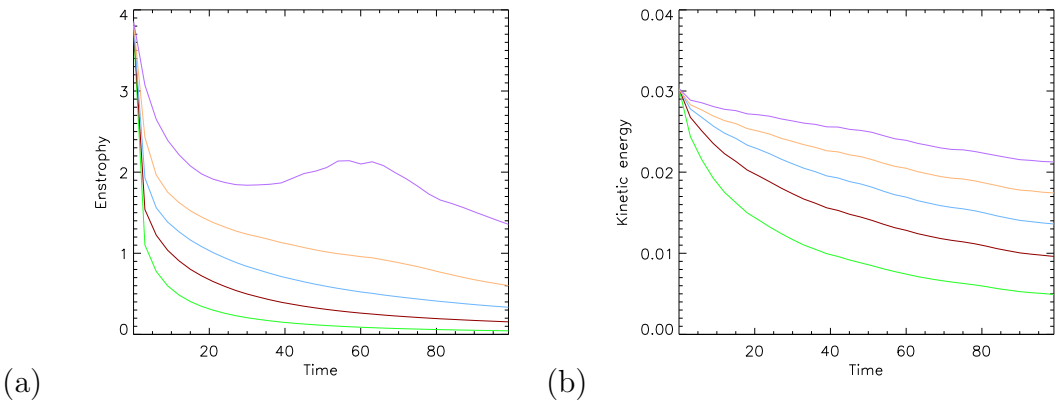

(a) (b)

Figure 4.20: (a) Enstrophy and (b) kinetic energy.

4.4.1 Volume Integrals

We begin with plotting enstrophy and kinetic energy again in Figure 4.20 to give an idea of how $\mathcal{C}$ evolves with Reynolds number. As we expected the enstrophy decreases at a lower rate for increased Reynolds number due to the viscous term dictating the annihilation rate of $\mathcal{C}$. We also see a clear peak in enstrophy for the $Re = 2000$ run indicating a formation of dense vorticity somewhere in the box, most likely a vortex sheet. The kinetic energy appears as expected, dissipating less for the higher Reynolds number runs.

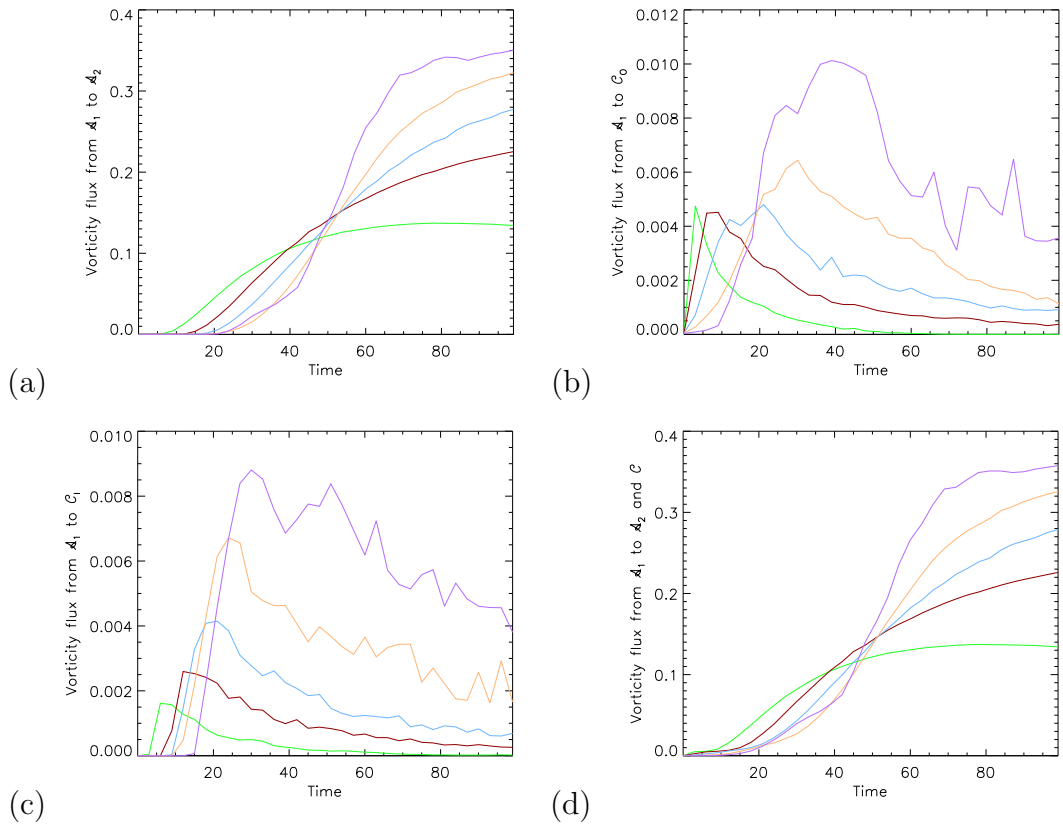

Figure 4.21: (a) Change in flux between $\mathcal{A}_1$ and $\mathcal{A}_2$, (b) change in flux between $\mathcal{A}_1$ and $\mathcal{C}_O$, (c) change in flux between $\mathcal{A}_1$ and $\mathcal{C}_I$ and (d) total flux reconnected.

4.4.2 Flux Evolution

We plot the flux in a similar manner to Figure 4.15 for the different Reynolds numbers in Figure 4.21. In (a) we see the flux reconnected between $\mathcal{A}_1$ and $\mathcal{A}_2$, the behaviour being very reminiscent of the simulations without $\mathcal{C}$ until we get to the $Re = 2000$ run which does not appear smooth like the other plots. We shall discuss this run in more detail later. For the earliest reconnection with $\mathcal{C}_O$ (see Figure 4.21(b)) we see a clear pattern, for low Reynolds numbers we see an earlier reconnection followed by a quick dissipation as $\mathcal{C}$ annihilates. The time this occurs becomes later as the Reynolds number is increased as the vortex sheet between $\mathcal{A}_1$ and $\mathcal{C}_O$ becomes strong enough for reconnection. Again for $\mathcal{C}_I$

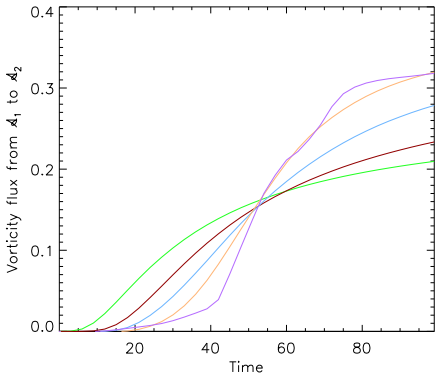

Figure 4.22: Reconnected flux between $\mathcal{A}_1$ and $\mathcal{A}_2$ measured by Stokes' Theorem.

reconnection (see Figure 4.21(c)) we see a delay compared to (b) as $\mathcal{C}_O$ makes way. We see a much stronger correlation with Reynolds number in the amount of flux reconnected here. This will be likely due to the later reconnection with $\mathcal{C}_I$ which means for the lower Reynolds number, $\mathcal{C}$ will have a lower absolute flux and thus less possible flux to be reconnected with. The total flux reconnected from $\mathcal{A}_1$ to $\mathcal{A}_2$ and $\mathcal{C}$ is plotted in Figure 4.21(d) to give an idea of what is left over as 'thread flux'. For the lower Reynolds number runs it remains similar to (a) due to the low amount of flux reconnected with $\mathcal{C}$. However we see a notable increase in the higher Reynolds number runs and the gap between the runs decreases before $t \approx 45$. This provides further motivation to later perform higher Reynolds number runs to see the reconnection between $\mathcal{A}_1$ and $\mathcal{C}$ before $\mathcal{C}$ annihilates itself.

Using Stokes' Theorem again to measure the reconnection rate we plot the estimated reconnected flux between $\mathcal{A}_1$ and $\mathcal{A}_2$ in Figure 4.22. This appears to give a good estimate apart from the lowest and highest Reynolds number runs, which give an overestimate and underestimate, respectively, compared to the brute force flux calculations discussed above. We know from Chapter 3 that this discrepancy for the lowest Reynolds number run is due to annihilation at the boundaries of

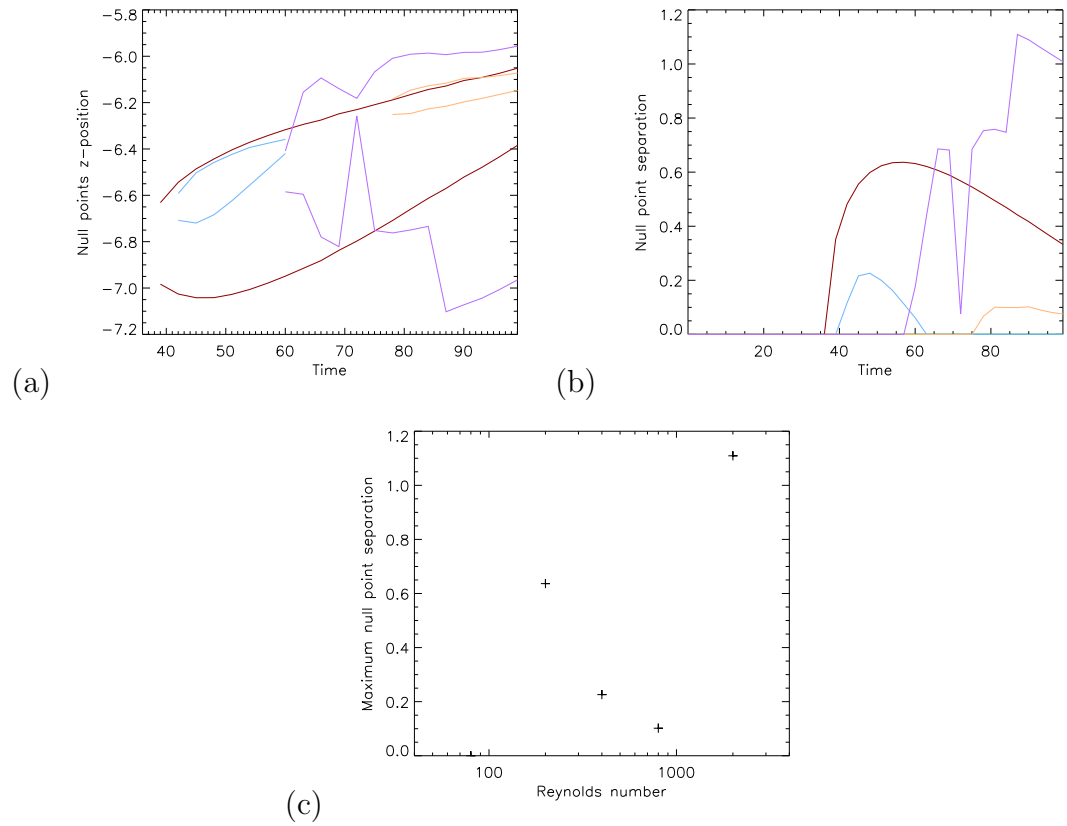

Figure 4.23: (a) Positions of null points as a function of time, (b) distance between null points and (c) maximum distance between null points as a function of Re.

the reconnected vortex rings and that this measurement more accurately represents the true reconnected amount. It is not as simple for the highest Re case as the difference could be due to the appearance of additional vortex rings which we have seen for the corresponding simulation runs without $\mathcal{C}$, or from the change in topology introduced along the central axis with the appearance of the nulls.

We again observe the behaviour of the null points for each of the simulations in Figure 4.23. Notably the $Re = 80$ run does not experience this generation of a pair of nulls. The $Re = 2000$ run also has time shots in which there are two pairs of null points. However, here we only plot the locations of the furthest apart pair of nulls, which explains the non-smooth appearance of the lines in the plots.

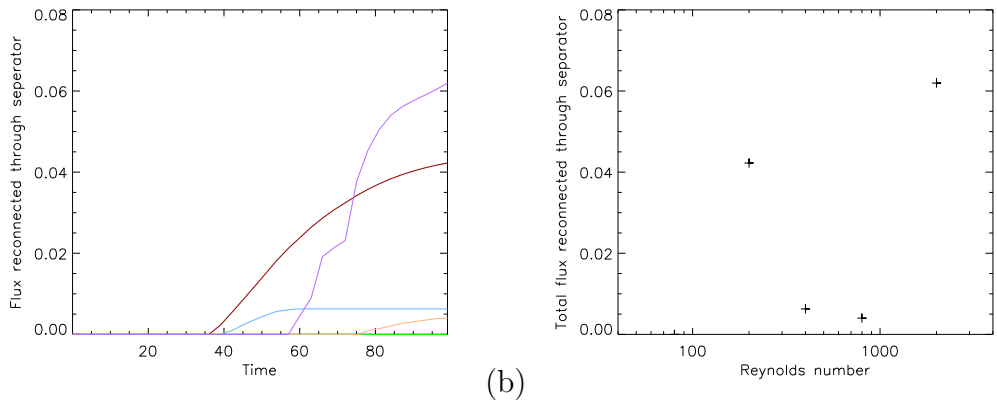

Figure 4.24: (a) Flux reconnected through separator as a function of time and (b) total flux reconnected through separator as a function of Re.

These multiple null pairs shall be discussed in Subsection 4.4.3.

Integrating along the separator again in Figure 4.24 we are able to see the amount of flux reconnected between the vortex tubes. Unexpectedly the lower Re run has a larger amount of flux reconnected through its separator possibly because it was easier for $\mathcal{A}_1$ and $\mathcal{A}_2$ to reconnect with $\mathcal{C}$ and create this separator whereas the lowest Re run did not have sufficiently strong anti-parallel reconnection to generate these nulls. The highest Re run in (a) appears out of place possibly due to the additional null pairs formed and different topology of the vortex fieldlines around the central axis with possible additional vortex rings around it.

4.4.3 $Re = 2000$ Simulation

The majority of the different Reynolds number simulations ran as expected in a similar manner to the anti-parallel case without $\mathcal{C}$, with lower Reynolds numbers having a smaller and slower reconnection as their vortex tubes dissipate. However this is not the case for the highest Reynolds number run of $Re = 2000$ where the topology of the system evolves in a different manner to the other simulations. We shall therefore look into this run in more detail to understand high Reynolds number perpendicular reconnection.

To better understand the reconnection process of the highest Reynolds number run we plot the vorticity fieldlines from both of the x and z boundaries to observe the evolution of the originally anti-parallel and perpendicular vorticity fieldlines. By $t = 15$ in (a) we see $\mathcal{C}$ twisting so that it can reconnect in an anti-parallel fashion with $\mathcal{A}_1$ and $\mathcal{A}_2$. At $t = 30$ in (b) the fieldlines from $\mathcal{A}_1$ and $\mathcal{A}_2$ and $\mathcal{C}$ have begun reconnecting but we also see some field lines from $\mathcal{C}$ (i.e. those that penetrate both top and bottom z boundaries) that have reconnected again and are now on the outside of $\mathcal{A}_1$ and $\mathcal{A}_2$. This double reconnection essentially allows $\mathcal{A}_1$ and $\mathcal{A}_2$ to pass through $\mathcal{C}$ (in a manner similar to the tunnel interaction described by Linton et al [37]), and allows them to reconnect at the central axis which we were not able to see in the lower Re runs. In (c) we are able to see anti-parallel fieldlines travelling to the top of the box very close to the central axis. Anti-parallel reconnection has begun but the reconnection region in the centre of the box looks complicated. From (d) through (f) we see long hairpins forming around the reconnected tubes like in the anti-parallel runs also with twisting of the reconnected tubes. $\mathcal{C}$ appears to be twisted as well with some complicated topology around the reconnection region that will need to be investigated. In future it would be of interest to study the helicity of each of the vortex tubes to

see if there is a re-distribution of the kinetic helicity in the process.

At this Reynolds number the null points are created with different eigenvalues than the lower Re runs. Instead of forming the separator line in the central axis like expected, the spines align themselves with the central axis and the fans form a spheromak [52] shown in Figure 4.26. This has been studied in the magnetic case but not before in the vortex reconnection. In the future with additional computational power this feature would be of interest to obtain more information on as of now we only have plots similar to Figure 4.26 to observe. The creation and subsequent instability of the spheromak in particular.

Increasing the Reynolds number to just 2000 has altered the reconnection process significantly with respect to the case at lower Re. As other simulations of vortex reconnection have already been accomplished up to $Re = 10^4$ it would be possible to do the same for this set-up in the future. With this we could look further into the possible spheromak generated and, as seen in Chapter 3, additional vortex rings around the central axis, which would now be influenced by $\mathcal{C}$ as well.

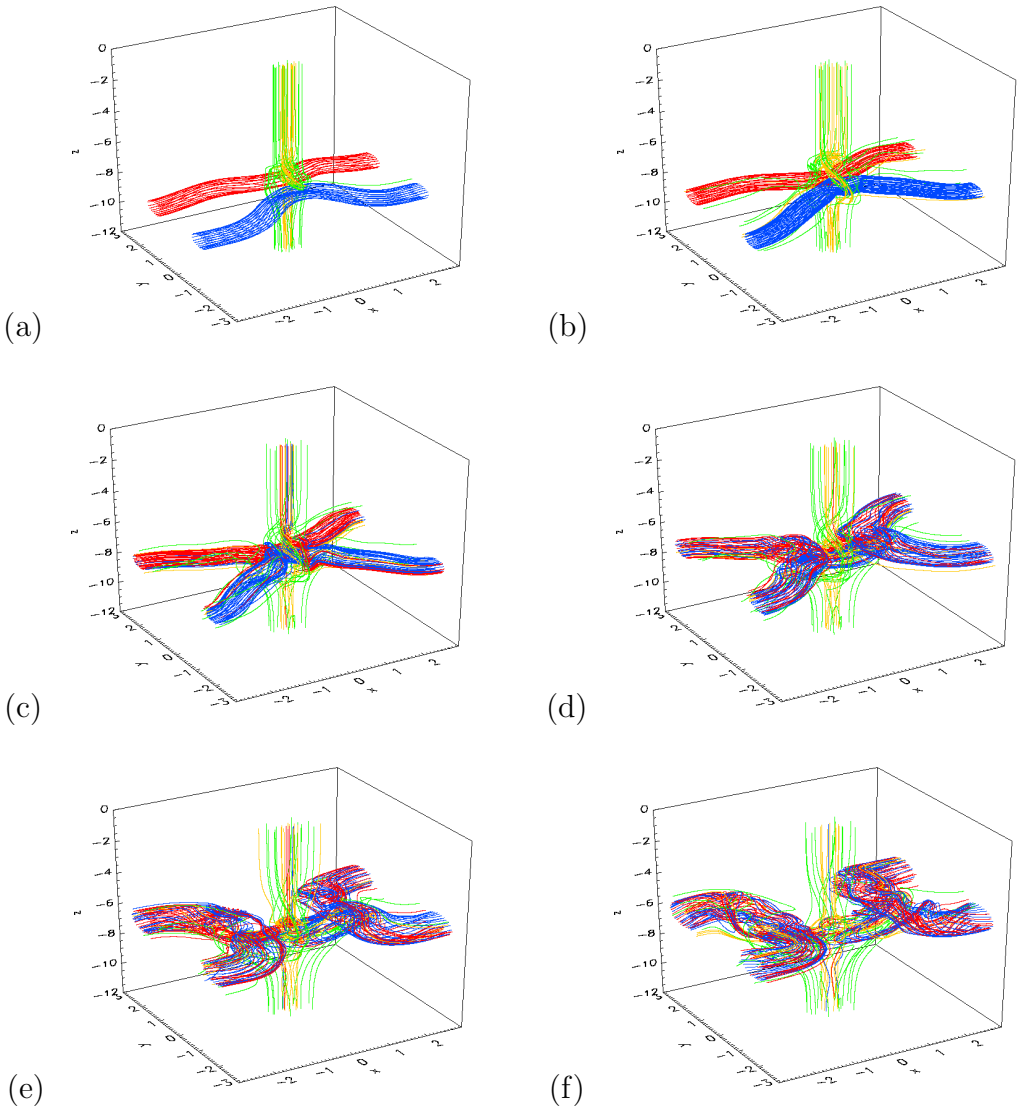

Figure 4.25: 30% of maximum vorticity fieldlines at $x = -3, 3$ boundaries (red and blue) and $z = -12, 0$ boundaries (green ($\mathcal{C}_O$) and yellow ($\mathcal{C}_I$)) at (a) $t = 15$, (b) $t = 30$, (c) $t = 45$, (d) $t = 60$, (e) $t = 75$ and (f) $t = 90$ for $Re = 2000$.

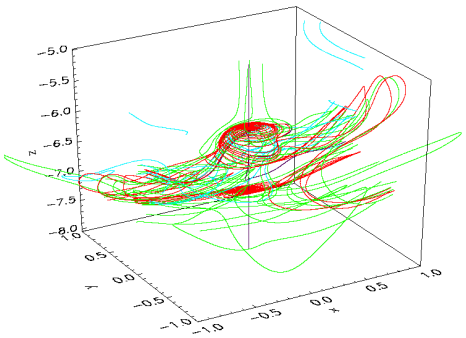

Figure 4.26: 30% of maximum vorticity fieldlines at $x = 0$ (green) and $y = 0$ (blue) with fans (red) and spines (black) plotted from null points at $t = 93$ for $Re = 2000$.

4.5 Conclusions

From this new set-up of vortex tubes we have accomplished the goals we set out in Chapter 1. We have been able to observe reconnection phenomena studied in the magnetic case but not yet in the vorticity case. 3D reconnection was observed between $\mathcal{A}_1$ and $\mathcal{A}_2$ and accurately measured with both Stokes' and the equivalent magnetic reconnection rate. This set-up also provided a way of generating vortex null pairs that form a separator which could be useful for future study. Lastly we were able to exhibit the formation of a spheromak within the system but were unable to study its features in detail. This set-up has improvements to be made already given the time. An alternative to the self-annihilating $\mathcal{C}$ given an alternative simulation code would provide the biggest difference to these simulations. It will be of interest to see if the nulls can be generated so easily for perpendicular tubes of similar vorticity. Studies of the kinetic helicity of each vortex tube would be of interest due to the apparent transfer of it between $\mathcal{A}$ and $\mathcal{C}$. Similarly to the future studies of Chapter 3 higher Reynolds number simulations would always be desirable to further study the turbulent effects it would introduce, in particular the generation of null points and any instabilities.

Chapter 5

Anti-Parallel Vortex Tubes with Axial Flow

5.1 Set-Up

We move onto a different set-up to observe vortex reconnection, this time adding axial flow to the vortex tubes in Chapter 2. From this we can create two scenarios to simulate, one with the axial flow in both tubes going in the same direction and one with opposite axial flow. The runs with the axial flow in the same direction will have zero net kinetic helicity $\int_V \boldsymbol{v} \cdot \boldsymbol{\omega} \, \mathrm{d}V = 0$, these will be referred to as zero net helicity runs further on, and will give a better idea of vortex reconnection behind aircraft due to the additional axial flow [16]. The opposite flow runs, now referred to as non-zero net helicity will allow us to observe vortex reconnection with non-zero helicity and we will be able to see how this affects the evolution and subsequent vortex reconnection. We choose the radial dependence of the axial flow such that the twist is constant for all radii with the aim of measuring the reconnection within each tube with the change in twist.

In cylindrical co-ordinates (r, ϕ, z') we have the following velocity field and corresponding vorticity field for a single unperturbed vortex tube,

$$v_{z'} = \pm v_0 \frac{\pi}{48} \left(1 - \tanh\left(8r^2\right)\right) \qquad v_\phi = \frac{1}{16r} \tanh\left(8r^2\right), \tag{5.1}$$

$$\omega_\phi = \frac{\partial}{\partial r} v_{z'} \qquad \omega_{z'} = \frac{1}{r} \frac{\partial}{\partial r} \left(r v_\phi\right), \tag{5.2}$$

$$\omega_\phi = \mp v_0 \frac{\pi r}{3} \left(1 - \tanh\left(8r^2\right)\right) \qquad \omega_{z'} = \left(1 - \tanh\left(8r^2\right)\right), \tag{5.3}$$

where r, ϕ, z' and v_0 are the radial distance from the vortex tube axis, the azimuth of the vortex tube, the component along the vortex tube and the axial flow factor that we will vary for different runs. These are plotted in Figure 5.1 with $v_0 = 1$.

For $v_0 = 1$ the vorticity fieldline will twist around the central axis exactly once when it reaches the boundary due to travelling $2\pi r$ azimuthally whilst travelling 6, the length of the box. The value of v_0 indicates the number of turns that the fieldlines will make around the axis of the vortex tube within the box. The same pull-back of a 1-form used in Chapter 2 is applied to the now twisted vortex tubes and these perturbed tubes are placed in the same configuration as the previous chapters with the tubes now lying along x plotted in Figure 5.2. The addition of axial flow introduces a non-zero $\boldsymbol{v} \cdot \boldsymbol{n}$ component at the boundary. However due to the periodicity of the new axial flow this should not cause any issue with conserving momentum within the system. We need to take care when calculating the change in flux in these simulations. For the zero net helicity runs we can no longer use the symmetry plane to observe the reconnection as both tubes will travel along x in the same direction and the axis through which they will reconnect will continue to move in x. However, the system still retains sufficient symmetry that the dividing plane will still provide accurate flux measurements. For the non-zero net helicity the opposite situation occurs as the perturbations

now move in opposite directions in x along the tubes and will now rotate around the central axis so symmetry plane flux measurements will be used but dividing plane measurements will not work.

For our experiments we ran five different scenarios for both the zero and non-zero net helicity case, with each scenario having different initial twist and thus helicity. We choose to run these at a Reynolds number of 800 as that provided little diffusion in the anti-parallel case in Chapter 3 but without the complications of additional vortex rings forming. At this Reynolds number we can use a resolution again of [120,240,480] with the same stretching in y as in the anti-parallel runs. The other parameters are again the same. We run with $v_0 = 0.1, 0.5, 1, 2, 3$ to compare the effects of the axial flow. This range of axial flow strengths means that we cover a range of configurations from a weakly twisted to a relatively strongly twisted case where the azimuthal vorticity is comparable to the axial vorticity. However, we are restricted by the maximum velocity not being supersonic in that we can not go much higher than $v_0 = 3$ for this current set-up. We will also compare both cases to the anti-parallel run of the same Reynolds number considered in this chapter to have a $v_0 = 0$. We demonstrate the corresponding colours in Figure 5.3 for future reference. Unless specified otherwise all figures will be for $v_0 = 1$.

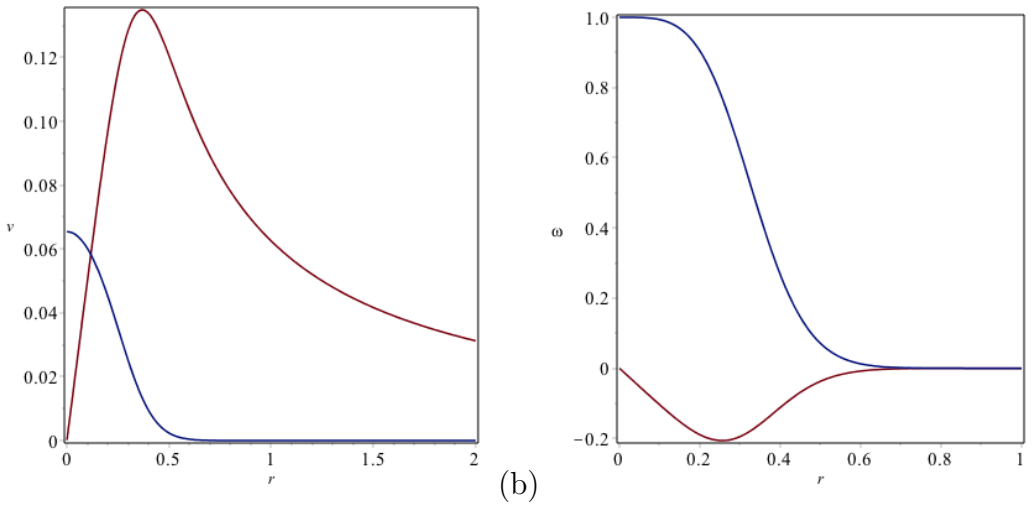

(a) (b)

Figure 5.1: (a) v_ϕ (red) and v_z (blue) as a function of radius and (b) ω_ϕ (red) and ω_z (blue) as a function of radius.

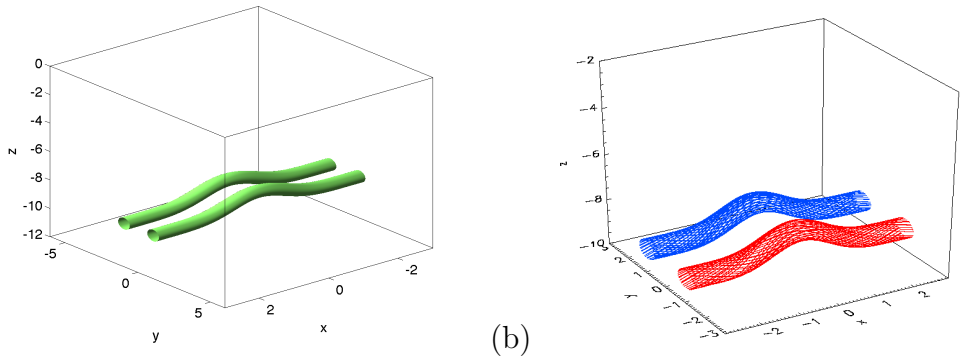

(a) (b)

Figure 5.2: (a) Vorticity isosurface and (b) vorticity fieldlines for initial condition with non-zero net helicity.

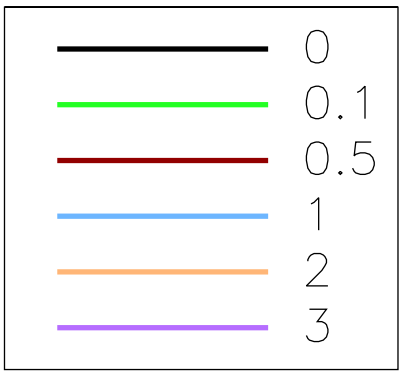

Figure 5.3: Plot colours corresponding to v_0 values.

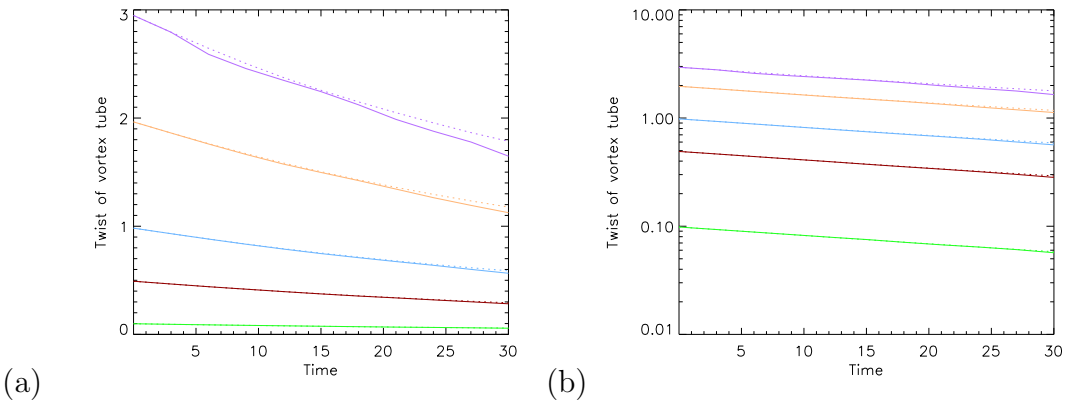

(a) (b)

Figure 5.4: Change in twist of each vortex tube before reconnection (solid) compared to change in twist predicted by (1.59) (dashed), (a) linear plot and (b) logarithmic plot.

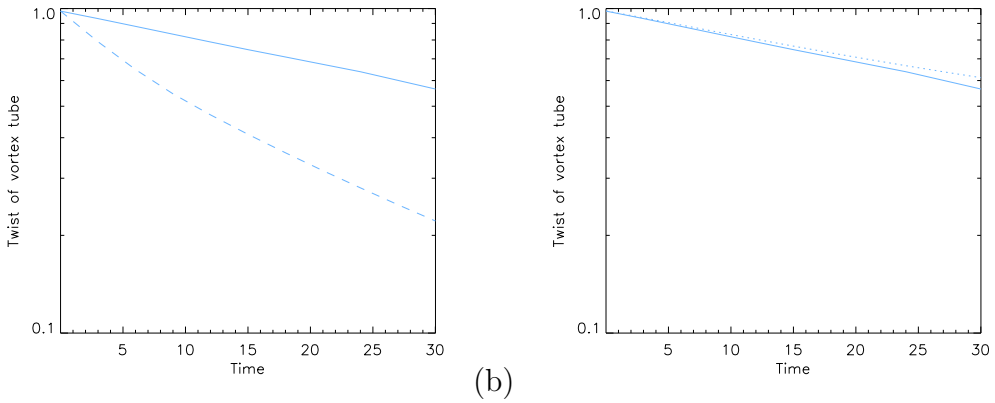

(a) (b)

Figure 5.5: Change in twist with $v_0 = 1$ for $Re = 800$ run (solid) compared to (a) $Re = 400$ run (dashed) and (b) $Re = 800$ run but with no perturbation (dotted).

5.2 Net Helicity Results

5.2.1 Reconnection within each Vortex Tube - Loss of Twist

With the addition of axial flow to the vortex tubes we now have an initial condition with a non-zero $(\nabla \times \boldsymbol{\omega})_{\|}$ term whereas in Chapter 2 this is zero everywhere in the box initially. This $(\nabla \times \boldsymbol{\omega})_{\|}$ term along the vortex tube leads to a loss

in net helicity and in twist. We define the twist of the fieldlines as how many rotations the fieldline makes around the central axis of the vortex tube in one period of the box. In Figure 5.4 we plot the average amount of twist of fieldlines around the central axis (solid) and compare it to the predicted loss of twist from the vortex reconnection rate (1.59). We can see that the twist loss is well measured by the reconnection rate $\nu \int (\nabla \times \boldsymbol{\omega})_{\parallel} \, \mathrm{d}l_{max}$. In Figure 5.4(b) we see that the loss is exponential and constant for all initial twists indicating that $(\nabla \times \boldsymbol{\omega})_{\parallel}$ increases linearly with the twist of the vortex tubes. Due to the ν term in the reconnection rate we can see in Figure 5.5(a) that the twist is conserved better at higher Reynolds number and that no twist would be lost for a hypothetical zero viscosity scenario. The loss of twist occurs regardless of the perturbation of the vortex tube as shown in Figure 5.5(b) where the slight difference between the two is only due to the longer vorticity fieldlines being perturbed, the $(\nabla \times \boldsymbol{\omega})_{\parallel}$ term is constant along the tube as we shall observe later. We measure only until $t = 30$ as the tubes begin reconnecting with each other and twist measurements become difficult but this time frame gives enough information about twist loss. However, in the future it would be interesting to observe the difference in twist loss for the bridges and threads. As seen in Figure 5.6 and the equations below we see that the loss of twist is not uniform along the tube's radius but in fact greater the further away from the tube's core we go due to the distribution of $(\nabla \times \boldsymbol{\omega})_{\parallel}$ and the vorticity distribution. This loss of twist in the runs with whole numbers of twist are particularly interesting after reconnection due to a fieldline no longer mapping to the same point on the other boundary leading to some interesting topology. This will be discussed in a later subsection.

In order to measure this loss in twist, consider the following in cylindrical coordinates (r, ϕ, z'). Consider axial flux, referred to as $F_{z'}$, for an infinitesimal width

dr:

$$\mathrm{d}F_{z'} = 2\pi r\omega_{z'}\,\mathrm{d}r. \tag{5.4}$$

Net axial flux is therefore

$$F_{z'} = \int_0^\infty 2\pi r\omega_{z'}\,\mathrm{d}r = \frac{\pi}{8}. \tag{5.5}$$

For the twist, τ, from the vortex reconnection rate (1.59) we can define the rate of loss of twist as

$$\frac{\partial\tau(r)}{\partial t} = \nu s\frac{\partial}{\partial r}(\nabla\times\boldsymbol{\omega})_\parallel \Big/ \left(\frac{\mathrm{d}F_{z'}}{\mathrm{d}r}\right), \tag{5.6}$$

where s is the length of the fieldline. For the average twist loss of the vortex tube, plotted as dashed line in Figure 5.4, we have

$$\frac{\partial\tau}{\partial t} = \nu s\frac{\left[(\nabla\times\boldsymbol{\omega})_\parallel|_{r=\infty} - (\nabla\times\boldsymbol{\omega})_\parallel|_{r=0}\right]}{F_{z'}}. \tag{5.7}$$

Now consider the initial state of a vortex tube with $v_0 = 1$. Here we have

$$(\nabla\times\boldsymbol{\omega})\cdot\boldsymbol{\omega} = -\frac{2}{3}\frac{\pi}{\cosh\left(8r^2\right)^4}, \tag{5.8}$$

$$|\boldsymbol{\omega}| = \frac{1}{3}\sqrt{\frac{\pi^2r^2+9}{\cosh\left(8r^2\right)^4}}, \tag{5.9}$$

$$(\nabla\times\boldsymbol{\omega})_\parallel = -\frac{2\pi}{\sqrt{\pi^2r^2+9}\cosh\left(8r^2\right)^2}, \tag{5.10}$$

$$(\nabla\times\boldsymbol{\omega})_\parallel|_{r=0} = -\frac{2\pi}{3} \qquad (\nabla\times\boldsymbol{\omega})_\parallel|_{r=\infty} = 0. \tag{5.11}$$

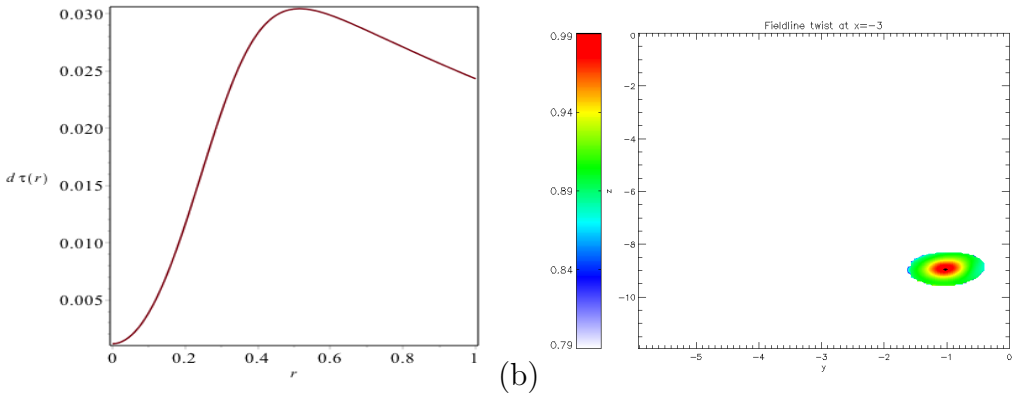

(a) (b)

Figure 5.6: (a) Rate of loss of twist, $\partial\tau(r)/\partial t$, as a function of radius and (b) twist of fieldlines plotted from $x = -3$ boundary at $t = 3$.

Substituting these values into (5.6) and (5.7) gives an estimate of

$$\frac{\partial\tau(r)}{\partial t} = \nu s \frac{32\pi^2 \sinh(8r^2) + \pi^2 \cosh(8r^2) + 288 \sinh(8r^2)}{(\pi^2 r^2 + 9)^{3/2} \cosh(8r^2)}, \tag{5.12}$$

$$\frac{\partial\tau}{\partial t} = -\frac{16}{3}\nu s. \tag{5.13}$$

We can see the loss of twist's dependance on radius from the central axis in Figure 5.6. In (b) we follow the fieldlines from the $x = -3$ boundaries and measure the twist around the central axis before reaching the $x = 3$ boundary. We see the loss increasing further from axis as predicted. However we do not see the outer regions that are expected to have more twist seen at higher radii in (a). This is due to the vorticity being too weak at radii above 0.6 to measure twist and thus were not plotted here.

5.2.2 Visualising the Reconnection Process - Vorticity Isosurfaces

To compare the evolution of the vortex tubes we plot the vorticity isosurfaces in Figure 5.7 to see how they differ from the $v_0 = 0$ run. From these plots it appears that the process is very similar to the $v_0 = 0$ case in that we still see the vortex tubes rotating towards each other and forming a vortex sheet. The bridges again form on top of the threads and split apart after reconnection. The main difference visible is the rotation/skewing of the vortex tubes apparent due to the addition of axial flow although this does not appear to change the overall structure of the reconnection process significantly.

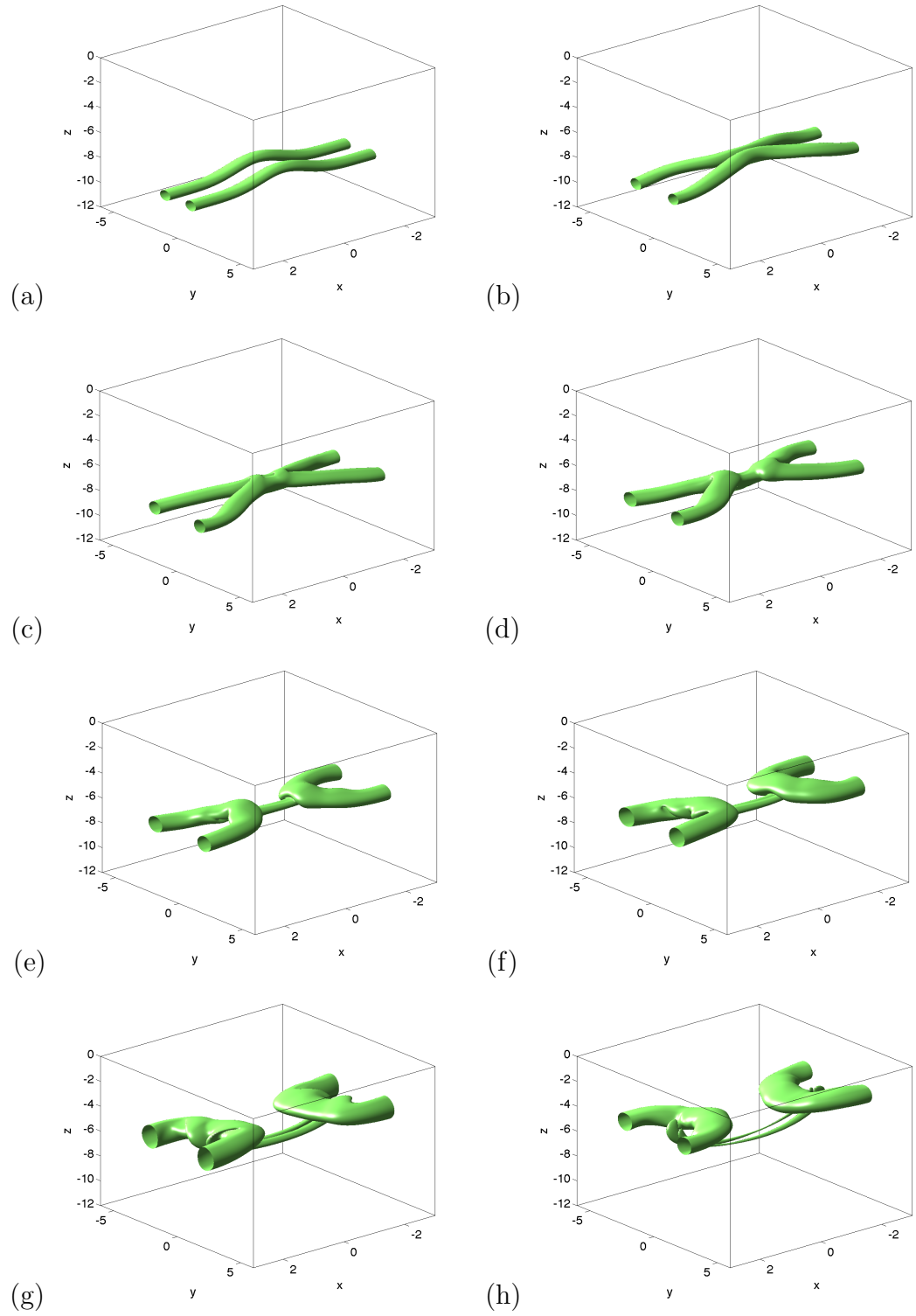

Figure 5.7: 30% vorticity isosurfaces at (a) $t = 0$, (b) $t = 30$, (c) $t = 45$, (d) $t = 60$, (e) $t = 75$, (f) $t = 90$, (g) $t = 120$ and (h) $t = 150$.

5.2.3 Visualising the Reconnection Process - Vorticity Fieldlines

We do the same for the vorticity fieldlines in Figure 5.8 and compare them to the $v_0 = 0$ case. Like the vorticity isosurfaces the process looks very similar to the $v_0 = 0$ run, the main difference being now that we can observe the twist of the fieldlines and the loss of twist with time. It is clear for the bridge vortex rings that a net twist has remained within the tube. We again see the slight skewing of the vortex tubes before reconnection causing a small rotation of the vortex sheets formed which will be discussed in the next subsection.

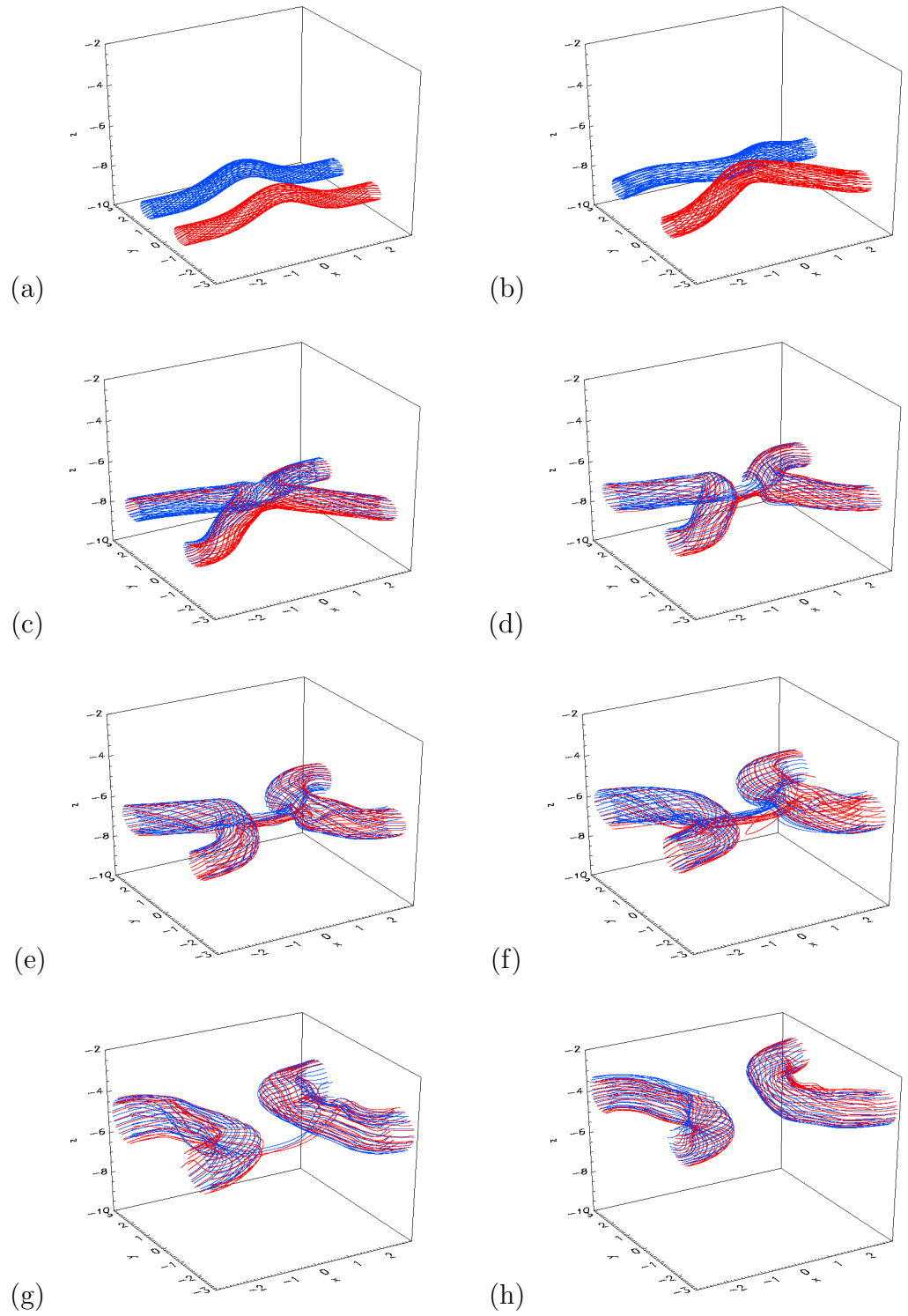

Figure 5.8: 30% vorticity fieldlines at (a) $t = 0$, (b) $t = 30$, (c) $t = 45$, (d) $t = 60$, (e) $t = 75$, (f) $t = 90$, (g) $t = 120$ and (h) $t = 150$.

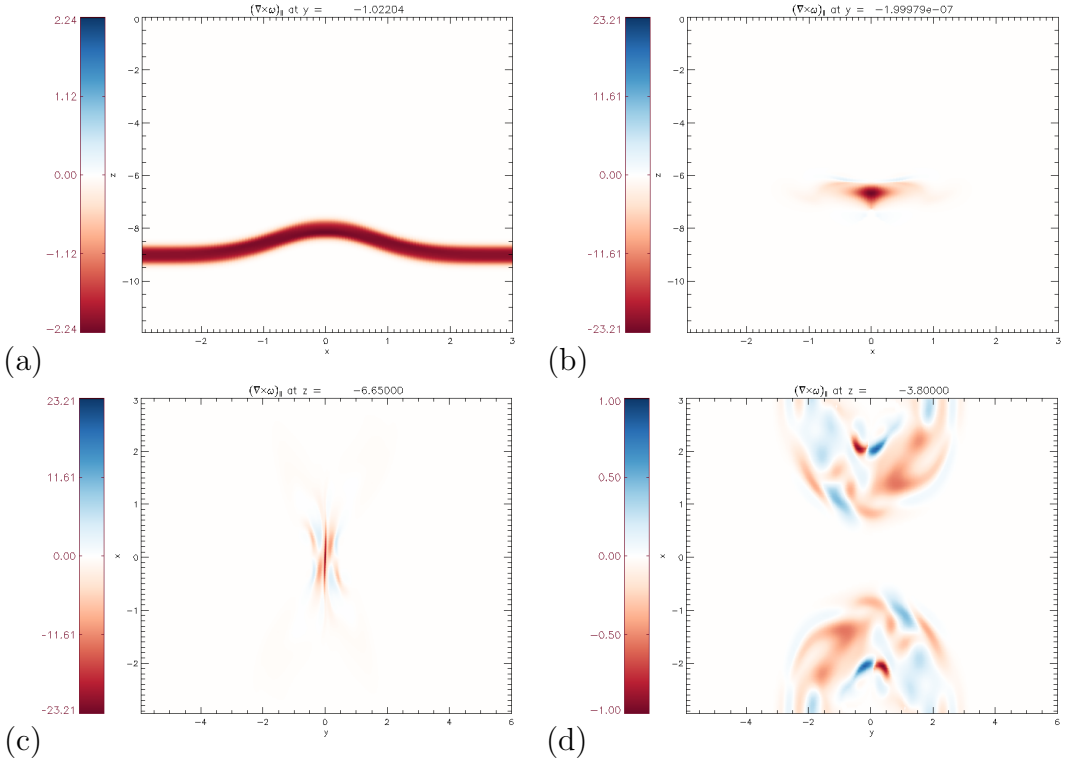

Figure 5.9: Contours of $(\nabla \times \boldsymbol{\omega})_{\parallel}$ at (a) $t = 0$ and $y = -1$, (b) $t = 57$ and $y = 0$, (c) $t = 57$ and $z = -6.65$ and (d) $t = 153$ and $z = -3.8$.

5.2.4 Reconnection Regions

In the $v_0 = 0$ case, integrating $(\nabla \times \boldsymbol{\omega})_{\parallel}$ along any vorticity fieldline will be zero due to the symmetries in the box as discussed in Subsection 2.2.11. However once we add axial flow to the vortex tubes in this current configuration to get a non-zero net helicity we no longer have these symmetries that guarantee the $(\nabla \times \boldsymbol{\omega})_{\parallel}$ measurements to be zero. With this non-zero $(\nabla \times \boldsymbol{\omega})_{\parallel}$ fieldline measurements now within our system we visualise the reconnection regions to observe the behaviour of $(\nabla \times \boldsymbol{\omega})_{\parallel}$ within the vortex tubes.

We plot the contours of $(\nabla \times \boldsymbol{\omega})_{\parallel}$ in Figure 5.9. In Figure 5.9(a) we see the reason for the loss of twist in the vortex tubes with $(\nabla \times \boldsymbol{\omega})_{\parallel}$ being distributed uniformly along the tube. We see a local maximum value of $(\nabla \times \boldsymbol{\omega})_{\parallel}$ found

in the central axis at $t = 57$ plotted in (b) and (c). In (c) we can see the slight rotation of the tubes due to the axial flow, seen as a bending of the vortex sheet out of the dividing plane. From figures (b) and (c) together we see that $(\nabla \times \boldsymbol{\omega})_{\parallel}$ is localised into a thin sheet between the two initial vortex tubes. Thus we have a well-localised region in which reconnection is occurring. This non-zero $(\nabla \times \boldsymbol{\omega})_{\parallel}$ in the central axis will allow us to measure the reconnection rate in a similar fashion to the perpendicular scenario in Chapter 4. This region means that the vorticity fieldlines are not reconnecting completely anti-parallel to each other but instead they reconnect at an angle. This gives a reconnection of vortex lines in the absence of a vorticity null line (X-line) as in the twist-free case discussed in Subsection 1.3.2. However, in many simulations we find that true three-dimensional vortex nulls - and associated separators appear, as discussed later. In Figure 5.9(d) we see the more chaotic contours of $(\nabla \times \boldsymbol{\omega})_{\parallel}$ within the bridge vortex rings as the axial flow begins to oscillate as seen in the $v_0 = 0$ case.

5.2.5 Null Points

As the vortex tubes begin to press against each other and reconnect the vorticity along the central axis of the box becomes non-zero. This is due to the angle of the vorticity fieldlines as they pass through the central axis due to the axial flow discussed in Subsection 5.2.4. This vorticity is always parallel to the central axis by symmetry and for all twists is initially negative. However further into the reconnection process some of the vorticity along the central axis becomes positive, leading to null points forming and thus a separator in the central axis. We plot the vorticity field as a unit vector in Figure 5.10 as the vorticity field is very weak for the null point lower in z. We can see the bottoms of the vortex tubes at the top of (b) to help visualise the null point's location respective to the main source of reconnection. In (a) we can see for the null point around $z \approx -7.3$ an inward fan and the corresponding outward spine in (b). For the lower, weaker null at around $z \approx -8.2$ we see the opposite. This is the case as when the pair of nulls are created, they are of opposite topological degree [45]. Due to the gaussian-like distribution of the tubes it is difficult to tell where null points exist for the majority of the run as the vorticity field is so weak around them. It would be of interest in the future to find a similar initial set-up that allows for the separator to have a stronger vorticity field and be a more important part of the reconnection.

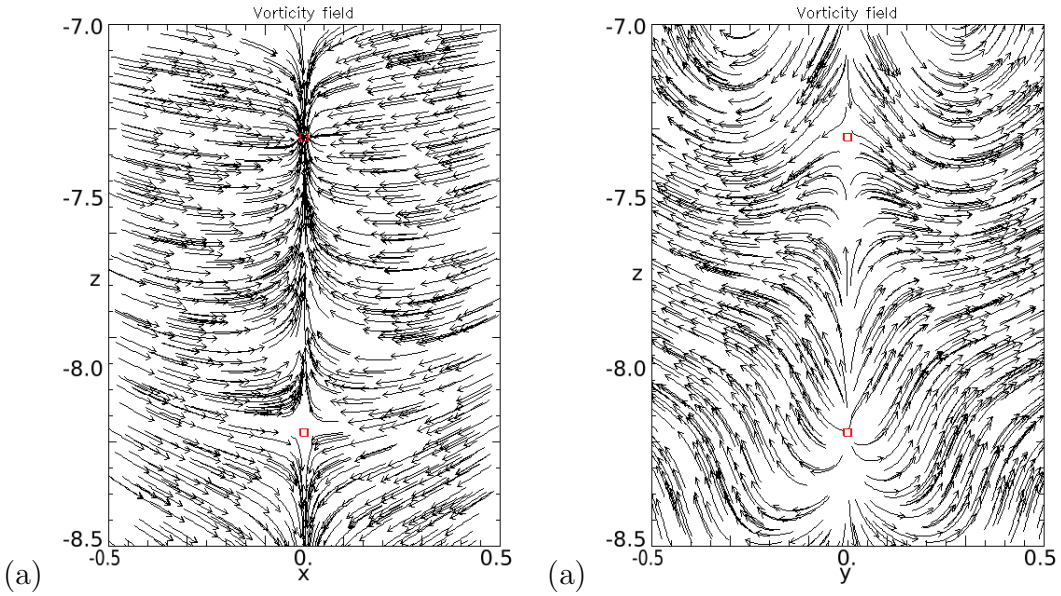

Figure 5.10: 3D null points (red squares) and the surrounding unit-vector vorticity field in (a) xz-plane and (b) yz-plane at $t = 45$.

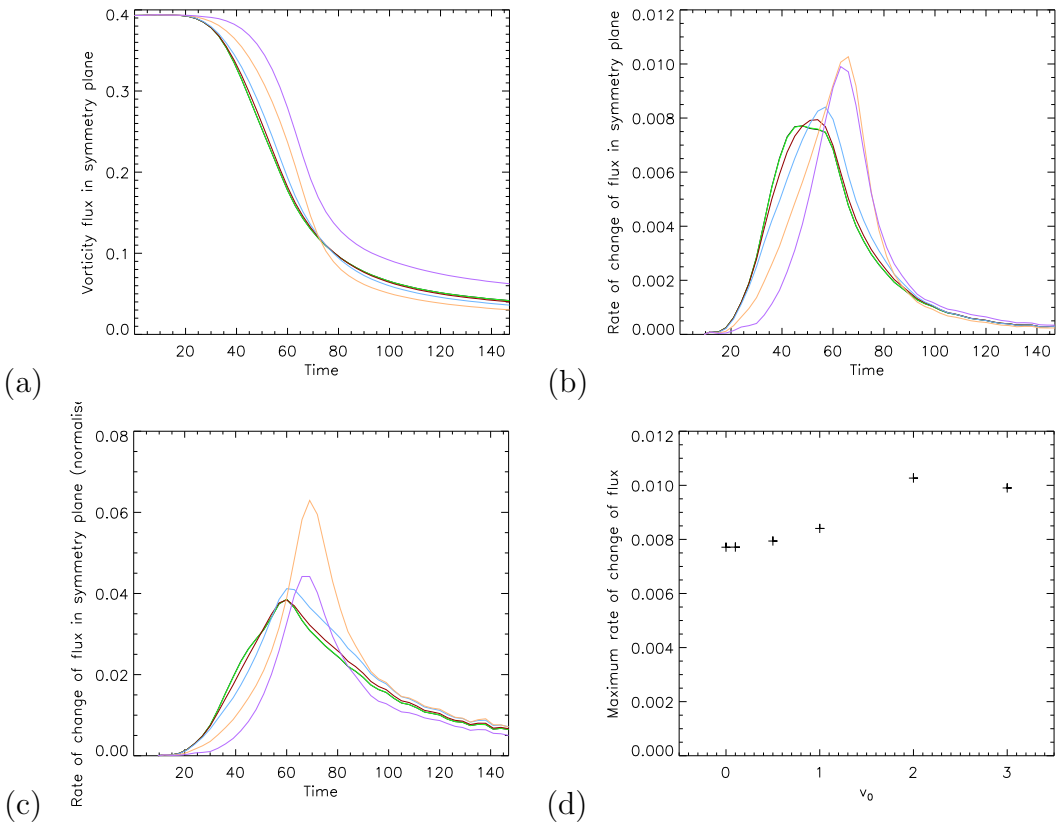

Figure 5.11: (a) Vorticity flux in symmetry plane, (b) rate of change of flux in symmetry plane, (c) rate of change of flux in symmetry/thread flux and (d) maximum rate of change of flux as a function of $\boldsymbol{v}_0$.

5.2.6 Flux Evolution

In the simulations described in Chapter 2 of reconnecting untwisted vortex tubes, we were able to analyse the reconnection process by measuring fluxes through both the diving plane and symmetry plane. However, since the rotation introduced by the axial flow causes some of the vortex tube to pass through the dividing plane without having been reconnected, here we concentrate on the symmetry plane for flux measurements. We can see these in Figure 5.11(a). For most of the twists up until and including 1 the change in flux appears to be quite consistent indicating that the small amount of axial flow and helicity at these levels does not affect the reconnection process and rate by a noticeable amount. With $v_0 = 2$

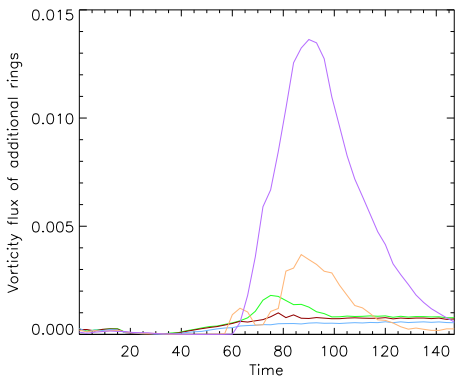

Figure 5.12: Vorticity flux of central axis ring.

(plotted in orange) we see a later and stronger reconnection that we would associate with a higher Reynolds number with more flux being reconnected at the end of the simulation. Moving to the case with $v_0 = 3$, we find that the pattern does not continue as expected. Instead, the reconnection is later, the maximum reconnection rate is roughly the same as the $v_0 = 2$ case seen in Figure 5.11(b) and (d) but the overall amount of flux reconnected is lower than all the other runs. Moreover, we can see from Figure 5.11(c) that the reconnection rate compared to the thread flux is far lower for the $v_0 = 3$ run compared to $v_0 = 2$. We hypothesise that this is due to the perturbations of the vortex tubes moving in opposite directions along the tubes due to the axial flow. This means that in the $v_0 = 3$ simulation they essentially 'miss' each other whereas for the lower twist runs the perturbations would still collide as the $v_0 = 0$ run. This explanation would also lead us to believe that there would now be vortex rings forming in-between the two perturbations as the reconnect with a small distance between them.

In Figure 5.12 we plot the flux of the vortex ring around the central axis. There is a small amount measured for all twists which we would expect as this was also seen in the $v_0 = 0$ twist run. We see as we hypothesised a larger amount for the

$v_0 = 3$ run although this is still short of the 0.3 difference between the $v_0 = 2$ and $v_0 = 3$ twist runs so does not entirely explain the discrepancy between the measured fluxes. We see vortex annihilation again for these vortex rings.

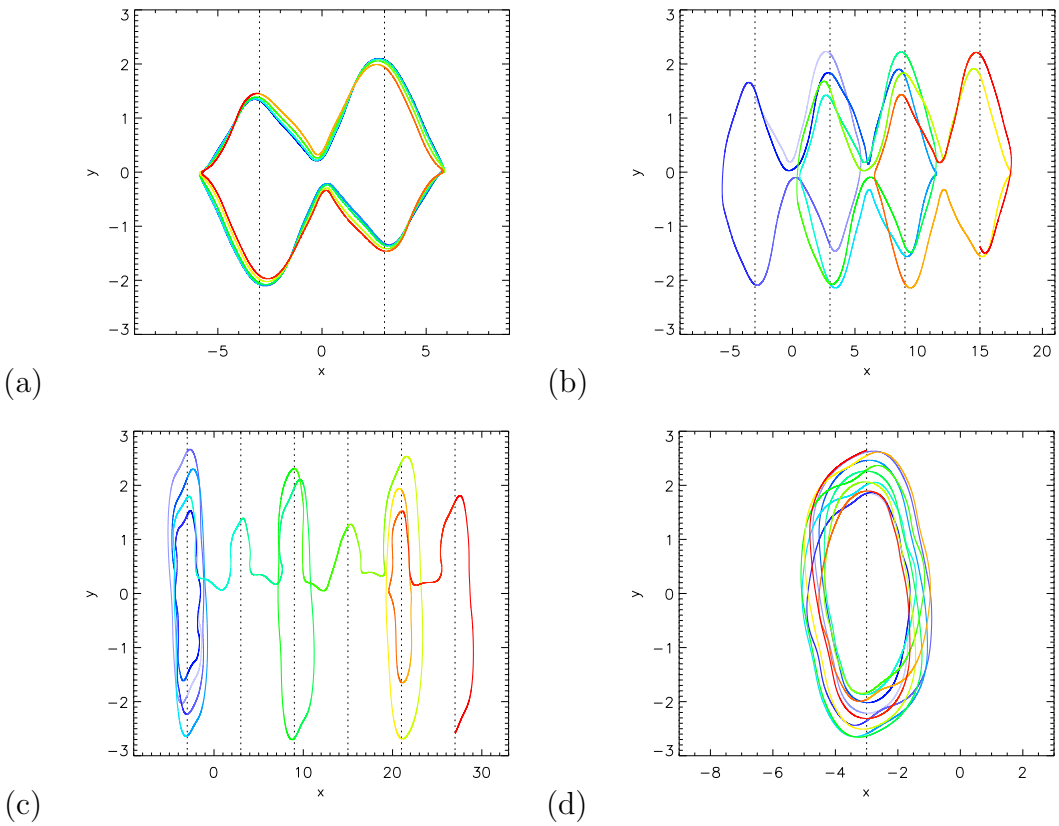

Figure 5.13: Vorticity fieldline plotted from 30% maximum vorticity contour at $x = -3$ (fieldline chosen arbitrarily), change in colour indicates crossing a x-boundary at (a) $t = 42$, (b) $t = 48$, (c) $t = 105$ and (d) $t = 135$ with $v_0 = 1$.

5.2.7 Global Topology

We examine now the global topology that results from the reconnection of flux tubes with axial flow (i.e. the topology when we consider multiple periods in the x-direction). In the $v_0 = 0$ run following reconnection the fieldlines that were not reconnected, known as threads, stretch to infinity and the reconnected fieldlines, known as bridges, form a closed ring centred at the dividing plane at $x = -3$ due to the symmetries of the system. With the twist introduced with the axial flow it is clear that for a fieldline with a non-integer twist it will no longer map to the same point on the next boundary, or mirror point if reconnected. This leads to a more complicated topology where vortex rings will stretch over several periods of

the box and fieldlines that still stretch to infinity but will go back on themselves. We plot some examples in Figure 5.13. If we were to map the vorticity contours at the boundary to threads and rings, as the reconnection occurs eventually an entire contour will map to a ring and this contour and all fieldlines within it will form a vortex ring like in the $v_0 = 0$ case whilst the outer contours will eventually map to a thread again. This is shown in Figure 5.13(d). This change from the simpler v_0 case causes some difficulties with visualising the vortex tubes. With the v_0 case it was possible to see the post reconnection system as the interaction between a single vortex ring and two weak anti-parallel vortex tubes. However we now have post reconnection, the same vortex rings before crossing only one boundary, and the rest of the vortex tube as a bundle of vorticity fieldlines that will at one point split from the fieldlines next to them. It is then much more complicated to visualise the process as the reconnection between all of these fieldlines and their evolution together so will be something interesting to pursue in future.

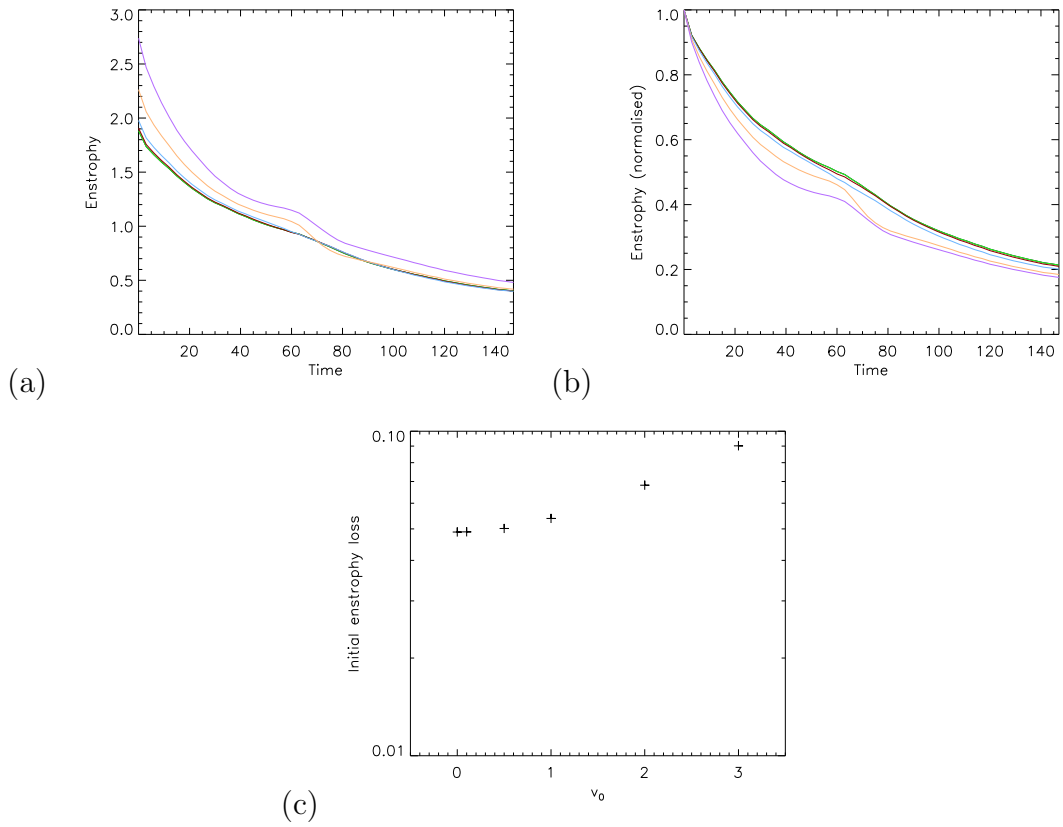

(a) (b) (c)

Figure 5.14: (a) Enstrophy, (b) enstrophy/initial enstrophy and (c) initial enstrophy loss as a function of twist.

5.2.8 Volume Integrals

We plot the enstrophy of each simulation in Figure 5.14 to observe the differences the addition of axial flow brings. In (a) we can see peaks for the runs with $v_0 = 2$ and $v_0 = 3$ but not for the lower twist simulations indicating a stronger vortex sheet forming for $v_0 = 2$ which is observed in its increased reconnection rate. However for $v_0 = 3$ this is not the case, the peak is then a product of something else which we hypothesise to be the additional vortex rings. All but the $v_0 = 3$ run dissipate to the same enstrophy as the $v_0 = 0$ case as the twist in each vortex tube is lost seen in Subsection 5.2.1. We see more evidence of this loss in twist from (b) and (c) where the initial enstrophy loss increases with twist as more twist and therefore enstrophy is lost.

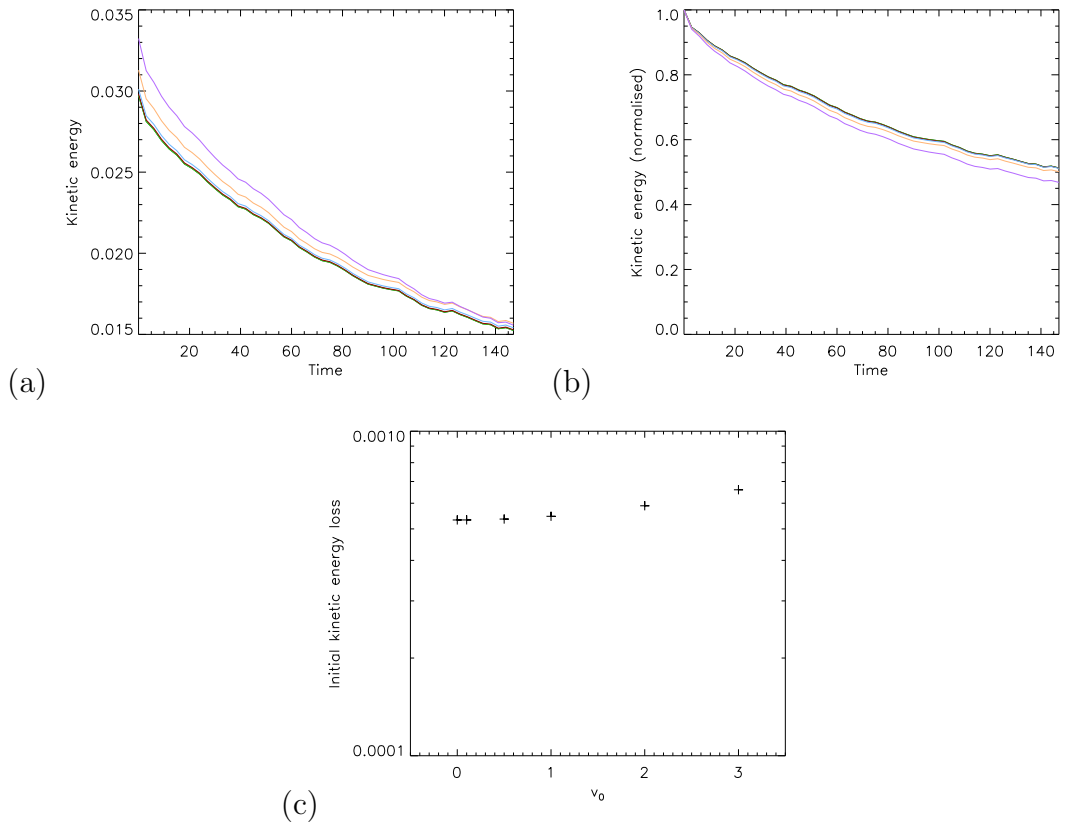

Figure 5.15: (a) Kinetic energy, (b) kinetic energy/initial kinetic energy and (c) initial kinetic energy loss as a function of twist.

From the kinetic energy plots in Figure 5.15 we see a similar scenario to Figure 5.14 as the twist is lost in each run they all approach the same kinetic energy as the $v_0 = 0$ run.

To compare the axial flow in all the runs we plot both the net absolute helicity and net helicity in Figure 5.16(a) and (b). In (b) we see a simple exponential loss in helicity, with no appearance of the axial flow oscillations we have seen before in Subsection 2.2.10. However for the absolute net helicity plotted in (a) these oscillations are apparent for all values of v_0. As the value of v_0 increases the oscillations to become less prominent. For the lower values of v_0 the absolute net helicity converges towards the $v_0 = 0$ case. To understand these differences further we plot the net positive and negative helicity in (c) and (d). Figure 5.16(d)

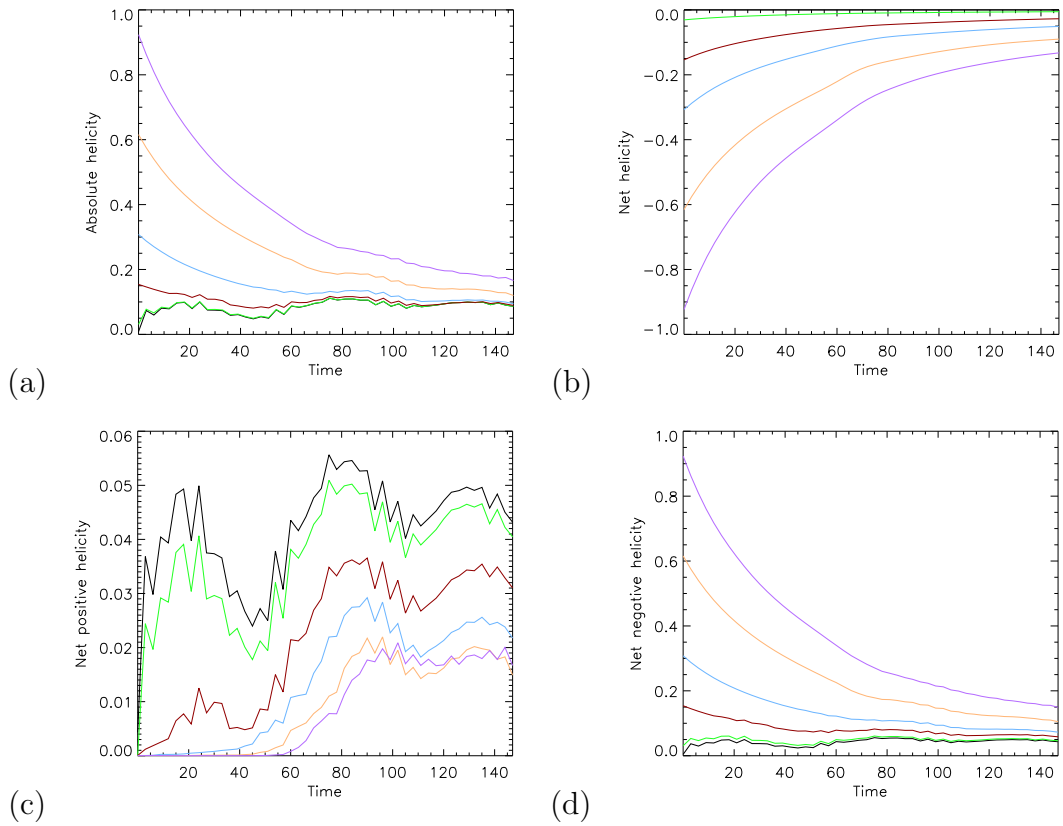

Figure 5.16: (a) Absolute net helicity, (b) total net helicity, (c) net positive helicity and (d) net negative helicity.

shows the lower values of v_0 converging towards the $v_0 = 0$ case but with the higher values looking exponential as in (b). In (c) we see the positive helicity, which for these runs measures axial flow in the opposite direction to which it started. As we would expect the lower initial axial flow values were easier to reverse. However even for the largest values of v_0 the axial flow was still able to be reversed from the oscillations post reconnection. It would be of interest to see if this is still the case at higher values of v_0.

5.3 Zero Net Helicity Results

5.3.1 Reconnection within each Vortex Tube - Loss of Twist

In the same fashion as in Subsection 5.2.1 each vortex tube loses twist and at the same rate as the non-zero net helicity simulations. The difference occurs as the tubes begin reconnecting, since the bridge has zero net twist due to the symmetry of the initial condition. This also changes the topology discussed in Subsection 5.2.7 for these new runs that will be discussed later in the chapter. In further studies it would be of interest to investigate how this switching of one tube's axial flow direction affects the loss of twist and helicity in both the threads and bridges.

5.3.2 Visualising the Reconnection Process - Vorticity Isosurfaces

Once again to compare to the $v_0 = 0$ run we plot the vorticity isosurfaces in Figure 5.17. In a similar fashion to the non-zero helicity isosurfaces in Figure 5.7 we see movement of the perturbations along the tubes, but in this case both in the same direction due to the change in axial flow for these runs. This perturbation movement leads to a change in the axis of reconnection meaning we can no longer use symmetry plane flux measurements to measure reconnection, as the $x = 0$ plane is no longer a plane of symmetry unlike the dividing plane which we will use for flux measurements later. In Figure 5.17(c) we see the bridges forming however there appears to be an imbalance with the left bridge being notably bigger than the right bridge. This asymmetry occurs because the vorticity fieldlines reconnect in an anti-parallel fashion at a null line (like the central axis in the $v_0 = 0$ case), but in this case the null line lies at an angle due to the twist of the vortex lines within the tubes. In Figure 5.17(d) this asymmetry continues and a hairpin structure appears in the right bridge whereas the left bridge remains quite smooth. Whilst it was simple to tell in all other simulations previous to this that the main reconnection would occur at the central axis of the box and thus where the perturbations would meet in this case it is not clear whether the reconnection is occurring slightly offset from the perturbation leading to these asymmetries in the bridges. The tubes evolve as expected in a similar fashion to the $v_0 = 0$ case for later times although the isosurfaces of the threads as they twist around the bridges appear very different on either side seen in (h). It is possible that the differences in either side of the reconnection led to different vortex ring profiles and strengths causing the threads to evolve quite differently around the rings.

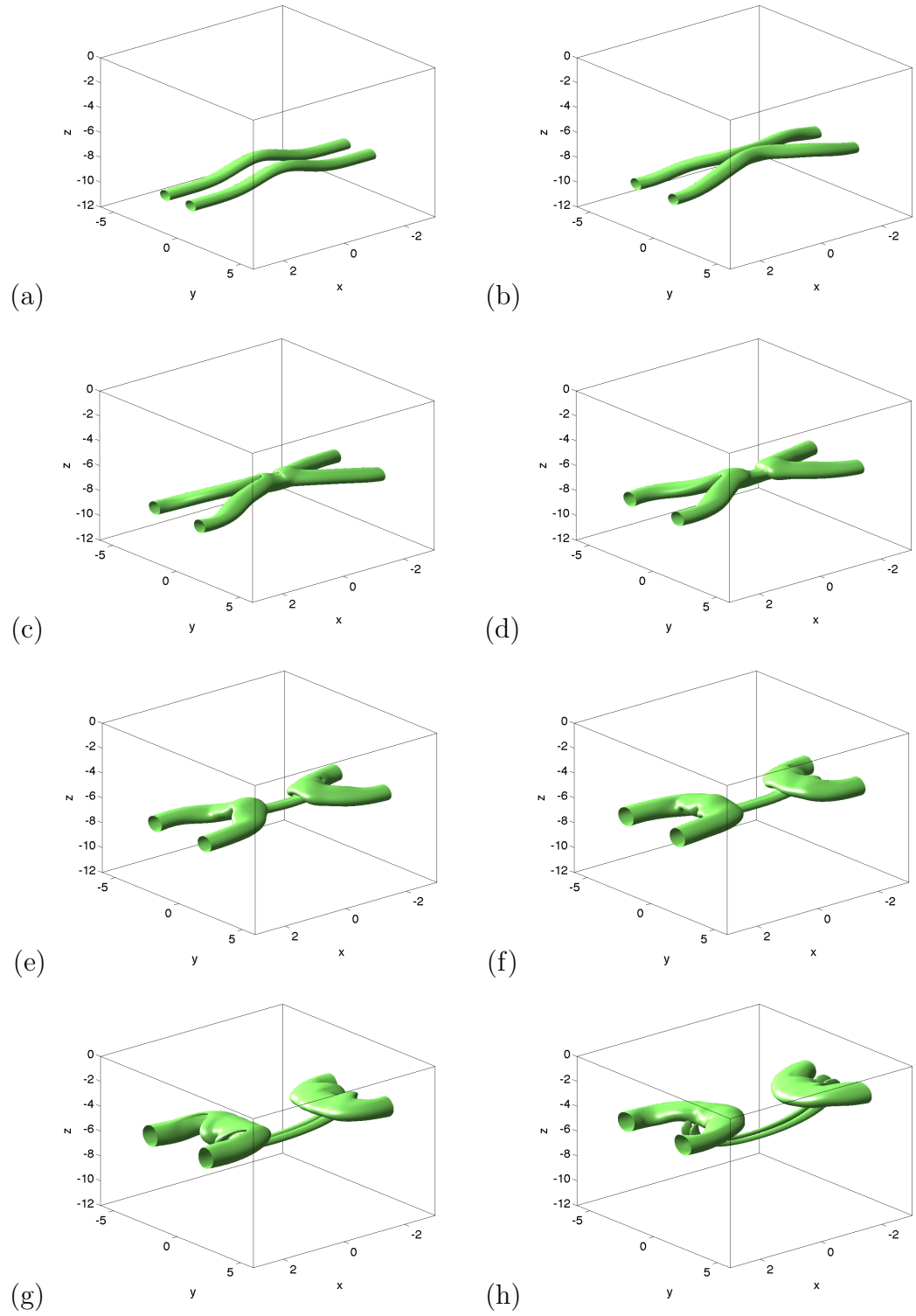

Figure 5.17: 30% Vorticity isosurfaces at (a) $t = 0$, (b) $t = 30$, (c) $t = 45$, (d) $t = 60$, (e) $t = 75$, (f) $t = 90$, (g) $t = 120$ and (h) $t = 150$.

5.3.3 Visualising the Reconnection Process - Vorticity Fieldlines

We plot some vorticity fieldlines in Figure 5.18 to compare to the $v_0 = 0$ run. Like in Figure 5.17 we see the movement of both the perturbations. Already from Figure 5.18(c) we can see the bridge fieldlines and their immediate zero net twist, also from (c) we can observe the asymmetry in the bridges once again although still unable to see the angle of the null line where they reconnected. In (d) we observe the hairpin structure of one half of the vortex ring but not the other which is similar to images of the Crow instability where the rings are not symmetric perpendicular to the plane's direction of travel. The rest of the images appear very similar to the $v_0 = 0$ case with the twisting oscillations appearing again in the bridge vortex rings. It will be interesting to see how these oscillations differ with an initial non-zero absolute helicity in the system.

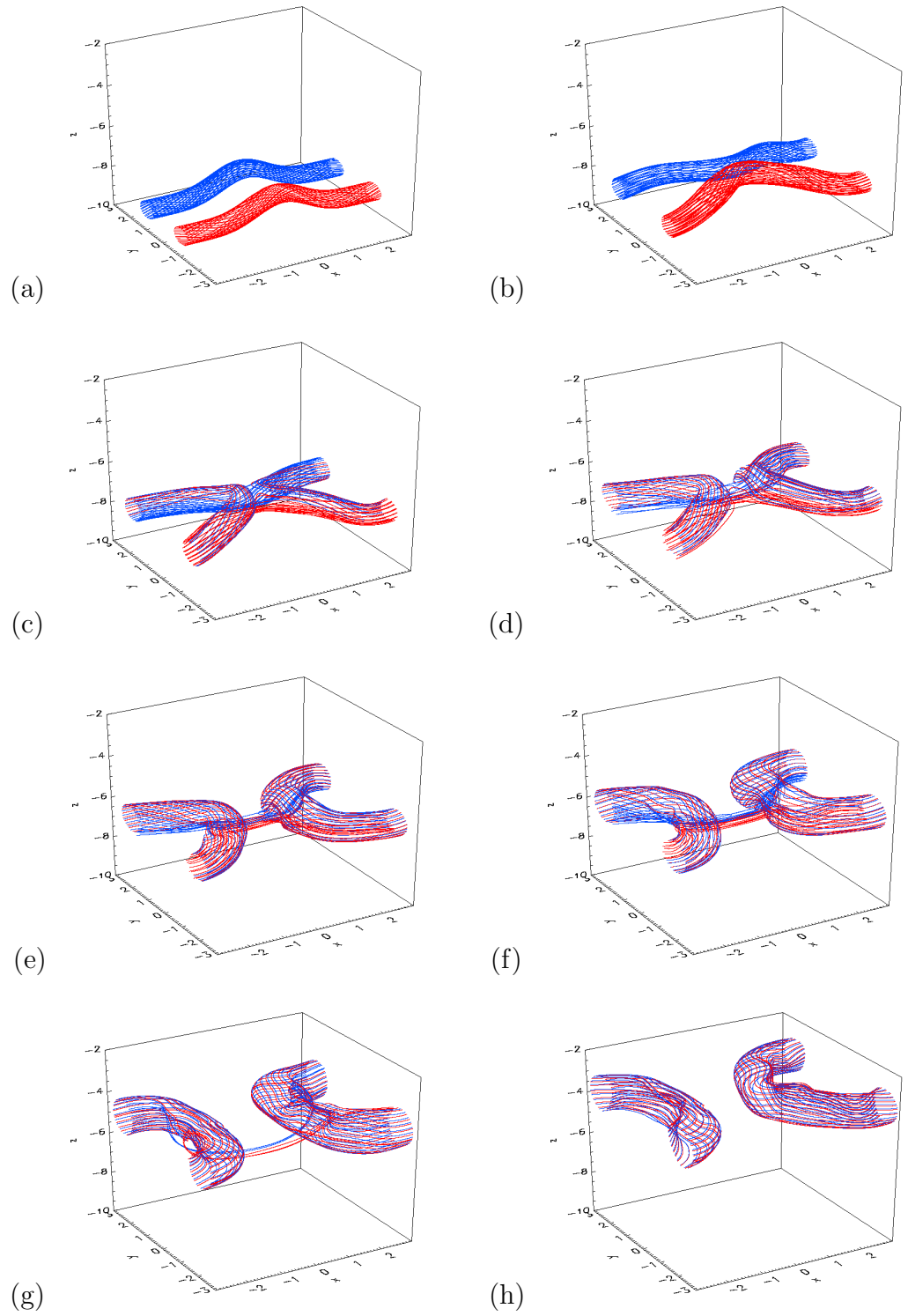

Figure 5.18: 30% Vorticity fieldlines at (a) $t = 0$, (b) $t = 30$, (c) $t = 45$, (d) $t = 60$, (e) $t = 75$, (f) $t = 90$, (g) $t = 120$ and (h) $t = 150$.

5.3.4 Dividing Plane Vorticity Contour Plots

To observe the asymmetry in the bridges that has been introduced by the addition of axial flow we plot the vorticity contours in the dividing plane in Figure 5.19 to provide better understanding of this change in evolution. At $t = 30$ we can see the null line between the two bridges at an angle as discussed previously. It is also clear that the maximum vorticity of either bridge is no longer the same as in the $v_0 = 0$ case. As the vorticity flux in each bridge must be equal, we see that the weaker vortex tube is larger than the other. The differences between the two bridges continue throughout the simulation as the angle in which the null line formed disappears. Later in the run the long hairpin fieldlines that have recently reconnected are much longer for the negative bridge, seen best in (e) and (f). This indicates that the point where they reconnected is along the threads in the direction opposite to the axial flow. This is unexpected due to the null line initially moving with the axial flow. This may be due to the asymmetric evolution of the threads seen in Figure 5.17 due to the different bridge strengths and sizes.

In Figure 5.20 we observe the maximum vorticity in the box, and the maximum/minimum ω_y in the dividing plane to better understand the difference between the two reconnected bridges. In (a) the maximum vorticity appears reminiscent of a slight increase of Reynolds number with the increase of twist which is consistent with the change in flux that will be discussed in Subsection 5.3.6. In (b) and (c) we see the maximum absolute ω_y in each bridge over time with a clear difference. With an increase in twist the positive bridge gets weaker, the negative bridge stronger and these extreme vorticities occur later. This could be due to the increased angle of the null line during reconnection leading to different shapes and sizes of the bridges leading them to have such different maximum/minimum

ω_y values. Plotted as a function of twist in (d) we see how these extremes behave, it appears almost linearly here. However, it would be interesting to see how these change with much higher values of twist that we were unable to model due to computational restrictions.

We observe the centroid locations of the bridges to better understand their movement in Figure 5.21. We see their separation in (a) with the black lines referring to the $v_0 = 0$ case, observed to be symmetric due to the lack of axial flow. As the twist increases the centroids move further from the $v_0 = 0$ case yet the separation of these appears to be consistent even with the increased twist. In (b) we observe the movement in z with the comparison being made to the near straight black line of both the centroids in the $v_0 = 0$ case. With increased twist we see a larger difference between the heights of the centroids because of the larger angle of the null line during reconnection. For the larger twist runs there is a period of lower velocity in x around $t = 80$ to 100. We are unsure of the reason for this change in velocity, but it may be due to the vortex ring now being at an angle. The self inducting motion of the vortex ring now propels in z and x and this x-motion leads to the loss in vertical velocity.

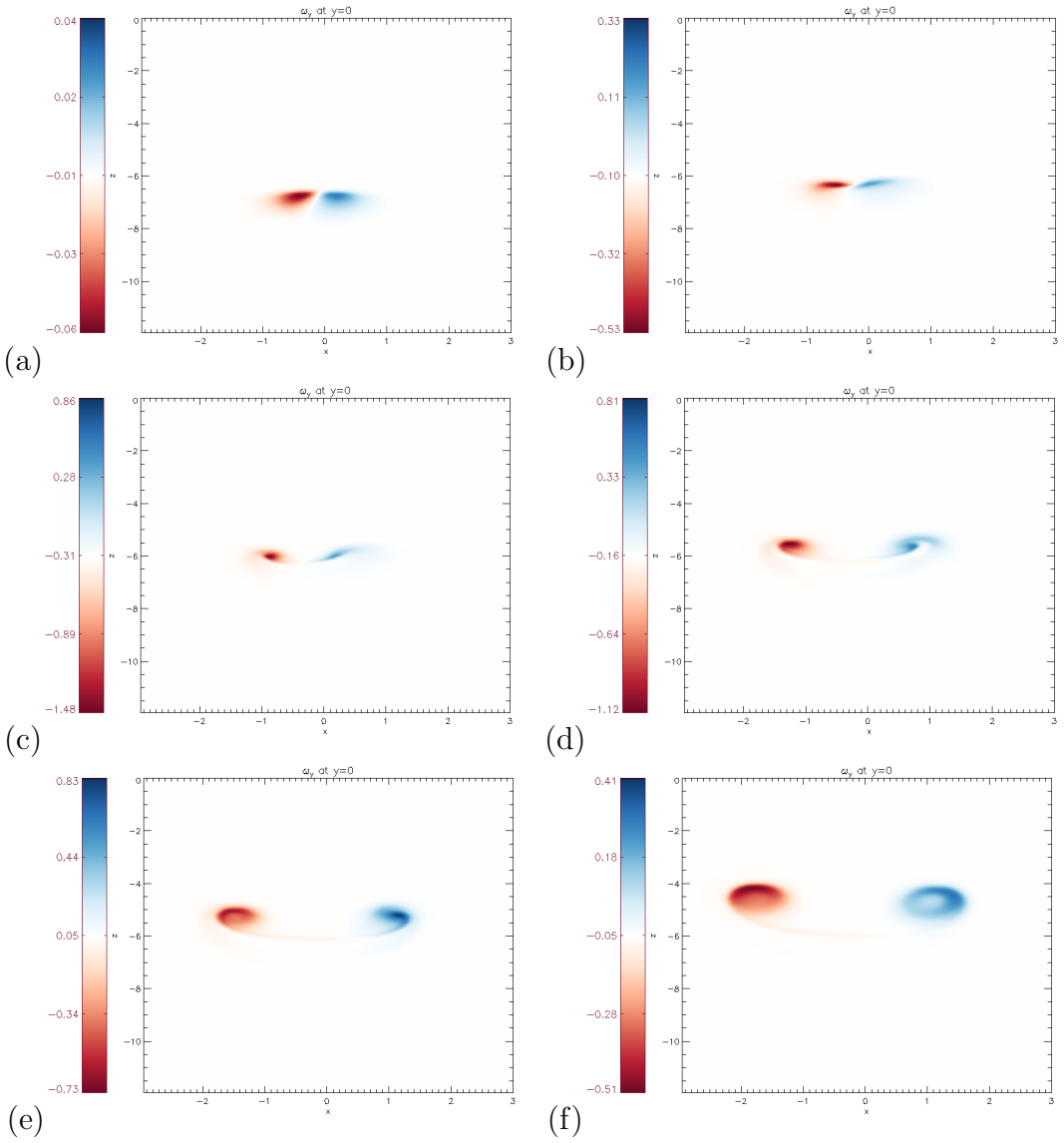

Figure 5.19: ω_y contours in dividing plane at (a) $t = 30$, (b) $t = 45$, (c) $t = 60$, (d) $t = 75$, (e) $t = 90$ and (f) $t = 120$.

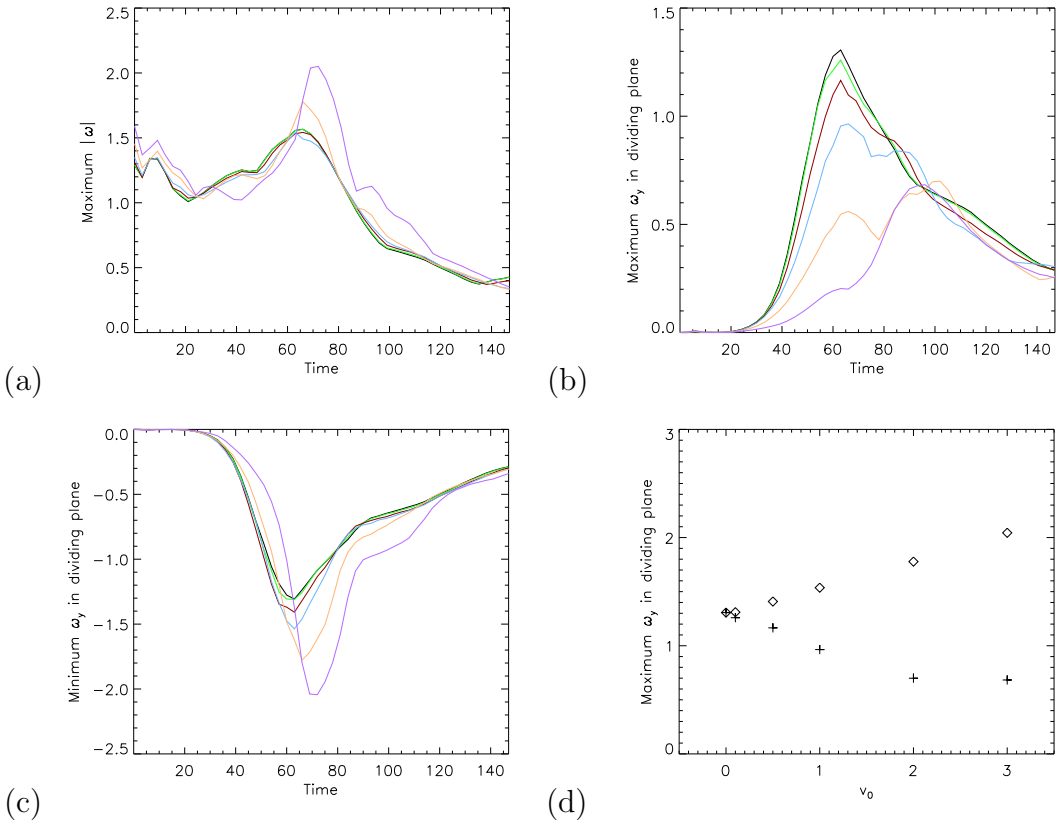

Figure 5.20: (a) Maximum $|\boldsymbol{\omega}|$ as a function of time, (b) maximum ω_y through dividing plane, (c) minimum ω_y through dividing plane and (d) maximum positive (diamonds) and negative (crosses) ω_y through dividing plane as a function of twist.

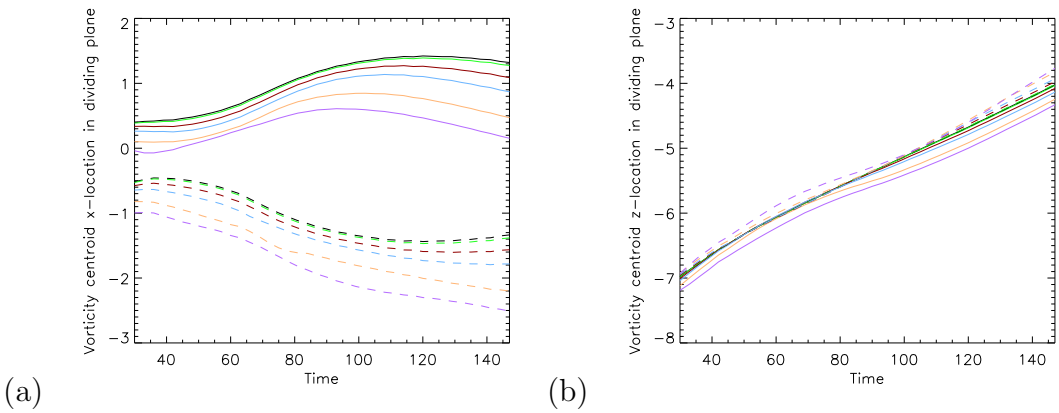

Figure 5.21: (a) Vortex bridge centroid x-positions in dividing plane and (b) vortex bridge centroid z-positions in dividing plane.

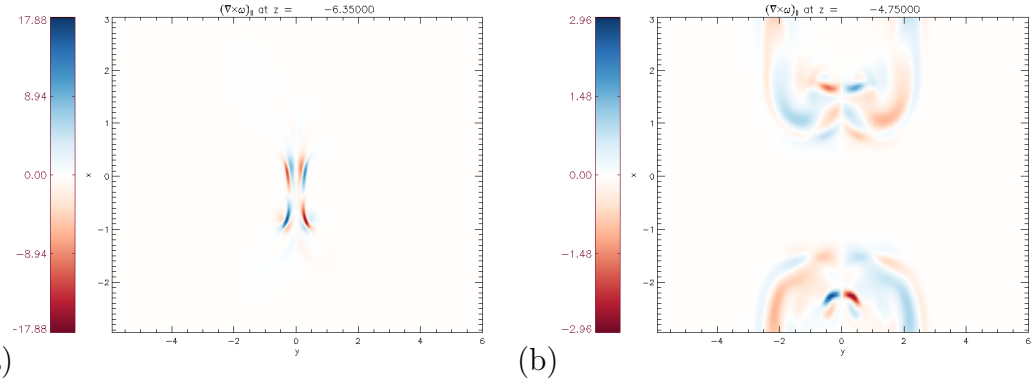

(a) (b)

Figure 5.22: Contours of $(\nabla \times \boldsymbol{\omega})_{\parallel}$ at (a) $t = 60$ and $z = -6.35$ and (b) $t = 120$ and $z = -4.75$.

5.3.5 Reconnection Regions

Observing some of the reconnection regions in Figure 5.22 we notice that $(\nabla \times \boldsymbol{\omega})_{\parallel} = 0$ in the dividing plane indicating that a 2D reconnection process is occurring here. This confirms our earlier discussion of the presence of an X-line in this plane, albeit one that is tilted with respect to the z-axis. We still see reconnection regions within the tube responsible for internal reconnection within the tube that changes the twist, analogous to those described in Subsection 2.2.11 for the $v_0 = 0$ runs. In (b) we again see the regions responsible for the twist oscillations seen in the $v_0 = 0$ case. The reason that the concentrations noted around $x = -2.5$ are stronger than those around $x = +2$ is that the vortex ring is at an angle to the slice of the box the image is taken from.

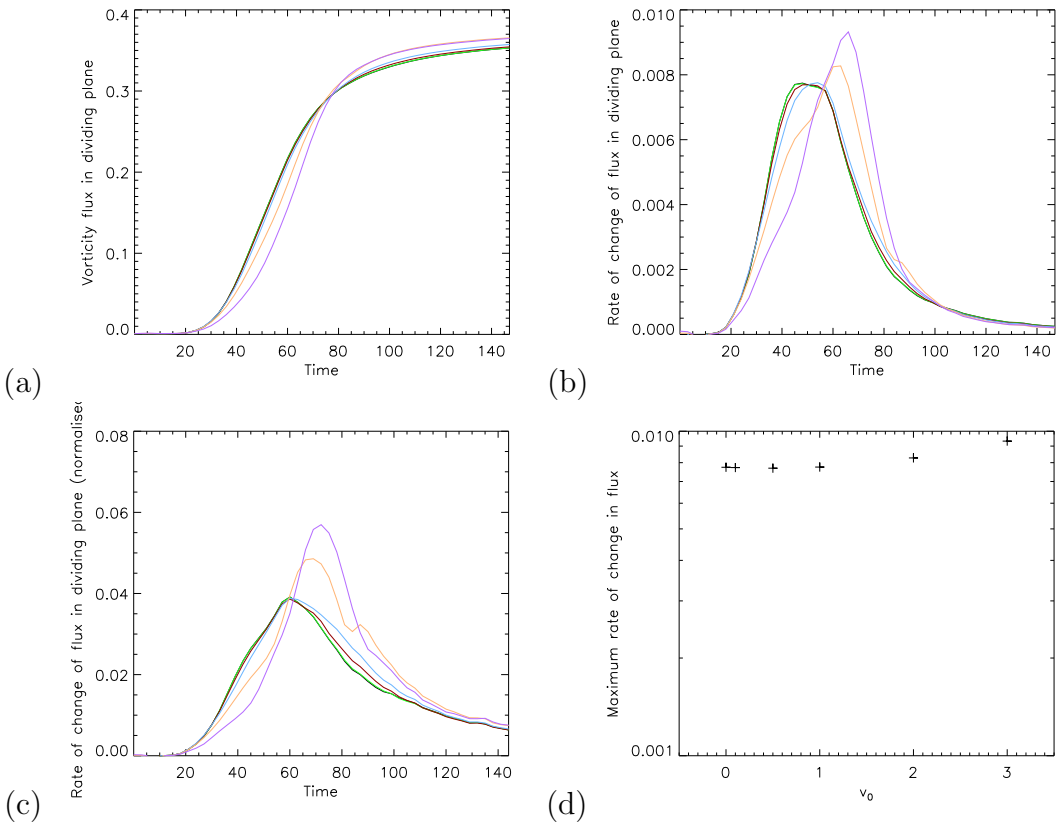

Figure 5.23: (a) Vorticity flux in dividing plane, (b) rate of change of flux in dividing plane, (c) rate of change of flux in dividing plane/thread flux and (d) maximum rate of change of flux as a function of $\boldsymbol{v}_0$.

5.3.6 Flux Evolution

In Figure 5.23 we visualise the change in vorticity flux through the dividing plane as a measure of reconnection. For value of v_0 up to 1 we see very little variation in the change in flux. However for values of v_0 great than 1 we see a notable jump of a later reconnection with a higher maximum reconnection rate with more flux reconnected by the end of the simulation. This later reconnection could possibly be due to the different shape of the vortex sheet formed or the change in angle of the null line. For future work we would like to be able to find this null line during the entire reconnection process to see how the $(\nabla \times \boldsymbol{\omega})$ changes with twist or whether the different angle leads to a longer integral line and thus the increased

reconnection rate. This change in flux rate with twist is very similar to a small increase in Reynolds number and it would also be of interest to see what Reynolds number value each twist increase would correspond to.

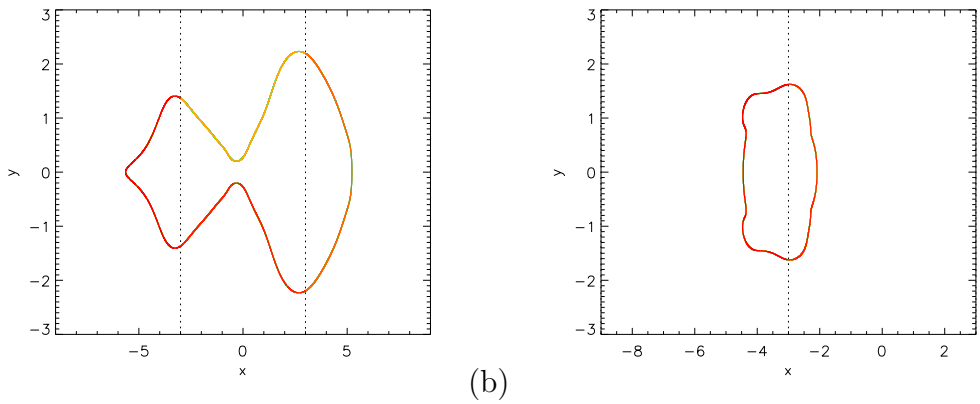

(a) (b)

Figure 5.24: Vorticity fieldline plotted from 30% maximum vorticity contour at $x = -3$ (fieldline chosen arbitrarily), change in colour indicates crossing a x-boundary at (a) $t = 48$ and (b) $t = 120$.

5.3.7 Global Topology

As discussed in Subsection 5.2.7 the topology of the system with axial flow is not as simple as the $v_0 = 0$ case. Due to the symmetry with the dividing plane of the initial condition, any vortex ring formed after reconnection will always be symmetric, and thus have no net twist, in the same fashion leading to a more easily understood configuration than the ones discussed in Subsection 5.2.7. We plot some examples in Figure 5.24 to visualise these better. In (a) we have an example of a thread that becomes a bridge and vice versa depending on the box you are viewing the particular fieldline from. In (b) we can see an example of a vortex ring with the twist oscillations being clear.

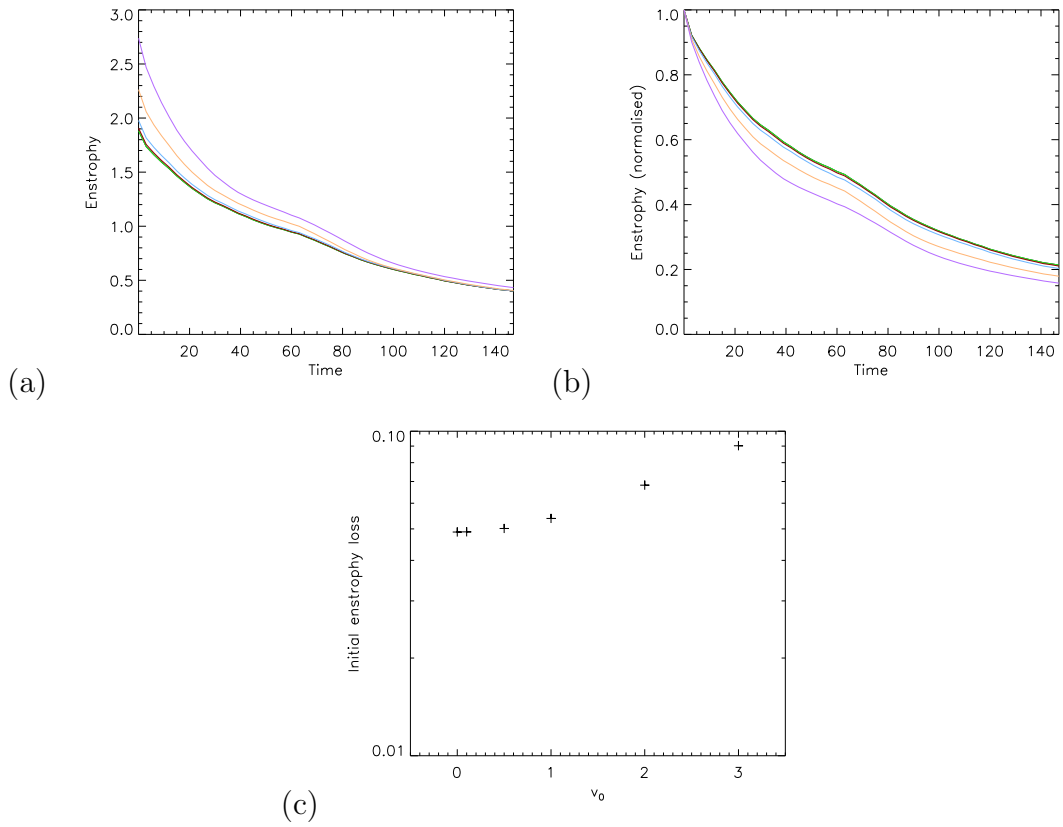

(a) (b) (c)

Figure 5.25: (a) Enstrophy, (b) enstrophy/initial enstrophy and (c) initial enstrophy loss as a function of twist.

5.3.8 Volume Integrals

As in the non-zero helicity runs the enstrophy and kinetic energy do not exhibit as significant differences from the $v_0 = 0$ case. We plot them in Figures 5.25 and 5.26 respectively. Due to the increased initial enstrophy and kinetic energy they experience a more rapid decay at early times, slowly approaching the same value of the $v_0 = 0$ run. It will be of interest to see how the values of these differ in the zero and non-zero helicity runs which shall be discussed later.

We plot only the absolute net helicity in Figure 5.27 as the net helicity is zero throughout the run. We see a quick dissipation of the absolute net helicity dropping towards the $v_0 = 0$ values that appear due to the twist oscillations of the

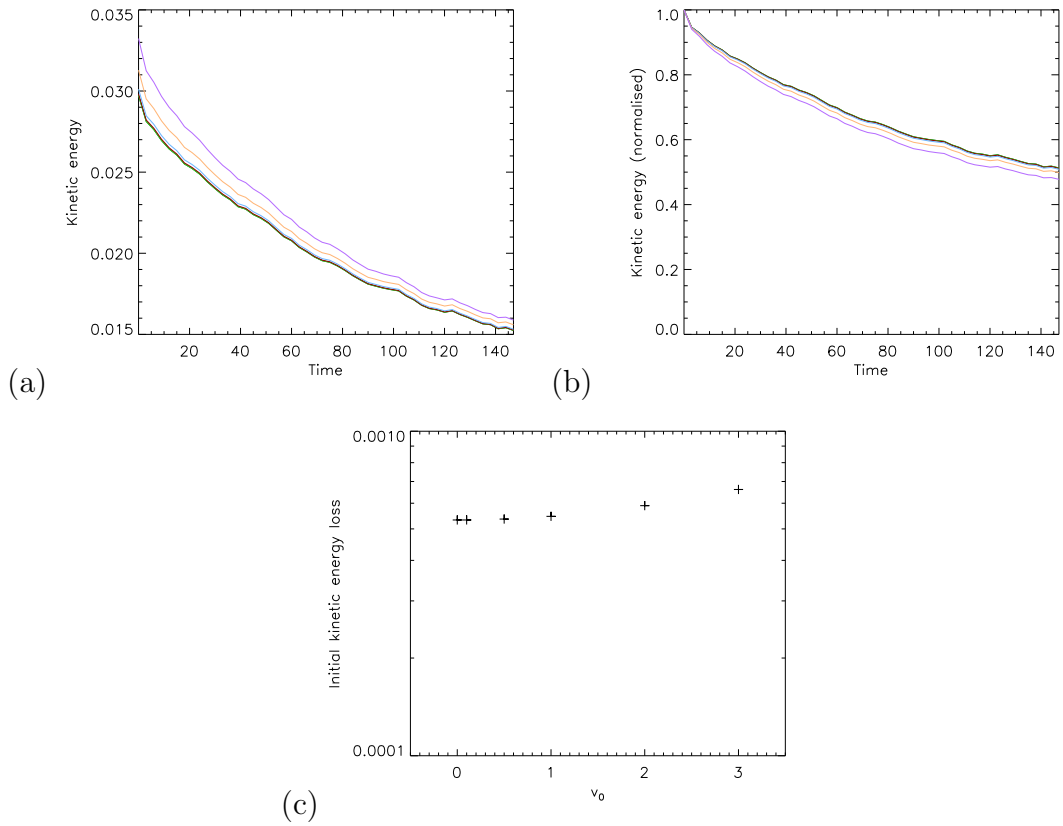

Figure 5.26: (a) Kinetic energy, (b) kinetic energy/initial kinetic energy and (c) initial kinetic energy loss as a function of twist.

vortex tubes. This again shall be of interest to compare to the non-zero helicity run as the evolution of the bridges having zero net twist will be different to the non-zero net twist vortex rings of the other simulations.

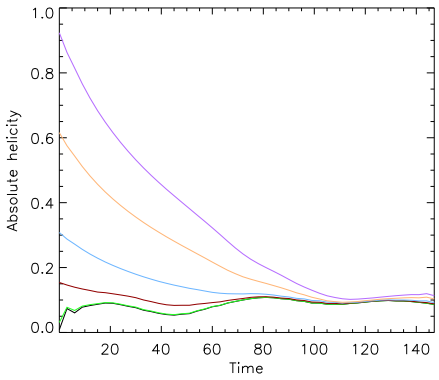

Figure 5.27: (a) Absolute net helicity.

5.4 Comparison of Zero and Non-zero Net Helicity

We now move on to briefly make a direct comparison between the two different sets of simulations with axial flow; those with non-zero net helicity and zero net helicity. Due to the similar initial conditions of these set-ups it will be of interest to see how the reconnection in these simulations differs when the axial flow of one of the tubes is reversed. We have shown in the previous sections that this change in axial flow has led to a different reconnection process due to the change in symmetry. In this section we aim to quantify these differences by comparing the change of flux and volume integrals.

5.4.1 Flux Evolution

We plot the thread flux for all the simulations in Figure 5.28(a) to better understand the differences between them and the same for their reconnection rates in (b) and (c). The low twist runs appear to differ very little from each other, most likely due to the twist of the tubes being small before reconnection, meaning that the movement of the perturbations along the tubes prior to reconnection is small. For the higher twists however it appears to be the case that the non-zero helicity runs have a higher reconnection rate than their zero helicity counterparts. In particular the $v_0 = 2$ zero helicity and $v_0 = 3$ non-zero helicity runs have a very similar thread flux. Due to the movement of the perturbations along the tube this becomes difficult to compare at even higher twists with the $v_0 = 3$ non-zero helicity run being a clear outlier due to the perturbations not colliding head-on. In future work it would be interesting to set-up initial conditions of higher twists with the perturbations initially offset such that they collide perfectly in

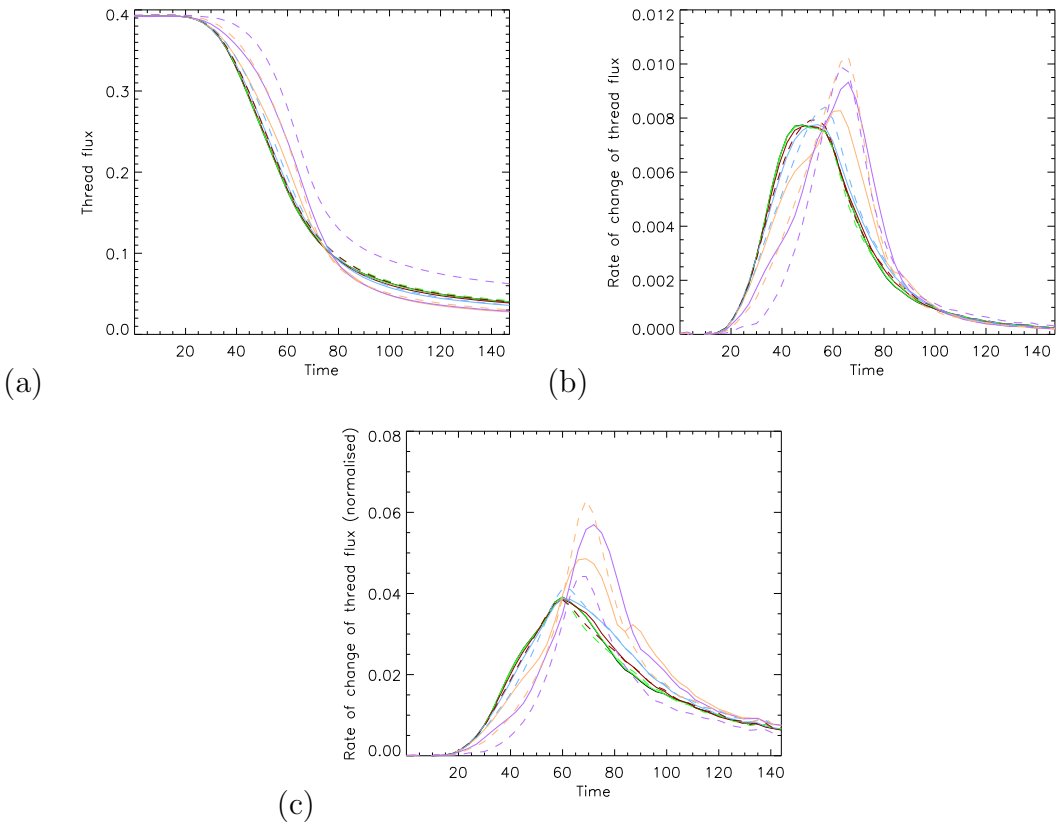

Figure 5.28: Comparison of zero helicity runs (solid) and non-zero helicity runs (dashed) (a) vorticity flux of threads, (b) reconnection rate and (c) reconnection rate/thread flux.

the central axis for maximum reconnection.

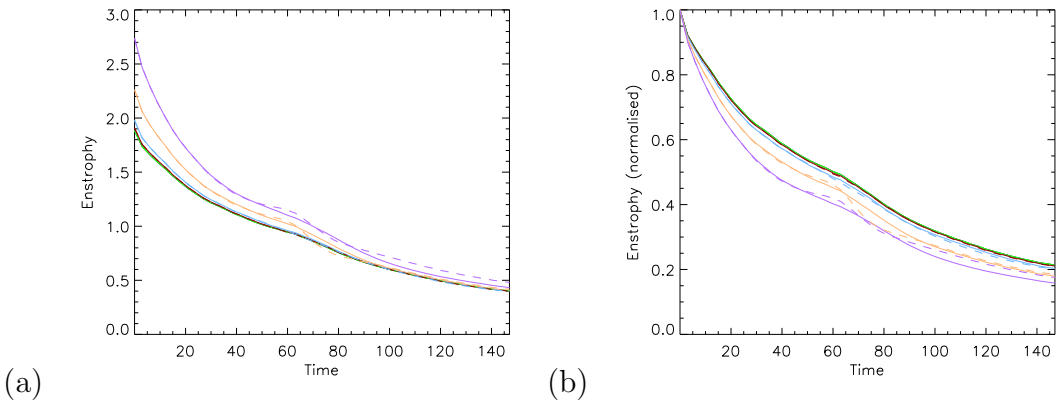

(a) (b)

Figure 5.29: Comparison of zero helicity runs (solid) and non-zero helicity runs (dashed) (a) enstrophy and (b) enstrophy normalised.

5.4.2 Volume Integrals

Plotting the enstrophy of all the runs in Figure 5.29 we see that for the majority of twists the evolution of the enstrophy is approximately the same between the zero and non-zero helicity cases. Up until $v_0 = 1$ the different process of reconnection has no effect on the enstrophy, meaning the vortex sheet formed during reconnection was similar for the zero and non-zero helicity runs at these values of v_0. At $v_0 = 1$ and upwards however, especially noticeable at $v_0 = 2$ and $v_0 = 3$, we see a larger enstrophy 'bump' in the non-zero helicity runs around $t \approx 60$. This is possibly due to the rotation of the vortex tubes leading to a longer vortex sheet forming between the tubes, which in turn leads to a higher enstrophy.

Plotting the kinetic energy for all runs in Figure 5.30 we see little difference between the curves, even for the higher values of v_0. This is consistent with previous results where the kinetic energy appears generally unaffected by the reconnection process so a different reconnection set-up will do little to change this.

We plot the net absolute helicity in Figure 5.31 to help visualise the difference in

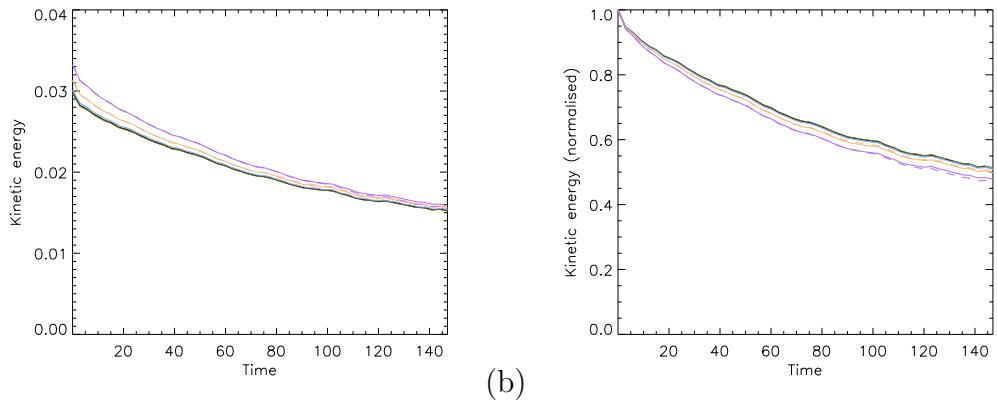

(a) (b)

Figure 5.30: Comparison of zero helicity runs (solid) and non-zero helicity runs (dashed) (a) kinetic energy and (b) kinetic energy normalised.

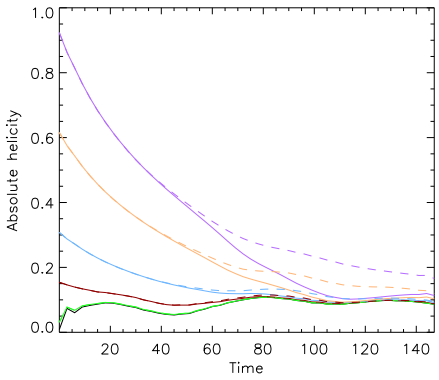

Figure 5.31: Comparison of the net absolute helicity for zero helicity runs (solid) and non-zero helicity runs (dashed)

the evolution of the twist once the vortex tubes reconnect. Up until $v_0 = 1$ the absolute helicity approaches the $v_0 = 0$ value before the reconnection occurs so no difference can be easily seen. For the higher values of v_0 we can see that the net absolute helicity diverges for the two cases around $t \approx 40$ when the reconnection begins. As the bridges in the non-zero helicity runs have net twist they preserve their helicity better than the zero net twist of the other runs.

5.5 Conclusions

From our addition of axial flow to the vortex tubes we have been able to alter the reconnection process considerably. An axial flow in the same direction in both tubes leads to a zero net helicity. As discussed in Section 5.3, we saw the biggest change with the null line where the vortex tubes reconnect moving along with axial flow away from the 'symmetry plane'. This movement led to difficulty defining the null line at a given time and would be something to work on in future, easily and consistently finding the null line in the dividing plane. With this information we would be able to compare the new length of the null line and the $\nabla \times \omega$ evolution along this line to see how it affects the reconnection rate, as now we only have the reconnection rate from the change in vorticity flux at different snapshots. The additional axial flow did lead to an increase in reconnection rate and amount of flux reconnected but without knowing the location of the null line it is difficult to find the reason for this increase.

The process was better understood in Section 5.2 due to the central axis of the box being the 'null line' throughout the simulation. In this case, the geometry of the configuration means that we no longer have a locally 2D reconnection process. Instead, $(\nabla \times \boldsymbol{\omega}) \cdot \boldsymbol{\omega}$ is non-zero in the vortex sheet meaning that the reconnection is fully 3D as seen before in the magnetic case. For higher values of v_0 it will be important to offset the perturbations of the tubes initially such that they collide together head-on to avoid the loss of reconnection we observed in the $v_0 = 3$ case.

With higher computational power both cases would be of interest to study further at higher Reynolds numbers to observe what instabilities may occur and new features such as the additional vortex rings could occur. We would like to study further the topology of both cases as reconnection occurs and complicates the simple initial structure. We would be able to map each point at the boundary to

the end point of that fieldline in the box. With that we would be able to estimate the amount of periods of the box it would have to travel before returning, or if it would return at all. This would be of interest to us in both cases, beginning with the zero net helicity case due to its simplicity with the symmetry preserved in the dividing plane.

Chapter 6

Anti-Parallel Vortex Tubes with Axial Flow

Chapter 7

Conclusions

In this thesis we have studied reconnection between vortex tubes in various configurations. Our focus was on studying the geometry of the vortex lines in the local vicinity of the reconnection site. We have shown each type of vortex reconnection discussed in Subsection 1.3.2. 2D annihilation was demonstrated in the low Re simulations of Chapter 3 as the anti-parallel vortex tubes dissipated and expanded so much that they formed a weak double vortex sheet all along the lengths of the vortex tubes. It was also seen in the additional vortex rings created around the central axis of the box for higher Re simulations in Subsections 3.1.7 and 5.2.6. For the goal of even higher Re simulations the formation and annihilation of these rings must be taken into consideration as their lifespans appear to be short but their contribution to the turbulence will be of importance. As Re is increased these rings will become more frequent and prevalent.

2D reconnection was demonstrated in Chapters 2 and 3 between the two anti-parallel vortex tubes, the rate of which was found by integrating $\nu\nabla\times\boldsymbol{\omega}$ along the central axis which coincided with an X-line along which the reconnection was occurring. Using Stokes' Theorem in this way we were able to see how the

formation of the double vortex sheet, creating a line of non-zero $\nabla \times \boldsymbol{\omega}$ with zero vorticity, caused the reconnection. We were able to show that an increase in Re led to a smaller (in z) double vortex sheet but the value of $\nabla \times \boldsymbol{\omega}$ was far greater. It was also shown that the reconnected bridges lowered the reconnection rate, so as the fieldlines reconnect they slow the reconnection process for all the fieldlines reconnecting after them. We also showed the changing in curvature of the threads as they wrap around the bridges, effectively halting the reconnection process as the threads begin separating. However, the threads continue to dissipate and continue reconnecting in a far slower manner we referred to as 'post'-reconnection. We were unable to show that the reconnection would ever end as the size of the box did not allow for this. This would be something we would like to monitor in future work.

We also believe 2D reconnection was observed in Chapter 4 between the anti-parallel tubes, $\mathcal{A}$, and the central tube, $\mathcal{C}$. This reconnection was similar to previous orthogonal vortex tube reconnection [6, 43, 60] where the tubes position themselves in such a way before reconnection that they are anti-parallel where they are reconnecting. For further study we would like to study this orthogonal set-up and observe the vorticity fieldlines as they reconnect more closely to confirm that this is in fact a 2D reconnection or whether it is similar to 3D reconnection between vortex tubes.

2D reconnection was observed in Section 5.3 after axial flow was introduced to the anti-parallel vortex tubes. The addition and subsequent increase in axial flow was found to cause an increase in the reconnection rate and total amount of flux reconnected. This addition of axial flow means that the null-line where the 2D reconnection occurs is dragged along the dividing plane with the axial flow. This creates difficulties with measuring reconnection along this null-line. In future work we would like to be able to find the location of this null-line within

the dividing plane and thus find the values of $\nabla \times \boldsymbol{\omega}$ parallel to this line. With this information we could discover the reasons behind the increased reconnection rate.

3D 'slipping' was first found in Chapter 2 occurring symmetrically along the vortex tubes. This was difficult to measure using estimates from Wyper and Hesse [59] but we were able to show that the flux reconnected due to slipping was of the order of the vorticity flux of the tube. This reconnection and its relation to the kinetic helicity and axial flow of the vortex tubes is something we would like to investigate further in future.

3D 'slipping' was measured more accurately in Section 5.2 for the anti-parallel tubes with axial flow. With a net slipping rate measurement for the vortex tubes we were able to demonstrate the loss of twist as a function of radius from the centre of the tube and its relation to reconnection regions. Observing this further into the run it became apparent that the overall topology of the system was no longer as simple as the case in Chapters 2 and 3. As the fieldlines were no longer mapping to the symmetrical points at the boundary, it was not always possible to describe them as simply bridges or threads. We believe this to be an area of interest for further study.

In both the perpendicular and the non-zero helicity axial flow set-up we were able to observe 3D reconnection between the vortex tubes. These initial set-ups will be useful for future work in observing this phenomenon. Both scenarios also saw the generation of null points along the central axis and separators between them. This has been studied before in the magnetic reconnection case but not before in the vortex reconnection case. The separators formed in the scenarios were small in relation to the radius of the vortex tubes so a change to the initial condition will be needed to form larger separators.

In our work we were able to demonstrate the reconnection process by observing the vorticity fieldlines compared to the more common way of observing the vorticity isosurfaces. Doing so allowed us to see the direction of the fieldlines throughout the process. This proved important when we were able to see the axial flow oscillations along the vortex tubes and the 3D reconnection between the tubes as they approach each other at an angle. In isosurface plots the threads of the system would disappear after reconnection when they become weaker so their evolution cannot be viewed. Controlling what fieldlines are plotted we were able to observe them during the entire run and observe their change in curvature and their wrapping around the bridges.

We see very similar results to Melander and Hussain [41] and Hussain and Duraisamy [24]. They discuss in detail the movement of the bridges and threads through vorticity isosurfaces and contour plots in the symmetry and dividing plane. They also observed the three distinct reconnection phases using the thread flux as a function of time. Their discussion on the curvature of the threads and the 'end' of the reconnection process is in line with our results.

We also compare our discussion on axial flow with van Rees et al. [56]. With no initial axial flow we see axial flow oscillations in the vortex tubes in a similar manner to van Rees et al. With initial axial flow they observe an increase in reconnection rate with increased axial flow as we have. The shifting in the null-line where the 2D reconnection occurs is also observed in their isosurface plots.

The ultimate goal for these simulations would be being able to model Reynolds numbers of the magnitude observed behind aircraft, we are still 2-3 orders of magnitude short. Current computational power is not enough for this goal, at least with the numerical method we have used. Reynolds numbers over double our highest have already been modelled [56]. As we observed from our highest

Re runs of $Re = 4000$ and $Re = 2000$ in Chapters 3 and 4 respectively the reconnection process already changes greatly compared to runs at $Re = 800$. Being able to simulate at $Re = 10^4$ for our three set-ups we would expect a great change in the process. From even more additional vortex rings, forming around the central axis and along the threads, and possibly being able to study in more detail the spheromak topology seen to form in Subsection 4.4.3. It would also allow us to preserve the initial twist in the axial flow simulations, meaning that more twist will exist during the reconnection process allowing us to observe its effect in greater amounts. As we have shown care must be taken at such high Reynolds numbers due to the instabilities that will occur that may affect the analysis of the system.

Other future work would consist of simulations of different topological set-ups, many of which have been accomplished for magnetic reconnection. Vortex reconnection of trefoil knots has been studied in Kerr [27] but more analysis can be done. Work for the magnetic case includes the set-ups of braids, knots and Borromean rings [9, 13, 47]. Using similar set-ups for the vortex case will allow us to further study the behaviour of kinetic helicity during vortex reconnection. Finding initial velocity fields for these will not be simple however and will require further investigation than has been done for the simpler vortex tubes we have created here.

Bibliography

[1] H. Anton, I. C. Bivens, and S. Davis. *Calculus: Late Transcendentals Combined*. Wiley, 2005.

[2] R. J. Arms and F. R. Hama. Localized-Induction Concept on a Curved Vortex and Motion of an Elliptic Vortex Ring. *Physics of Fluids*, 8:553–559, April 1965.

[3] W. T. Ashurst and D. I. Meiron. Numerical study of vortex reconnection. *Physical Review Letters*, 58:1632–1635, April 1987.

[4] D. Ayala and B. Protas. Extreme Vortex States and the Growth of Enstrophy in 3D Incompressible Flows. In *APS Meeting Abstracts*, November 2014.

[5] R. Betchov. On the curvature and torsion of an isolated vortex filament. *Journal of Fluid Mechanics*, 22:471–479, 1965.

[6] O. N. Boratav, R. B. Pelz, and N. J. Zabusky. Reconnection in orthogonally interacting vortex tubes: Direct numerical simulations and quantifications. *Physics of Fluids A*, 4:581–605, March 1992.

[7] J. D. Buntine and D. I. Pullin. Merger and cancellation of strained vortices. *Journal of Fluid Mechanics*, 205:263–295, August 1989.

[8] M. D. Bustamante and R. M. Kerr. 3D Euler about a 2D symmetry plane. *Physica D Nonlinear Phenomena*, 237:1912–1920, August 2008.

[9] S. Candelaresi, F. Del Sordo, and A. Brandenburg. Decay of trefoil and other magnetic knots. In A. Bonanno, E. de Gouveia Dal Pino, and A. G. Kosovichev, editors, *Advances in Plasma Astrophysics*, volume 274 of *IAU Symposium*, pages 461–463, June 2011.

[10] S. Chandrasekhar. *Hydrodynamic and hydromagnetic stability*. Dover classics of science and mathematics. Dover Publications, cop. 1961, New York, 1981. Publi pour la 1re fois en 1961 chez Clarendon Press.

[11] S. C. Crow. Stability theory for a pair of trailing vortices. *AIAA Journal*, 8:2172–2179, December 1970.

[12] P. A. Davidson, Y. Kaneda, and K. R. Sreenivasan. *Ten Chapters in Turbulence*. Cambridge University Press, 2013.

[13] F. Del Sordo, S. Candelaresi, and A. Brandenburg. Magnetic-field decay of three interlocked flux rings with zero linking number. *Physical Review E*, 81(3):036401, March 2010.

[14] M. R. Dhanak and B. de Bernardinis. The evolution of an elliptic vortex ring. *Journal of Fluid Mechanics*, 109:189–216, August 1981.

[15] C. R. Doering and L. Lu. Maxial Enstrophy Generation in the 3D Navier-Stokes Equations. In *APS Division of Fluid Dynamics Meeting Abstracts*, November 2006.

[16] J. Feys and S. A. Maslowe. Elliptical instability of the Moore-Saffman model for a trailing wingtip vortex. *Journal of Fluid Mechanics*, 803:556–590, September 2016.

[17] T. Frankel. *The Geometry of Physics: An Introduction*. Cambridge University Press, 2004.

[18] J. F. Garten, J. Werne, D. C. Fritts, and S. Arendt. Direct numerical simulations of the Crow instability and subsequent vortex reconnection in a stratified fluid. *Journal of Fluid Mechanics*, 426:1–45, January 2001.

[19] Garten, J. F., Werne, J., Fritts, D. C., and Arendt, S. The effects of ambient stratification on the crow instability and subsequent vortex reconnection. *ESAIM: Proc.*, 7:151–160, 1999.

[20] J. M. Greene. Reconnection of vorticity lines and magnetic lines. *Physics of Fluids B*, 5:2355–2362, July 1993.

[21] M. Hesse, T. G. Forbes, and J. Birn. On the Relation between Reconnected Magnetic Flux and Parallel Electric Fields in the Solar Corona. *The Astrophysical Journal*, 631:1227–1238, October 2005.

[22] M. Hesse and K. Schindler. A theoretical foundation of general magnetic reconnection. *Journal of Geophysics Research*, 93:5559–5567, June 1988.

[23] G. Hornig. The Geometry of Magnetic and Vortex Reconnection. In C. F. Barenghi, R. J. Donnelly, and W. F. Vinen, editors, *Quantized Vortex Dynamics and Superfluid Turbulence*, volume 571 of *Lecture Notes in Physics, Berlin Springer Verlag*, page 373, 2001.

[24] F. Hussain and K. Duraisamy. Mechanics of viscous vortex reconnection. *Physics of Fluids*, 23(2):021701–021701, February 2011.

[25] J. E. A. John. *Gas dynamics*. Allyn and Bacon series in engineering. Allyn and Bacon, 1984.

[26] R. Kerr, D. Virk, and F. Hussain. Effects of Incompressible and Compressible Vortex Reconnection. In H.K. Moffatt and A. Tsinober, editors, *Topological Fluid Mechanics: Proceedings of the IUTAM Symposium*, pages 500–514, 1989.

[27] R. M. Kerr. Simulated Navier-Stokes trefoil reconnection. *ArXiv e-prints*, September 2015.

[28] R. M. Kerr and F. Hussain. Simulation of vortex reconnection. *Physica D Nonlinear Phenomena*, 37:474–484, July 1989.

[29] S. Kida and M. Takaoka. Vortex reconnection. *Annual Review of Fluid Mechanics*, 26:169–189, 1994.

[30] S. Kida, M. Takaoka, and F. Hussain. Reconnection of two vortex rings. *Physics of Fluids A*, 1:630–632, April 1989.

[31] C. Kittel and H. Kroemer. *Thermal Physics*. W. H. Freeman, 1980.

[32] J. Klapp, A. Medina, A. Cros, and C.A. Vargas. *Fluid Dynamics in Physics, Engineering and Environmental Applications*. Environmental Science and Engineering. Springer Berlin Heidelberg, 2012.

[33] D. Kleckner and W. T. M. Irvine. Creation and dynamics of knotted vortices. *Nature Physics*, 9:253–258, April 2013.

[34] H. Kudela and A. Kosior. Vortex particle method in parallel computations on graphical processing units used in study of the evolution of vortex structures. *Fluid Dynamics Research*, 46(6):061414, December 2014.

[35] E. A. Kuznetsov and V. P. Ruban. Dynamics of Vortex and Magnetic Lines in Ideal Hydrodynamics and MHD. In T. Passot and P.-L. Sulem, editors, *Nonlinear MHD Waves and Turbulence*, volume 536 of *Lecture Notes in Physics, Berlin Springer Verlag*, page 346, 1999.

[36] C. B. Laney. *Computational Gasdynamics*. Cambridge University Press, 1998.

[37] M. G. Linton, R. B. Dahlburg, and S. K. Antiochos. Reconnection of Twisted Flux Tubes as a Function of Contact Angle. *The Astrophysical Journal*, 553:905–921, June 2001.

[38] J. E. Marsden and A. Tromba. *Vector Calculus*. W. H. Freeman, 2003.

[39] J. S. Marshall, P. Brancher, and A. Giovannini. Interaction of unequal anti-parallel vortex tubes. *Journal of Fluid Mechanics*, 446:229–252, November 2001.

[40] P. C. Matthews. *Vector Calculus*. Springer Undergraduate Mathematics Series. Springer London, 2012.

[41] M. V. Melander and F. Hussain. Cross-linking of two antiparallel vortex tubes. *Physics of Fluids*, 1:633–636, April 1989.

[42] M. V. Melander and F. Hussain. Topological Aspects of Vortex Reconnection. In H.K. Moffatt and A. Tsinober, editors, *Topological Fluid Mechanics: Proceedings of the IUTAM Symposium*, pages 485–499, 1989.

[43] M. V. Melander and N. J. Zabusky. Interaction and 'apparent' reconnection of 3D vortex tubes via direct numerical simulations. *Fluid Dynamics Research*, 3:247–250, September 1988.

[44] K. Moffatt. *Magnetic Field Generation in Electrically Conducting Fluids*. Cambridge Monographs on Mechanics. Cambridge University Press, 1978.

[45] N. A. Murphy, C. Parnell, A. L. Haynes, and D. Pontin. The Emergence, Motion, and Disappearance of Magnetic Null Points. In *AAS/Solar Physics Division Meeting*, volume 44 of *AAS/Solar Physics Division Meeting*, page 100.103, July 2013.

[46] Å. Nordlund and K. Galsgaard. A 3D MHD code for Parallel Computers. Technical report, Niels Bohr Institute for Astronomy, Physics and Geophysics, 1995.

[47] D. I. Pontin, S. Candelaresi, A. J. B. Russell, and G. Hornig. Braided magnetic fields: equilibria, relaxation and heating. *Plasma Physics and Controlled Fusion*, 58(5):054008, May 2016.

[48] D. S. Pradeep and F. Hussain. Effects of boundary condition in numerical simulations of vortex dynamics. *Journal of Fluid Mechanics*, 516:115–124, October 2004.

[49] E. Priest and T. Forbes. *Magnetic Reconnection: MHD Theory and Applications*. Cambridge University Press, 2000.

[50] E. R. Priest, G. Hornig, and D. I. Pontin. On the nature of three-dimensional magnetic reconnection. *Journal of Geophysical Research (Space Physics)*, 108:1285, July 2003.

[51] A. Pumir and R. M. Kerr. Numerical simulation of interacting vortex tubes. *Physical Review Letters*, 58:1636–1639, April 1987.

[52] M. N. Rosenbluth and M. N. Bussac. MHD stability of Spheromak. *Nuclear Fusion*, 19:489–498, April 1979.

[53] P. G. Saffman. *Vortex Dynamics:*. Cambridge University Press, Cambridge, 001 1993.

[54] M. J. Shelley, D. I. Meiron, and S. A. Orszag. Dynamical aspects of vortex reconnection of perturbed anti-parallel vortex tubes. *Journal of Fluid Mechanics*, 246:613–652, January 1993.

[55] P. R. Spalart. Airplane Trailing Vortices. *Annual Review of Fluid Mechanics*, 30:107–138, 1998.

[56] W. M. van Rees, F. Hussain, and P. Koumoutsakos. Vortex tube reconnection at Re = 10^4. *Physics of Fluids*, 24(7):075105–075105, July 2012.

[57] D. Virk, F. Hussain, and R. M. Kerr. Compressible vortex reconnection. *Journal of Fluid Mechanics*, 304:47–86, 1995.

[58] W. Weiguo, S. Changchun, and C. Yaosong. Numerical study of vortex reconnection for two anti-parallel vortex tubes. *Acta Mechanica Sinica*, 11:209–218, August 1995.

[59] P. F. Wyper and M. Hesse. Quantifying three dimensional reconnection in fragmented current layers. *Physics of Plasmas*, 22(4):042117, April 2015.

[60] N. J. Zabusky and M. V. Melander. Three-dimensional vortex tube reconnection: Morphology for orthogonally-offset tubes. *Physica D Nonlinear Phenomena*, 37:555–562, July 1989.